Control of Failure Modes of Civil-Infrastructures Experiencing Large Soil Deformations Caused by Surface Fault Ruptures

地震断層近傍の地盤変形の空間分布を考慮した
構造物の破壊モードの制御

REPORT OF RESEARCH PROJECT
2000 GRANT-IN-AID FOR SCIENTIFIC RESEARCH (A)
(No. 12355020)
JAPAN SOCIETY FOR THE PROMOTION OF SCIENCE

May, 2003

Kazuo KONAGAI, Leader of the Project
Institute of Industrial Science
University of Tokyo

Muneo HORI, Earthquake Research Institute, University of Tokyo
Kimiro MEGURO, Institute of Industrial Science, University of Tokyo
Takashi MATSUSHIMA, Institute of Engineering Mechanics and Systems, Tsukuba Univ.
and
Yoshikazu YAMAGUCHI, Fill Dam Division, Public Works Research Institute

Control of Failure Modes of Civil-Infrastructures Experiencing Large Soil Deformations Caused by Surface Fault Ruptures

(地震断層近傍の地盤変形の空間分布を考慮した構造物の破壊モードの制御)

REPORT OF RESEARCH PROJECT
2000 GRANT-IN-AID FOR SCIENTIFIC RESEARCH (A)
(No. 12355020)
JAPAN SOCIETY FOR THE PROMOTION OF SCIENCE

May, 2003

Kazuo KONAGAI, Leader of the Project
Institute of Industrial Science
University of Tokyo

Muneo HORI, Earthquake Research Institute, University of Tokyo
Kimiro MEGURO, Institute of Industrial Science, University of Tokyo
Takashi MATSUSHIMA, Institute of Engineering Mechanics and Systems, Tsukuba Univ.
and
Yoshikazu YAMAGUCHI, Fill Dam Division, Public Works Research Institute

PREFACE

The 1999 ChiChi Earthquake in Taiwan, Kocaeli and Duzce Earthquakes in Turkey were a serious threat of possible destructions of mega-cities that spread over some hidden fault traces, and poses us difficult problems to minimize the fault-inflicted damage. In some less populated regions, limiting development within known and active fault zones would be very effective, and in California, USA, a law to this effect has been enacted since the early 1970s. This law, "Alquist-Priolo Fault Zoning act" (California Geological Survey, 2002), requires the State Geologists to establish regulatory zones (Earthquake Fault Zones) around the surface traces of active faults. Before a project is permitted, a geological investigation is required, and the construction of a building is permitted only if the building is located more than 50 feet off a fault trace. A similar zoning act has been enacted in Auckland, New Zealand (Wellington Regional Council, 2002) as well.

It is, however, noted that the laws in California and New Zealand deal with strike-slip faults, while about two thirds of active faults in Japan are thrust faults. As contrasted with strike-slip faults, a bundle of thrust faults make up a "wider brush" with many fault traces hidden in areas off the most suspicious line recognized from surface configurations. In addition, these areas are often densely populated in such overpopulated countries as Taiwan and Japan. It is therefore very difficult simply to limit development within active fault zones. Such a novel concept necessarily requires extensive discussions so that a social consensus is reached. For this, it is very important to grasp how soils and rocks immediately next to active fault traces would be deformed With this knowledge provided, we could discuss possible ways to "control failure modes" of civil-infrastructures, and thus to minimize losses of life and damage to a variety of structures.

This report summarizes fruits of the 3-years JSPS project (No. 12355020). As is the case of many reports, this report is an outgrowth of different peer-reviewed papers published in both domestic and international journals and ongoing reports that appeared in the two International Workshops organized by the JSPS project team. Chapters in this report are, thus, based on these papers. However, they are so arranged that the outline of this study and remaining problems would be brought in full relief.

Acknowledgement here may be in order. I am indebt to many people whose suggestions and criticisms have helped us with this project. Especially, Dr. Hiroyuki Kameda and Dr. Neil Briton, Director General and EqTAP Chief Coordinator, Earthquake Disaster Mitigation Research Center, National Research Institute for Earth Science and Disaster Prevention, gave us important pieces of advice for a possible integrated approach involving social sciences. Keynote lectures were provided at two workshops by the following outstanding researchers, Prof. Jonathan Bray, University of California, Berkeley, USA, Prof. Risat Ulusay. Hacettepe University, Turkey, Prof. Derin URAL, Istanbul Technical University, Turkey, Dr. Kung Chen Shan, Vice President, SINOTECH, Taiwan, Prof. Yasutaka IKEDA, Univ. of Tokyo, Prof. C.H. Chen, National Taiwan University, Dr. Raymundo Punongbayan, Executive Director, Earthquake and Megacities Initiative, Metro Manila, Philippines, Dr. Takefumi Takahashi, Executive Director, Metropolitan Expressway Public Corporation (former Director General for Disaster Management, Cabinet Office) and Prof. Masanori Hamada, Waseda University. Their lectures, covering a variety of aspects of fault-induced damage, provided excellent overviews of fault-related research, social issues and possible remedial measures. Dr. Naoya Yamaguchi, Mr. Jorgen Johansson, former and present Research Associates, and Mr. Toshihiko Katagiri,

Technical Associate at Konagai Lab., have devotedly tried out some new ideas in our experiments. Regarding the results obtained through experiments and numerical simulations, we had frequent opportunities to discuss with Dr. Akira Sangawa, National Institute of Advanced Industrial Science and Technology (AIST), Guest Professor at IIS, University of Tokyo, Prof. Takashi Nakata, Hiroshima University, Dr. Yoshitaka Murono, Railway Technical Research Center, Guest Associate Professor, IIS, University of Tokyo, and the members of the JSCE technical committee. The discussions were very constructive. Lastly, grateful acknowledgment is made to Ms. Tomomi Sannomiya, Secretary at Konagai Lab., for her help in preparing necessary materials for this final report.

Kazuo KONAGAI
Leader of the project

EqTAP: Earthquake and Tsunami
IIS: Institute of Industrial Science, University of Tokyo
AIST: National Institute of Advanced Industrial Science and Technology
EDM: Earthquake Disaster Mitigation Research Center, National Research Institute for Earth Science and Disaster Prevention

Publication list

(Peer-reviewed papers)

Konagai, K. and J., Johansson: Two Dimensional Lagrangian Particle Finite Difference Method for Modeling Large Soil Deformations, *Structural Eng./ Earthquake Eng.* **18(2)**, 91s-95s, 2001.

Konagai, K. and M. Numada: Pseudo-three dimensional Lagrangian Particle Finite Difference Method for modeling long-traveling soil flows, *Journal of Japan Society of Dam Engineers*, **12(2)**, 123-128, July, 2002.

Matsushima, T., Ishii, T. and Konagai, K.: Observation of grain motion in the interior of a PSC test specimen by Laser-Aided Tomography, *Soils & Foundations*, Japanese Geotechnical Society, **42(5)**, 27-36, 2002.

Matsushima, T. and Konagai, K: Grain-Shape Effect on Peak Strength of Granular Materials, *Computer Methods and Advances in Geomechanics*, Proc. 10ACMAG, Desai et al. eds., **1**, pp.361-366. 2001.

Ramancharla P. K. and Meguro K.: Non-linear static modeling of Dip-Slip faults for studying ground surface deformation using Applied Element Method, *Structural Eng./Earthquake Eng.,* Japan Society of Civil Engineers, **9(2)**, 169-178, 2002.

Meguro K and Ramancharla P. K.: Numerical Study on the characterictics of the ground responses in the Near-Fault regions, *Proc. 11th Japan earthquake engineering Symposium* , Japanese Geotechnical Society, 397-400, 2002.

Terada, K., Hori, M., Kyoya, T. and Kikuchi, N.: Simulation of the multi-scale convergence in computational homogenization approach, International Journal of Solids and Structures, Vol. 37, pp. 2285-2311, 2000.

Hori, M., and Oguni, K.: Bifurcating initiation and evolution of periodic micro-defects, Materials Science and Engineering, A285, pp. 122-129, 2000.

Anders, M. and Hori, M.: Three-dimensional stochastic finite element method for elasto-plastic body, Int. J. Numer. Meth. Engng., Vol. 51, 449-478, 2001.

Hori, M.,, Anders, M, and Mizutani, T.: Analysis of periodic shear band formation: model experiments and numerical simulation, in Bifurcation and Localization Theory in Geomechanics (ed. by H.B. Muhlhaus, et. al), pp. 311-319, 2001.

Sasaki, K. Terada, K. Ikeda and Hori, M.,: Appropriate number of unit cells in a representative volume element for micro-structural bifurcation encountered in a multi-scale modeling, Comput. Methods, Appl. Mech. Engrg. 191, pp. 2561-2585, 2002.

M.L.L. Wijerathne, Kenji Oguni and Muneo Hori: Tensor field tomography based on 3D photoelasticity, Mechanics of Materials, Vol. 34, No. 9, pp. 533-545, 2002.

Hori, M.,, M. Anders and H. Gotoh; Model experiment and numerical simulation of surface earthquake fault induced by lateral strike slip, Structural Eng./Earthquake Eng., JSCE, Vol. 19, No. 2 (special issue) pp. 227-236, 2002.

Nakagwa, H., Hori, M. and Oguni, K.: Spectral finite element method for surface earthquake fault problem, Proceedings of 4th Int. Conf. Compu. Stoch. Mech., 2002.

Hori, M., Ichimura, T. and Nakagawa, H.: On analysis methods for stochastic model: application to earthquake problems, J. Strcut./Earthquae Eng., JSCE, 2003.

CONTENTS

Chapter 1

INTRODUCTION

In terms of death toll, we had had some quiet 40 years in Japan since the devastating Fukui Earthquake of 1948 (M=7.3), which killed 3,769 people. Seismic activity in Japan, however, has seemingly increased since the 1993 Kushiro Earthquake, which was then followed by intense earthquakes in rapid succession. And the January 17, 1995, South Hyogo Earthquake (Kobe Earthquake hereafter) was responsible for the total of 6432 deaths and serious destruction of urban facilities in Kobe, a mega city spreading over a bundle of hidden faults along the Rokko Mountains. The Kobe Earthquake stimulated a sharp rise in demand for rational design procedures for urban facilities, and revisions of these design codes were made reflecting lessons learned from the Kobe Earthquake. However few lines in these codes describe remedial measures for possible destructions caused by fault dislocations.

In its background was the good luck of Japan that most of seismic faults activated in the past one century appeared off important civil-infrastructures and/or urbanized areas, and a limited number of damaged facilities can be enumerated in only a "one-page" list. But we should not forget that we have been expanding cities in the past several decades without paying due regard to seismic faults (see **Figures 1** and **2**). This situation seems to be the same to all Asian Pacific regions. With a rapid population growth in the 20th century, many people are now living in a more disaster prone area where nobody used to live.

Aug. 17, 1999 Kocaeli Earthquake in Turkey and Sept. 21, 1999 ChiChi Earthquake in Taiwan were a serious threat to mega cities (JSCE, 1999). One of the most spectacular aspects of these earthquakes was the damage to structures inflicted directly by faulting, which poses difficult problems to us about minimizing the fault-related damage. In Chi-Chi earthquake, Taiwan, the activated fault appeared branching east off the recognized trace of the Chelungpu fault in the vicinity of Feng-Yuan City, and crossed the Shih-Kang dam causing three of its spillways to be completely destroyed by a vertical offset reaching 10 meters. In the Kocaeli earthquake, faulting and the resulting ground ruptures caused the collapse of hundreds or more buildings and modern engineered structures. A discussion on this issue, thus, must be based on a quite different scenario from those for ordinary designs in which ground accelerations and/or velocities are crucial factors.

The aims of this JSPS project (No. 12355020) are (1) to investigate the previous examples of faulting and fault-related damages, (2) to develop efficient and reliable tools for predicting possible extents of fault-induced soil deformations, (3) to discuss the possible measures for minimizing losses of life and damage to a variety of structures, and with all abovementioned, (4) to enable decision makers to better understand the nature of the hazard and to assist them to identify appropriate ameliorative actions. It was timely that the Japan Society of Civil Engineers (JSCE) organized a technical committee for establishing remedial measures for damage to

civil-infrastructures, and it was thus a natural course of events that the JSPS research activity of this project incorporated works of many others, especially with respect to risk identification and analysis. Some of its important activities were then further expanded as a subject of **EqTAP** project (Development of **E**arth**q**uake and **T**sunami Disaster Mitigation Technologies and Their Integration For the **A**sia-**P**acific Region"). The policy for the **EqTAP** research was that disasters were to be investigated not merely from a scientific/engineering perspective, but from an integrated approach involving social sciences as well, and its fruits could be used to establish more comprehensive earthquake disaster prevention plan. To answer this demand, the JSPS project team, together with the JSCE technical committee, organized two workshops inviting outstanding researchers from USA, Turkey, Taiwan, and Philippines, and discussed an assumed scheme for Seismic-Fault-Zoning Act as a chart for integrating these individual works. In this scheme, thrust faults receive due attention because noticeable number of active fault systems in Japan and Taiwan are thrust faults. Zoning for thrust faults is in general more difficult than that for strike-slip faults because a bundle of thrust faults often make up a "wider brush" with many fault traces hidden in areas off the most suspicious line recognized from the surface configuration.

This report summarizes fruits of the 3-years JSPS project (No. 12355020). Among the missions, making up a digital database of previous examples of faulting and fault related damages is the essential basis for further advanced discussions. Chapter 1 describes some examples taken from this database. Chapter 2 describes newly developed tools for predicting possible extents of fault-induced soil deformations, and Chapter 3 discusses possible remedial measures for damage to some important civil infrastructures.

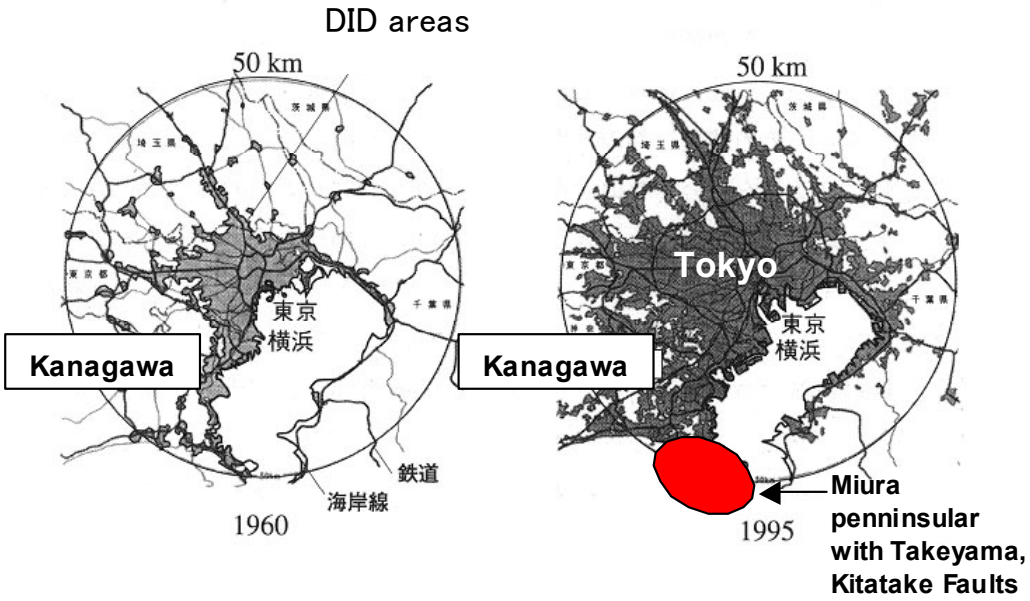

Figure 1 Expansion of DID area in Metro Tokyo and Yokohama
(White paper of the Metro police, 1999)
DID: Densely Inhabited District, a district consisting of mutually adjoining National Census areas, each of which has a population density larger than 4000 inhabitants per square kilometer, and having a combined population larger than 5000.

(a) Areal photos

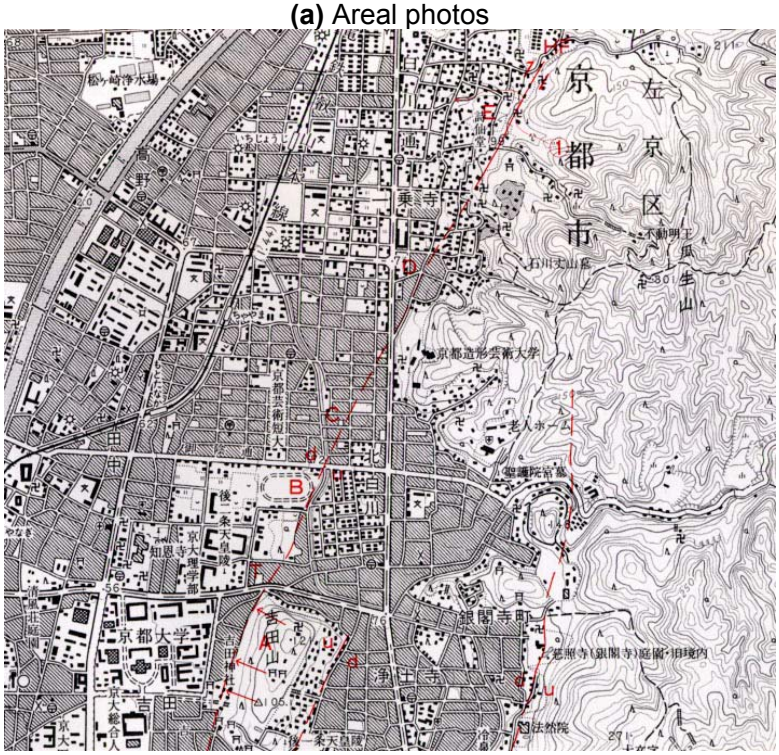

(b) Location of Hanaore fault

Figure 2 Hanaore Fault crossing Kyoto
(Watanabe, M. and Suzuki, Y., 1999.)

(a) The pair of photographs can be perceived as a single image in terms of depth. (b) Based on 14C dating of exposures at three trenches excavated across the fault, a surface-rupturing earthquake is estimated to have occurred on the northeastern splay of the Hanaore fault an around mid 16th century. As for its southern part, however, at least one event seems to have occurred since 2000B.C. And Kyoto, a historical city with 2.6 millions population, has never experienced this fault activation.

REFERENCES

Watanabe, M. and Suzuki, Y (1999): 3D photographs of seismic fault traces, *Kokon Shoin Press*.
White paper of the Metropolis (1999).
JSCE Reconnaissance Team (1999):

Chapter 2

PREVIOUS EXAMPLES OF FAULT-INDUCED DAMAGE

2.1 INTRODUCTION

Making up a digital database of previous examples of faulting and fault related damages is certainly an essential basis for further advanced discussions. During the term of the JSPS research project, the investigators devoted themselves to collecting as many examples as possible. For this purpose, they made investigation trips to some affected areas including Turkey, Taiwan, Philippines and Iran, and organized international workshops twice asking contributions from these areas. The data archive is thus an integration of works of many other researchers. The collected materials are listed in **Tables 2.1** and **2.2**. Fault-related failures will fall into two broad categories: ground rupture-induced and ground shaking-induced failures. This chapter describes examples focusing mostly on ground rupture-induced failures. The examples taken herein include damage to tunnels, dams and slope failures.

Table 2.1. Ground rupture-inflicted damage examples

Structure	Contents
Tunnels	Tanna Tunnel (1930 North Izu Eq., Japan), Crack map of the tunnel etc. (from RTRI)
	Inatori Tunnel (1978 Off the IzuOshima island Eq.) Crack map of the tunnel, Buckled rail: Even off the fault rupture plane, buckling of rails can occur, and cause derailment etc. (from RTRI)
	Rokko Tunnel (1995 Kobe Eq.), Crack maps etc. (from RTRI)
	Outlet tunnel of Kakkonda hydropower station (1998 Mid-North Iwate Eq, Japan), Crackmap of the damaged tunnel etc. (from Tohoku Electric Power Co. Ltd)
	Outlet tunnel of ShihKang Dam (1999 ChiChi Eq., Taiwan, from JSCE reconnaissance team etc.).
Dam	ShihKang area (1999 ChiChi Eq., Taiwan), Taiwan: Survey map of Sihkang area . (from Collaborators in Taiwan incl. Kung C.S.), Crack map of the dam (from Konagai K., Sugimura Y., Miura S.) etc
Bridges	Bol viaduct (1999 Duzce Eq., Turkey) (from Kawashima K.)
	ShiWei Bridge (1999 ChiChi Eq., Taiwan) Rigid body motions of piers (from Kosa, K. and Yamaguchi, E.)
	BeiFong Bridge (1999 ChiChi Eq., Taiwan) Movement of piers, Ground movement along the bridge (from Kawashima K.)
	WuShi Bridge (1999 ChiChi Eq., Taiwan) Movement of piers, Ground movement along the bridge (from Kawashima K. and Kosa, K.)

(The table continues on the next page)

(This table continues from the previous page).

Soils	Yalova-Izmit areas (1999 Kocaeli Eq., Turkey), Survey map etc. showing subsidence of ground (from ULSAY, R., Haceteppe Univ., URAL, D., Istanbul Technical Univ. and the Japan Geotechnical Society team)
	Tiger Head Hill landslide (1999 ChiChi Eq., Taiwan), Sketch of the landslide mass, etc. (from Collaborators in Taiwan and from Kamai, T.)
Others	Traces of faulting found at ruins (many eqs. In Japan) (from Sangawa, A, AIST)

Table 2.2. Ground shaking-inflicted damage examples

Dam & reservoir	Kasho dam (2001 West Tottori Eq., Japan) Analysis of seiche (from Ohmachi, T.)
Dwellings	Abdarreh village (2002 Changureh Eq., Iran)

Abbreviations
RTRI Railway Technical Research Institute
AIST National Research Institute of Advanced Industrial Science and Technology

2.2 DAMAGE TO TUNNELS

2.2.1 Tanna Tunnel (1930 North-Izu Earthquake):

Construction of 7.8km-long Tanna Tunnel was planned to bypass a railway route winding up across mountains in Hakone and Tanzawa area. The construction started in 1918 and was making little progress when it was crossing the fault-fracture zone beneath the Tanna basin (**Figure 2.1**). The most serious problem there was water inflow through fractured rocks, and measures taken included injecting grout, and using pressurized excavation chamber. In addition, a number of branch holes were excavated to drain waters, and the total length of these branches reached 16 km, two times as long as the main tunnel. An intense earthquake (M7.0) occurred at 4:03AM JST, Nov. 26, 1930, exactly when two of the branches (drainage holes) reached its fault rupture plane.

There were four points **(a)-(d)** seriously damaged:

(a) & (b) Cut surfaces of two drainage holes, South #2 and #3, reaching the fault rupture surface at 3660m and 3662m depths respectively from the western entrance (Figure 2.2): Since these tunnels were pushed through a fractured rock, they were needed to be supported soon after the excavation. In Drainage hole #3, Pi-shaped steel frame were quickly set up at a regular interval of about 1.5m, and the wall was then boarded up with many pieces of wood. The dislocated rock drew both the end frame and several pieces of wood into the mountain. **Figure 2.3** shows the cut surface of Drainage hole #3. Several pieces of wood were seen half embedded in the left side of the rock.

(c) Point at 3265-3325m from the west entrance:
About a 60 m stretch of the tunnel crown at this point had not been covered up with concrete yet, and therefore exposed frames could not sustain a large soil pressure. A soil mass of about 1200 m^3 fell all of sudden into the main tunnel killing 3 persons.

(d) Point at 3050 m from the west: A branch of the Tanna fault seems to have dislocated, and cracked the concrete lining. The east side of this point has subsided by about 23 cm.

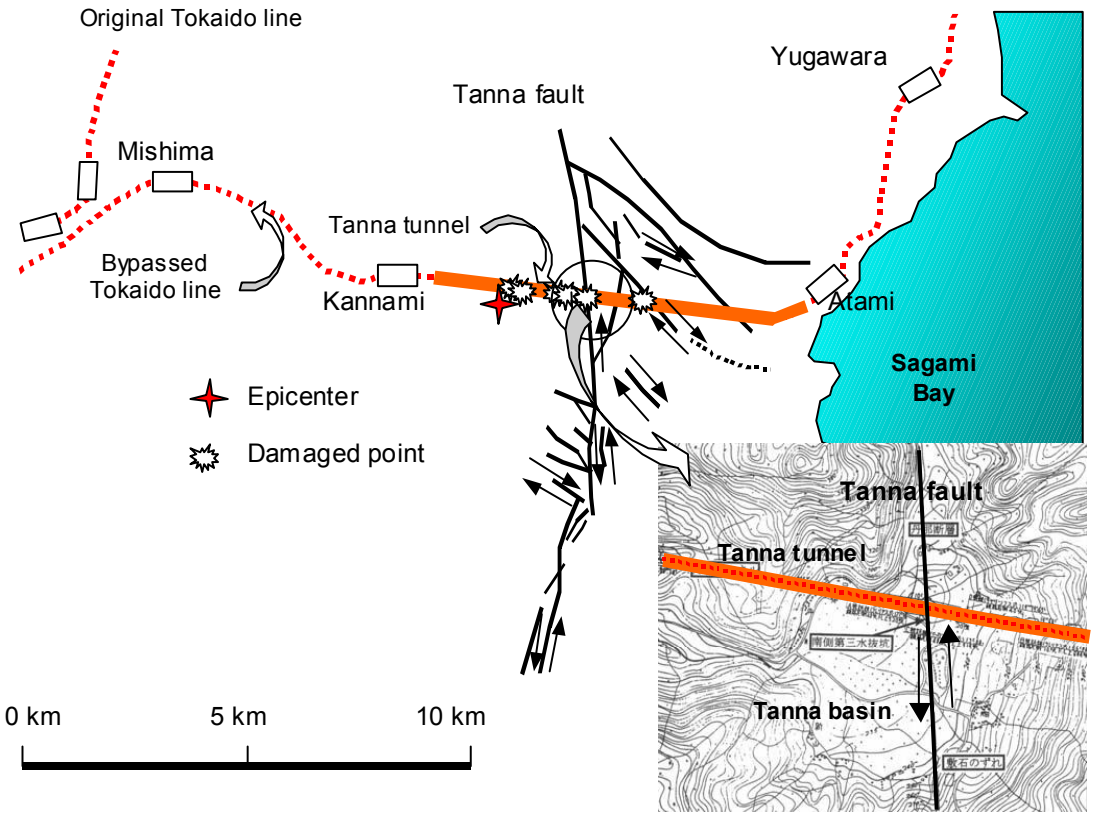

Figure 2.1. Tanna tunnel and the Tanna fault system.

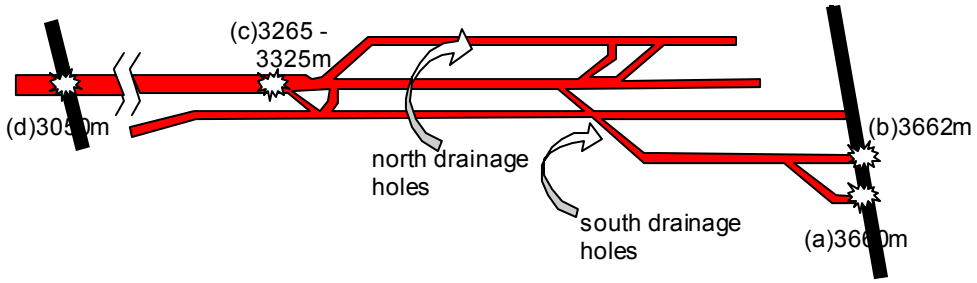

Figure 2.2 Drainage holes and damaged points

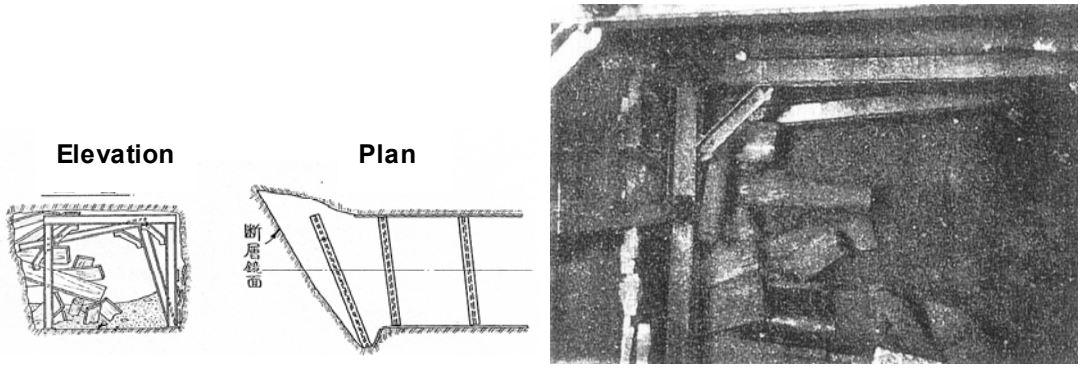

Figure 2.3. Drainage hole #3

2.2.2. **Outlet Tunnel of 2nd Kakkonda Hydropower Station (1998 Mid-north Iwate Earthquake):** Shizukuishi, Iwate Prefecture, is located in the middle of the Shizukuishi Basin surrounded by peaks of northern Oou mountains and Mt. Iwate, mostly volcanoes rising to elevations of more than 1,000 meters. The volcanoes were quite active during the Quaternary Period, and this area has been covered deep with their products. Rivers from these mountains have carried over centuries volcanic ashes and other suspended matters in their waters, and have formed the basin[1)]. An intense earthquake shook Shizukuishi area at 16:58, September 3, 1998, injuring 10 people. An intensity 6-weak on the Japan-Meteorological Agency (JMA) scale of 7 was registered in Shizukuishi (**Figure 2.4(a)**). The hypocenter of the earthquake (39.8N, 140.9E, focal depth = 10 km, origin time 16:58, JMA) was located about 20 km north-west of Morioka city. The magnitude of the main shock was 6.1 on JMA scale.

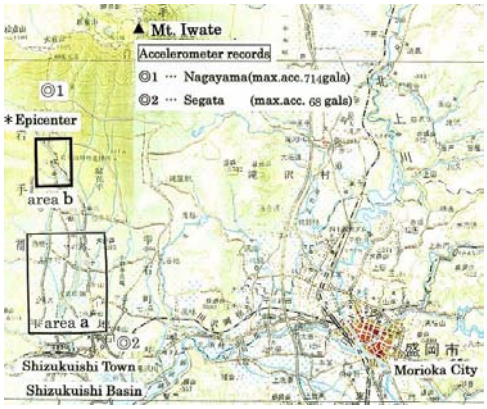

(a) Shizukuishi Area

(b) Fault mark appeared in paddy field

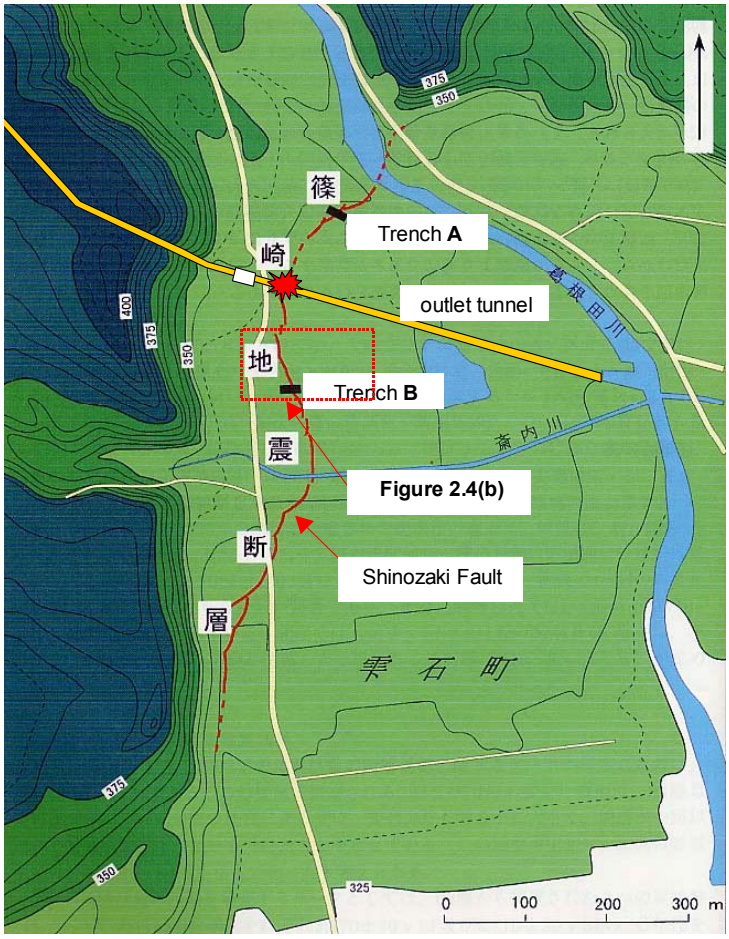

(c) Area **a** in **Figure 2.4(a)** (right)

Figure 2.4. Shinozaki Fault appeared in the 1998 Mid-north Iwate Earthquake

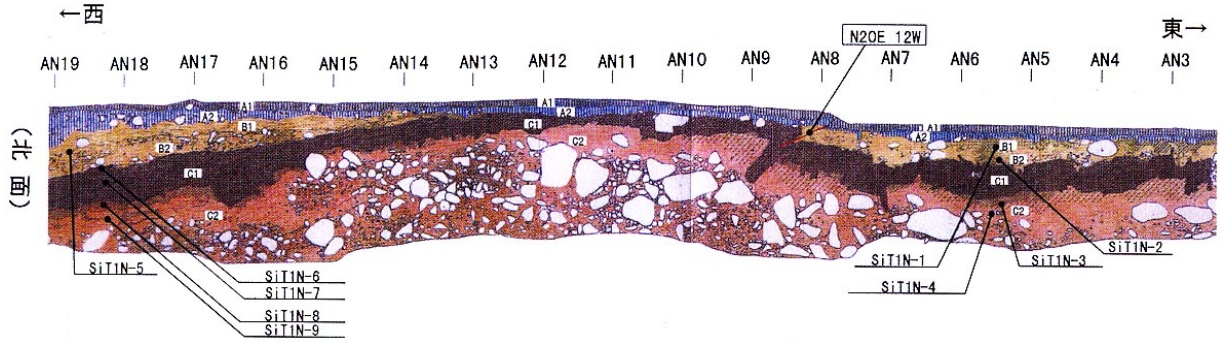

Figure 2.5. North wall of Trench **A** across the Shinozaki Fault (Azuma et al., 1999)

The area was on strict guard against a possible eruption of Mt. Iwate, because frequent volcanism-related tremors had been observed for a month. Though this symptom did not lead to any actual eruption after all, JMA had taken a quick action of spreading a dense observation network over the area. The earthquake that followed this symptom was, thus, eventually recorded by these seismometers. After this earthquake, it was first suspected that the earthquake might have some link with this volcanic activity. But fault rupture planes, which appeared in this earthquake, evidenced that the dip-slip movement of this fault caused this earthquake.

The focal depth of this earthquake was quite shallow enough for its fault rupture planes to appear on the ground surface; the fact is quite unusual for earthquakes of this magnitude. The fault rupture planes were found roughly lined up at irregular intervals near a scarp formed along the Kakkonda glen. One of the rupture planes which appeared in a paddy field had a straight raised mark extending a 880 m distance, clearly showing a compressive dip-slip movement of this fault (**Figure 2.4**). The average upward movement of the hanging wall of this fault reached or exceeded 10 cm in this paddy field. An investigation team from the Active Fault Research Center, National Research Institute of Advanced Industrial Science and Technology (AIST), excavated two trenches (Trench **A** and Trench **B**) across this fault mark (Azuma et al., 2000). **Figure 2.5** shows a sketch of the north walls of Trench **A**. There were seven layers (A1, A2, A3, B1, B2, C1 and C2) observed on the exposed wall, which fall into four broad categories: (1) A1-A3: Surface cultivated soils, (2) B1 and B2: fine and coarse sands including gravels, respectively, and (3) C1: old volcanic products of about 2500 years ago, and (4) C2: the layer including large boulders. A west-dipping fault rupture trace was found on the exposed wall forcing its way up through Layers C1, B2 and B1. The strike and dip of this plane were N20°E and 12°W, respectively. The seven Layers on the hanging wall side were slightly bent upward.

These rupture planes that appeared on the ground surface form a part of Shizukuishi-Seien fault belt whose presence has been suggested by many geologists[1)]. Continual movement of this fault belt has formed the scarp along the Kakkonda river, and by virtue of this configuration, some hydroelectric power stations were constructed along the Kakkonda river. A concrete outlet tunnel of the second Kakkonda hydroelectric power station runs across the fault rupture plane exactly beneath the paddy field. As an inevitable consequence, the circular tunnel wall was cracked up into several large pieces and smaller fragments (**Figures 2.6** and **2.7**). Some pieces of the cracked wall were pushed in the tunnel reducing the tunnel's cross-section. One cracked piece of about 2 m high and 2 m wide completely fell down onto the invert allowing the soil with big boulders (30 ~ 50 cm) to fall into the tunnel. This movement of the fault was also responsible for the damage to a concrete drain (Sainai river) crossing the paddy field. Another fault plane branching east off the major fault crossed the Kakkonda river and buckled the pavement of the prefectural route 100 (Konagai, et al. 1999). An open aqueduct leading to the second Kakkonda hydroelectric power station was also damaged. Diagonal cracks found on its concrete walls are suggestive that the aqueduct might have experienced compressive force in its axial direction. No clear evidence of fault dislocation was found there.

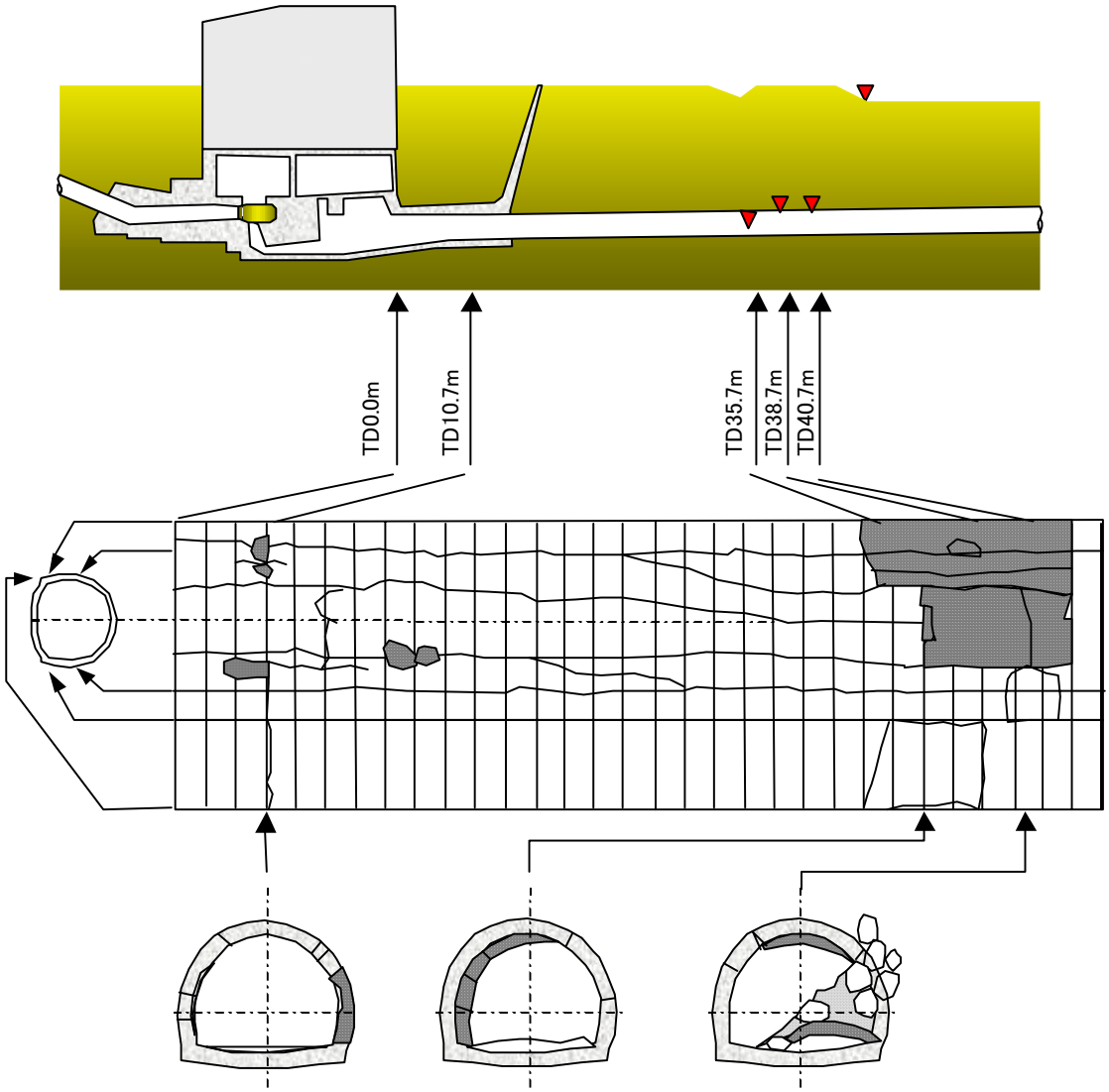

Figure 2.6. Development and cross-sections of cracked tunnel（after Hashimoto, 1998）

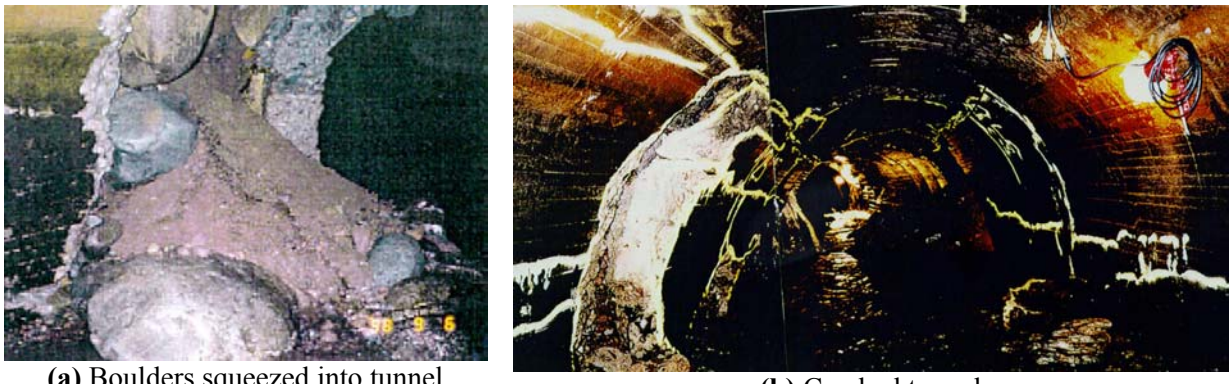

(a) Boulders squeezed into tunnel

(b) Cracked tunnel

Figure 2.7. Outlet tunnel of 2nd Kakkonda Hydropower station
(Photo: Tohoku Electric Power Co. Ltd.)

2.2.3. **Inatori Tunnel (1970 Off-Izu Oshima Earthquake):**

A fault appeared in the 1970 Off Izu Oshima Earthquake (M7.0) across Inatori railway tunnel (906 m long) of the Izukyu line (**Figure 2.8**). The northeastern half of the tunnel was pushed seaside, and an 85 cm lateral displacement was reached at the east mouth of the tunnel, while its western mouth was pushed about 20 cm up. The tunnel was the most seriously deformed at around the point where the tunnel was cut by the fault. **Figures 2.9(b)**, **(c)** and **(d)** show cross-sections at 31.055km, 31.035 km and 31.010 km points from Ito (North starting station of the Izukyu line) respectively. These cross sections were all pushed slightly out of shape exactly like those of a kinked water hose. As the consequence, crowns were bent up against soils, and some parts of their inner surfaces broke up into flakes. Some sidewall blocks were thrust forward lying between two less deformed blocks. Some invert concrete blocks were pushed up. Though cracked, the lining fortunately held the soil pressure probably because the surrounding soils had been softened by solfataric and/or hydrothermal activities.

Rails were buckled at several points (**Figure 2.10(a)**). The biggest buckling was found at **Point A,** near the southwestern mouth of the tunnel where the tunnel goes through a debris deposit. Assuming that the shape of the buckled rail is expressed as:

$$f(x)=\begin{cases} A\sin\dfrac{\pi x}{L_0}\sin\dfrac{\pi x}{L_1} & \cdots\cdots 0\le x\le L_0 \\ 0 & \cdots x<0,\quad L_0<x \end{cases} \tag{2.1}$$

with

$$\sin\frac{2\pi L_0}{L_1}=0 \tag{2.2}$$

The average strain ε induced over the L_0 distance is obtained by

$$\begin{aligned} \varepsilon &= \frac{1}{L_0}\int_0^{L_0}\left(\sqrt{1+\left(\frac{df}{dx}\right)^2}-1\right)dx \\ &\cong \frac{1}{2L_0}\int_0^{L_0}\left(\frac{df}{dx}\right)^2 dx \end{aligned} \tag{2.3}$$

Substituting Equation (2.1) in Equation (2.3), one obtains:

$$\varepsilon\cong\frac{\pi^2}{4}\left(\frac{A}{L_0}\right)^2\left\{1+\left(\frac{L_0}{L_1}\right)^2\right\} \tag{2.4}$$

Overall strain of about 0.00114% was calculated for the total 50m buckling at Point A (**Figure 13**). This overall strain, however, may not reflect the strain of the soil supporting the rail. A rail buckling often takes place where ties are exposed and the rail loses its lateral support. **Figure 12b** shows that rails were buckled where they were pushed up. The overall strain thus depends greatly on the distance where rails were lifted off their subsoils. As for **Point A**, one can say that there was about 5.7 cm shortening of the subsoil.

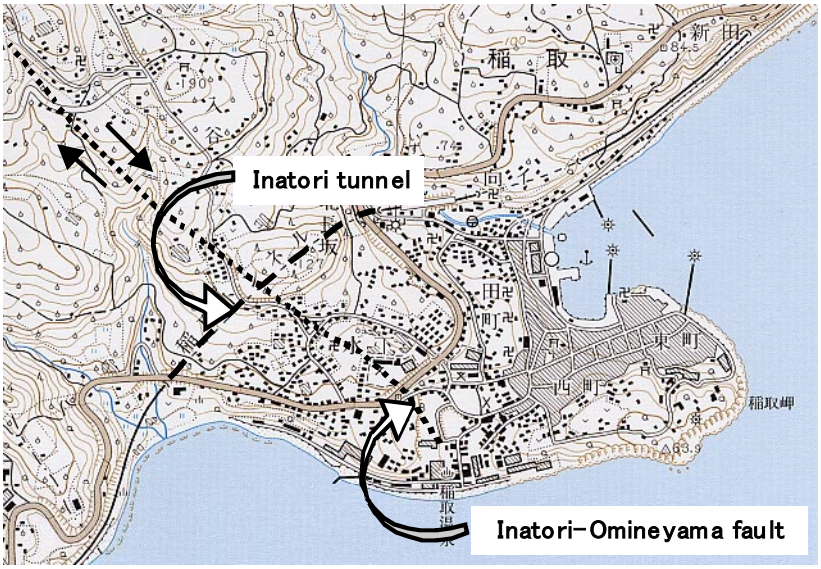

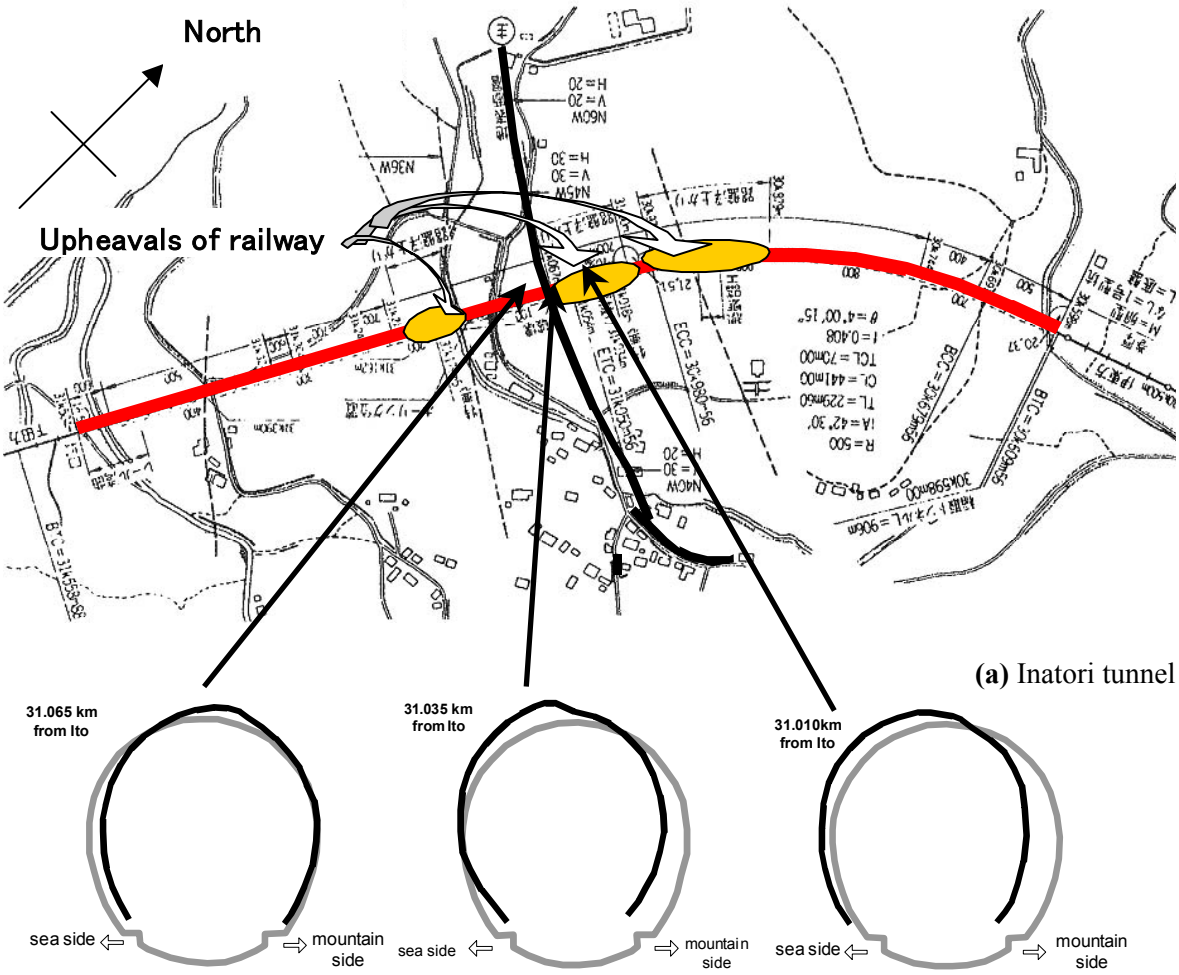

(a) Inatori tunnel

(a) 31.055km Point **(b)** 31.035 km Point **(c)** 31.010 km Point

Figure 2.8. Deformed cross sections of Inatori tunnel

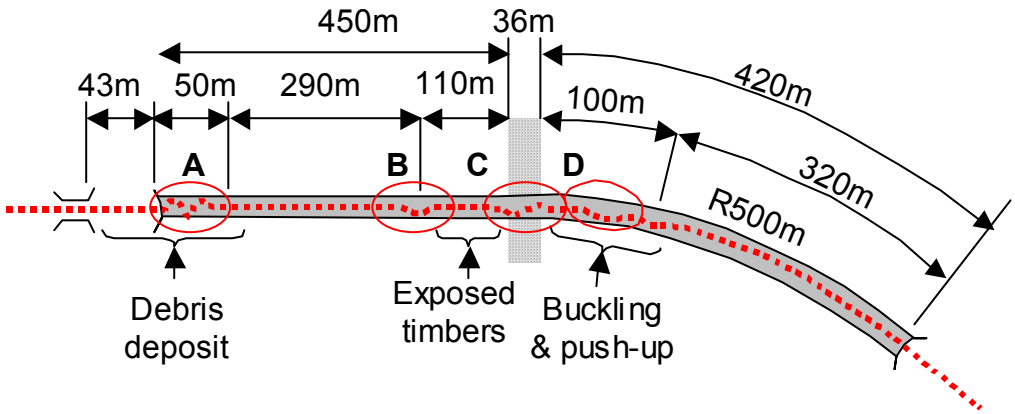

(a) Locations of bucked rails

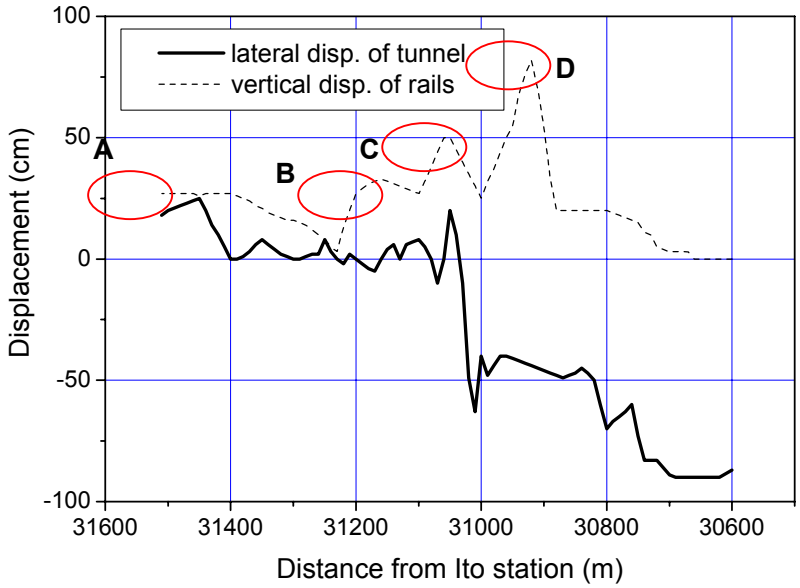

(b) Pushup of rails and lateral displacements of Inatori tunnel

Figure 2.9. Buckled rails and tunnel deformation

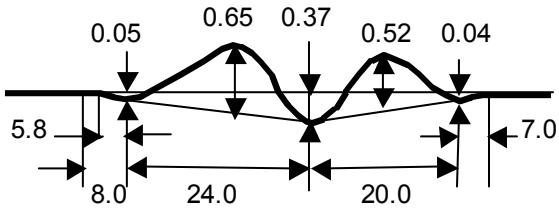

Figure 2.10. Rail buckling at **Point A** in **Figure 2.9**.

2.3 DAMAGE TO DAMS

2.3.1 ShihKang Dam (1999 ChiChi Earthquake, Taiwan):

The Central Geological Survey (CGS), Taiwan, has confirmed that 51 active and/or suspicious faults longer than 5 km exist, and are classified as follows:

(1) **1st category active faults (9):**

a) activated at least once in the past 10,000 years,
b) having caused some damage to existing structures,
c) responsible for earthquake occurrences,
d) having deformed alluvial soil deposits, and
e) whose presences are clearly recognized from surface geological configurations.

(2) **2nd category active faults (15):**

a) activated at least once in the past 10,000 years, and
b) having deformed diluvial terraces.

(3) **Suspects (27):**

a) with ambiguous features in Quaternary configurations,
b) with ambiguous features in laterite soils, and
c) looking alike but without any clear evidences.

The earthquake, with a magnitude of 7.3 (Central Weather Bureau, **CWB**) took place at 1:47 AM, local time on 21, Sept., 1999. The epicenter was located at latitude 23.85°N and longitude 120.81°E. **Figure 2.11** shows the main shock and aftershocks. The earthquake that originated at a shallow focal depth of 6.99 km produced spectacular reverse faulting. The activated fault seems to have appeared exactly along the CheLungPu Fault, whose presence had been already recognized and classified into the 2nd category of active faults. Hence, the activated fault, in this section hereafter, will be referred to as the CheLungPu Fault. The activated fault, however, appeared branching east off the recognized trace of the CheLungPu in the vicinity of Feng-Yuan City, and crossed the Shih-Kang area. Zooming in on this area, it is found that this branch also shoots out further thinner separate branches. Some details of this area will be given later on. **Figure 2.12** shows dislocation vectors along the CheLungPu Fault (Otsuki, 1999). The different diameters of gray circles show the extent of vertical offsets, and arrows represent net slips. The offsets, in general, increase as we go north, and the maximum net offset of 13.5m is reached at Point 10, the second largest net offset of 11.1m at Point 12. **Figure 2.13** shows elevation increments measured over 7 km distance in ChunShinHin town across the fault. The eastern side of the fault seems to have been continuously pushed up, this might be interpreted as an early sign of the event.

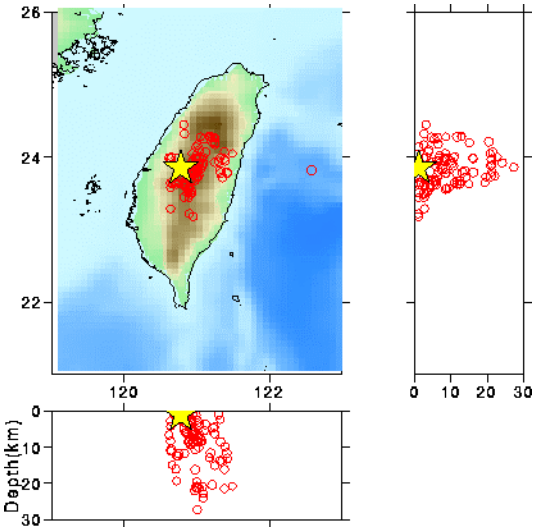

Figure 2.11 Aftershocks distribution of the Sept. 23, 1999 ChiChi Earthquake, Taiwan (http://wwweic.eri.u-tokyo.ac.jp/topics/taiwan/yoshin2e.html)

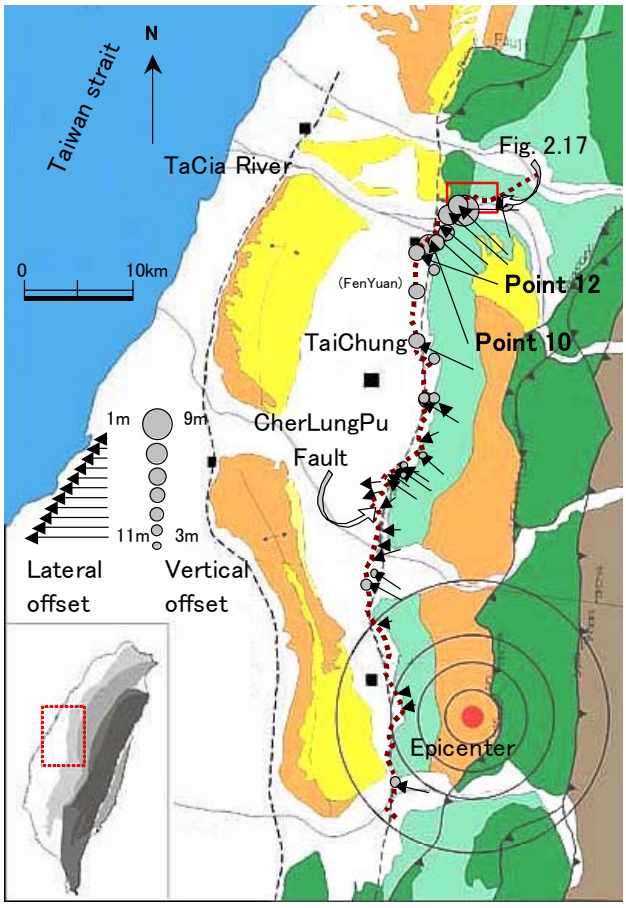

Figure 2.12. Dislocations along Chelungpu fault (Otsuki and Yang, 2000)

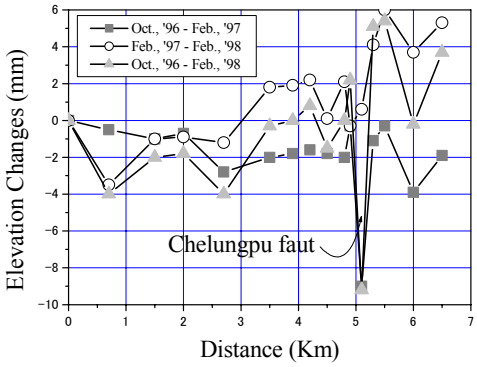

Figure 2.13. Elevation increments measured over 7 km distance in Chunshinhin town

Figure 2.14 Ta-Chia River

Shih-Kang Dam was built across the Ta-Chia river where the river's fan-shaped plain begins to spread gradually towards the East China Sea (**Figure 2.14**). The dam site lies over a shallow sandy and gravelly soil deposit spreading over a laminated mass of mud stone, silt stone and sand stone of the Pliocene Epoch, Tertiary Period. The construction of the dam began with the excavation of this shallow sandy and gravelly soil deposit down to the underlying rock surface, and was completed in 1977.

The Shih-Kang Dam, 25 m tall and 357 m long with 18 gates lined up, has a total concrete bulk of 141,300 m^3 (**Figure 2.15 "Plan", "Elevation"** and **"general spillway cross-section"**). The reservoir with a capacity of 3.38 million m^3 collects water from a catchment area of 1,061 km^2 in the Chung-Yang Mountains, and provides a steady supply of water for irrigation, etc. An intake tunnel on the left abutment of the dam leads the water through a diluvial terrace down to the Feng-Yuan water-treatment plant.

The construction of the dam was preceded by some necessary geological investigations. The contours in **Figure 2.15 (above)** describe the configuration of the base rock of the Tertiary period overlaid with sands, gravels and other suspended matters that the Ta-Chia river has carried over centuries. **Figure 2.15 (middle)** shows that the base rock surface is quite shallow in the middle of the river bed, 3 to 4 m below the soil surface, and reaches 10 to 13 m depths on both sides. These sedimentary base rocks of the Tertiary period can be recognized from their stratified features. The strata of these rocks run, in general, in about N40°E-40°S direction, and meet the dam axis at an angle of 60 degrees. The strata planes have a dip of about 40 degrees down towards southwest. Hammer blows on these rocks do not create any sharp sounds, suggesting that the compressive strengths of the rocks are some 100 kgf/cm^2 or less. When the base rocks were exposed after the excavation for

constructing this dam, no clear evidence of the presence of a fault was found (Water Resources Bureau, Ministry of Economic Affairs, Taiwan).

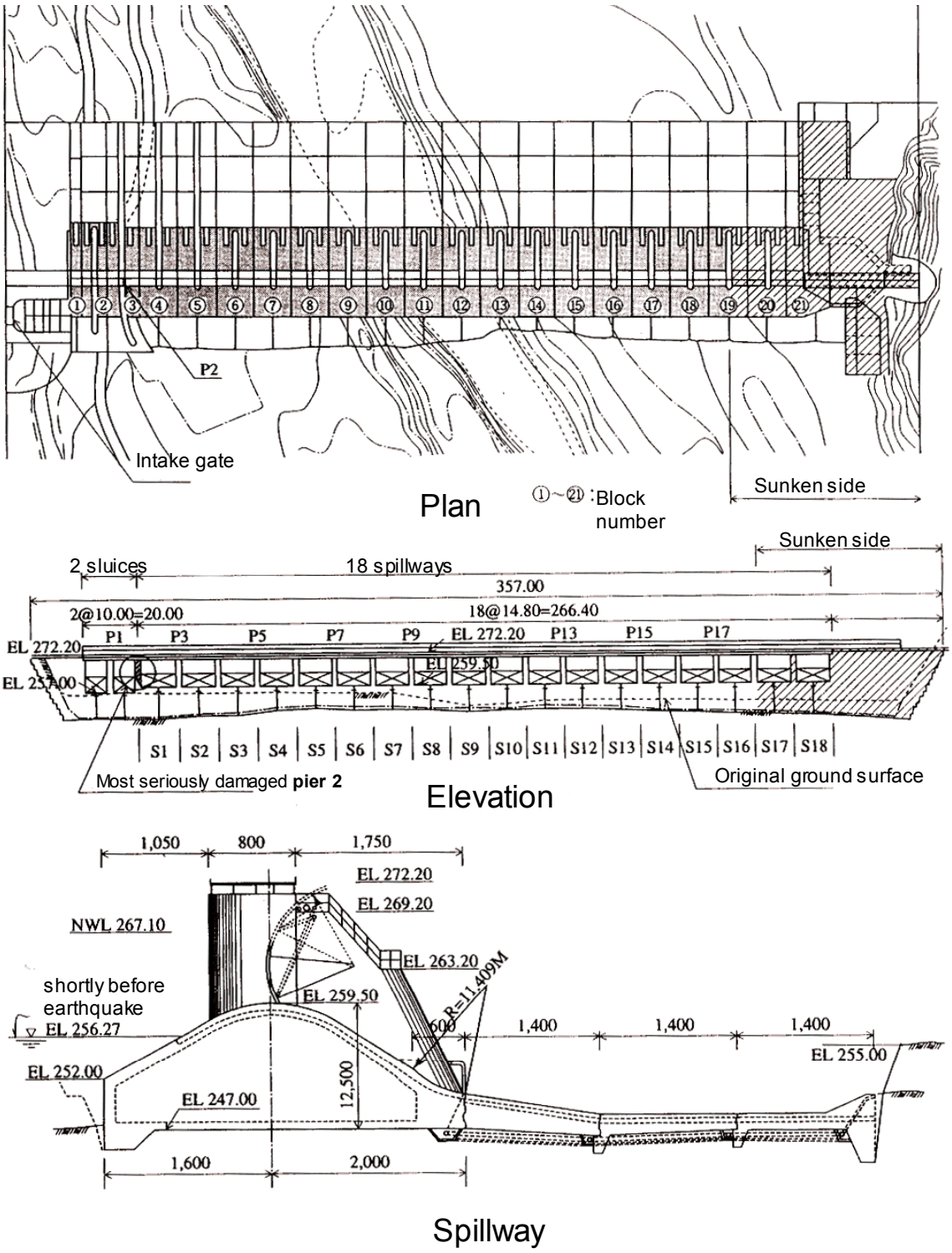

Figure 2.15. Shih-Kang Dam

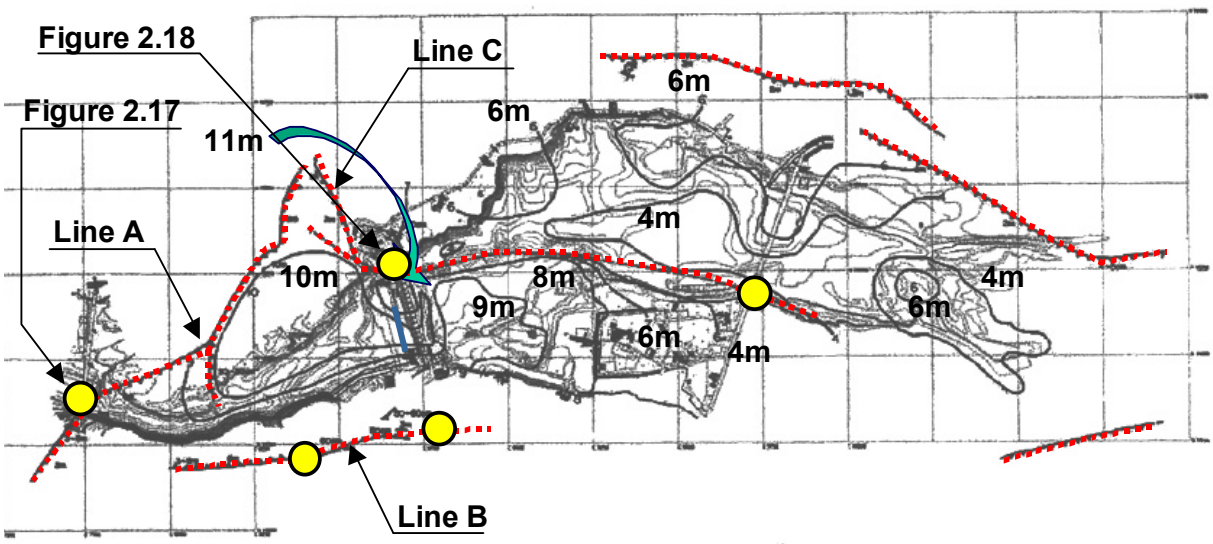

Figure 2.16. Ground upheaval in ShihKang area (After Kung, C.S., 2001)
Thin and thick contour lines show the original configuration and ground upheaval caused by faulting.

Figure 2.17. Bei-Fong bridge and fault-created Waterfall

Figure 2.18. Broken spillways of ShihKang dam

As has been mentioned, the fault rupture planes appeared branching east off the recognized trace of the CheLungPu fault in the vicinity of Feng-Yuan City, and crossed the Shih-Kang area. The complicated features of this fault rupture emerge as one zooms in on the Shih-Kang area. Thick contour lines in **Figure 2.16** show the ground upheaval in ShihKang. In this figure, line ***A*** forms a part of the northeast extension of the CheLungPu Fault. Line ***A*** crossed the Ta-Chia river near the Bei-Fon bridge, where the southeast side of the fault rose up by about 6 m with respect to the other side, causing a water fall to appear (**Figure 2.17**). This line, however dies out as it climbs the north hillside, and another line, ***C***, appears abruptly several of hundred meters east off Line ***A***. Line ***C*** crossed the northern end of the Shih-Kang dam causing three spillways of the Shih-Kang dam (No. 16-18) to be destroyed (**Figure 2.18**). The vertical offset of 10-11 m was reached at this point.

As was shown in **Figure 2.15**, the dam is made up of 21 blocks whose numbers are put in circles in **Figure 2.15 (top)**. A pier sticks upright in the middle of a block, and a pair of blocks put side by side forms a spillway or a sluice. As is illustrated in **Figure 2.15 (bottom)**, all 18 spillways are equal in their cross-sections; 12.5m high and 36m wide of bulk concrete. There are two sluices on the left side of the dam.

Table 2.2. Elevations of points on dam body (unit: m)

No.	EL of SL2	EL of SP1	EL of SP2	EL of SP3	EL of SP4	EL of SP5	EL of SP6	EL of SP7	EL of SP8	EL of SP9	EL of SP10	EL of SP11	EL of SP12	EL of SP13	EL of SP14	EL of SP15
A1	280.74	280.83	280.98	281.13	281.25	281.34	281.45	281.57	281.63	281.67	281.7	281.76	281.71	281.68	281.69	281.64
A1'	266.08	268.44	268.46	268.44	268.29	268.96	268.91	269.07	269.15	269.08	269.2	269.07	269.11	269.21	269.08	269.1
A2	280.4	280.45	280.6	280.73	280.88	281	280.1	281.22	281.34	281.4	281.45	281.45	281.51	281.47	281.44	281.41
A2'	268.29	268.45	268.46	268.55	268.82	268.94	268.99	269.1	269.08	269.23	269.25	269.17	269.09	269.13	269.25	269.14
B1	273.65	273.83	273.94	274.08	274.18	274.34	274.48	274.57	274.71	274.74	274.77	274.78	274.76	274.78	274.75	274.73
B1'	263.61	265.47	265.81	265.97	266.06	266.14	266.33	266.19	266.39	266.7	266.66	266.63	266.69	266.79	266.81	266.63
B2	273.67	273.82	273.94	274.07	274.2	274.34	274.5	274.6	274.72	274.76	274.76	274.77	274.79	274.78	274.75	274.79
B2'	265.77	265.77	265.84	265.98	266.09	266.27	266.13	266.43	266.86	266.62	266.77	266.73	266.26	266.74	266.93	266.68
C1	267.47	270.06	270.25	270.39	270.47	270.6	270.73	270.54	270.61	270.63	270.64	270.65	270.61	270.6	270.59	270.81
C2	267.54	270.07	270.3	270.43	270.49	270.64	270.75	270.56	270.62	270.63	270.65	270.66	270.6	270.59	270.59	270.84
C3		270.21	270.29	270.44	270.55	270.67	270.75	270.61	270.61	270.62	270.66	270.66	270.62	270.59	270.58	271
C4		270.23	270.34	270.45	270.57	270.7	270.78	270.61	270.63	270.66	270.65	270.63	270.6	270.57	270.55	271.43
D1	259.9	260.71	260.91	261.11	261.17	261.35	261.43	261.66	261.71	261.55	261.65	261.7	261.72	261.72	261.7	261.68
D2	259.64	260.74	260.97	261.06	261.19	261.36	261.53	261.69	261.73	261.59	261.7	261.68	261.75	261.73	261.72	261.67
D3		260.81	261.06	261.14	261.25	261.42	261.6	261.69	261.76	261.61	261.65	261.7	261.71	261.75	261.67	261.67
D4		260.91	261.11	261.14	261.32	261.42	261.56	261.76	261.82	261.65	261.65	261.7	261.73	261.72	261.7	261.7
E1		268.73	268.94	268.95	269.25	269.28	269.29	269.44	269.52	269.47	269.43	269.48	269.4	269.42	269.38	269.37
E2		268.68	268.94	269.04	269.08	269.28	269.29	269.54	269.52	269.49	269.46	269.44	269.37	269.39	269.37	269.36
E3		268.79	268.95	269.08	269.1	269.22	269.32	269.51	269.45	269.5	269.47	269.41	269.4	269.37	269.39	269.25
E4		268.84	268.81	269.01	269.14	269.18	269.24	269.49	269.49	269.48	269.46	269.43	269.41	269.39	269.36	269.25

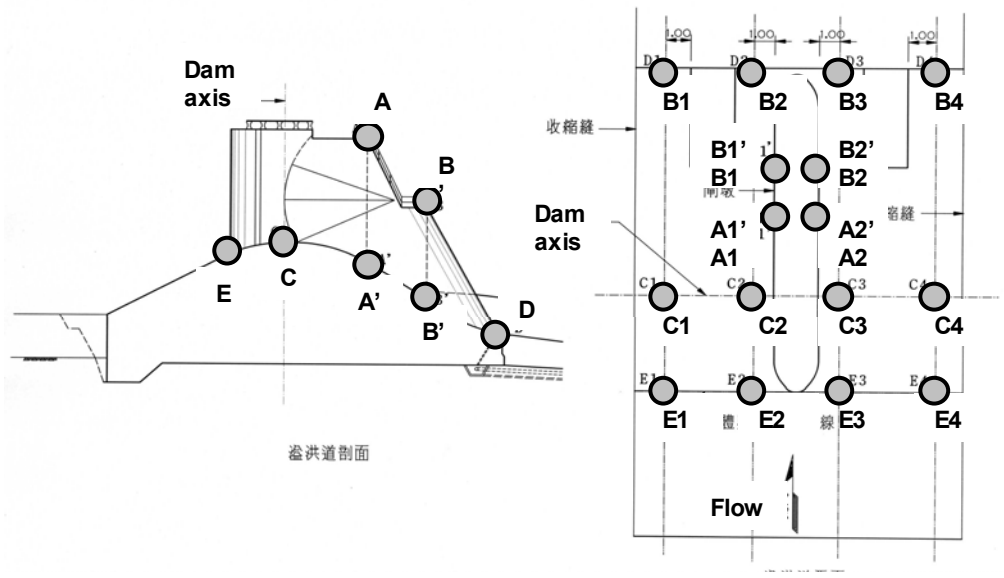

Locations of points

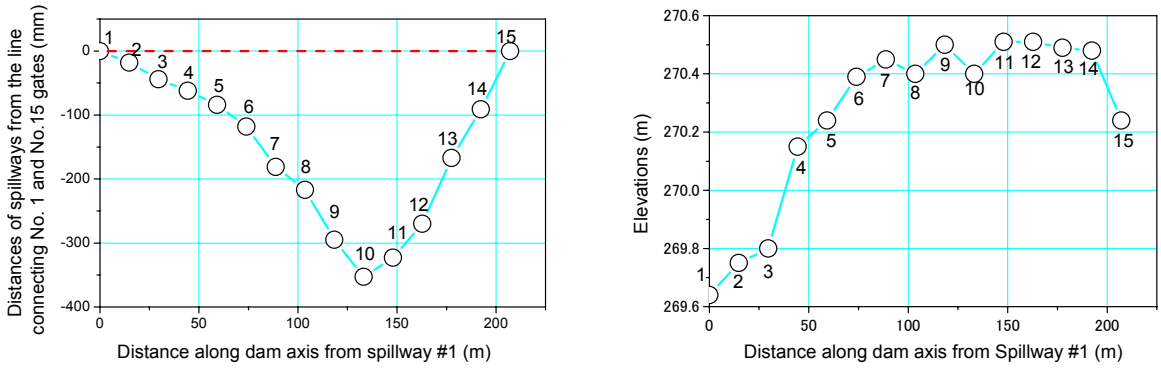

Figure. 2.19. Deformation of dam body along its axis

Kung (2001) measured elevations of total 312 points on the dam body (**Table 2.2**). **Figure 2.19** shows the deformation of dam body along its axis measured shortly after the earthquake. Horizontal distances of spillways were measured from the line connecting Spillways #1 and #15. Though the vertical elevations are not completely identical with those (C points) listed in Table 2.2, the deformation pattern in **Figure 2.19** and that from Table 2.2 (Kung, 2002) are about the same in shape and size. The entire dam body thus seems to have been warped both upward and towards upstream side.

Sugimura, Y. and Jyh, (Sugimura, 1999, Konagai et al., 2000) mapped cracks that appeared on the dam body. Cracks excluded from the figure include those lying under water, the upstream slopes of spillways behind gates, and spillways with their gates open. The seriously and/or completely destroyed spillways #16-18 were also excluded from this mapping. Major cracks on spillways were found between spillways #6 and #16, namely on blocks ⑧-⑱. In general, diagonal cracks were found on most damaged spillways, and transverse joints between blocks were opened in such a way that the openings on the upstream side were wider than those on the downstream side.

Diagonal cracks on blocks ⑨, ⑩, ⑪, ⑫, ⑭, ⑯, ⑰ and ⑱ reach the piers, and the crack on Block ⑪ further extends diagonally up through Pier 10 (see **Figure 2.25**). The largest crack openings of 20 mm, 8mm and 40 mm are reached on Block ⑪, Pier 10 and the block joint between ⑩ and ⑪, respectively (see **Figure 2.20**).

Cracks along horizontal construction joints were found on four piers #9, #10, #15 (**Figure 2.21**), #16 and #17. No major cracks were found on blocks more than 200 m away from fault ***C***. In this less-damaged part also, Piers #1-#5 were found to be cracked. The cracks on Piers #1-#5, however, have some different features from those found on the piers closer to fault ***C***. Some small fragments of concrete came off a jagged horizontal crack on the sluice-side wall of Pier #2 (**Figure 2.22**), and the rupture surface inferred from the cracks seems to run diagonally down through this pier to the other (spillway-side) wall of the pier. It is noted here that the concrete bulk of the sluice is 2.5m higher than the next spill way.

Upper construction joints of Piers #3 and #4 were cracked as illustrated in **Figure 2.23**. A crack that developed diagonally up through Pier #1 is illustrated in **Figure 2.24**, whereas the crack found on Pier #5 seems to have developed upright from a similar position.

Simply supported RC bridges span all spillways and sluices. They all came off their bearings. The cracks on the dam body caused 6 gates (5 for spillways and one for sluice) to be inoperable.

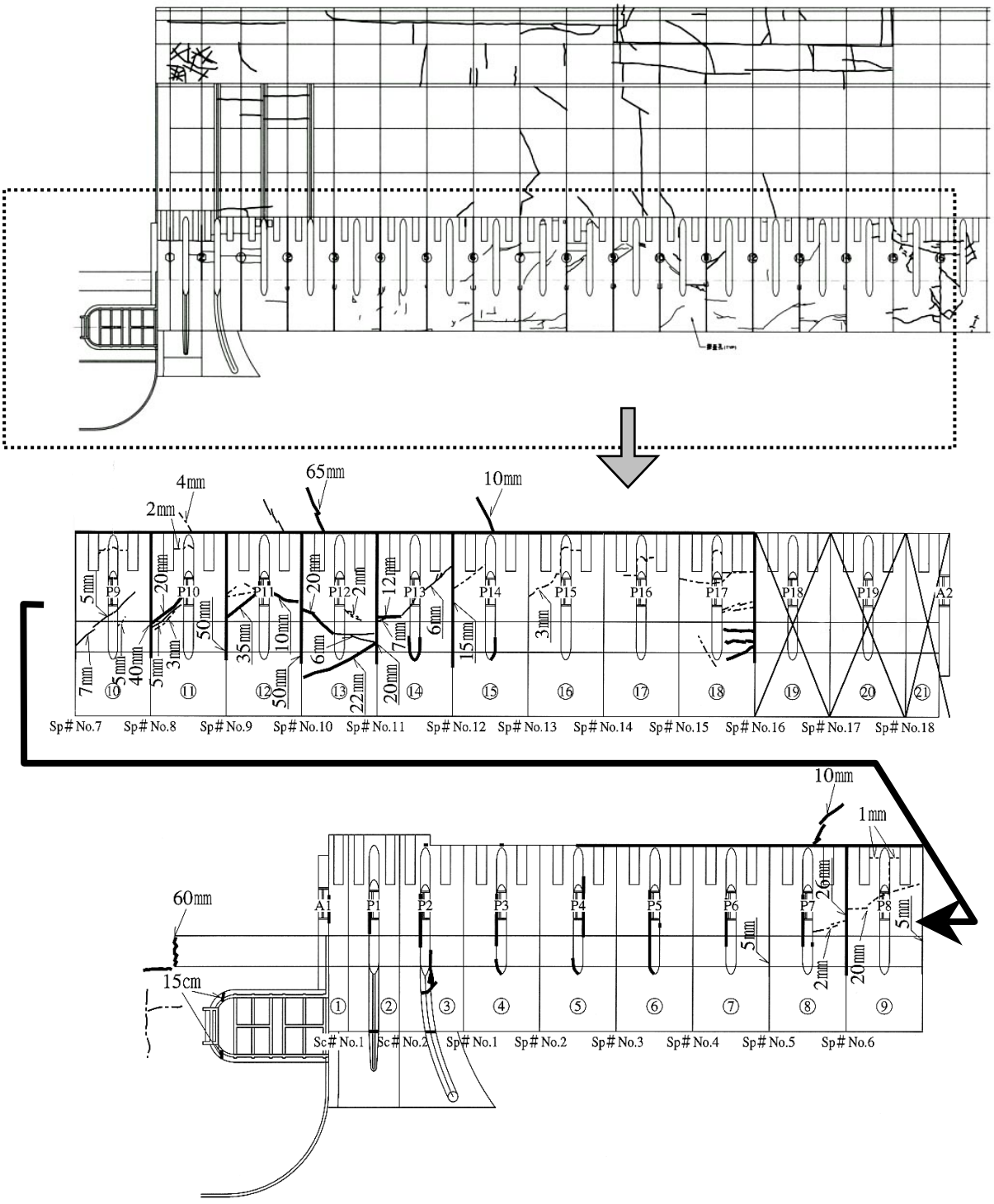

Figure 2.20. Crack map of ShihKang dam (Sugimura et al, 1999)

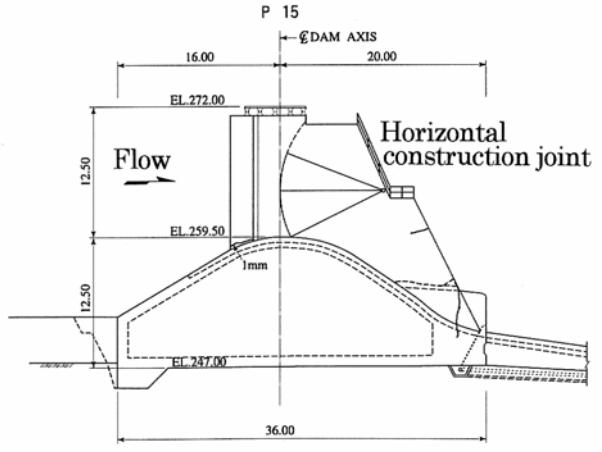

Figure 2.21. Cracks on Pier #14

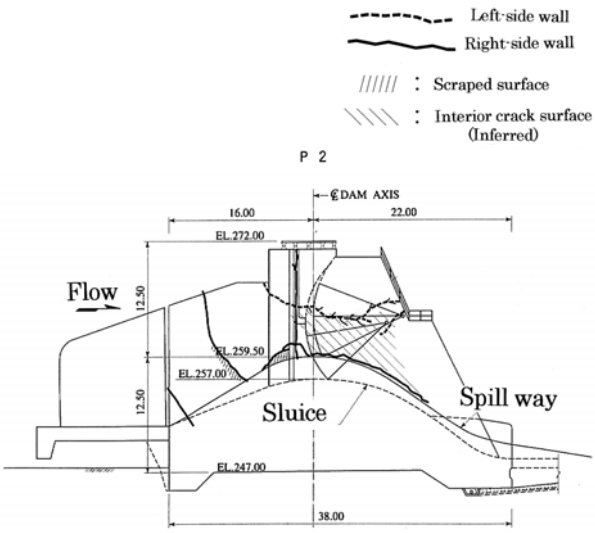

Figure 2.22. Cracks on Pier #2

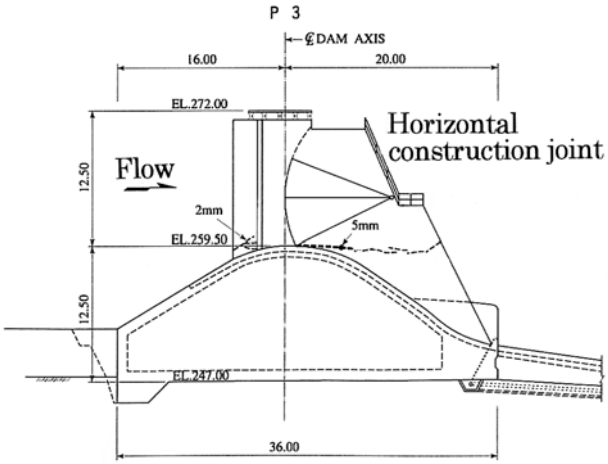

Figure 2.23. Cracks on Pier #3

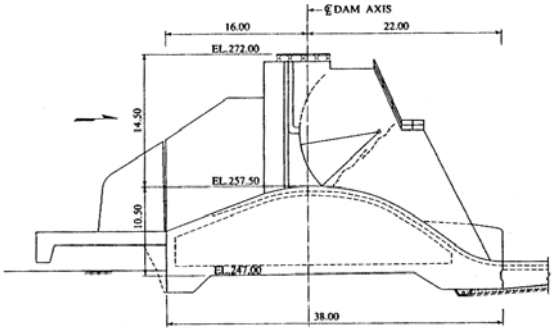

Figure 2.24. Cracks on Pier #1

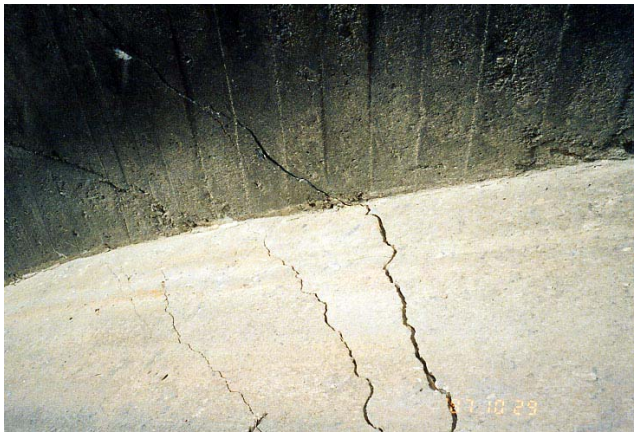

Figure 2.25. Cracks extending diagonally up through Pier #10

Figure 2.26. Cracks on Pier #2

It is noted that the structure on the hanging wall side of the fault had suffered more serious cracking than the footwall side. Since the dam was constructed directly upon the base sedimentary rock mass, the pattern of cracks on the dam body might indicate how the base rock was deformed during the earthquake. Ground upheaval in **Figure 2.16** shows that the peak value (+11 m) of upheaval was reached near Line C on the hanging wall side, and this fact is consistent with both the deformation pattern shown in Figure **2.19** and the crack pattern in **Figure 2.20**.

However, the base rock deformation may not be the sole cause of the dam body deformation. It was an urgent task to restore the water supply function and to provide necessary flood control for the coming flood season. Therefore, grout injection was carried out for the remaining gates, preserving the completely damaged gates as a memorial park. **Figure 2.21** shows the variation with the axial distance of the volume of grout injected. A noticeable amount of grout was poured into hidden cracks in the right side of the dam body; this suggests that this part of the dam body may have come off the base sedimentary rock due to a large axial force induced in it. This may have made the upheaval of the dam body even more remarkable.

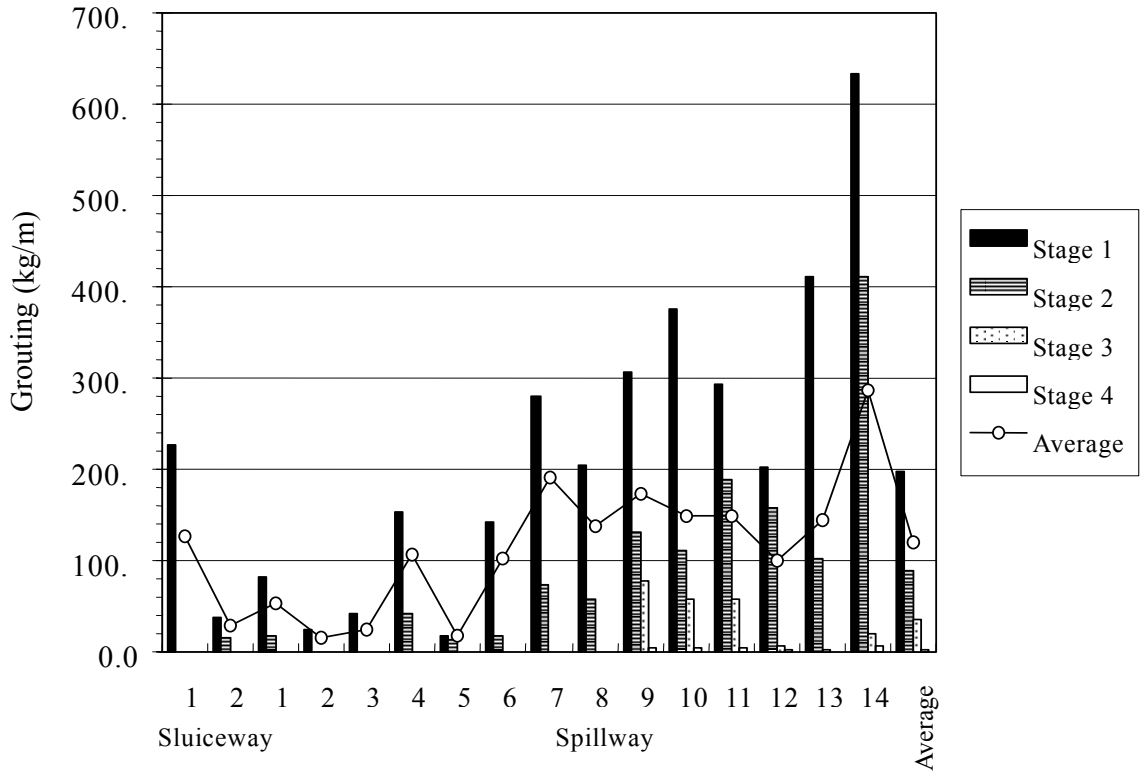

Figure 2.21. Variation with the axial distance of the volume of grout injected (Kung, C.S., 2000)

2.4 FAULT-INDUCED LANDSLIDES

Landslides occur on a regular basis throughout the world as part of the ongoing evolution of surface configurations (Kramer S., 1994). They are mostly due to heavy precipitations, and about 1000 landslides are triggered every year in Japan. However, when landslide-prone zones were superimposed on a seismic fault map, one can recognize that many landslides are found scattered along active fault traces. Intense ground shakes must have been responsible for these landslides, but we should not forget that fault dislocations can cause landslides. Examples follow.

2.4.1. Tiger Head Hill slide (1999 ChiChi earthquake, Taiwan):

Cher-Lung-Pu fault winds along eastern hillsides in Tai-Chung County, and shoots branches where it reaches Tou-Bien Creek (**Figure 2.22**). Some of these branches crossed Yi-Chiang Bridge causing collapse of its western spans. The main fault rupture, after going another 700 m along the east bank of Tou-Bien-Kun Creek, crossed the river and hit the slope of Tiger Head Hill. A slow and steady motion of the soil has been observed since 1992, the time when the top part of the hillside was cut flat for developing a residential area. Tiger Head Hill is geologically made up of Jin-Shui Shale bedrock dipping southeast. Debris of about 10m thick slipped down the slope and surged 200m across Tou-Bien-Kun Creek, and dammed it. The slid soil mass is estimated to be about 1.5 million cubic meters. Extension of the soil has created a graben, a 50m-deep and 100m-wide down-dropped soil block 400m along the top scar.

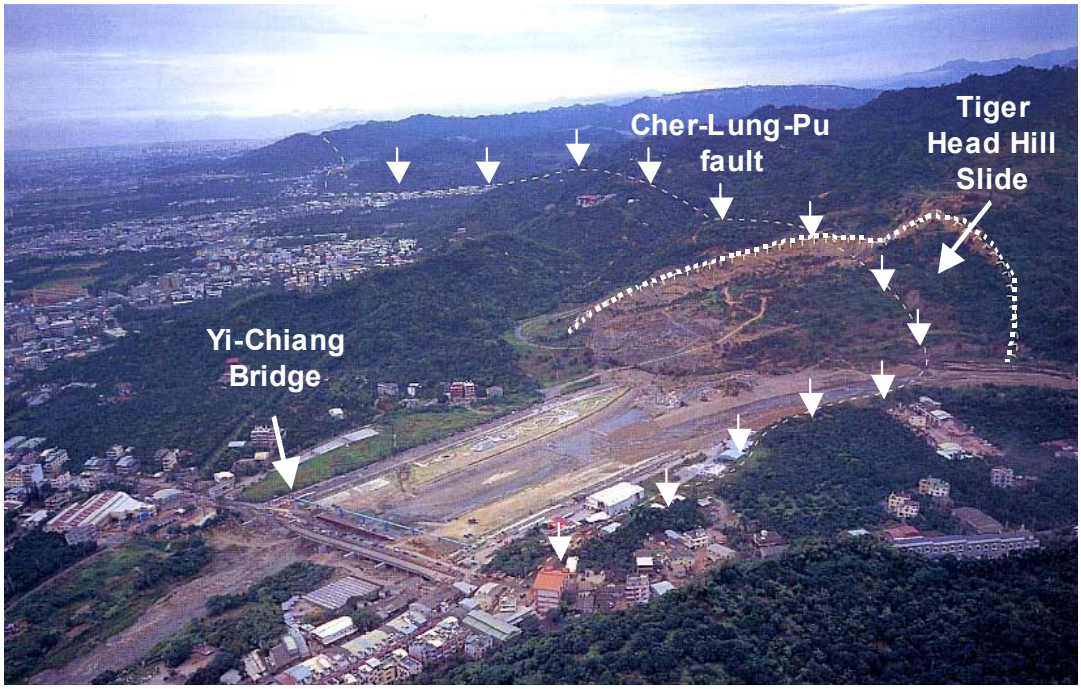

Figure 2.22. Tiger Head Hill Slide and Yi-Chieng Bridge

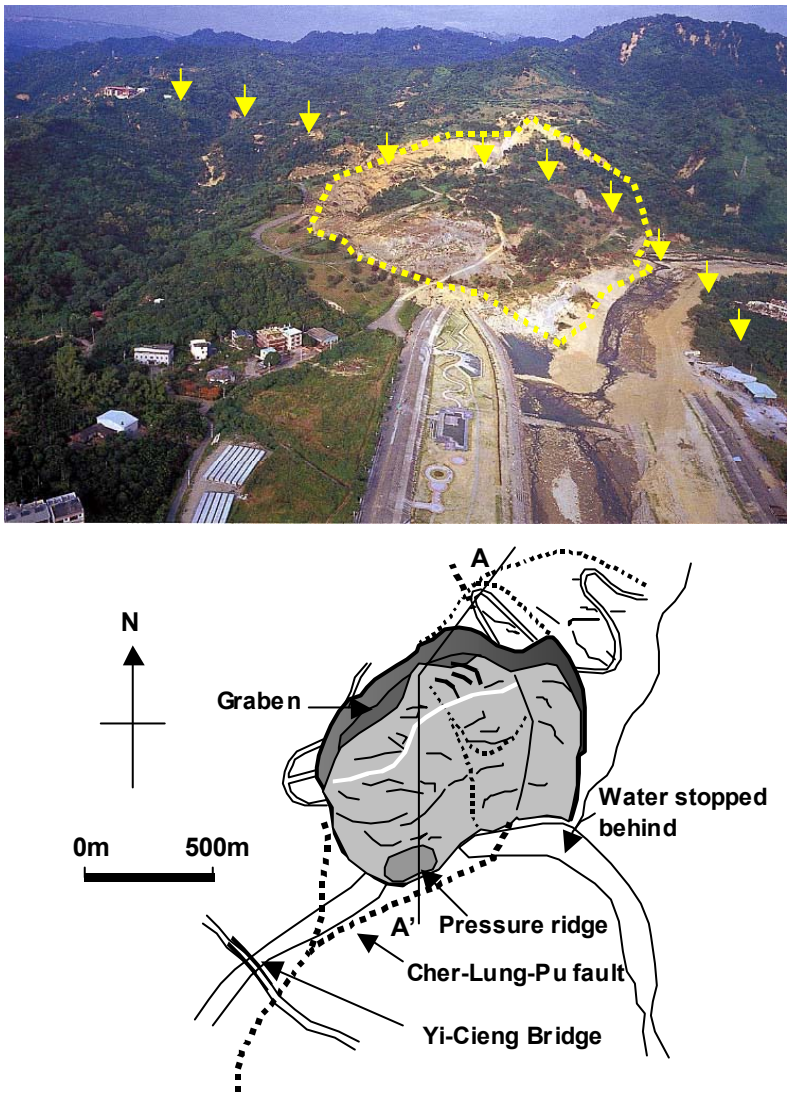

(a) Plan of Tiger Head Hill Slide

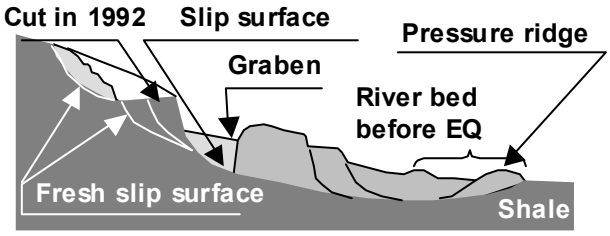

(b) Cross-section **A-A'**

Figure 2.23. Plan and cross-section of Tiger Head Hill Slide (after Kamae, S. and Shuzui, H., 2002)

2.5 INTENSE SHAKES

Over the past few decades, significant effort has been devoted to understand the problem of ground shaking. In the conventional attenuation relationship, peak ground acceleration reaches the maximum values at the closest distance from the fault. However, real damage distributions do not always support the theory.

2.5.1. 2002 Changureh Earthquake, Iran:

The dry and barren plateau dominates most of Iran that lies in southwestern Asia. The plateau, lying at height of 900 to 1,500 m above the sea level, has a continental climate, with cold winters and hot summers. An intense earthquake occurred in western Iran, about 225 km west of Tehran at 7:28 local time, June 22, 2002. Though the moderate moment magnitude of 6.4(ERI, University of Tokyo) – 6.5 (USGS) calculated for this earthquake was not particularly large compared with the major earthquakes that ever occurred in this country, seriously ravaged villages were found along east-west oriented valley in the west of Abegarm, and 261 people were reportedly killed and 1,300 injured.

The epicenter and the damaged area are located in a fold and thrust (low-angle reverse fault) belt in the north of Zagros tectonic boundary (**Figure 2.24**). This belt trends NW-SE direction. Mountain ranges and valleys of about 30 km wide run along the belt. Reverse fault movements have been responsible for large earthquakes including 1962 Ipak (Buin-Zahra) earthquake.

In this barren area, its surface geology is easily observed. Hills are mainly composed of Miocene siltstones with their southern area covered with Quaternary fan deposits. Two deformation lines are recognized in the valley. The northern deformation line is near the main stream of the valley. Bedding of Miocene siltstone dips north, while on the southern deformation line near Abdarreh, siltstone layers dip south. The 1:200,000 scale tectonic map of this area shows these deformation lines as thrusts. The topographic feature is consistent with its geologic structure. The Quaternary terraces are deformed along the northern line, and a low land extends behind the hill near the south line.

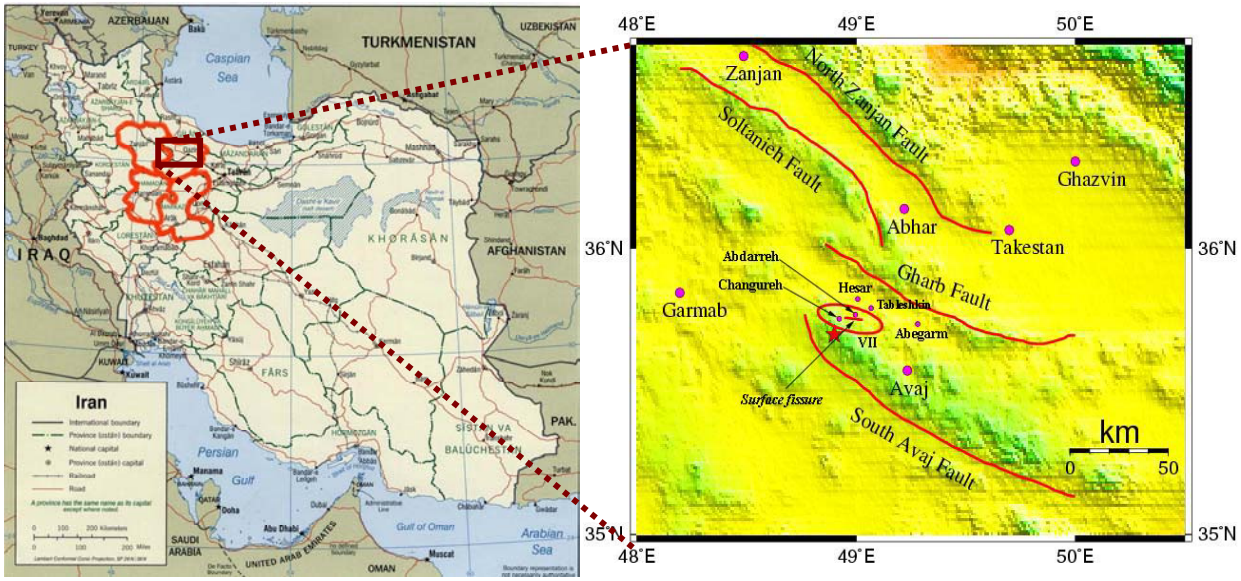

Figure 2.24 Faults and seismicity of the zone:

☆ Epicenter

Magnitude (MW): 6.5
Time: 07:28:21.61 (local)
Location: 35.63N 48.95E
Focal Depth: 10 km
Fault Mechanism: reverse
(Source: USGS, NEIC)

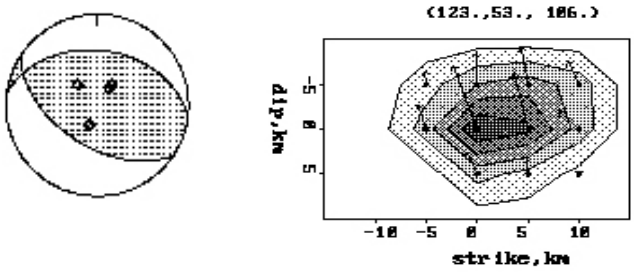

Figure 2.25 Focal mechanism and slip distribution (Kikuchi and Yamanaka, 2002, ERI)

Kikuchi and Yamanaka, Earthquake Research Institute, University of Tokyo, put up their fault plane solution (**Figure 2.25**, http://wwweic.eri.u-tokyo.ac.jp/EIC/EIC_News/020622.html) that indicates that the main shock occurred on a reverse fault of about NW-SE trend. That mechanism is consistent with the tectonic setting of this area. The Moment Magnitude M_W of 6.4 was calculated for the main shock, while 6.5 was calculated by USGS. The focal depth was about 7 km (ERI, 2002).

A surface fault related to this earthquake appeared across the epicenter area of the main shock. According to Sassan, Eshighi, Mehdi Zare and Mohammad R. Mahdavifar, IIEES, surface fissures are continually lined up 3 km straight across the barren terraces between Changureh and Abdareh (**Figure 2.26**).

An about 700m part of the surface fault extending east from Abdareh was traced. The rupture runs straight across the mountain ridges, and is related to the compressional mechanism. The southern hanging wall side has been pushed about 5-10 cm up. This trace of the fissures trends N70°W, and is approximately orthogonal to the axis of the focal solution for this earthquake given by NEIC and Harvard university (2002).

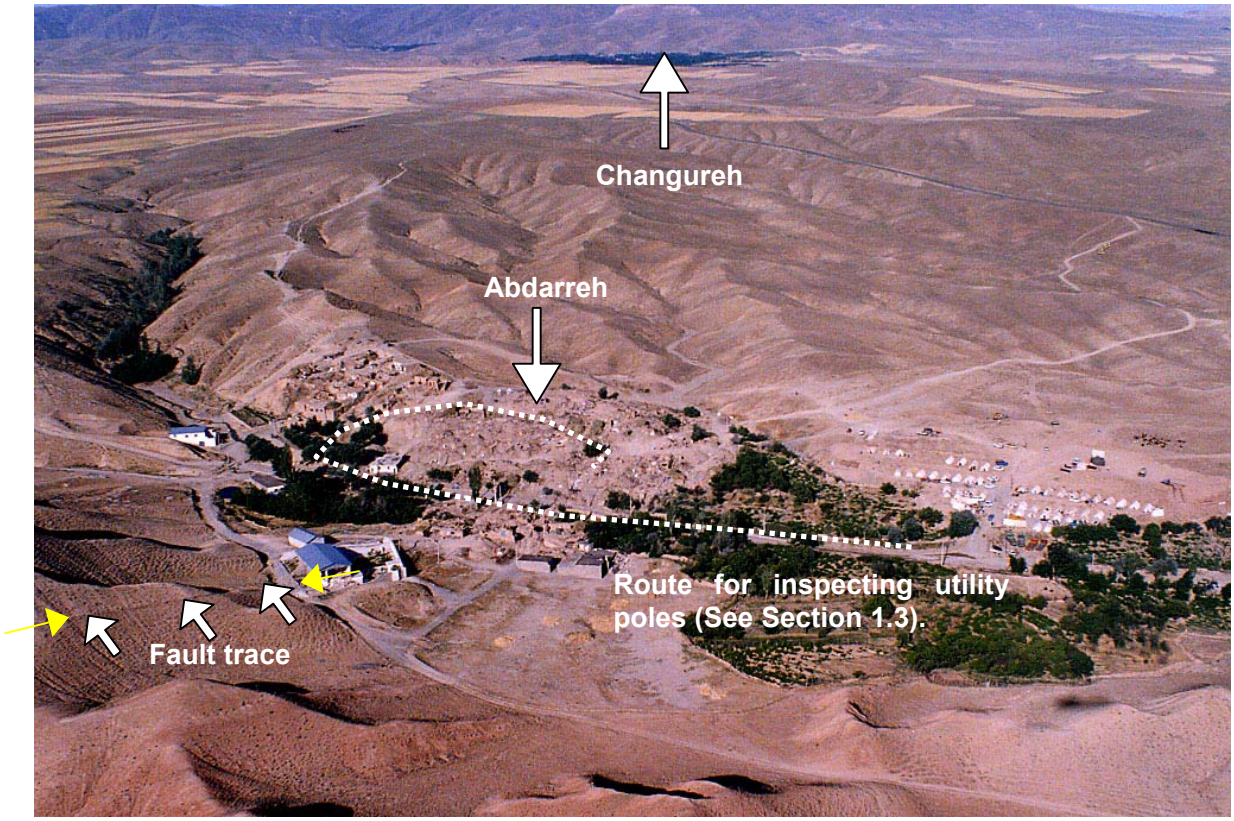

Figure 2.26 Surface fault trace and affected areas

A trench was excavated at a narrow valley approximately 500 m east of Abdareh (**Figure 2.27**). The site was chosen in expectation of finding charcoals that would allow dating possible previous events. Since the location was inaccessible by any machines, the trench was dug by hand, and was 3 m wide, 5 m long and about 1.2 m deep with east and west side walls cutting straight in the middle of the valley and along the mountainside (**Figures 2.28, 2.29**).

Figure 2.29 shows a sketch of the east and west walls of the trench. Layer A is the weathered soil covering thin both the mountainside and the valley. Layer B is composed of granule and less matrix. Layer C contains semi-angular pebbles. Layer D is a matrix rich bed. Maximum grain size of 2 cm is reached in this layer. Layer E is a clearly imbricated gravel bed. The average and maximum gravel sizes are about 1 cm and 5 cm, respectively. Layer F is a paleo-soil covering a gravel bed of layer G. Layer H is also a paleo-soil bed, but is overlain by gravels of layer G. Layer I is a gravel bed covered by layer H. Maximum gravel size of layer I is about 5 cm. Layer F, G, H are overlain by layer E with unconformity. The fault found clearly from surface to layer E. It is recognized as open rupture and there is no displacement along the fault. In the layers below layer F, the fault is hardly recognized.

On the west-side wall, layer H and I are considered to be extensions of those on the east wall. The uppermost bed of the valley sediment, layer J, is a sandy soil with much matrix. Layer K is a thin bed of silt or very fine sand. Layers L and M are sand and gravel beds. The matrix is rather rich in layer L than layer M. Layers N and O are paleo-soil and gravel beds overlain by layer I. Though the surface fissures lined up across the valley have clearly proven the presence of the fault at the slope foot, no clear fault dislocation was observed on the west-side wall probably because the strain caused by the faulting has spread over the uncemented soil. Nothing indicating previous fault dislocations was found in the trench.

On the east edge of Abdarreh, surface soil was scraped off to observe the fault trace on a silt rock (**Figure 2.30**). The silt rock dips to south. Tufficious fine sand and silt film is caught thin in the silt rock and faulting occurred on its bedding plane. Most southern part of the tufficious sand has developed into clay of 2-3 cm thick probably because of the continual fault dislocations. Siltstone among the thin tufficious sand film has been weakened.

A “bedding plane fault” can be considered as a by-product of folding, and causes a moderate earthquake of M6 class.

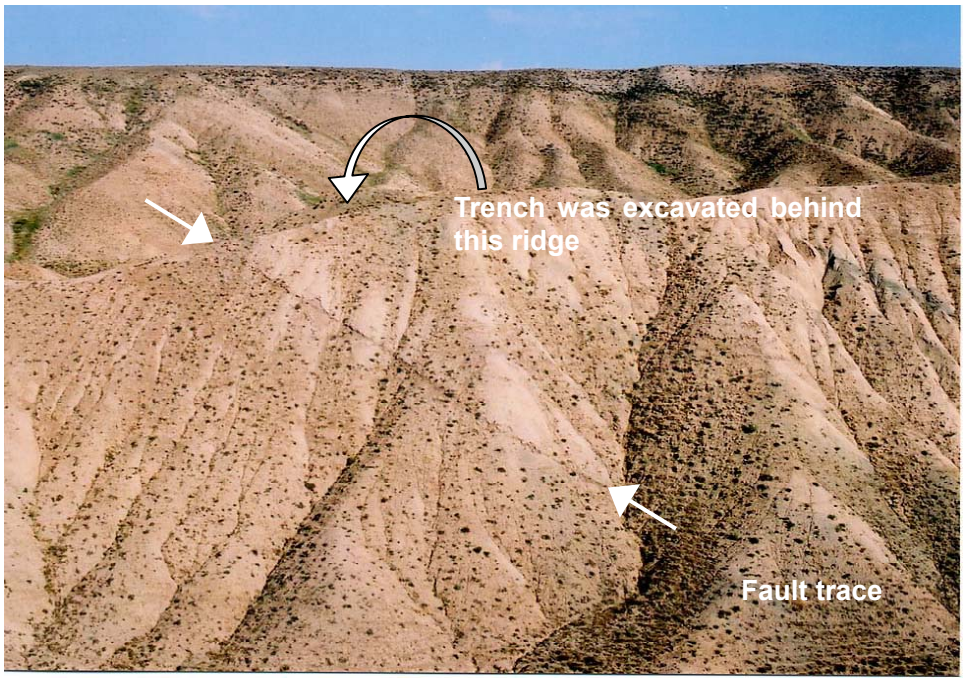

Figure 2.27 Surface fault trace and location of trench

Figure 2.28 Excavated trench

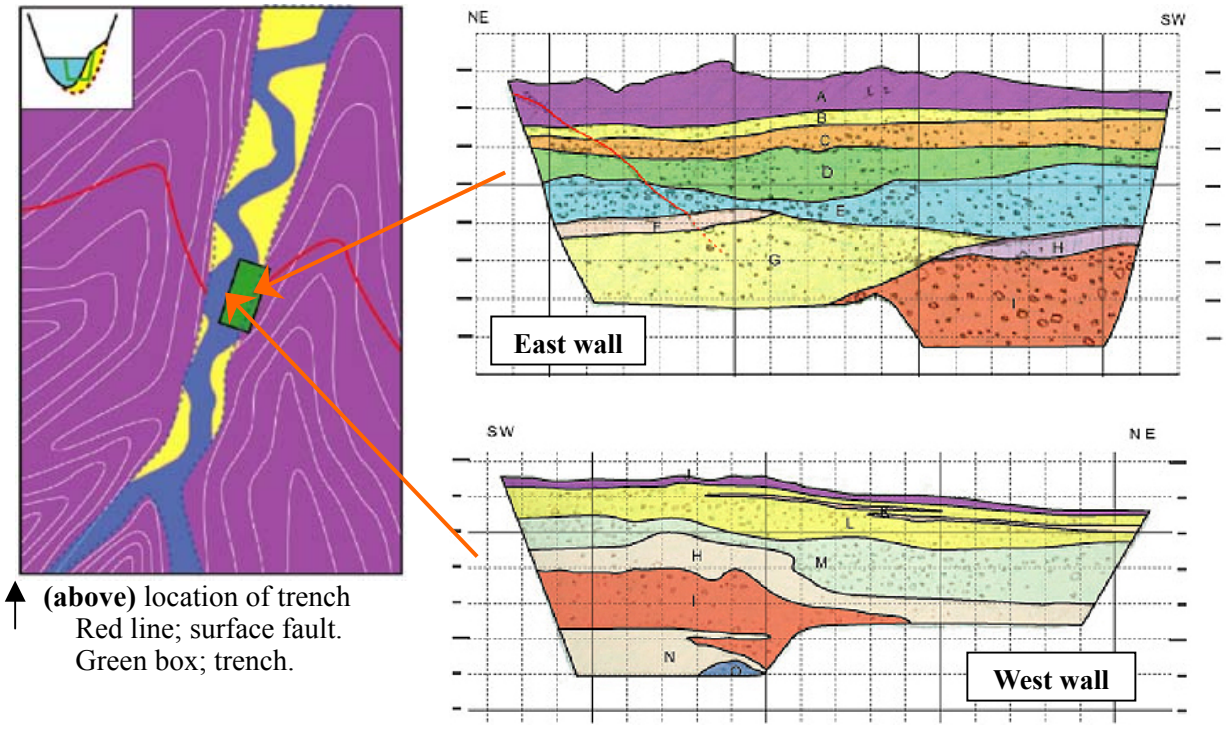

Figure 2.29 Illustration of trench. (by Azuma and Goto, 2002)

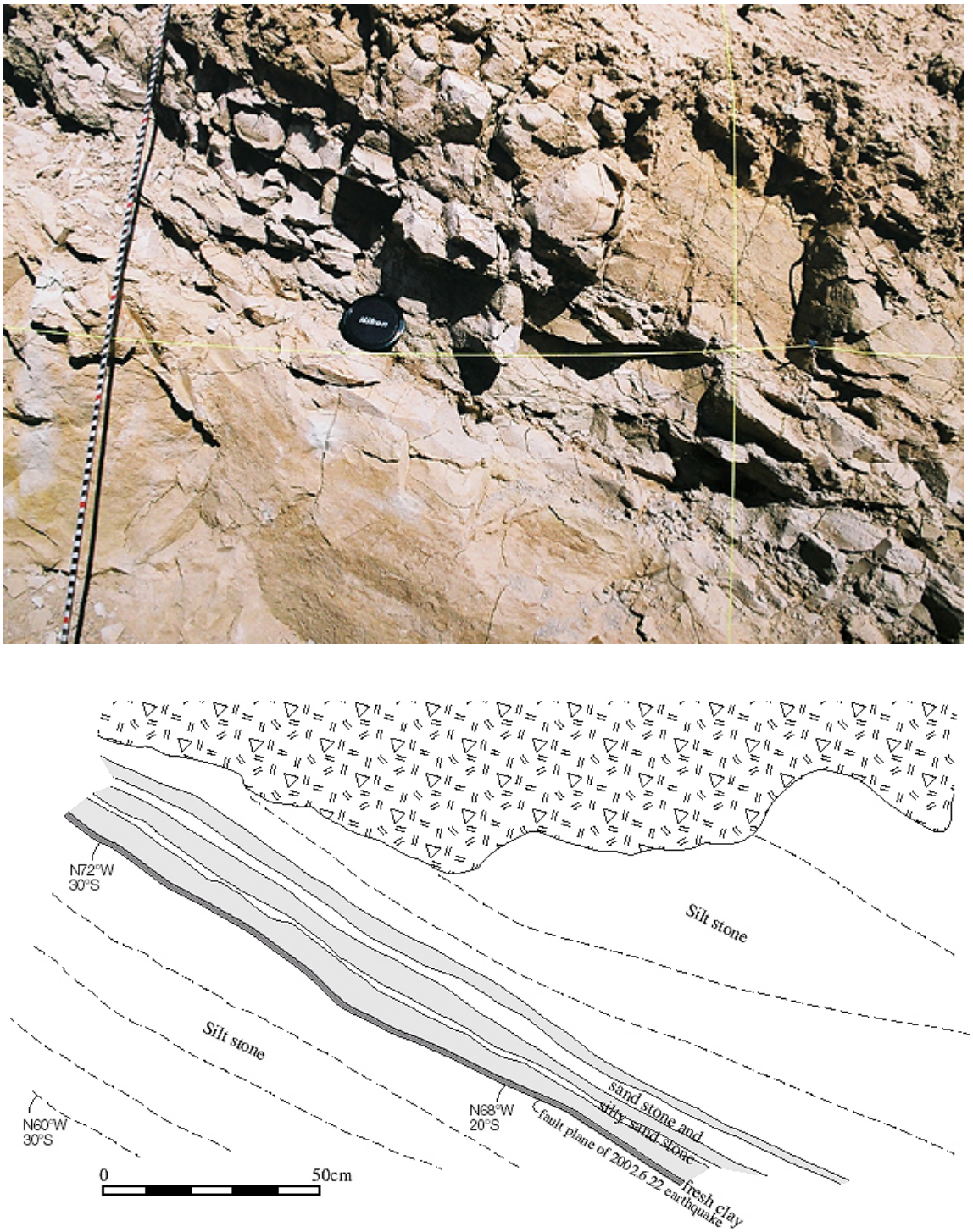

Figure 2.30 Exposed surface of silt rock (photo by Goto)

Abdarreh was one of the hardest hit villages by this earthquake. A gentle ridge, the northeast extension of a sand rock terrace rising behind, dips gently towards its northeast lowland. This ridge is densely covered with adobe dwellings, and most of them were flattened in the earthquake.

Distribution of cracked utility poles is considered to be a good index for estimating possible spatial distribution of intense ground motions. Observed crack intensities on total 28 utility poles were roughly classified into the following 5 groups:

Group 1: no visible crack. (**White**)
Group 2: with hair cracks (>0.1 mm, **Light yellow**)
Group 3: with cracks (0.1-0.2 mm, **Yellow**)
Group 4: with cracks (0.2-0.3 mm, **Dark yellow**)
Group 5: with cracks (<0.3 mm, **Brown**) that can be seen at a distance of about 2m

Figure 2.31 shows the observed distribution of crack intensities. In this figure, the route taken for the inspection is lined up with the utility poles (colored circles). The route goes straight from right to left along a valley, and turns sharply up towards the ridge when it reaches the southern edge of the village. Then it comes slightly back along the ridge. Several arrows near the bend of the route indicate the inferred directions of strong ground motions. The other line of dark sphere marks is the fault trace. It goes across another mountain ridge that rises east of the village, and meets the route. It is noted that the fault trace seemingly divides the utility poles into two groups; cracked poles on the hanging wall side and less damaged on the foot wall side. This clear contrast suggests that the shake on the hanging wall side must have been more intense than that on the foot wall, and thus must have been responsible for serious destruction of the village. The arrows show that the motion was intense in the normal direction to the fault trace.

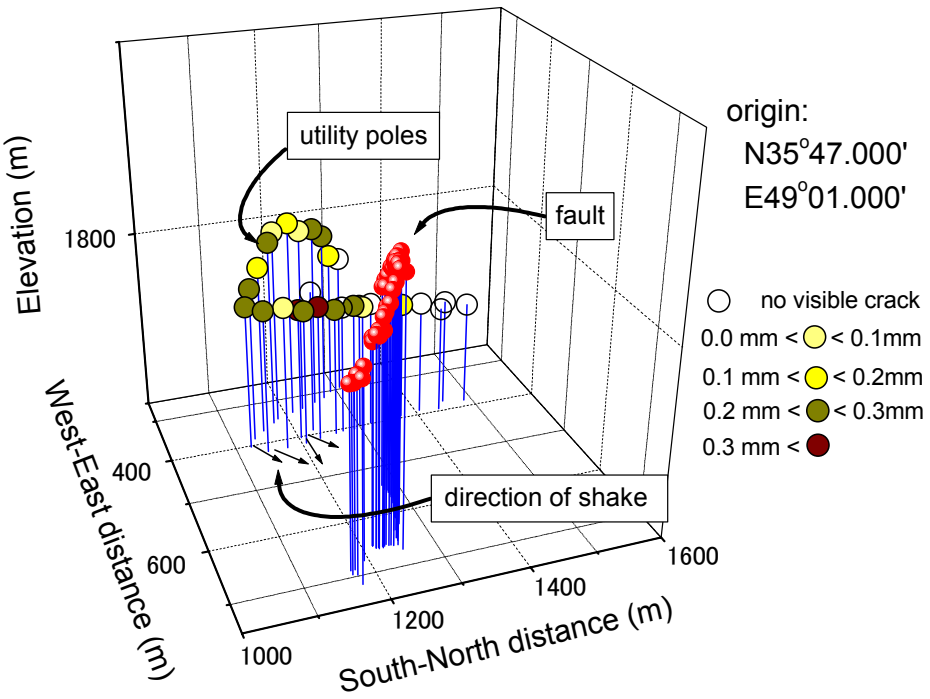

Figure 2.31 Locations of cracked utility poles

2.6 SUMMARY

The Kobe Earthquake stimulated a sharp rise in demand for rational design procedures for urban facilities, and revisions of these design codes were made reflecting lessons learned from the Kobe Earthquake. However few lines in these codes describe remedial measures for possible destructions caused by fault dislocations. In its background was the good lack of Japan that most of seismic faults activated in the past one century appeared off important civil-infrastructures and/or urbanized areas, and a limited number of damaged facilities can be enumerated in only a “one-page” list. However, we should not forget that with a rapid population growth in the 20th century, many people are now living in a more disaster prone area where nobody used to live. In reality, recent statistics on disasters showed a continuous trend towards ever-increasing number of catastrophes with ever-increasing costs (Munich Re, 1997). With this trend, natural disasters will soon become a "budget time bomb" which no government could afford the costs. It is therefore necessary to solicit the participation of the people in disaster management. For this reason, the digital data that JSPS/JSCE/EqTAP taskforce is archiving should be explained in terms of some key parameters that are easily understood by stakeholders.

Examples introduced herein showed that noticeable strains can be induced even off an activated fault, and no underground structure is seemingly able to hold in a large fault dislocation. However, the example of Inatori tunnel showed that a tunnel could be deformed slightly out of shape if the surrounding soil is remarkably softened. From this viewpoint, Inatori tunnel was a lucky case to be sure, but re-localization of strain appeared as buckling of rails. A rail buckling is likely to appear where rails were pushed up and lose their lateral supports.

A seismic fault can cause landslides when it hit weathered slopes. Even if a soil mass on a slope slips a little, it certainly increases soil deformation and may cause serious destructions of structures.

Deformations and intense shakes cannot be discussed separately. Over the past few decades, significant effort has been devoted to understand the problem of ground shaking. In the conventional attenuation relationship, peak ground acceleration reaches the maximum values at the closest distance from the fault. However, real damage distributions do not always support the theory. After the 2002 Changureh Earthquake, cracks appeared on utility poles in Abdarreh village were investigated. It was found that the fault trace divided the utility poles into two groups; cracked poles on the hanging wall side and less damaged on the footwall side. This clear contrast suggests that the shake on the hanging wall side must have been more intense than that on the footwall, and thus must have been responsible for serious destruction of the village.

REFERENCES

Kamai, T. and Shuzui, H. (2002). “Landslides in urban region,” *Riko-Tosho Press*.

Konagai, K., Mikami, A., Katagiri, T., Ahsan, R. and Maruyama, D. (1999). “Report of damage caused by the Mid-North Iwate Earthquake of September 3, 1998,” *Bull., Earthquake Resistant Structure Research Center*, IIS, University of Tokyo, **32**, 3-13.

Yoshikawa, K. (1979). “Examples of damage to railway tunnels,” *RTRI Report,* **1123 (497)**.

Watanabe, M. and Suzuki, Y (1999): “3D photographs of seismic fault traces” *Kokon Shoin Press*.

White paper of the Metropolis (1999).

Chapter 3

NUMERICAL TOOLS

3.1 INTRODUCTION

In California, United States; New Zealand; and also in Taiwan after the 1999 earthquake, so called fault zoning acts have been established. These fault-zoning acts restrict construction within a certain zone along known fault traces and will certainly be one way of reducing the risks for new buildings and infrastructures, but for structures already built along or across a fault line, other remedial measures are needed. Furthermore fault-zoning acts themselves basically do not describe such details as the possible extent of deformations and/or possible recurring times of faulting.

In highly populated countries such as Japan and other east and south east-Asian countries, it is not easy to impose a Californian or New Zealand-type fault-zoning act due to the lack of space. In these countries, building code provisions based on engineering principles are needed to allow for construction along the fault-lines if certain design requirements are met. Such a building code provisions would also be attractive for less populated countries, such as United States and New Zealand, as well, since it will allow for more economical construction. Another issue is the difference between strike-slip and dip-slip faults. Deformations along a strike-slip are liable to be localized in a narrower zone along the fault line whereas the deformations along a dip-slip fault will affect areas further away from the fault line. In Japan, there are some 90 dip-slip fault systems with several faults in each and with a lot buildings and infrastructure along them.

For providing results in the form of possible extent and probabilities of deformation along these fault lines, much research is necessary. Specifically, numerical tools are needed to estimate possible deformations induced in structures embedded in or resting on a soil deposit affected by fault surface rupture; see Bray *et al.* (1994), Ke and Bray (1995), Taniyama and Watanabe (1998), and Onizuka *et al.* (2002). For the surface earthquake fault, however, it is not easy to apply ordinary numerical simulation methods due to the difficulty in modeling behaviors of soils that experience large deformations. This chapter summarizes tools newly developed by the JSPS team members for predicting possible extents of fault-induced soil deformations. They include Non-linear Spectral Stochastic Finite Element Method (NL-SSFEM) by Hori, M. et al., Applied Element Method (AEM) by Meguro, K. and Material Point Method (MPM) combined with a Hypo-plastic soil model by Johansson, J. and Konagai, K. NL-SSFEM (Section **3.2**) allows a probabilistic estimation of both the fault formation and the possible configuration. AEM simulations show that the peak response is not likely the largest exactly above a surface rupture rather it is larger at some point further away from the rupture plane (Section **3.3**). The Material Point Method (MPM), by virtue of its scheme formulated in an arbitrary Lagrangian-Eulerian description of motion, allows the problem of mesh distortions to be eliminated, and thus large deformation of soils is easily described. MPM is further extended for 3D analyses, and lastly in this chapter, behavior of a pile group subjected to soil deformation caused by faulting at its bedrock is numerically studied using the 3D MPM (Section **3.5**).

3.2 NON-LINEAR SPECTRAL STOCHASTIC FINITE ELEMENT METHOD (by Hori, M.)

3.2.1. Introduction

Hori et al. (2001 and 2002) have developed a new numerical method for simulating earthquake fault surface ruptures. The simulation is for unconsolidated surface layers, which are soft such that the fault rupture is dissipated within them. The shallower the soils are, the more substantial are the data for their mechanical properties, and yet, necessary amount of data for a numerical simulation are not always available. As will be explained, a stochastic model is thus constructed in order to take the uncertainty of the mechanical properties of the layers into consideration; see Hori *et al.* (2003). The developed simulation method provides a probabilistic estimation of the fault behavior; see **Figure 3.1** for the input and output of the simulation.

It is to be emphasized that the present simulation method requires two sets of input data, geotechnical information about surface unconsolidated layers and geological (or seismological) information of the fault plane and the fault geometry. In using the simulation method, therefore, it is indispensable to integrate works of experts from such different fields as geotechnical engineering, geology and computational mechanics.

A major difficulty in the numerical simulation of surface fault rupturing arises in modeling the subsoil structures properly. The available amount of data is not always enough for an entire domain of soil having a complicated layered structure. A stochastic model describing uncertainty of the subsoil structure in terms of probabilistic variables is an alternative to a deterministic model. The stochastic finite element method described within here uses this approach.

In this stochastic model, it is assumed that the surface soil deposit has elasto-plastic features, and that Young's modulus, E, for this medium exhibits Gaussian spatial distribution with its correlation length and variance (L and σ) given as;

$$Cor(E(\boldsymbol{x}), E(\boldsymbol{y})) = \sigma \exp\left(-\frac{|\boldsymbol{x} - \boldsymbol{y}|}{L} \right) \tag{3.1}$$

where *Cor* stands for the correlation, and $\boldsymbol{x}$ and $\boldsymbol{y}$ are the locations of two points. Poisson's ratio, ν, is assumed to be uniform over the entire medium. An associate flow rule with a yield function of Dracker-Prager type is used for the soil. Given the cohesion and the internal friction angle, c and ϕ, the yield function is given as;

$$f(\sigma_{ij}) = J - (c + \tan\phi\, I), \tag{3.2}$$

where I and J are the first and second invariants of the stress tensor. While they can be measured in laboratory tests, these parameters, namely, E, ν, c and ϕ, are approximately estimated from N-values and the ground type category. Stochastic parameters, L and σ, will be decided based on the engineering judgment, e.g. by looking up borehole data of the target site.

The NL-SSFEM is used to solve a boundary value problem for this stochastic model, assuming small deformations and a quasi-static state. Unlike conventional stochastic finite element methods, which use perturbation expansion to random variables, the SSFEM that is originally proposed by Ghanem and Spanos (1991) takes advantage of the function expansion of the random fields in physical and probabilistic spaces, which results in an accurate and efficient computation of a stochastic model; see Appendix of Section 3.2 for a brief explanation of the NL-SSFEM. It is to be emphasized that the NL-SSFEM is an alternative to the Monte-Carlo simulation of generating many different sets of input data of one specific problem, computing the behavior for each input data set and making statistical analysis for all results; the Monte-Carlo simulation requires a huge amount of numerical computations to solve non-linear problems of three-dimensional elasto-plastic bodies.

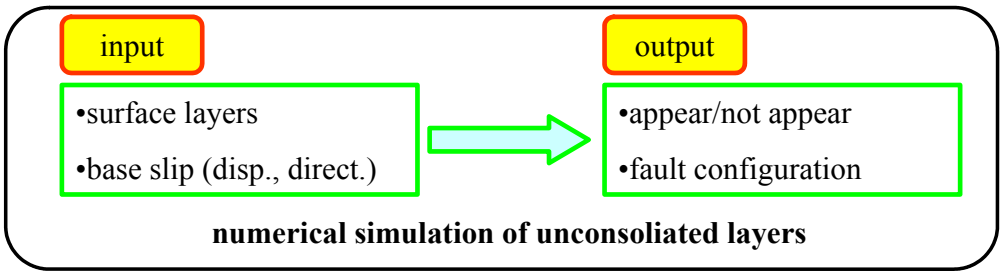

Figure 3.1. Input and output of numerical simulation of surface earthquake fault

Table 3.1. Material properties of model experiments

	2D	3D
mean Young modulus [kN/m^2]	20000	1225
Poisson ratio	0.25	0.25
density [g/cm^3]	1.6	1.6
friction angle [deg]	40	51
cohesion [kN/m^2]	38	38
standard deviation of Young modulus [%]	15	30
correlation length of Young modulus [m]	0.5	0.5

3.2.2 Reproduction of Model Experiments

We first seek to reproduce several results of model experiments made by Tani and others (1991, 1997), for verifying the validity of the NL-SSFEM as a numerical simulation tool for computing the surface earthquake fault ruptures. Both two-dimensional problems (normal or reverse faulting) and the three-dimensional problems (lateral faulting) are studied. The model experiments used sand boxes in which Toyoura sand (toyoura sand does not have cohesion)!? is loosely packed. **Table 3.1** summarizes the parameters of the material properties used for both the two and three-dimensional simulations of the model experiments. The base of the sand box is moved to simulate the faulting, and this base movement, *U*, is used as a boundary condition for the simulation.

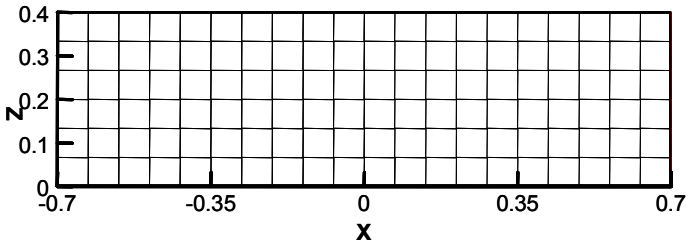

Figure 3.2. Configuration and meshing of two-dimensional problem.

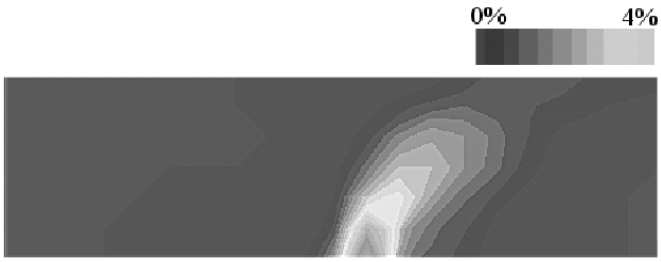

Figure 3.3. Pattern of shear band formation: distribution of maximum shear strain

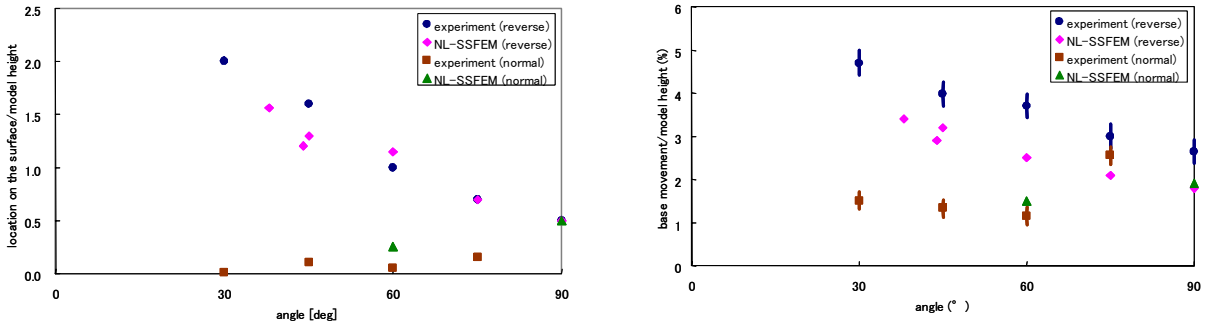

a) location b) base movement

Figure 3.4. Comparison of simulation results with experimental data

Two-dimensional problem

Figure 3.2 shows the configuration and meshing used for the two-dimensional simulation of the model experiments. The right side of the base ($x > 0$, $z = 0$) is moved upward or downward with proper angle to simulate normal or reveres faulting, respectively. **Figure 3.3** presents a typical pattern of the shear band formation; a distribution of the mean and standard deviation of the maximum shear strain is plotted.

The following two parameters are compared with the observed ones: 1) the location on the sample surface at which the shear bands reach; and 2) the amount of the base movement that causes shear bands to appear. **Figures 3.4a) and 3.4b)** show the comparison of the location and the base movement, respectively. As is seen, the agreement is satisfactory.

Three-dimensional problem

Figure 3.5 shows the configuration and the boundary conditions of the sample used for the three-dimensional problem. The periodicity along the sliding direction is assumed, and the interval is determined to minimize the external work that is needed to make the shear bands reach the surface. In **Figure 3.6**, the evolution of the shear band as the base displacement U is increased is displayed; the distribution of the maximum shear strain on four horizontal cross sections is shown. Although the formation of the regularly arranged oblique shear bands or the Riedel shears is reproduced, the shear band structure is different from the actual *embolic* structure in which shear bands overlap each other. This is mainly due to the coarse discretization of the model and the usage of a simple constitutive relation.

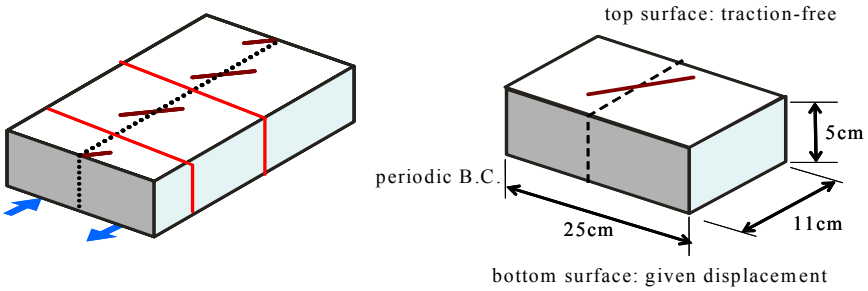

Figure 3.5. Configuration and boundary conditions of three-dimensional problem.

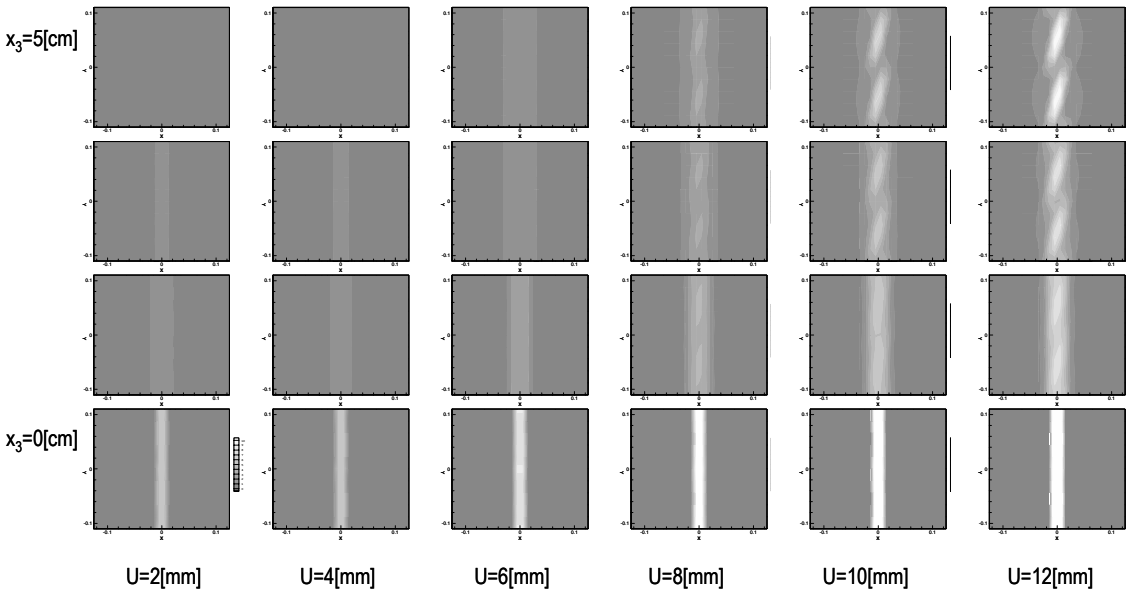

Figure 3.6 Evolution of shear bands as base moves: distribution of maximum shear strain on four horizontal cross sections form bottom (x_3=0[cm]) to top (x_3=5[cm])

Table 3.2. Comparison of shear band configuration.

	orinetation [deg]			interval [cm]			width [cm]		
depth[cm]	3	5	7	3	5	7	3	5	7
experiment	26	31	27	11			2.5～5.0	2.5～11.0	2.5～10.0
NL-SSFEM	23	29	31	11			1.8	3.0	3.0

Table 3.3. Comparison of critical base movement.

	mean [mm]			SD [mm]		
depth [cm]	3	5	7	3	5	7
exerirment	5	7	8	1	1	-
NL-SSFEM	5.3	8.6	11.1	0.80	0.21	0.16

We first compare the configuration of the Riedel shears, i.e., the orientation, the interval, and the length. **Table 3.2** summarizes the comparison of these parameters for the three cases of the experiment in which the sample thickness is 3, 5 and 7[cm]. As is seen, the agreement is satisfactory. We next compute the failure probability, which gives the probability that the Riedel shears reach the sample surface and is defined as a function of the base displacement, U. For the comparison, we obtain from the failure probability the mean and standard deviation of the critical base movement at which the shear band appears, and compare them with the experimental data in **Table 3.3**. It is seen that the NL-SSFEM succeeds to reproduce the experiment data of U that leads to the failure fairly well.

3.2.3 Simulation of the Nojima Earthquake Fault

Since the basic validity is verified, we examine the applicability of the NL-SSFEM to numerically simulate an actual surface earthquake fault. The Nojima earthquake fault is studied, and the target is the Nashimoto District, which has various data ranging from geological structures to ground structures and properties as well as data for the fault mechanism. We construct a stochastic model for the unconsolidated layers (which belong to the Osaka Layers) as the flat single layer of the thickness 9[m]; the material properties estimated from the measured N-values are summarized in **Table 3.4**. According to the available data, we set the dip angle of the fault plane as 90[deg] and the direction of the fault displacement as 45[deg]. The lateral faulting is coupled with normal faulting.

Table 3.4. Material properties used for Nojima Earthquake Fault simulation

mean Young modulus [kN/m^2]	6125
Poisson ratio	0.25
density [g/cm^3]	2.1
friction angle [deg]	51
cohesion [kN/m^2]	38
standard deviation of Young modulus [%]	30
correlation length of Young modulus [m]	2

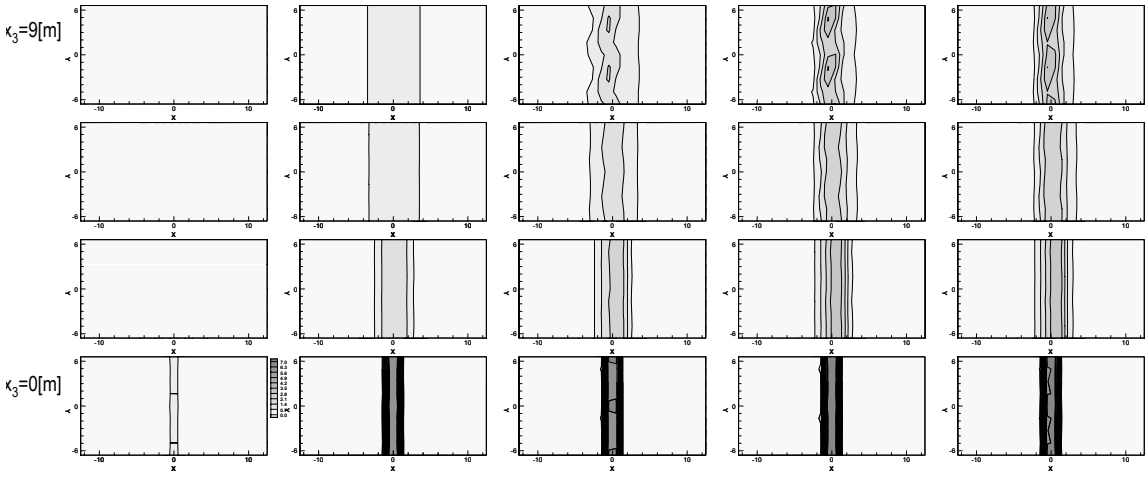

Figure 3.7. Rupture processes in surface layers: distribution of mean maximum shear strain on horizontal cross sections from the bottom (x_3=0[m]) to the top (x_3=9[m]).

As a typical example of the simulation, **Figure 3.7** shows the rupture processes within the stochastic model of the unconsolidated layers. As is seen, the formation of echelon faults is reproduced. Similar echelon faults are simulated for other dimensions of the stochastic model. The computed structure, however, is too simple compared with the expected embolic or flower structures. As mentioned in the preceding section, this is the limitation of the numerical simulation of the present NL-SSFEM with the coarse discretization and a simple constitutive relation.

First, we compare the configuration of the simulated echelon fault with the observation. **Table 3.5** summarizes the comparison of the configuration parameters, the orientation and the interval. The computed parameters are in good agreement with the observed ones. This agreement is owing to the good quality of the data that are input to the NL-SSFEM; parametric studies are being carried out to examine the sensitivity of the configuration on the input data, from which we understand the quality of the data input to the NL-SSFEM. Next, we compute the failure probability and plot it in **Figure 3.8**. It is certainly true that there are no direct evidences that support or deny the accuracy of the computed failure probability. However, the estimation that the bed rock displacement that forms the surface earthquake fault is around 0.5[m] appears reasonable, and hence it suggests the usefulness of the numerical simulation of the fault behavior.

Table 3.5. Comparison of surface earthquake fault configuration.

	observed	NL-SSFEM
fault	left echelon	left echelon
angle to strike direction [deg]	22-35	25
interval of echelon faults [m]	4.0-6.0	6
width of echelon faults [m]	0.5-1.5	1.4

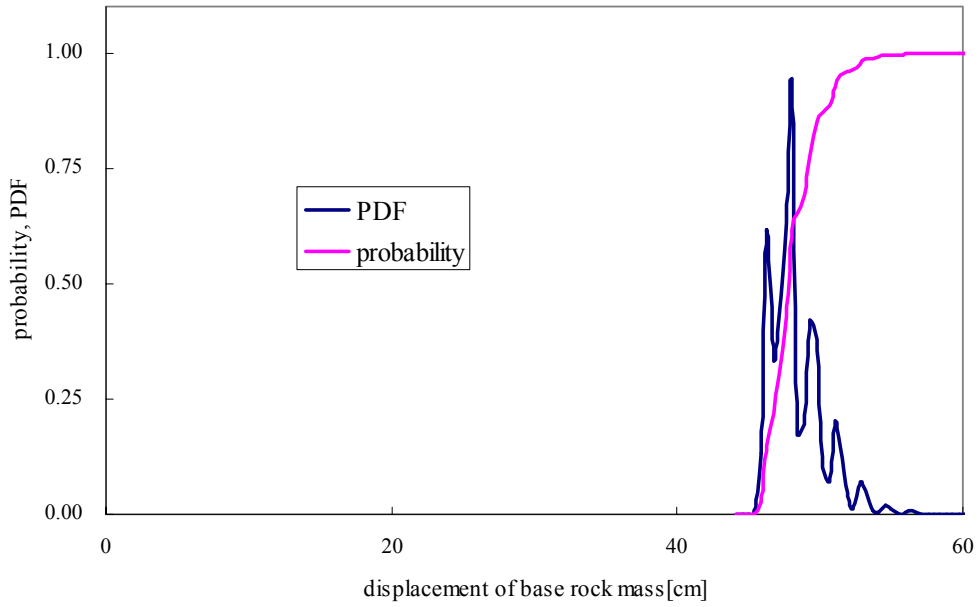

Figure 3.8. Failure probability of the Nojima Earthquake Fault.

3.2.4. Simulation of the CheLungPu Earthquake Fault

In this section, the Chelungpu Earthquake Fault is studied as a different type of earthquake fault than the Nojima earthquake fault. Based on the trench investigation, we construct a stochastic model for the unconsolidated layer as the flat single layer of 1.2[m] height with 4.8[m] width; the material properties are set to be those of fine sand and silty sand as shown in **Table 3.6**. According to the available data, we model this fault as a reverse fault with the dip angle of 60^{O}.

As a typical example of the simulation, **Figure 3.9** shows the rupture processes within the stochastic model of the unconsolidated layer. As is seen, fault evolution along a straight line is reproduced. Similar type of straight line is observed in the Chelungpu earthquake fault. Because the thickness of the unconsolidated layer is small, simple configuration of the fault is easy to expect (although it is not easy to reproduce).

Table 3.6. Material properties used for Chelungpu Earthquake Fault

mean Young modulus [kN/m^2]	20000
density [g/cm^3]	1.6
Poisson ratio	0.25
friction angle [deg]	40
cohesion [kN/m^2]	35
initial compressive strength [kN/m^2]	150
initial tensile strength [kN/m^2]	32
standard deviation of Young modulus [%]	30
correlation length of Young modulus [m]	1.0

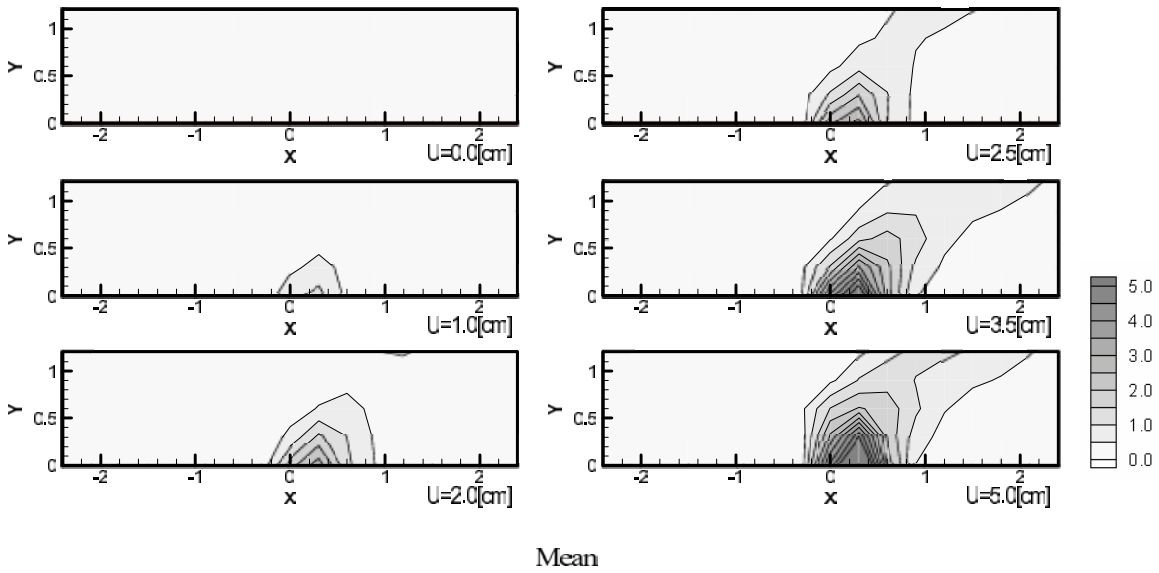

Figure 3.9. Rupture process in the unconsolidated surface layer: distribution of mean maximum shear strain

The configuration of the simulated reverse fault is compared with that observed at the Chelungpu Earthquake Fault. Quantities to be compared are i) the critical base lift (D) and ii) the horizontal distance between the point where the displacement gap is introduced at the base and the place where the fault appears on the surface (W). **Table 3.7** summarizes the comparison of the configuration parameters. The simulated width of the reverse fault, W, shows good agreement with the observed one. On the other hand, D, the critical base lift obtained from NL-SSFEM seems to be much smaller than the observed one. However, as mentioned in the comment to the table, D for the actual fault is the maximum dislocation on the ground surface, which is much more than enough to let the earthquake fault reach to the surface. In this sense, we have no reference to evaluate the agreement in D. Next, we compute the failure probability and plot it in **Figure 3.10**. Again, as mentioned in the simulation of the Nojima Earthquake Fault, it is certainly true that there are no direct evidences that support or deny the accuracy of the computed failure probability. However, the estimation that the base lift that forms the surface earthquake fault is around 0.045[m] appears reasonable for the thickness of the Chelungpu Earthquake Fault, and hence it suggests the usefulness of the numerical simulation of the fault behavior.

Table 3.7. Comparison of fault configuration

	D [m]	W [m]
Chelungpu fault	(1.3)	1.4
SSFEM	0.045	1.2

※ (・) shows the maximum dislocation of real fault on the ground surface.

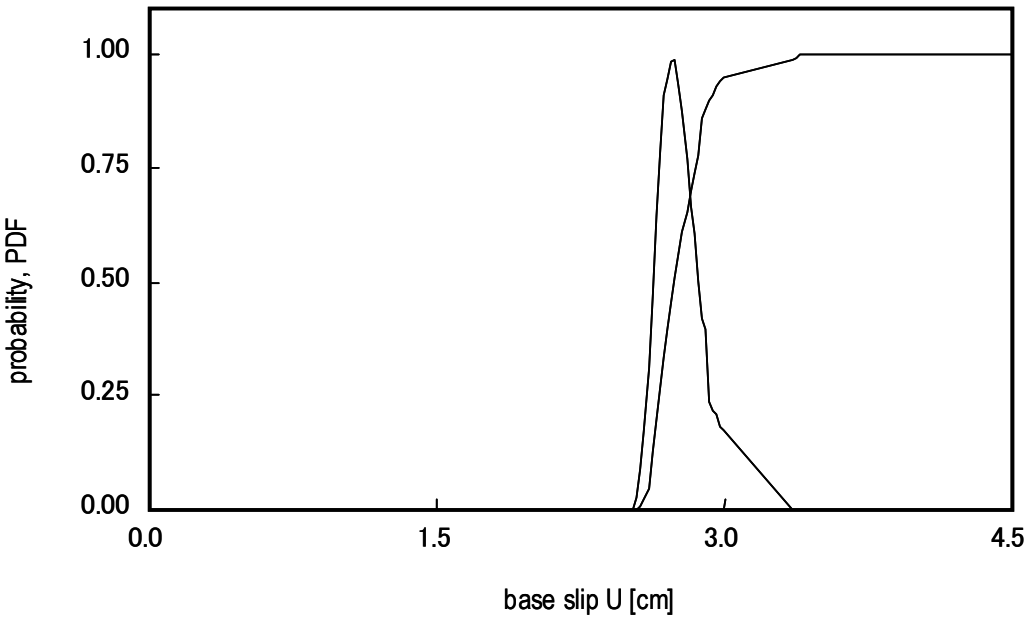

Figure 3.10. Failure probability of the Chelungpu Earthquake Fault.

3.2.5. Summary

We have studied the applicability of the NL-SSFEM to numerically simulate the behavior of the surface earthquake fault ruptures within soft unconsolidated layers. It is shown that the NL-SSFEM is able to provide a probabilistic estimation of the fault formation as well as the possible configuration. The reproduction of the two- and three-dimensional model experiments is satisfactory, and the configuration of the Nojima Earthquake Fault is simulated although the NL-SSFEM cannot reproduce the complicated embolic structures. Also, the simulation of the Chelungpu Earthquake Fault shows good agreement in the fault configuration with the actual fault. These results demonstrate the usefulness of the numerical simulation to probabilistically estimate the actual surface earthquake faults.

While the NL-SSFEM can be improved, we may not expect that data of good quality are available for all targets in which faults are hidden and earthquake fault surface ruptures can form. Therefore, improving the NL-SSFEM for the fault problem is not a first priority though desired. We plan to apply the NL-SSFEM to solve more practical problems related to the earthquake fault surface ruptures.

Appendix of SECTION 3.2: NL-SSFEM

The SSFEM was originally proposed by Ghanem and Spanos (1991), as an efficient general numerical analysis method of solving various probabilistic continuum problems; see Honda (2002). The key issue of the SSFEM is the function expansion in the probabilistic space. In the present NL-SSFEM, the correlation given to Young's modulus is used to take the Karhunen-Loeve (KL) expansion for it, such that the bases of the physical spaces and the probabilistic spaces are defined. Then, the polynomial chaos (PC) expansion, which is given as the multi-dimensional Hermit polynomials of the bases defined by the KL expansion, is applied to the random vector-valued function for displacement. That is,

$$E(x,\omega) = \sum_n E^n \varphi^n(x)\xi^n(\omega), \tag{3.3}$$

$$u_i(x,\omega) = \sum_m u_i^m(x)\Gamma^m(\omega), \tag{3.4}$$

where ω stands for an event in the probabilistic space. While the KL expansion, Equation (3.3), is for the Gaussian random field, the PC expansion, Equation (3.4), is applicable to more general probabilistic distributions. The SSFEM is extended to solve non-linear problem in incremental form, with suitable treatment of the mean of the random variables from which the linearization of the non-linear problem is made. This completes the formulation of the NL-SSFEM; see Anders and Hori (2001) and Hori *et al.* (2002). **Figure 3.11** presents the basic algorithm of the NL-SSFEM.

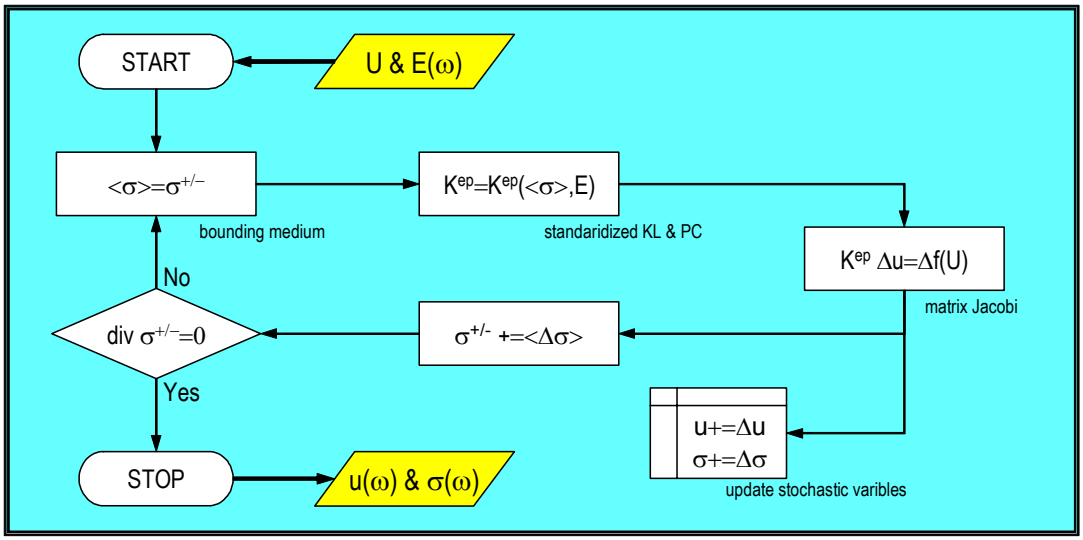

Figure 3.11. Algorithm of NL-SSFEM.

References of SECTION 3.2

Anders, M. and Hori, M. (2001). "Three-dimensional stochastic finite element method for elasto-plastic body." *Int. J. Numer. Meth. Engng*., Vol. 51, 449-478.

Bray, J.D., Seed, R.B. and Seed, H.B. (1994). "Earthquake fault rupture propagation through soil," *J. Geotech. Eng.*, Vol. 120, No. 3, ASCE, 543-561.

Ghanem, R.G. and Spanos, P.D. (1991). *Stochastic finite elements: a spectral approach*, Springer, New York.

Honda, R. (2001). "Analysis of wave propagation in random media by spectral stochastic finite element method,", *J. Struct. Mech. Earthquake Eng.*, Vol. 710/I-60, JSCE, 337-346 (in Japanese).

Hori, M., Anders, M. and Gotoh, H. (2002). "Model experiment and numerical simulation of surface earthquake fault induced by lateral strike slip." *Structural Eng./Earthquake Eng,* Vol. 19, No. 2, JSCE, 227-236.

Hori, M., Ichimura, T. and Nakagawa, H. (2003). "Analysis methods of stochastic model: application to strong motion and fault problems," *Structural Eng./Earthquake Eng,* (accepted).

Ke, T-C. and Bray, J.D. (1995). "Modeling of particulate media using discontinuous deformation analysis," *J. Eng. Mech.*, Vol. 121, No. 11, ASCE, 1234-1243.

Konagai, K. (2000). Proceedings of International workshop for seismic fault-induced failures, JSCE.

Ohmatchi, T., Kojima, N. and Murakami, A. (2002). "Ground displacement and change in reservoir water level due to seismic rupturing of a hidden fault underlying a dam site," *J. Struct. Mech. Earthquake Eng.*, Vol. 710/I-60, JSCE, 337-346 (in Japanese).

Onizuka, N. Hakuno, M. Suzuki, T., Iwashita, W. and Hori, M. (2002). "Model experiment on rupture propagation of surface grounds due to dip-slip fault movements of bacements," *J. Geotech. Eng.*, Vol. 701, No. 58, JSCE, 29-38 (in Japanese).

Tani, K. and Ueta, K. (1991). "Shape and location of discontinuity in sand induced by fault displacement in bed rock," in *Proc. 26 Japan National Conf. on Geotech. Eng.*, 1185-1188, JSGE (in Japanese).

Tani, K., Ueta, K. Abe, S., Nakada, Y. and Hayashi, Y. (1997). "Deformation structure of surface unconsolidated layer along the Nojima Earthquake Fault," *J. Geotech. Eng.*, Vol. 568/III-39, JSCE, 21-39 (in Japanese).

Taniyama, T. and Watanabe, H. (1998) "Deformation of sandy deposits by reverse faulting," *J. Struct. Mech. Earthquake Eng.*, Vol. 591/I-43, JSCE, 313-3258 (in Japanese).

3.3. APLIED ELEMENT METHOD (by Meguro, K.)

3.3.1 Introduction

Many researchers conducted experiments to understand the phenomena of surface failure. Cole and Lade (1984) tried to determine the surface fault rupture location and the affected zone width in an alluvium deposit over a dip-slip fault using their fault test box. They hypothesized that the results would be applicable to cohesive materials. Lade et al. (1984) attempted to determine multiple failure surfaces by shearing sand in a fault test box. The results of the sand box model tests showed that the displacement fields were basically the same for different materials. Onizuka et al. (1999) investigated bedrock stresses induced by reverse dip-slip faults using aluminum rods. Bray (1990) studied rupture patterns in clay models subjected to dip-slip faulting under a 1-g gravitational field. The range of the bedrock dip angle varied from 60 to 90 degrees for both normal and reverse faults. Tani et al. (1994) conducted a 1-g model experiment of dip-slip faulting using dry Toyoura sand. The results of their first test series indicated that the necessary base offset for the rupture to propagate up through the deposit to its surface varied with the fault orientation. The essential features observed in these experiments were consistent with those reported by Cole and Lade (1984).

Although the above-mentioned experimental methods provide a basic understanding of the extension of the zones affected by faulting, the actual field conditions are hardly replicated. This is mainly due to the difficulties involved in the control of the material properties and the modeling of the boundary conditions. Furthermore, a large amount of data is necessary for establishing reliable relationships between seismic fault parameters and resulting surface deformation.

Alternatively, the surface failure phenomenon may be grasped with numerical models. This approach has the advantage of easily controlling material properties, model size, boundary conditions, etc. It is obvious that the accuracy and reliability of any numerical approach largely depends on the validity of the mathematical conceptualization of the critical states of materials (Bray, 1990). However, if the numerical modeling limitations are clearly understood, these analyses are very useful for engineers to understand the problem in question.

A soil mass is not a continuum, rather it consists of finite-sized particles. Inter-particle forces determine the soil overall macroscopic features. Once shear or tension cracks develop within a soil mass, its behavior becomes difficult to describe with the conventional numerical methods based on the principles of continuum mechanics. For this reason, the Distinct Element Method (DEM) has been extensively used in the field of soil mechanics. In spite of its suitability for the soil analysis, the DEM has a serious drawback. Because the DEM is based on an explicit time-marching calculation scheme, it requires small time increments, i.e. large calculation time, to guarantee the stability of the calculation (Hakuno and Meguro, 1993). To overcome this limitation, the Applied Element Method was used in the present study.

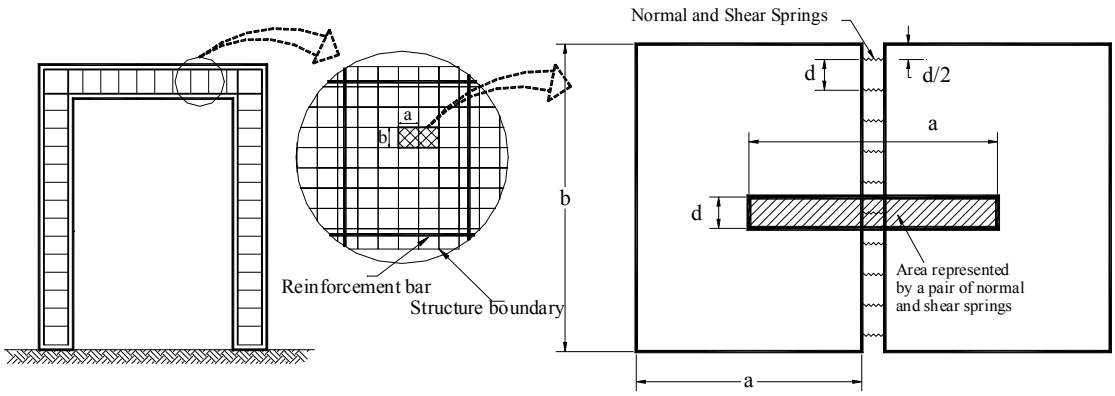

(a) Element generation for AEM (b) Spring distribution and area of influence of each pair of springs

Figure 3.12. Modeling of structure in AEM

3.3.2 Formulations

In the Applied Element Method (Meguro et al., 1997, 2000), the structure is modeled as an assemblage of small rectangular elements as shown in **Figure 3.12(a)**. Two neighboring elements are assumed to be connected by pairs of normal and shear springs lined up along the element-element interface (**Figure 3.12(b)**). Each pair of springs represents stresses and deformations for a certain area (hatched area in **Figure 3.12(b)**). The spring stiffness is given by:

$$K_n = \frac{E \times d \times T}{a} \quad \text{and} \quad K_s = \frac{G \times d \times T}{a} \tag{3.5}$$

where, d is the space between adjacent spring pairs, T is the element thickness, a is the length of the representative area, and E and G are the material Young's and shear moduli, respectively. These equations indicate that the spring stiffness is calculated as if they connect element centerlines.

In 2D-AEM, each element has three degrees of freedom. Although each of the structure elements moves as a rigid body, the structure as a whole is flexible. This flexible behavior is considered through the connecting springs where internal stresses and deformations occur. The governing equation is:

$$[K_G][\Delta] = [F] \tag{3.6}$$

where, $[K_G]$ is the global stiffness matrix; $[\Delta]$ the displacement vector and $[F]$ the applied load vector.

The global stiffness matrix is assembled by summing up the contributions of all the connecting springs. The stiffness matrix of one pair of normal and shear springs is a 6x6 matrix whose upper-left quarter is:

$$\left[\begin{array}{c|c|c} \begin{array}{l}\mathrm{Sin}^2(\theta+\alpha)K_n \\ +\mathrm{Cos}^2(\theta+\alpha)K_s\end{array} & \begin{array}{l}-K_n\mathrm{Sin}(\theta+\alpha)\mathrm{Cos}(\theta+\alpha) \\ +K_s\mathrm{Sin}(\theta+\alpha)\mathrm{Cos}(\theta+\alpha)\end{array} & \begin{array}{l}\mathrm{Cos}(\theta+\alpha)K_sL\mathrm{Sin}(\alpha) \\ -\mathrm{Sin}(\theta+\alpha)K_nL\mathrm{Cos}(\alpha)\end{array} \\ \hline \begin{array}{l}-K_n\mathrm{Sin}(\theta+\alpha)\mathrm{Cos}(\theta+\alpha) \\ +K_s\mathrm{Sin}(\theta+\alpha)\mathrm{Cos}(\theta+\alpha)\end{array} & \begin{array}{l}\mathrm{Sin}^2(\theta+\alpha)K_s \\ +\mathrm{Cos}^2(\theta+\alpha)K_n\end{array} & \begin{array}{l}\mathrm{Cos}(\theta+\alpha)K_nL\mathrm{Cos}(\alpha) \\ +\mathrm{Sin}(\theta+\alpha)K_sL\mathrm{Sin}(\alpha)\end{array} \\ \hline \begin{array}{l}\mathrm{Cos}(\theta+\alpha)K_sL\mathrm{Sin}(\alpha) \\ -\mathrm{Sin}(\theta+\alpha)K_nL\mathrm{Cos}(\alpha)\end{array} & \begin{array}{l}\mathrm{Cos}(\theta+\alpha)K_nL\mathrm{Cos}(\alpha) \\ +\mathrm{Sin}(\theta+\alpha)K_sL\mathrm{Sin}(\alpha)\end{array} & \begin{array}{l}L^2\mathrm{Cos}^2(\alpha)K_n \\ +L^2\mathrm{Sin}^2(\alpha)K_s\end{array} \end{array}\right] \tag{3.7}$$

All the parameters are shown in **Figure 3.13**. Further details of the AEM formulation and applications are found elsewhere (Meguro et al., 1997, 2000).

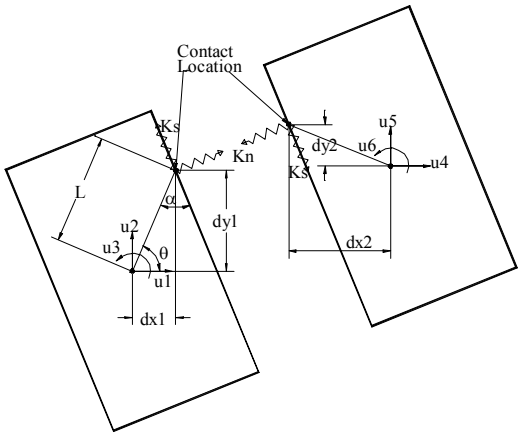

Figure 3.13. Spring connectivity

3.3.3 Material model

Since one of the major objectives of this study was to demonstrate the feasibility of the AEM for the analysis of the surface fault rupture phenomena, a simple hyperbolic model was used for the soil. In this model, it is assumed that the soil stress-strain curve follows a hyperbolic shape bounded by two asymptotes for small and large strains, respectively. The asymptote for small strains, denoted G_o, represents the elastic modulus whereas the horizontal asymptote for large strains, denoted τ_f, represents the soil strength. The stress-strain curve with is thus described by the following equation:

$$\tau = \frac{G_o \times \gamma}{1 + \frac{\gamma}{\gamma_\Gamma}} \tag{3.8}$$

where G_o is the initial shear modulus, γ is the shear strain, and γ_Γ is the reference strain equal to τ_f / G_o.

In the normal direction, the spring tensile stress was limited by the soil tensile strength. Once this limit was reached, the spring was assumed broken and did not carry load anymore.

3.3.4 Model Preparation

Figure 3.14 and **Figure 3.15** show a typical reverse fault and the idealization used for the present study. The model was 1km long and 150m deep and several observations points were considered as shown in the figure. It is assumed that these dimensions are sufficient to prevent any effect of the boundaries on the deposit behavior next to the fault. The model base was assumed fixed, whereas vertical displacements were allowed at the side boundaries. The base fault was located at the center of the model bottom.

The material properties used for the analysis are shown in **Table 3.1**.

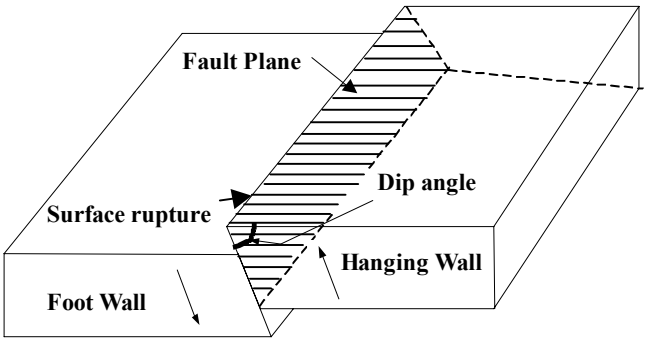

Figure 3.14. Fault terminology

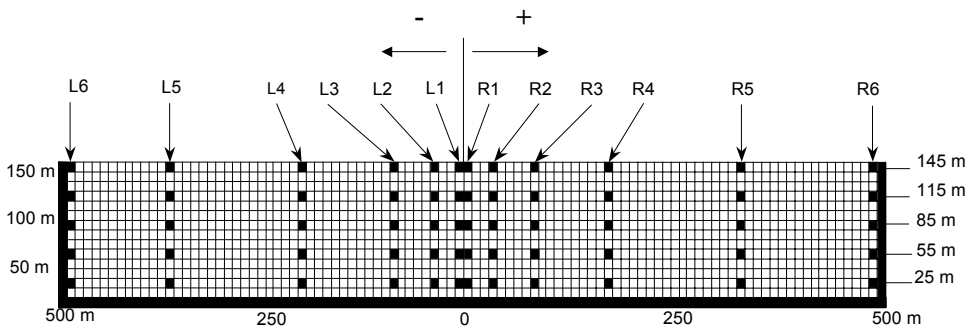

Figure 3.15. Numerical model for fault rupture study and analysis observation points

Table 3.1 Material Properties

	E (kN/m^2)	γ (kN/m^3)	f_c (kN/m^2)	f_t (kN/m^2)
Bedrock	$66x10^6$	26.5	$2.5x10^4$	$2.5x10^3$
Soil deposit	$20x10^5$	18.0	$1.5x10^4$	$1.5x10^3$

At first, the model self-weight was applied in a static way. After this, the dynamic analysis of the surface fault rupture was carried out.

3.3.5. Fault slip rate

A fault is characterized by five parameters: fault length (L), fault width (W), rupture velocity (VR), final offset (D), and rise time (t). In the analysis presented in this chapter, only the last two are relevant. Both are directly related with the fault slip rate and were found to strongly influence the dynamic surface fault rupture process.

To understand the slip rate effect, linear elastic analyses were performed for two slip functions, namely, the ramp and cosine curves shown in **Figure 3.16**. **Figure 3.17 and 3.18** show the response characteristics for the two considered functions. From this set of figures, it is clear that different input base displacements caused different vibration features. In **Figure 3.17(c)**, a sudden rise and a drop in the velocity exactly at the starting and ending of the ramp function is observed. For this reason, the input base displacement following the cosine model was considered appropriate and was adopted the analysis that followed.

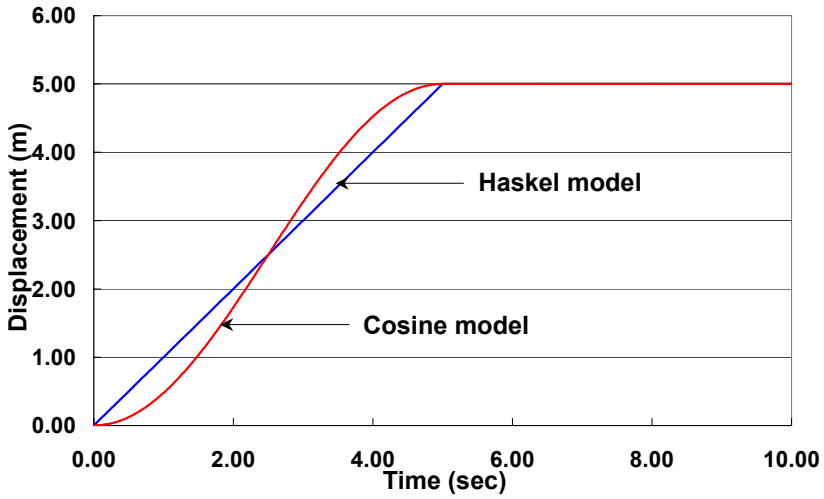

Figure 3.16. Slip function

3.3.6. Case Study

Permanent ground displacements that accompany a seismic event are the consequence of the fault slip and are referred as the static displacement field or coseismic displacements (Hall et al., 1995, Tatcher, 1986). This displacement field differs from the ground displacements induced by the seismic waves, which are generated during earthquake's rupture propagation also referred as dynamic displacement field. Despite their name, near–fault static displacements are developed within the short time span that related to the slip rise time. Because of this, it can be considered that the coseismal displacement is a dynamic phenomenon.

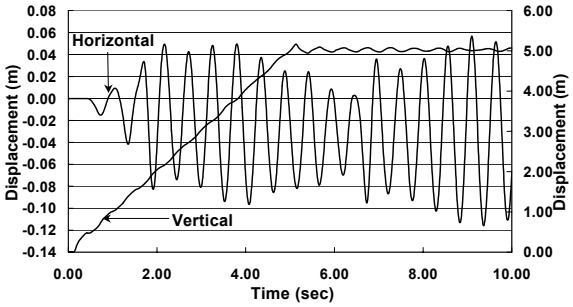

(a) Horizontal and vertical displacement time history Element "R5" (Haskell model)

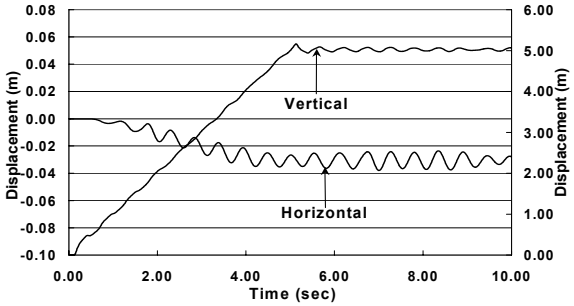

(a) Horizontal and vertical displacement time history Element "R5" (Cosine model)

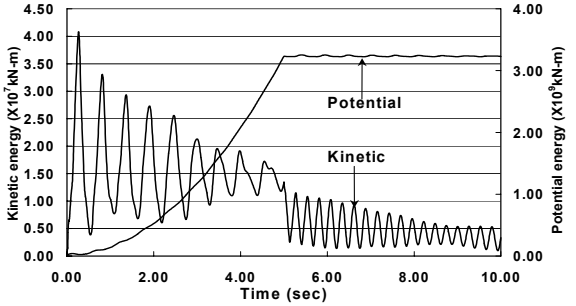

(b) Kinetic and potential energy changes in the system (Haskell model)

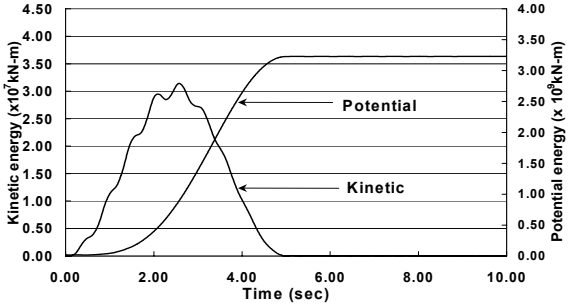

(b) Kinetic and potential energy changes in the system (Cosine model)

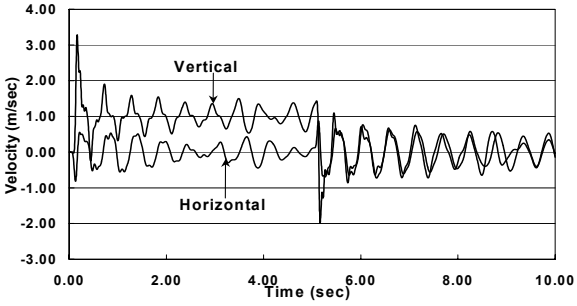

(c) Velocity time history of element "R5" on hanging wall (Haskell model)

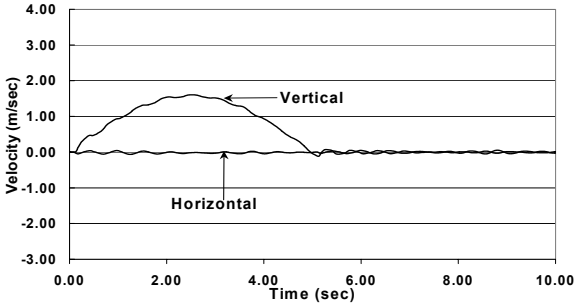

(c) Velocity time history of element "R5" on hanging wall (Cosine model)

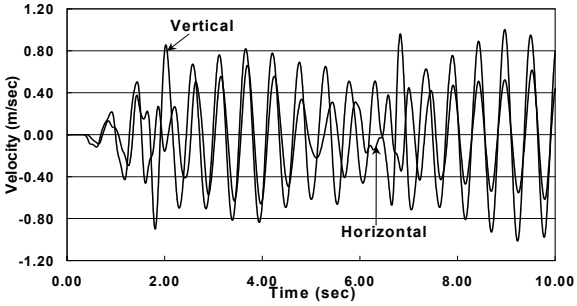

(d) Velocity time history of element "L5" on footwall (Haskell model)

Figure 3.17 Effect of slip function on the response of soil deposit (Haskell model)

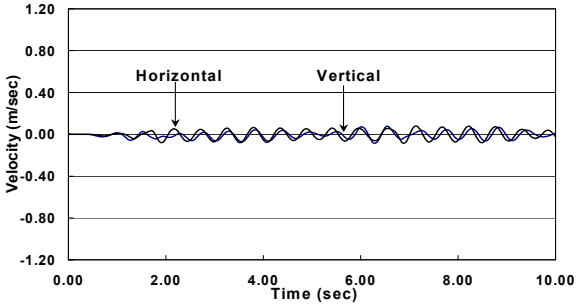

(d) Velocity time history of element "L5" on footwall (Cosine model)

Figure 3.18 Effect of slip function on the response of soil deposit (Cosine model)

The coseismic displacements are evidenced in their time histories as motion pulses with a ramp-type shape. **Figure 3.19** shows a record obtained during the 1999 Chi-chi earthquake in Taiwan which exhibits this feature. In order to compare the numerical analysis results with the near field seismic records obtained during Chi-chi earthquake, the 2D model shown in **Figure 3.15** was used.

For comparing the results with real near field records with large displacement, the closed form approximation of the static displacement was considered. The pulse-like displacement time history that represents the base motion is shown in **Figure 3.20** based on a Gaussian-type function (Kostadinov, 2000):

$$d_{sp}(t) = \frac{\sqrt{2\pi}}{n} V_{sp} T_p \Phi\left[\frac{(t - t_c)}{T_p / n}\right] \tag{3.9}$$

where V_{sp} is the amplitude of static velocity pulse, T_p, the velocity pulse duration, t_c time at which the pulse is centered, n, constant equal to 6 and t, time. The term T_p/n corresponds to the standard deviation and controls the actual spread of the pulse with respect to the given pulse duration and Φ is the normal probability function.

Although, the wave amplitude attenuates due to material and radiation damping, in the present study only the former was considered because the discussion focuses at a location very close to the fault trace and therefore only the material damping is relevant.

Figures 3.21(a) and **(b)** show the vertical and horizontal displacement time histories, respectively. From **Figure 3.21(a)** it can be seen that from L3 to L5, the displacement is similar to the input displacement. However, it decreases towards the footwall side where it is nule. From **Figure 3.21 (b)**, it can be seen that the effect of hanging wall displacement on the horizontal surface deformation is significant in the near fault region and towards the footwall.

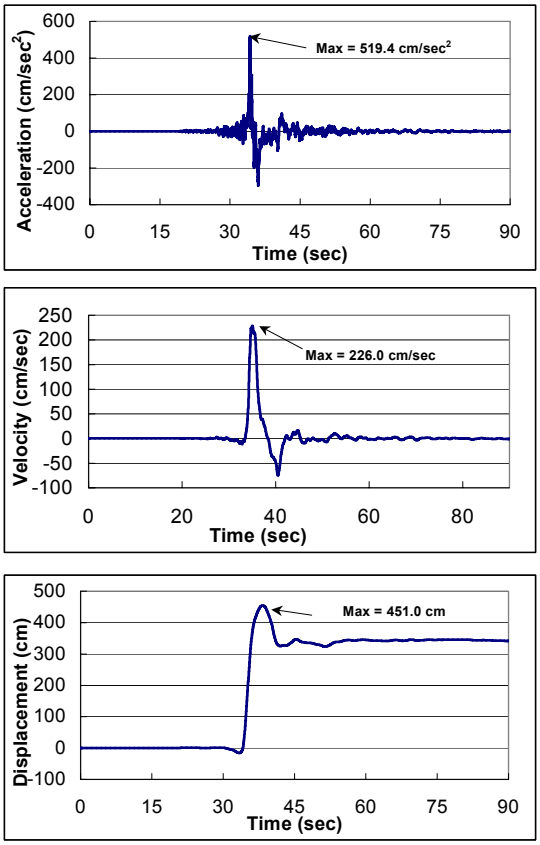

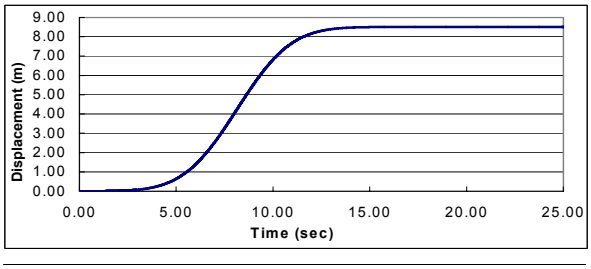

Figure 3.19 (Left). Acceleration Velocity and displacement time history of the records obtained at Shihkan (TCU068) during the 1999 Chi-chi, Taiwan earthquake (Lee et al, 1999)

Figure 3.20 (Above).
Assumed static input displacement

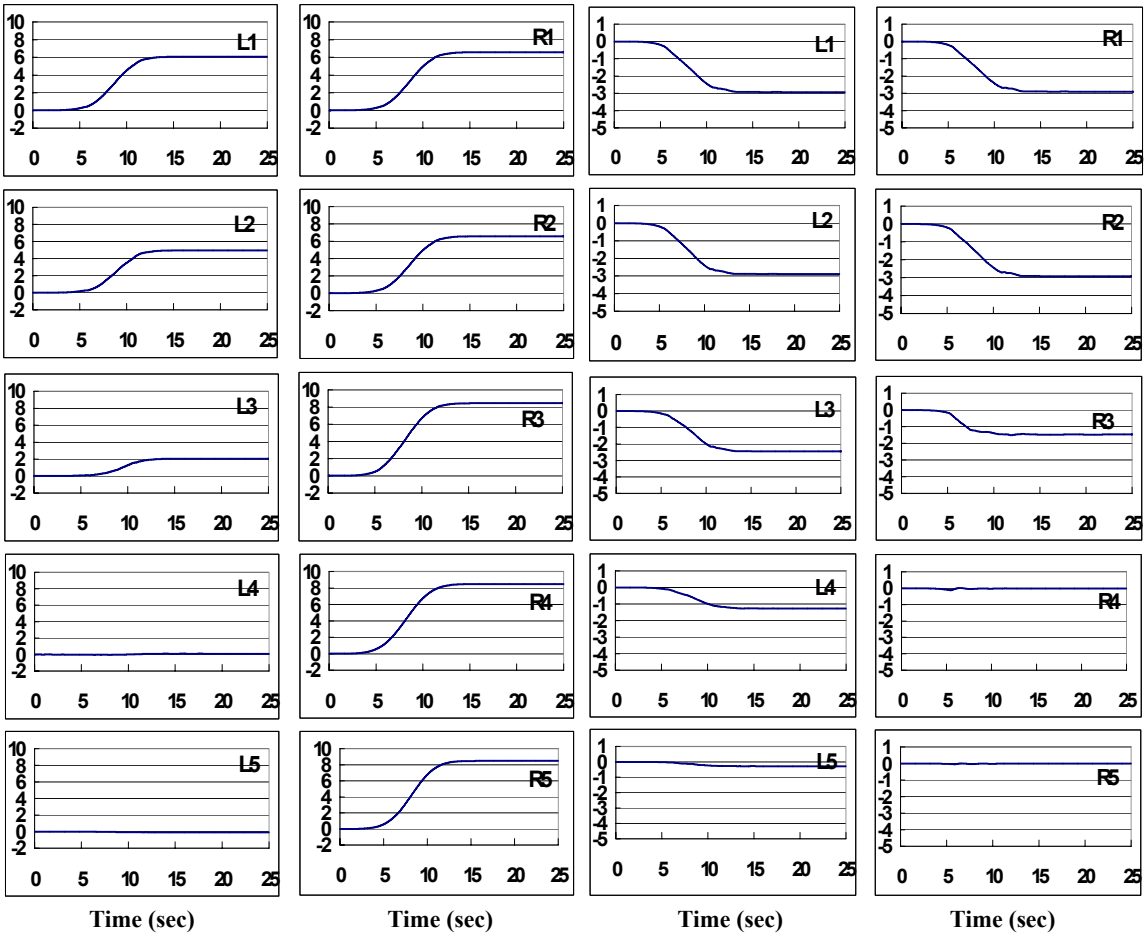

(a) Vertical surface displacement **(b)** Horizontal surface displacement

Figure 3.21. Vertical and horizontal displacement time histories (at L1~L5 and R1~R5)

Figures 3.22(a) and **(b)** show the vertical and horizontal acceleration time histories. From this figure, it can be seen that the acceleration on the surface attenuates as distance from the fault increases. The spatial distributions of the final surface deformation in the horizontal and vertical directions are shown in **Figure 3.23**. It is clear that the surface vertical displacement is proportional to the hanging wall displacement. On the footwall side, however, there is a slight negative vertical displacement. As for the horizontal displacements, it is apparent that the deformation occurred in a wide region on the footwall side. This is not observed in the hanging wall in which stresses were released due to the tension crack appearance.

Figure 3.24 show the attenuation of peak ground acceleration, velocity and displacement. In each graph right and left upright broken lines correspond to the base fault location and the possible surface rupture location, respectively. **Figure 3.24(a)** shows that both horizontal and vertical PGA values increase as we approach the center of the soil model, and then reach their peak values shortly after crossing the surface rupture location. After the peak values are reached, they go downwards to the right, towards the hanging wall direction. In general, the damage exactly above the surface rupture is mainly due to the large relative permanent displacement. However, slightly off the fault, the damage is often less serious than that found a little far away from the surface rupture. This phenomenon has being reported during past earthquakes (Hakuno et al., 1997). However, due to the sparse distribution of seismometers, no recorded data could describe clearly this phenomenon. In this sense, the proposed model can capture this feature of the phenomenon.

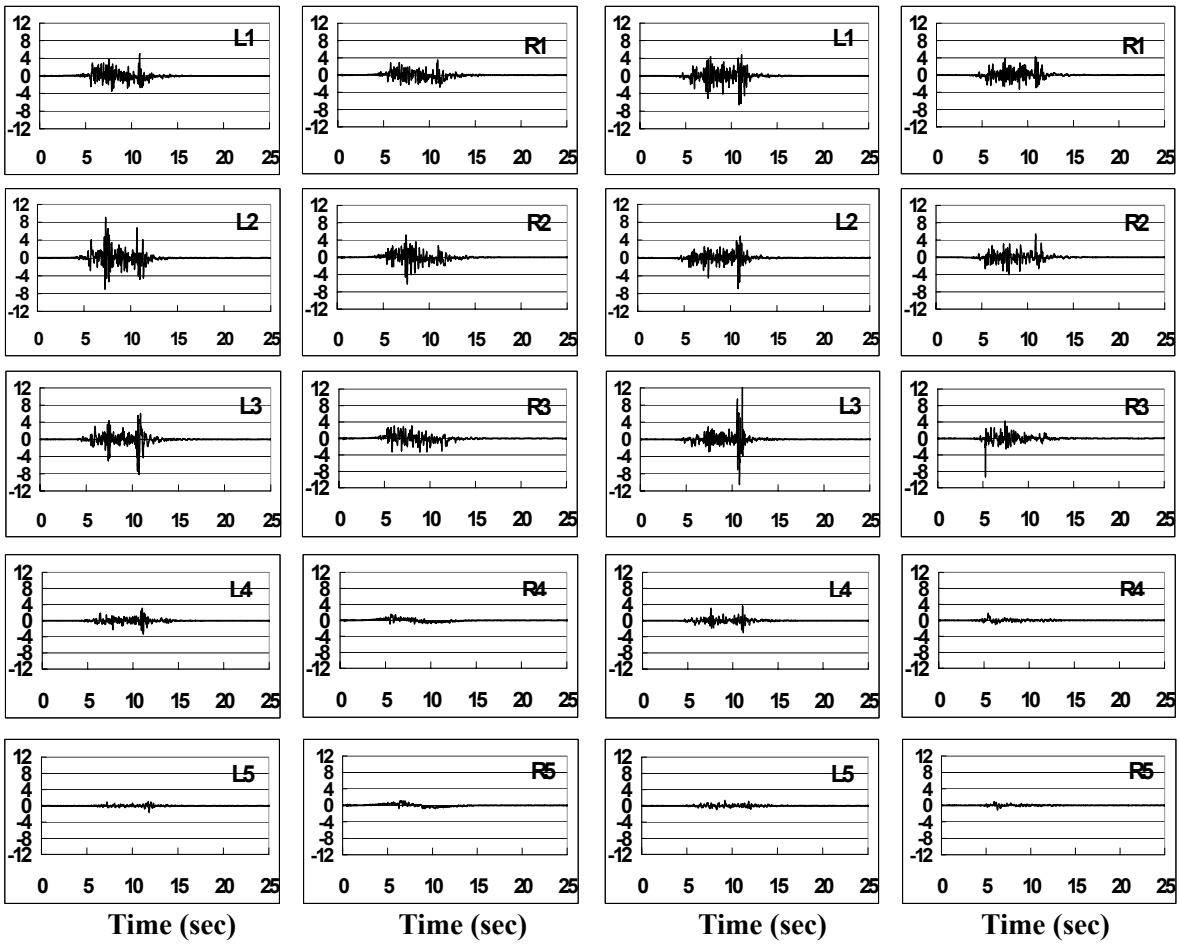

(a) Vertical acceleration time histories **(b)** Horizontal acceleration time histories

Figure 3.22. Vertical and horizontal acceleration time histories (at L1~L5 and R1~R5)

Figure 3.24(b) shows the attenuation of peak ground velocity (PGV) with distance. It can be seen that the vertical velocity component is highest on the hanging wall side and reduces towards the footwall. The horizontal velocity, on the other hand, is lowest near the surface rupture location, slightly increases towards the hanging wall direction and then attenuates with the distance. **Figure 3.24(c)**, which shows the peak ground displacement (PGD) attenuation, is very similar to the graph shown in **Figure 3.23**.

In general, **Figure 3.24** shows that peak responses are not maximum near the place where the surface rupture takes place. Instead, they reach their maximum values slightly away from the surface rupture towards the hanging wall direction. This is due to the high non-linearity observed near the surface fault rupture, as evidenced from the deposit crack pattern shown in **Figure 3.25**. Because of this, the response in the region next to the surface rupture becomes lower than the response in the adjacent areas.

A parametric study was conducted to find the influence of the material elastic properties on the surface deformation and crack propagation. Four kinds of soil properties with shear wave velocities equal to 745, 527, 373 and 264 m/s, respectively, were considered. The fault displacement considered is the one shown in **Figure 3.20**. **Figure 3.26** shows the final surface displacement. It is apparent that the deformation is absorbed within the soil deposit in case of soft soil. If a harder soil lies on top of the fault, the influence area on the surface is larger. **Figure 3.27** shows the crack patterns for the four considered soils. It is clear that soft soil deposits tend to have narrower shear bands than harder soils.

The above-discussed study is important because geological observations of surface ruptures associated with historical earthquakes have indicated that surface ruptures occurred without exceptions on pre-existing faults. Moreover, there is evidence indicating that moderate to large-scale faults have repeatedly moved. The repetitive nature of faulting provides a basis for predicting future fault activity by using geologic information. Therefore, the study on the fault rupture propagation is useful to establish the possible locations of the faults appearing on the surface in future earthquakes. This provides valuable information to engineers for the design of structures located on vulnerable areas.

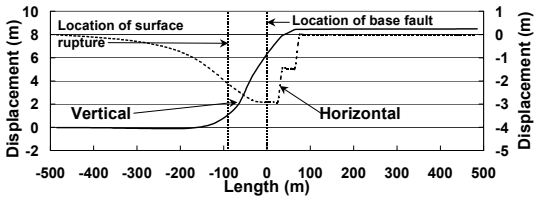

Figure 3.23. Final surface displacement

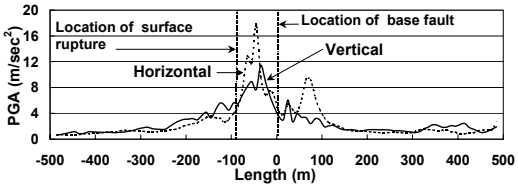

(a) Peak ground acceleration (PGA)

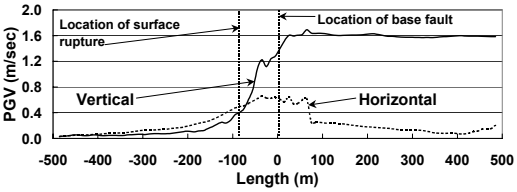

(b) Peak ground velocity (PGV)

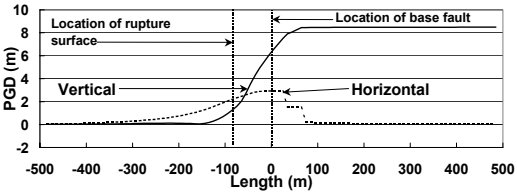

(c) Peak ground displacement (PGD)

Figure 3.24. Attenuation of peak ground responses

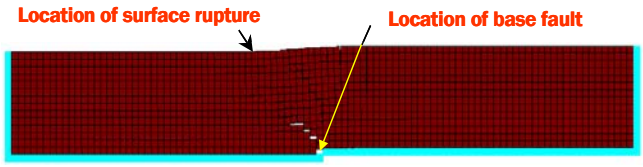

(a) Element location

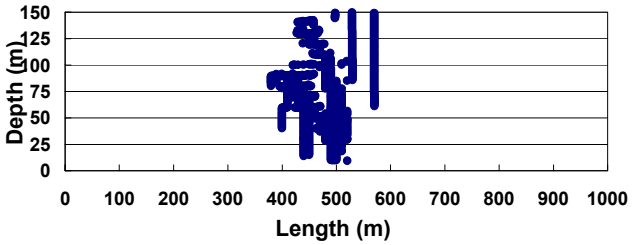

(b) Crack propagation

Figure 3.25. Element location and crack propagation responses

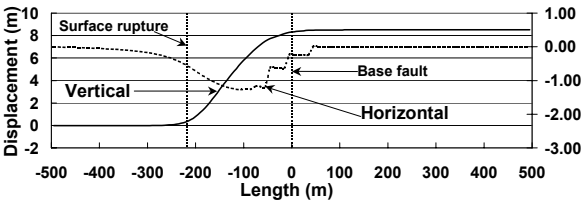

(a) Vs=745 m/s

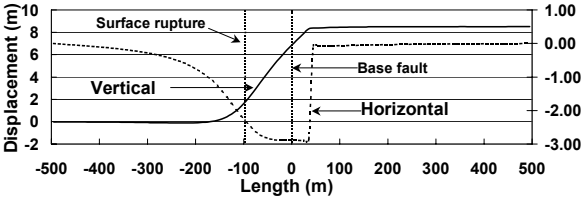

(b) Vs=264 m/s

Figure 3.26. Final surface displacement for different soil deposits

3.3.7. Summary

A new application to Applied Element Method (AEM) was proposed in this study. Dynamic fault rupture propagation was modeled using the 2D-AEM. The analysis showed that the peak responses next to the surface rupture are not the maximum. Instead they attain higher values slightly away from the surface rupture towards the hanging wall side.

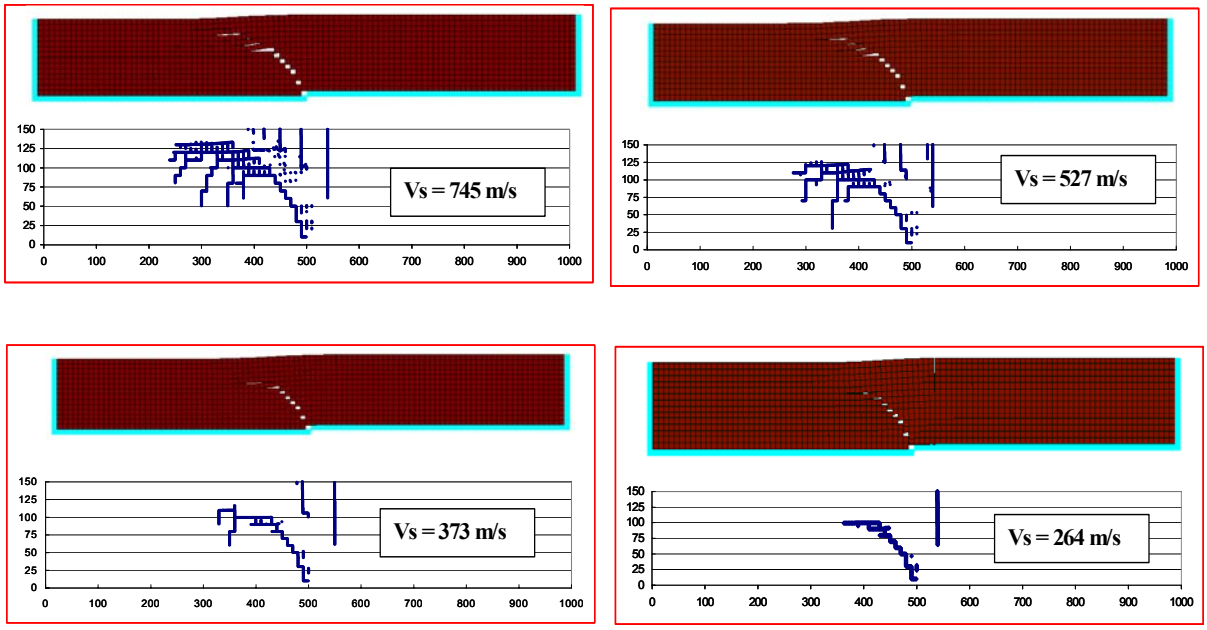

Figure 3.27. Element location and crack propagation in different soil deposits

References of SECTION 3.3

Ben-Menahem, A., and M.N. Toksoz: Source mechanism from spectra of long period surface waves, *Journal of Geophysical Research* 68: 5207-5222, 1963.

Bray, J.D., *The effects of tectonic movements on stresses and deformations in earth embankments*, Dissertation doctor of philosophy, University of California, Berkeley, 1990.

Cole, D. A., Jr., and Lade, P. V., Influence zones in alluvium over dip-slip faults, *Journal of Geotechnical Engineering*, ASCE, Proc. Paper 18788, Vol. 110, No. GT5, pp. 599-615, 1984.

Hakuno, M., Meguro, K.: Simulation of concrete-frame collapse due to dynamic loading, *Journal of Engineering Mechanics*, ASCE, Vol. 119, No. 9, September, 1993.

M. Hakuno, T. Imaizumi, H. Kagami, J. Kiyono, Y. Ikeda, I. Towhata, M. Hori, K, Meguro, T. Khosrow, A. Reza, H. Taniguchi and H. Tsujiba: Preliminary Report of the Damage Due to the Qayen Earthquake of 1997, Northeast Iran, *Journal of Natural Disaster Science*, 19 (1), 67-87, 1997.

Hall, J.F., Heaton, T.H., Halling, M.W. and Wald, D.J., Near-source ground motion and its effects on flexible buildings, *Earthquake Spectra*, 11(4), 569-605, 1995.

Haskell, N.A. Radiation pattern of surface waves from point sources in a multi-layered medium, *Bulletin of Seismological Society of America* 54: 377-394, 1964.

Japan Society of Civil Engineers (1999a), *The 1999 Kocaeli earthquake, Turkey, Investigation into damage to civil engineering structures*, Earthquake Engineering Committee, Japan Society of Civil Engineers.

Japan Society of Civil Engineers (1999b), The 1999 Ji-Ji earthquake, Taiwan, *Investigation into damage to civil engineering structures*, Earthquake Engineering Committee, Japan Society of Civil Engineers.

Lade, P. V., Cole, D. A., Jr., and Cummings David, Multiple failure surfaces over dip-slip faults, *Journal of Geotechnical Engineering*, ASCE, Proc. Paper 18789, Vol. 110, No. GT5, pp. 616-627, 1984.

Lee, W.H.K., T.C. Shin, K.W. Kuo, and K.C. Chen, CWB free-field strong motion Data from the 921 Chi-Chi Earthquake: Volume 1. digital acceleration files on CD-ROM, pre-publication version

(December 6, 1999), Seismology Center, Central weather bureau, Taipei, Taiwan, 1999.
Meguro, K. and Tagel-Din H., A new efficient technique for fracture analysis of structures, *Bulletin of Earthquake Resistant Structure Research Center*, Institute of Industrial Science, The University of Tokyo, No. 30, 1997.
Meguro, K. and Tagel-Din, H., Applied element method for structural analysis: Theory and application for linear materials, *Structural Eng./Earthquake Eng.*, JSCE, Vol. 17, No. 1, 21s-35s, 2000.
Kostadinov, M. V., *Utilization of strong motion parameters for earthquake damage assessment of grounds and structures*, A dissertation submitted to the department of civil engineering (Ph.D. Thesis), University of Tokyo, 2000.
Onizuka, N., Hakuno, M., Iwashita, K. and Suzuki, T., Deformation in grounds and bedrock stress induced by reverse dip-slip faults, *Journal of Applied Mechanics*, JSCE, Vol. 2, pp. 533-542, 1999 (in Japanese).
Tagel-Din, H., *A new efficient method for nonlinear, large deformation and collapse analysis of structures*, Ph.D. thesis, Civil Eng. Dept., The University of Tokyo, 1998.
Tani, K., Ueta, K., and Onizuka, N.: Scale effects of Quarternary Ground Deformation observed in Model Tests of vertical Fault, Proceedings 29th Japan National Conference of Soil Mechanics and Foundation Engineering, pp. 1359-1562, 1994 (in Japanese).
Tatcher, W., Geodetic measurement of active tectonic processes,' Active tectonics (studies in geophysics) 155-163, National Academy Press, 1986.

3.4. MODELING OF LARGE DEFORMATIONS OF SATURATED SOILS DURING FAULT SURFACE (by Johansson, J. and Konagai, K.)

3.4.1 Introduction

For studying large deformations of soils, numerical methods such as FEM or FDM have been widely used. For example, the finite difference based FLAC (Fast Lagrangian Analysis of Continua, Cundall, 1979) successfully calculates large strains by using low-order strain elements. However, when dealing with large strains, highly distorted elements often account for inaccurate results.

In the field of computational fluid dynamics, where history-dependent materials are less common, purely Eulerian methods are often used. Sulsky et al.(1994) extended it further to solid mechanics. Their method evolved from a particle-in-cell method (Brackbill et al., 1986, 1988) is referred to as the Lagrangian Particle Method (LPM) or the Material Point Method (MPM). In LPM, unconnected Lagrangian material points carry all Lagrangian variables such as mass, stress, strain, position, strength etc; the points, as an entire cluster, describe the mass of the material. A Eulerian mesh is used to solve the equations of motion in each time step. Data mapped from the material points in one cell of the mesh contribute to cell's nodes, and the equations of motion are solved at each nodes of the Eulerian mesh. The material points' variables are updated with mesh solution, and then, the Eulerian mesh is shifted back to its original position for the following calculation cycle. Any mesh type can be chosen to suit the typical problem, but a fixed Eulerian mesh is the simplest.

Konagai and Johansson (2001a and 2001b) developed LPFDM (Lagrangian Particle Finite Difference Method) based on the LPM scheme of calculation. The method was intended to be a projection of FLAC formulations on the LPM scheme so that the method allows for extremely large deformations of soils retaining the merits of FLAC. Johansson later on implemented hypo-plasticity model into the Material point Method; The hypo-plasticity model is capable of modeling many of important characteristics of soil. This paper describes an extension of this method to model the process of pore water pressure buildup in a granular fabric during surface fault ruptures.

3.4.2 Formulations

Solid-fluid interaction formulation

A coupled solid fluid (u-w) scheme described by (Chan et al., 1991) is adopted and adjusted for implementation in the Material Point Method. It is assumed that the soil deposit is fully saturated, Darcy's law is valid, solid grains are incompressible, and thermal changes are negligible. Further assumptions are given below along with the derivation. The governing equations are given for a Lagrangian frame moving with the solid-fluid mixture in terms of solid-fluid mixture momentum equilibrium (see e.g. Zienkiewicz et al. (1990); Lewis and Schrefler (1998) or chapter 2 in Zienkiewicz et al. (1999))

,

$$-\sigma_{ij,j} - \rho_m \cdot \ddot{u}_i - \rho_f \left(\ddot{w}_i + \dot{w}_j \dot{w}_{i,j}\right) + \rho_m b_i = 0 \tag{3.9}$$

fluid equilibrium,

$$-p_{,i} - \left[k_{ki}\right]^{-1} \cdot \dot{w}_k - \rho_f \ddot{u}_i - \frac{\rho_f}{n}\left(\ddot{w}_i + \dot{w}_j \dot{w}_{i,j}\right) + \rho_f b_i = 0 \tag{3.10}$$

and mass conservation,

$$\dot{w}_{i,i} + \dot{\varepsilon}_{i,i} + \frac{n\dot{p}}{K_f} = 0 \tag{3.11}$$

For a description and sign convention of the variables in above formulas are shown in **Table 3.8**. Equation (3.10) is further simplified by assuming isotropic permeability $k_{ki} = k$ and neglecting the underlined convective terms to obtain the two governing equations

$$-\sigma_{ij,j} - \rho_m \cdot \ddot{u}_i - \rho_f \ddot{w}_i + \rho_m b_i = 0 \tag{3.12}$$

$$-p_{,i}-\frac{\dot{w}_k}{k}-\rho_f\ddot{u}_i-\frac{\rho_f}{n}\ddot{w}_i+\rho_f b_i=0 \tag{3.13}$$

where the total stresses, σ_{ij} are obtained from the effective stresses and pore water pressure

$$\sigma_{ij}=\sigma'_{ij}-\delta_{ij}p \tag{3.14}$$

and the effective stresses are obtained from an appropriate constitutive law e.g. hypo-plasticity.

$$\dot{\sigma}'_{ij}=f\left(\sigma'_{ij},\varepsilon_{ij},\cdots\right) \tag{3.15}$$

For the explicit scheme derived below Equation (3.11) used for updating the excessive pore pressure by multiplying with the time increment, Δt, to obtain

$$\Delta p=\Delta t\cdot\dot{p}=-\Delta t\frac{K_f}{n}\left(\dot{w}_{ii}+\dot{\varepsilon}_{ii}\right) \tag{3.16}$$

On the other hand if an implicit scheme is desired, Equation (3.11) should be integrated in time to obtain a direct expression for the pore water pressure and inserted in to Equation (3.13) and it may be easier to use the absolute displacement of water instead of the relative displacements as here (see further chapter 3 in Zienkiewicz et al. (1999)).

Table 3.8. Variable description.

Variable	Description	Remark
σ_{ij}	Total Stress	Compression negative
u_i	Solid matrix displacements	
$\rho_m=(1-n)\rho_s+n\rho_f$	Solid-Fluid Mixture density	
ρ_f	Fluid density	
ρ_s	Solid density	
N	Porosity	
w_i	Water displacement relative to solid matrix	
b_i	Body force on solid-fluid mixture	e.g. gravity
P	Pore pressure	Compression positive
k'_{ki}	Permeability	Unit: $\left[L^3T^{-1}M^{-1}\right]$
G	Gravity	Unit: $\left[LT^{-2}\right]$
ε_{ii}	Volumetric strain of solid-fluid mixture	
K_f	Water bulk modulus	

Finite element discretization:

The governing equations and boundary conditions are first for clarity discretized spatially with finite elements to establish the equation system and then the material point concept is introduce in the following section. The mixture and fluid displacements take the following forms:

$$u_i(x_i,t)=u_I(t)N_I^u(x_i),\quad w_i(x_i,t)=w_I(t)N_I^w(x_i),\quad I=1,\cdots N_n \tag{3.17}$$

Where the $N's$ are finite element shape functions. Upper case letter represent nodal number, lower case letter are refers to Cartesian coordinate and summation convention is applied. Lower case letters *m*, *c*, and *f* are applied to mixture, coupling and fluid terms. (The notation is somewhat relaxed to reduce space and time of the derivation, hopefully the concept and procedures will be clear to the any reader anyway). Multiplying Equation (3.12) and Equation (3.13) with the interpolation function N_i^u and N_i^w, respectively as weighting functions and integrate over the domain the following two equations are obtained.

$$\int_\Omega N_I^u(\sigma_{ij,j} - \rho_m \ddot{u}_i - \rho_f \ddot{w}_i + \rho_m b_i)d\Omega = 0 \tag{3.18}$$

$$\int_\Omega N_I^w(-p_{,i} - \frac{\dot{w}_i}{k} - \rho_f \ddot{u}_i - \frac{\rho_f}{n}\ddot{w}_i + \rho_f b_i)d\Omega = 0 \tag{3.19}$$

Integrating first term of the Equation (3.18) by parts gives

$$\int_\Omega N_I^u \sigma_{ij,j} d\Omega = \int_S N_I^u n_i \sigma_{ij} dS - \int_\Omega N_I^u \sigma_{ij} d\Omega = f_{mIi}^{ext,tractions} - f_{mIi}^{int} \tag{3.20}$$

where $f_{mIi}^{ext,tractions}$ and f_{mIi}^{int} are external traction forces and internal forces respectively. The second term in Equation (3.18) gives the mixture mass matrix

$$-\int_\Omega N_I^u \rho_m \ddot{u}_i d\Omega = -\int_\Omega N_I^u \rho_m N_J^u d\Omega \ddot{u}_{Ji} = -M_{mIJ}\ddot{u}_{Ji} \tag{3.21}$$

the third term becomes the mixture-fluid coupling mass matrix

$$-\int_\Omega N_I^u \rho_f \ddot{w}_i d\Omega = -\int_\Omega N_I^u \rho_f N_J^w d\Omega \ddot{w}_{Ji} = -M_{cIJ}\ddot{w}_{Ji} \tag{3.22}$$

and the final term gives the body-forces applied to the solid-fluid mixture

$$-\int_\Omega N_I^u \rho_m b_i d\Omega = f_{mIi}^{body\ forces} \tag{3.23}$$

Now turning to the second governing Equation (3.19) the first term becomes

$$-\int_\Omega N_I^w \rho_{,i} d\Omega = -\int_\Omega N_I^w n_i p dS + \int_\Omega N_I^w p d\Omega = f_{fIi}^{ext,pressure} + f_{fIi}^{int} \tag{3.24}$$

which is the externally applied pressure on the fluid and internal forces due to the pore pressure. The second term becomes

$$-\int_\Omega N_I^w \frac{\dot{w}_i}{k} d\Omega = -\int_\Omega N_I^w \frac{1}{k} N_J^w d\Omega \dot{w}_{Ji} = -C_{fIJ}\dot{w}_{Ji} \tag{3.25}$$

where C_{fIJ} is the fluid damping matrix. The third term becomes

$$-\int_\Omega N_I^w \rho_f \ddot{u}_i d\Omega = -\int_\Omega N_I^w \rho_f N_J^u d\Omega \ddot{u}_{Ji} = -M_{cIJ}\ddot{u}_{Ji} \tag{3.26}$$

where $M_{cJI} = M_{cIJ}^T$ is the fluid-mixture coupling mass matrix which is transpose of the mixture-fluid coupling mass matrix. From the fourth term the fluid mass matrix is given as

$$-\int_\Omega N_I^w \frac{\rho_f}{n}\ddot{w}_i d\Omega = -\int_\Omega N_I^w \frac{\rho_f}{n} N_J^w d\Omega \ddot{w}_{Ji} = -M_{fIJ}\ddot{w}_{Ji} \tag{3.27}$$

and finally the last term gives the body forces applied on the fluid

$$\int_\Omega N_I^w \rho_f b_i d\Omega = f_{fIi}^{body\ forces} \tag{3.28}$$

The above terms from Equations (3.18)and (3.19) is assembled into the equation system

$$\begin{bmatrix} M_{mIJ} & M_{cIJ} \\ M_{cIJ}^T & M_{fIJ} \end{bmatrix} \begin{Bmatrix} \ddot{u}_{Ji} \\ \ddot{w}_{Ji} \end{Bmatrix} + \begin{bmatrix} C_m & \mathbf{0} \\ \mathbf{0} & C_{fIJ} \end{bmatrix} \begin{Bmatrix} \dot{u}_{Ji} \\ \dot{w}_{Ji} \end{Bmatrix} + \begin{bmatrix} f_{mIi}^{int} & \mathbf{0} \\ \mathbf{0} & f_{fIi}^{int} \end{bmatrix} = \begin{Bmatrix} f_{mIi}^{ext,tractions} + f_{mIi}^{body\ forces} \\ f_{fIi}^{ext,tractions} + f_{fIi}^{body\ forces} \end{Bmatrix} \tag{3.29}$$

where *Cm* is an artificial damping matrix applied to the solid-fluid mixture.

Material point discretization and a simple modification

Here follows the derivation of the material point version of (3.29). In the original material point method, a material point represents a material density discretely with a constant mass according to a Dirac delta function as

$$\rho(x_i, t) = \sum_{p=1}^{n_p} m_p \delta\left(x_i - X_p(t)\right) \tag{3.30}$$

since the material points are following the Lagrangian frame. If we use a Lagrangian frame for representing the solid part of the porous material its density can be written as:

$$\rho_s(x_i,t)=\sum_{p=1}^{n_p} m_{sp}\delta\left(x_i-X_p(t)\right) \tag{3.31}$$

The pore fluid (water) percolates with the velocity w_i relative to the solid's Lagrangian frame. One way to deal with this would be to introduce completely Lagrangian fluid material points. But this would require more exchange of information since e.g. the fluid pressure at the fluid points would have to be interpolated to the solid points to compute the effective stresses which is used in relevant constitutive laws. Under the assumption that the fluid percolation velocity relative to the solid is small we can keep the location fluid points and solid points in the same Lagrangian point through out the calculation there is no need for the extra information exchange and thus a relative decrease in computation time and less tedious coding. To allow for this simplification we need to account for the fluid percolation relative to the solid by correspondingly changing the fluid point masses according to the divergence of the relative velocity

$$\Delta m_{fp}=-\Delta t\rho_f V_{mp}\dot{w}_{i,i} \tag{3.32}$$

where the fluid density ρ_f is assumed to be constant even though the water is slightly compressible. The total mass of a solid-fluid mixture material point is now represented by a sum of the constant solid mass and the variable fluid mass

$$m_{mo}=m_{sp}+m_{fp} \tag{3.33}$$

and the solid-fluid mixture density is

$$\rho_m(x_i,t)=\sum_{p=1}^{n_p}(m_{sp}+m_{fp})\delta\left(x_i-X_p(t)\right) \tag{3.34}$$

The volume of a material point representing the solid-fluid mixture becomes

$$V_{mp}=\frac{m_{sp}+m_{fp}}{\rho_m} \tag{3.35}$$

which has to be updated according to the volumetric change of the mixture, $\dot{\varepsilon}_{ii}$.

Applying the concept of discrete density to the individual terms in (3.29) and invoking

$$\int_\Omega d\Omega=\sum_{p=1}^{N_p}V_{mp} \tag{3.36}$$

where N_p is the number of material points within Ω, we derive the material point formulation as follows. The solid-fluid mixture mass matrix becomes

$$M_{mIJ}=\int_\Omega N_I^u\rho_m N_J^u d\Omega=\sum_{p=1}^{N_p}N_I^u\left(m_{sp}+m_{fp}\right)N_J^u \tag{3.37}$$

the coupling solid-fluid mass matrices, with $\rho_f V_{mp}=m_{fp}/n$ become

$$M_{cIJ}=\int_\Omega N_I^u\rho_f N_J^w d\Omega=\sum_{p=1}^{N_p}N_I^u\left(m_{sp}+m_{fp}\right)N_J^w=\sum_{p=1}^{N_p}N_I^u\frac{m_{fp}}{n}N_J^w=M_{cJI}^T \tag{3.38}$$

and the fluid mass matrix becomes

$$M_{fIJ}=\int_\Omega N_I^w\frac{\rho_f}{n}N_J^w d\Omega=\sum_{p=1}^{N_p}N_I^u\frac{\rho_f}{n}V_{mp}N_J^w=\sum_{p=1}^{N_p}N_I^u\frac{m_{fp}}{n^2}N_J^w \tag{3.39}$$

The solid-fluid mixture artificial damping matrix, C_m, remains the same as in the FE discretization, but the fluid damping matrix, C_{fIJ}, changes to

$$C_{fIJ}=\int_\Omega N_I^w\frac{1}{k}N_J^w d\Omega=\sum_{p=1}^{N_p}N_I^w\frac{1}{k}V_{mp}N_J^w=\sum_{p=1}^{N_p}N_I^w\frac{\rho_{fg}}{k'}V_{mp}N_J^w=\sum_{p=1}^{N_p}N_I^w\frac{g}{k'}\frac{m_{fp}}{n}N_J^w \tag{3.40}$$

The in internal forces of the solid-fluid mixture and the fluid now becomes, respectively

$$f_{mIi}^{int} = \int_{\Omega} N_{I,j}^{u} \sigma_{ij} d\Omega = \sum_{p=1}^{N_p} N_{I,j}^{u} V_{mp} \sigma_{ij} \tag{3.41}$$

$$f_{fIi}^{int} = \int_{\Omega} N_{I,i}^{w} p d\Omega = \sum_{p=1}^{N_p} N_{I,j}^{w} V_{mp} p \tag{3.42}$$

Here the volume of the solid-fluid mixture material point is invoked again since the governing Equation (3.13) is derived with respect to the total volume of the solid-fluid mixture. Then all terms on the left hand side in Equation system (3.29) have been changed to material point equivalent terms. On the right hand side the solid-fluid mixture external traction, $f_{mIi}^{ext,tractions}$, and the fluid external pressure, $f_{mIi}^{ext,pressure}$, remains the same as in the FE discretization. The body force terms of the solid-fluid mixture and the fluid becomes, respectively

$$f_{mIi}^{ibody\ force} = \int_{\Omega} N_I^u \rho_m b_i d\Omega = \sum_{p=1}^{N_p} N_I^u \left(m_{sp} + m_{fp}\right) b_{pi} \tag{3.43}$$

$$f_{fIi}^{ibody\ force} = \int_{\Omega} N_I^w \rho_f b_i d\Omega = \sum_{p=1}^{N_p} N_I^w \frac{m_{fp}}{n} b_{pi} \tag{3.44}$$

where b_{pi} is the body force acting on the solid-fluid mixture material point.

Time discretization

To keep the current simple explicit scheme of FEMP it is desirable to solve the Equations system (3.219 by diagonalizing/lumping the mass and damping matrices and using staggered central differences. The lumping results in block diagonal system

$$\begin{bmatrix} M_{mI} & M_{cI} \\ M_{cI} & M_{fI} \end{bmatrix}^k \begin{Bmatrix} \ddot{u}_{Ii}^k \\ \ddot{w}_{Ii}^k \end{Bmatrix} + \begin{bmatrix} C_{mI} & \mathbf{0} \\ \mathbf{0} & C_{fI} \end{bmatrix}^k \begin{Bmatrix} \dot{u}_{Ii}^k \\ \dot{w}_{Ii}^k \end{Bmatrix} + \begin{bmatrix} f_{mIi}^{int} & \mathbf{0} \\ \mathbf{0} & -f_{fIi}^{int} \end{bmatrix}^k = \begin{Bmatrix} f_{mIi}^{ext,tractions} + f_{mIi}^{body\ forces} \\ f_{fIi}^{ext,tractions} + f_{fIi}^{body\ forces} \end{Bmatrix}^k \tag{3.45}$$

where the diagonal consists of 2 by 2 matrices which has to be solved for each degree of freedom at discrete times, t_k. I is the node number, i is the Cartesian direction and the k on the matrices means that they are computed for each time step. Approximating the mixture accelerations and velocities with

$$\ddot{u}_{Ii}^k = \frac{1}{\Delta t}\left(\dot{u}_{Ii}^{k+1/2} - \dot{u}_{Ii}^{ki1/2}\right) \tag{3.46}$$

respectively

$$\dot{u}_{Ii}^k = \frac{1}{2}\left(\dot{u}_{Ii}^{k+1/2} + \dot{u}_{Ii}^{ki1/2}\right) \tag{3.47}$$

and likewise the fluid accelerations and velocities, the lumped system (3.45) is rewritten for each degree of freedom

$$\frac{1}{\Delta t}\widetilde{M}_I \dot{\widetilde{u}}_{Ii}^{k+1/2} + \frac{1}{2}\widetilde{C}_I \dot{\widetilde{u}}_{Ii}^{k+1/2} = \widetilde{F}_{Ii}^k + \frac{1}{\Delta t}\widetilde{M}_I \dot{\widetilde{u}}_{Ii}^{k-1/2} - \frac{1}{2}\widetilde{C}_I \dot{\widetilde{u}}_{Ii}^{k-1/2} \tag{3.48}$$

where the $\widetilde{M}_I$ and $\widetilde{C}_I$ represents the terms collected from the corresponding matrices, $\widetilde{F}_{Ii}$ contains the collected internal, external and body-forces, $\dot{\widetilde{u}}_{Ii}$ is the velocities vector

$$\dot{\widetilde{u}}_{Ii} = \begin{Bmatrix} \dot{u}_{Ii} \\ \dot{w}_{Ii} \end{Bmatrix} \tag{3.49}$$

and Δt is the time step. Multiplying Equation (3.48) with the time step and collecting the terms on the left hand side we obtain

$$\left(\widetilde{M}_I + \frac{\Delta t}{2}\widetilde{C}_I\right)\dot{\widetilde{u}}_{Ii}^{k+1/2} = \Delta t \widetilde{F}_{Ii}^k + \widetilde{M}_I \dot{\widetilde{u}}_{Ii}^{k-1/2} - \frac{\Delta t}{2}\widetilde{C}_I \dot{\widetilde{u}}_{Ii}^{k-1/2} \tag{3.50}$$

from which $\dot{\tilde{u}}_{Ii}$ can be solved for

$$\dot{\tilde{u}}_{Ii}^{k+1/2} = \left(\tilde{M}_I + \frac{\Delta t}{2} \tilde{C}_I \right)^{-1} \left(\Delta t \tilde{F}_{Ii}^{k} + \tilde{M}_I \dot{\tilde{u}}_{Ii}^{k-1/2} - \frac{\Delta t}{2} \tilde{C}_I \dot{\tilde{u}}_{Ii}^{k-1/2} \right) \tag{3.51}$$

The new velocities are used to update the position of the solid-fluid mixture material points, computation of the strain rates for the stress updates, and fluid divergence for updating the mass of the fluid material points. See the appendix for a derivation of explicit formulas for the solid and fluid velocities.

Initial conditions

To start the time stepping procedures, it is assumed that the initial mixture and fluid velocities are zero,

$$\dot{\tilde{u}}_{Ii}^{k=0} = 0 \tag{3.52}$$

which implies

$$\dot{\tilde{u}}_{Ii}^{1/2} = -\dot{\tilde{u}}_{Ii}^{-1/2} \tag{3.53}$$

Putting Equation (3.53) into Equation (3.50) gives the velocities

$$\dot{\tilde{u}}_{Ii}^{K=1/2} = \frac{\Delta t}{2} \tilde{M}_I^{-1} \tilde{F}_{Ii}^{k=0} \tag{3.54}$$

and the velocity increments

$$\Delta \dot{\tilde{u}}_{Ii}^{K=1/2} = \frac{\Delta t}{2} \tilde{M}_I^{-1} \tilde{F}_{Ii}^{k=0} \tag{3.55}$$

The inverse to the mass matrix is

$$\tilde{M}_I^{-1} = \begin{bmatrix} M_{mI} & M_{cI} \\ M_{cI} & M_{fI} \end{bmatrix}^{-1} = \frac{1}{M_{mI} M_{fI} - M_{cI}^{\,2}} \begin{bmatrix} M_{fI} & -M_{cI} \\ -M_{cI} & M_{mI} \end{bmatrix} \tag{3.56}$$

$$\dot{u}_{Ii}^{1/2} = \frac{\Delta t / 2}{M_{mI} M_{fI} - M_{cI}^{\,2}} \left[M_{fI} \left(f_{mIi}^{ext,tractions} + f_{mIi}^{body\ forces} - f_{mIi}^{int} \right) - M_{cI} \left(f_{mIi}^{ext,pressure} + f_{mIi}^{body\ forces} + f_{mIi}^{int} \right) \right] \tag{3.57}$$

$$\dot{w}_{Ii}^{1/2} = \frac{\Delta t / 2}{M_{mI} M_{fI} - M_{cI}^{\,2}} \left[- M_{cI} \left(f_{mIi}^{ext,tractions} + f_{mIi}^{body\ forces} - f_{mIi}^{int} \right) + M_{mI} \left(f_{fIi}^{ext,pressure} + f_{fIi}^{body\ forces} + f_{fIi}^{int} \right) \right] \tag{3.58}$$

Boundary conditions

For the analysis of the numerical examples given below three different types of combinations of boundary conditions have been used:

1. Both solid and fluid velocities are prescribed.
2. Solid velocities are prescribed and fluid velocities are not prescribed.
3. Both solid and fluid velocities are non-prescribed.

Combination 1 is used for motion perpendicular to a impermeable boundary. The second combination is used for the motion parallel to a rough boundary were solid velocities are prescribed and the fluid is free to move parallel along the wall or for motion perpendicular to a permeable wall. The third type is used for the motion parallel to a slippery boundary. In the explicit scheme adopted here type 1 is implemented by computing the appropriate velocity increments and for type 3 nothing is done since it really no constraints are applied to the velocities. Type 2 requires one to solve for forces acting on the solid corresponding to the prescribed velocities from Equation (A4) and use these forces to compute the fluid velocity increments with Equation (A7). Other possible boundary conditions would include external nodal forces due to pressure on the fluid, point or linear loads on the solid-fluid mixture.

Critical time-step and stability

A discussion on the critical time step for 1-D explicit MPM is available in Wieckowski et al. (1999). In general a smaller time-step then for a regular explicit FEM is required. The stability of the Material Point Method is highly dependent on the order of updating stress strain. The original procedure was modified by Sulsky et al. (1995) and a higher stability was achieved. Bardenhagen (2002) suggested a different update, which also improves stability. The main difference between the two modifications is a slight difference in conservation of energy.

3.4.3. Seepage Problem

A simple 2-D plane strain seepage problem has been chosen to show the abilities and problems of the method. It is shown that the specific way of computing strains and internal forces are very important to obtain reliable result. An elastic soil in gravitational equilibrium is contained in a box 2.5 by 1 meter and is surrounded by impermeable horizontal walls with a bottom than can allow fluid flow out of the box at the left most 0.75 meters. The input data shown in **Table 3.9** are all the same for the 4 cases and the initial pressure are shown in **Figure 1**. The problem is solved with different ways of strain computations with and without averaging the fluid pressure and its increment. The solid velocities are damped out with high viscous mass proportional damping as to avoid any oscillations of the solid, which would affect the fluid flow. Cases with different amount of damping were computed to confirm that the neither directions nor the magnitudes of the fluid velocities were affected by the damping value. **Figure 3.29** shows fluid velocities and pressures results from 4 different cases, which are described below (see also **Table 3.10**). Case 1: The strains are computed with usual derivative of the bilinear interpolation. As seen in **Figure 3.29 (a)** and **(b)** the fluid pressure is unstable and show a typical checker boarding due to the so called Babuska-Brezzi instability (see further(Hughes, 1983) or (Bathe, 1996)).

Table 3.9. Input data for seepage problem.

Parameter	Value
Solid Elastic Modulus	1.0×10^{6} Pa
Poisson ratio, v	0.3
Fluid bulk modulus	1.0×10^{8} Pa
Fluid density	1000 kg/m^3
Solid density	2650 kg/m^3
Porosity	0.5
Hydraulic conductivity	1.0×10^{-2} m/s
Gravity	9.82 N/kg

Table 3.10. Examined cases

Case	Normal strain	B-bar	Averaging of fluid pressures
1	×		
2		×	
3	×		×
4		×	×

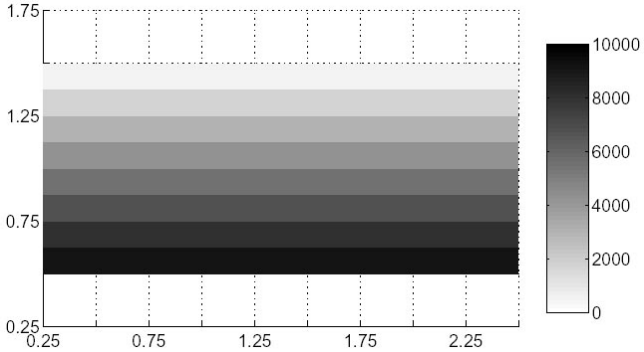

Figure 3.28. Initialpressure[Pa]duetogravityinseepageexample

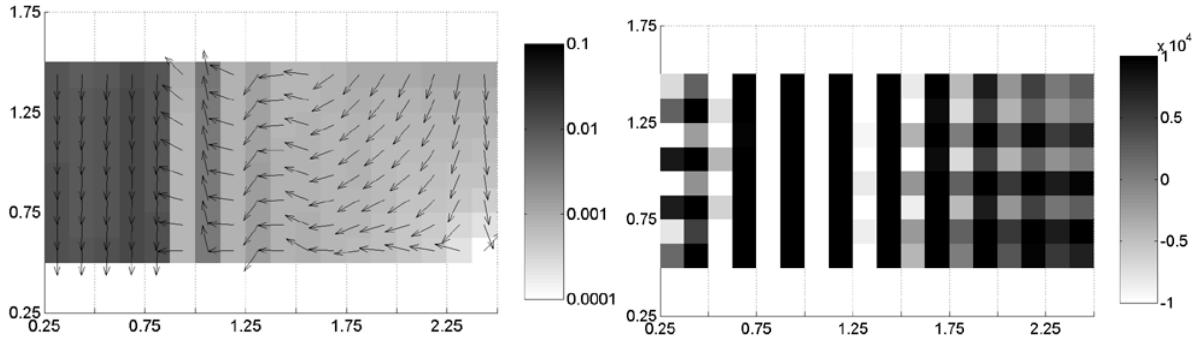

(a) Case 1: Fluid Velocities **(b)** Case 1: Fluid Pressure

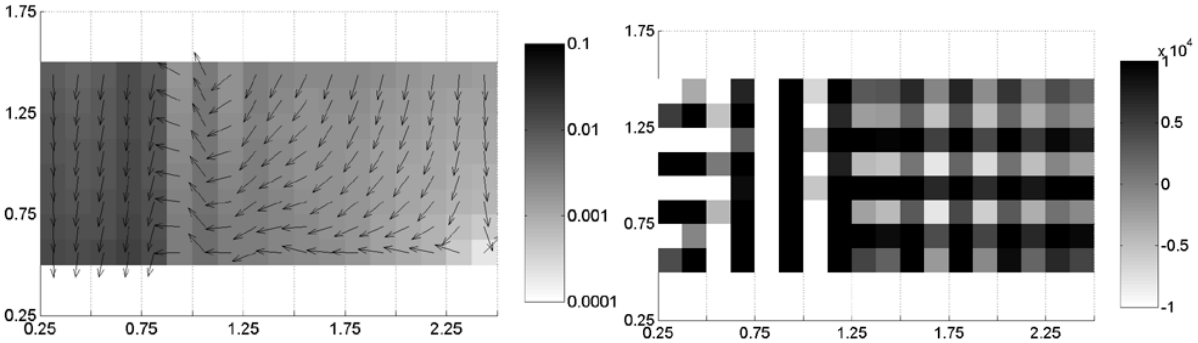

(c) Case 2: Fluid Velocities **(d)** Case 2: Fluid Pressure

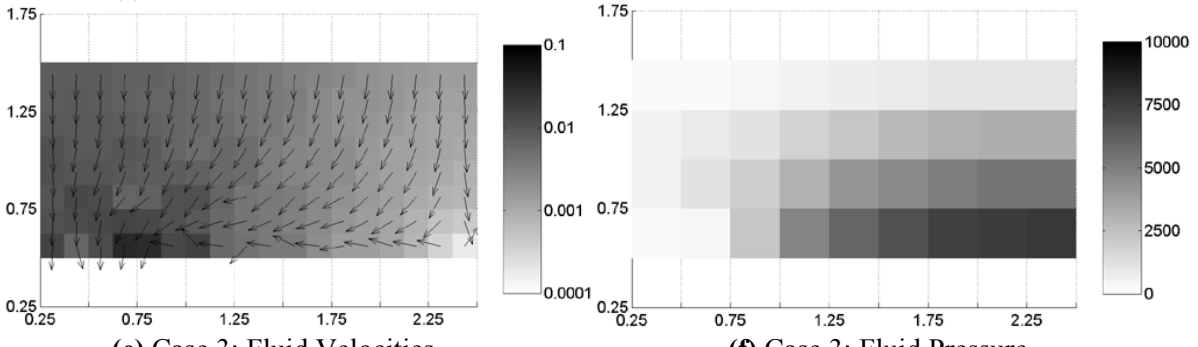

(e) Case 3: Fluid Velocities **(f)** Case 3: Fluid Pressure

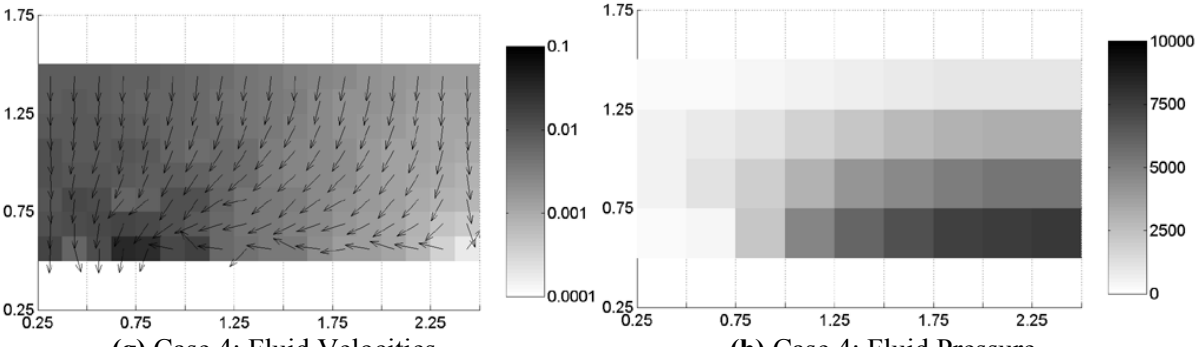

(g) Case 4: Fluid Velocities **(h)** Case 4: Fluid Pressure

Figure 3.29. Fluid velocities and pressure for cases 1-4.

Case2: To circumvent the Babuska-Brezzi instability the B-bar method (Hughes, 1983) of computing strains and internal forces where adopted. As a special case of the B-bar method the mean dilatation method (Nagtegaalet al., 1974) is used here. The results improve slightly but still the checker boarding is observed.

Case 3: Hughes (1983) also discusses the need for smoothing the pressure and its increments. The

strains and internal forces are compute as for Case 1 but the pressure and its increment is averaged for each element. Now the fluid velocity show a more physical pattern and the pressure distribution is smooth and goes toward zero along the left boundary which is natural for a material in free flow. One can imagine a small stone falling through air (neglecting the air resistance) it will be completely stress free.
Case 4: In this case the B-bar method from case 2 was combined with an averaging of the fluid pressure and as seen the result is equal to the ones of case 3 showing the importance of smoothing the pressures.

3.4.4. Fault Surface Rupture Experiments

To obtain experimental results in order to verify the numerical model and to study in detail the effects on the deformation buildup due to a dip-slip fault when pore water is present in a soil a new model experiment has been designed.

Experiment setup and preparation

A box measuring 1.2 by 1.2 meters in plan and 60 cm deep was constructed (see **Figure 3.30**). A 40 cm diameter piston in the middle of the box, which is attached to a hydraulic actuator, is used to lift/push up the soil to create the fault surface rupture. Toyoura sand with a mean diameter, D_{50}, of 0.2 mm was pluviated into the box to assure repeatability and homogeneity. To be able to see the induced deformation the sand deposit was inter-layered with thin (3-5 mm) horizontal layers of colored toyoura sand every 5 cm (see **Figure 3.31**). The sand density was $1580\,kg/m^3$ corresponding to a void ratio, *e*, of 0.68.

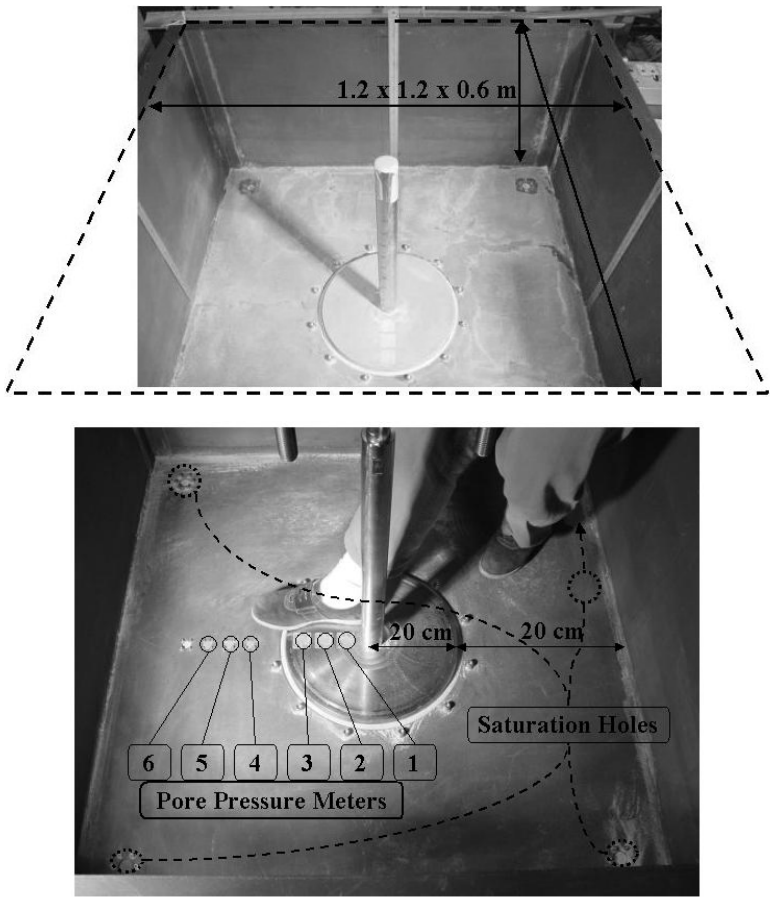

Figure 3.30: View inside the experiment box

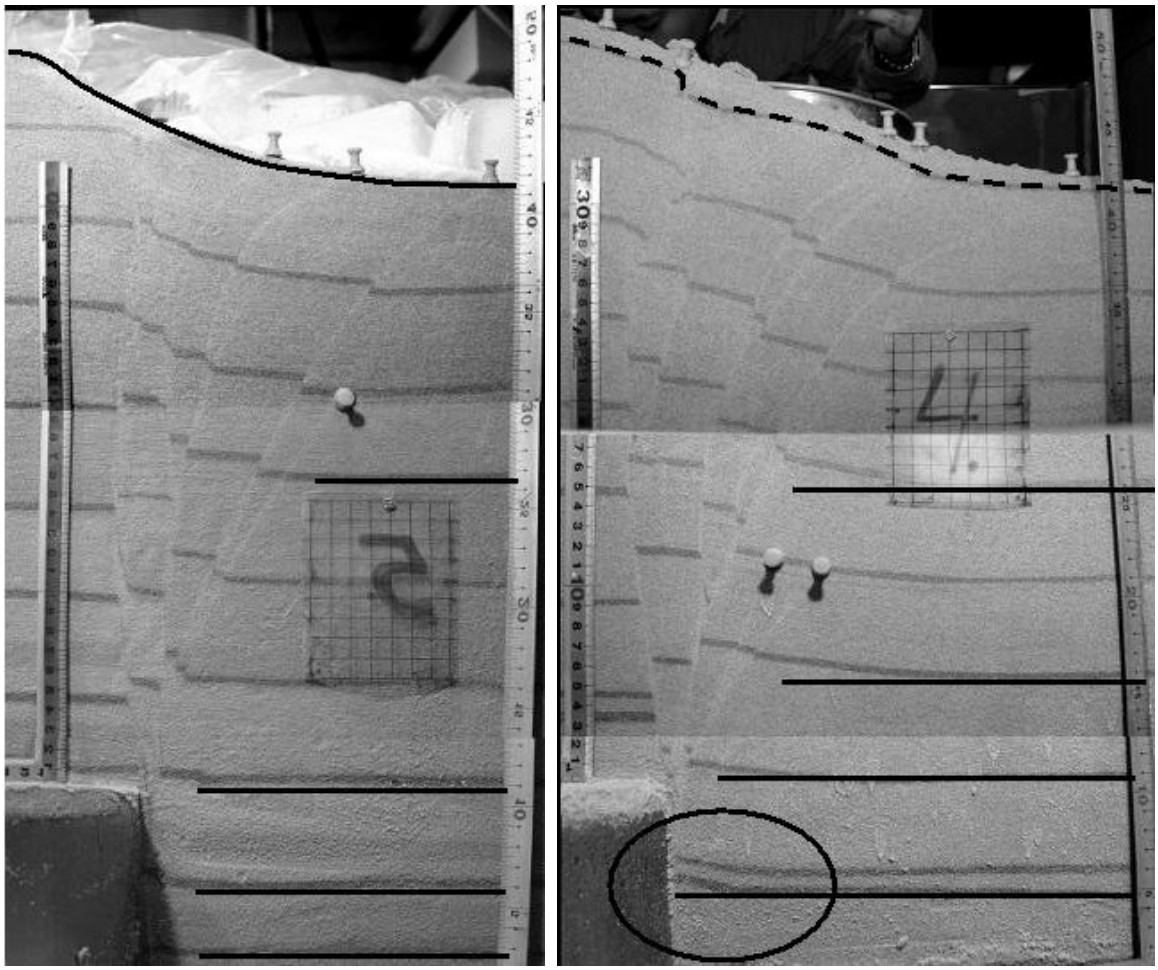

Figure 3.31. Dry (left) and Saturated (right) Fault Experiment

Experiment results

After the experiment the dry sand was first saturated and immediately drained and the saturated sand was drained . The moist sand could then be easily cut along a vertical planes as to study the built up deformations. Two cuts from a dry and a saturated case are shown in **Figure 3.31**. The soil deformation has localized into narrow shear-band and offset the dark horizontal lines. The shear-band or rupture planes are also readily seen as brighter lines crossing through darker less deformed zones.

It is interesting that in the saturated case soil far away from the fault is deformed. The horizontal solid lines added as guides to the eye to see the upward bending of the soil when approaching the fault. It seems that the negative pore water pressure (according to measurement performed during the experiment, but not shown here) increases the failure strength of the soil, which then behaves elastically for a larger deformation than in the case of the dry sand. Also the surface deformation shows a different character as seen in **Figure 3.31**.

3.4.5. Fault Surface Rupture Simulations

A hypo-plastic model (Herle and Gudehus, 1999) which is capable of modeling many of important characteristics of the soil is employed to describe the behavior of dense Toyoura sand used in the experiment (see 4 for a simple description of input parameters and values. A detailed description is given in the reference above). **Figure 3.32** shows the maximum shear strain after a total uplift of 10 cm in 40 cm deep and 60 cm wide soil deposit for a dry soil.

Table 3.11. Hypoplastic parameters

Parameter	Value	Unit	Description
φ_c	30.0	[deg]	Critical state friction angle
h_s	2600×10^6	[Pa = N/m^2]	Stiffness parameter
n	0.27	[1]	Stiffness
e_{d0}	0.61	[1]	Minimum void ratio in stress free condition
e_{c0}	0.98	[1]	Critical state void ratio in stress free condition
e_{i0}	1.1	[1]	Maximum void ratio in stress free condition
α	0.18	[1]	Fitting parameter
β	1.1	[1]	Fitting parameter
$e_{initial0}$	0.65	[1]	Initial void ratio (measured in experiment)
E_{small}	100.0	[Pa]	Very small confining pressure stiffness (for numerical stability)
Fluid bulk modulus	1.0×10^8	[Pa]	

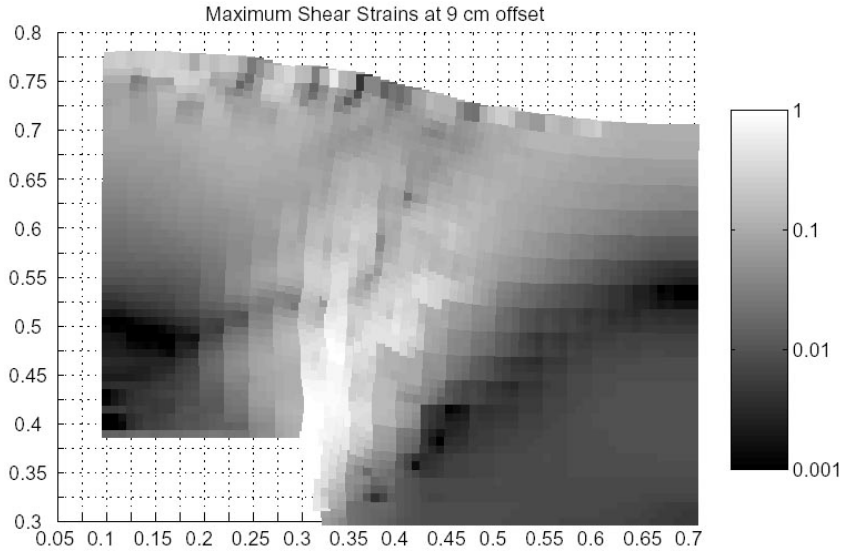

Figure 3.32. Maximum shear strains for dry case. Observe the logarithmic strain scale, 1=100%strain.

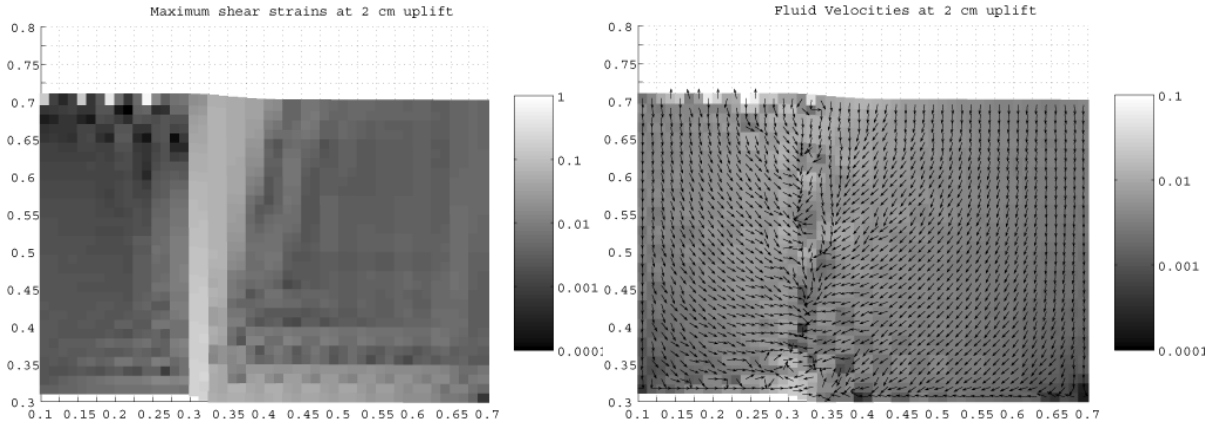

Figure 3.33. Maximum shear strains (a) and fluid velocities (b) for saturated case. Observe the logarithmic scales: (a) 1=100%strain, (b) [m/s]

For the saturated case the results suffers from checker board effects of the pressure instability mentioned in the previous section as seen in Figure 6, which shows the maximum shear strains and fluid velocities at a 2 cm uplift of the base rock. The fluid velocities flow downwards and towards the dilating soil within the shear band.

An extension to circumvent the incompressibility related problems by using element strain increment averaging in combination with viscous or elastic hourglass (Flanagan and Belytschko, 1981) control is currently under investigation. Possibly a more recent extension of the hour-glass control will be implemented (Kuessner and Reddy, 2001).
2001).

3.4.6 Summary

Even though some numerical difficulties related to incompressibility remains to be solved the simple numerical scheme shows great promise for modeling large deformations of saturated soil deposits. Several different ways of computing strains were tried out for the seepage problem whereas for the saturated case only the b-bar method is presented here. Element strain increment averaging has also been tried out but hour-glassing deformations are quite large so some type of hour-glass control is necessary. Currently a way of circumventing the incompressibility problem for the solid part is under development and will be presented in a future publication.

APPENDIX: Explicit Expressions for Solid and Fluid Velocities

A somewhat lengthy derivation of explicit formulas for the solid and fluid velocities follows below.

The terms in the first parenthesis in (3.51) can be further simplified to

$$\left(\widetilde{M}_I+\frac{\Delta t}{2}\widetilde{C}_I\right)^{-1}=\begin{bmatrix} M_{mI}+\frac{\Delta t}{2}C_{mI} & M_{cI} \\ M_{cI} & M_{fI}+\frac{\Delta t}{2}C_{fI}\end{bmatrix}^{-1}= \\ \frac{1}{\left(M_{mI}+\frac{\Delta t}{2}C_{mI}\right)\left(M_{fI}+\frac{\Delta t}{2}C_{fI}\right)-M_{cI}{}^2}\begin{bmatrix} M_{fI}+\frac{\Delta t}{2}C_{fI} & -M_{cI} \\ -M_{cI} & M_{mI}+\frac{\Delta t}{2}C_{mI}\end{bmatrix} \tag{3.59}$$

Calling the fraction in Equation (3.59) Q, the explicit form of velocities, which are suitable for direct implementation in a computer code becomes

$$\dot{u}_{Ii}^{k+1/2}=Q\left(M_{fI}+\frac{\Delta t}{2}C_{fI}\right)\left[\Delta t\left(f_{mIi}^{ext,tractions}+f_{mIi}^{body\ forces}-f_{mIi}^{int}\right)+\left(M_{mI}+\frac{\Delta t}{2}C_{mI}\right)\dot{u}_{Ii}^{k-1/2}+\right. \\ \left.+M_{cI}\dot{w}_{Ii}^{k-1/2}\right]-QM_{cI}\left[\Delta t\left(f_{mIi}^{ext,pressure}+f_{mIi}^{body\ forces}+f_{mIi}^{int}\right)+M_{cI}\dot{u}_{Ii}^{k+1/2}+\left(M_{fI}+\frac{\Delta t}{2}C_{fI}\right)\dot{w}_{Ii}^{k-1/2}\right] \tag{3.60}$$

and

$$\dot{w}_{Ii}^{k+1/2}=-QM_{cI}\left[\Delta t\left(f_{mIi}^{ext,tractions}+f_{mIi}^{body\ forces}-f_{mIi}^{int}\right)+\left(M_{mI}-\frac{\Delta t}{2}C_{mI}\right)\dot{u}_{Ii}^{k-1/2}+M_{cI}\dot{w}_{Ii}^{k-1/2}\right]+ \\ QM_{cI}\left(M_{mI}+\frac{\Delta t}{2}C_{mI}\right)\left[\Delta t\left(f_{mIi}^{ext,pressure}+f_{mIi}^{body\ forces}+f_{mIi}^{int}\right)+M_{cI}\dot{u}_{Ii}^{k+1/2}+\left(M_{fI}-\frac{\Delta t}{2}C_{fI}\right)\dot{w}_{Ii}^{k-1/2}\right] \tag{3.61}$$

Collecting terms related to the mixture velocity, $\dot{u}_{Ii}$, and related to fluid velocity, $\dot{w}_{Ii}$, respectively, Equations (3.60) and (3.61) becomes

$$
\begin{aligned}
\dot{u}_{Ii}^{k+1/2} = & Q\left(M_{fI}+\frac{\Delta t}{2}C_{fI}\right)\left(\left(M_{mI}-\frac{\Delta t}{2}C_{mI}\right)-M_{cI}{}^{2}\right)\dot{u}_{Ii}^{k-1/2}+\\
& Q\Delta t\left(M_{fI}+\frac{\Delta t}{2}C_{fI}\right)\left(f_{mIi}^{ext,tractions}+f_{mIi}^{body\ forces}-f_{mIi}^{int}\right)+\\
& QM_{cI}\Delta t\left(f_{mIi}^{ext,pressure}+f_{mIi}^{body\ forces}+f_{mIi}^{int}\right)+\\
& Q\left(\left(M_{fI}+\frac{\Delta t}{2}C_{fI}\right)M_{cI}-M_{cI}\left(M_{fI}-\frac{\Delta t}{2}C_{fI}\right)\right)\dot{w}_{Ii}^{k-1/2}
\end{aligned}
\tag{3.62}
$$

$$
\begin{aligned}
\dot{w}_{Ii}^{k+1/2} = & Q\left(-M_{cI}\left(M_{mI}-\frac{\Delta t}{2}C_{mI}\right)+\left(M_{mI}+\frac{\Delta t}{2}C_{mI}\right)M_{cI}\right)\dot{u}_{Ii}^{k-1/2}+\\
& -QM_{cI}\Delta t\left(f_{mIi}^{ext,tractions}+f_{mIi}^{body\ forces}-f_{mIi}^{int}\right)+\\
& Q\left(M_{mI}+\frac{\Delta t}{2}C_{mI}\right)\left(\Delta t\left(f_{mIi}^{ext,pressure}+f_{mIi}^{body\ forces}+f_{mIi}^{int}\right)\right)+\\
& Q\left(-M_{cI}M_{cI}+\left(M_{mI}+\frac{\Delta t}{2}C_{mI}\right)\left(M_{fI}-\frac{\Delta t}{2}C_{fI}\right)\right)\dot{w}_{Ii}^{k-1/2}
\end{aligned}
\tag{3.63}
$$

To update the velocities of the material points the nodal acceleration or velocity increments,

$$\Delta\dot{u}_{Ii}^{k}=\Delta t\ddot{u}_{Ii}^{k}=\left(\dot{u}_{Ii}^{k+1/2}-\dot{u}_{Ii}^{k-1/2}\right) \tag{3.64}$$

and the fluid velocity increments

$$\Delta\dot{w}_{Ii}^{k}=\Delta t\ddot{w}_{Ii}^{k}=\left(\dot{w}_{Ii}^{k+1/2}-\dot{w}_{Ii}^{k-1/2}\right) \tag{3.65}$$

are necessary. Putting Equations (3.62) and (3.63) into Equations (3.64) and (3.65), respectively give the increments

$$
\begin{aligned}
\Delta\dot{u}_{Ii}^{k} = & Q\left(\left(M_{fI}+\frac{\Delta t}{2}C_{fI}\right)\left(M_{mI}-\frac{\Delta t}{2}C_{mI}\right)-M_{cI}{}^{2}-\frac{1}{Q}\right)\dot{u}_{Ii}^{k-1/2}+\\
& Q\Delta t\left(M_{fI}+\frac{\Delta t}{2}C_{fI}\right)\left(f_{mIi}^{ext,tractions}+f_{mIi}^{body\ forces}-f_{mIi}^{int}\right)+\\
& -QM_{cI}\Delta t\left(f_{fIi}^{ext,pressure}+f_{fIi}^{body\ forces}+f_{fIi}^{int}\right)+\\
& Q\left(\left(M_{fI}+\frac{\Delta t}{2}C_{fI}\right)M_{cI}-M_{cI}\left(M_{fI}-\frac{\Delta t}{2}C_{fI}\right)\right)\dot{w}_{Ii}^{k-1/2}
\end{aligned}
\tag{3.66}
$$

and

$$
\begin{aligned}
\Delta\dot{w}_{Ii}^{k} = & Q\left(-M_{cI}\left(M_{mI}-\frac{\Delta t}{2}C_{mI}\right)+\left(M_{mI}+\frac{\Delta t}{2}C_{mI}\right)M_{cI}\right)\dot{u}_{Ii}^{k-1/2}+\\
& QM_{cI}\Delta t\left(f_{mIi}^{ext,tractions}+f_{mIi}^{body\ forces}-f_{mIi}^{int}\right)+\\
& -QM_{cI}\left(\Delta t\left(f_{fIi}^{ext,pressure}+f_{fIi}^{body\ forces}+f_{fIi}^{int}\right)\right)+\\
& Q\left(-M_{cI}{}^{2}+\left(M_{mI}+\frac{\Delta t}{2}C_{mI}\right)\left(M_{fI}-\frac{\Delta t}{2}C_{fI}\right)-\frac{1}{Q}\right)\dot{w}_{Ii}^{k-1/2}
\end{aligned}
\tag{3.67}
$$

Expanding Q inside the parenthesizes gives

$$\Delta\dot{u}_{Ii}^{k} = Q\Bigg[\left(M_{fI}+\frac{\Delta t}{2}C_{fI}\right)\left(M_{mI}-\frac{\Delta t}{2}C_{mI}\right)-M_{cI}{}^{2}+$$
$$-\left(M_{mI}+\frac{\Delta t}{2}C_{mI}\right)\left(M_{fI}+\frac{\Delta t}{2}C_{fI}\right)-M_{cI}{}^{2}\Bigg]\dot{u}_{Ii}^{k-1/2}+$$
$$Q\Delta t\left(M_{fI}+\frac{\Delta t}{2}C_{fI}\right)\left(f_{mIi}^{ext,tractions}+f_{mIi}^{body\ forces}-f_{mIi}^{int}\right)+ \tag{3.68}$$
$$-QM_{cI}\Delta t\left(f_{fIi}^{ext,pressure}+f_{fIi}^{body\ forces}+f_{fIi}^{int}\right)+$$
$$Q\left(\left(M_{fI}+\frac{\Delta t}{2}C_{fI}\right)M_{cI}-M_{cI}\left(M_{fI}-\frac{\Delta t}{2}C_{fI}\right)\right)\dot{w}_{Ii}^{k-1/2}$$

$$\Delta\dot{w}_{Ii}^{k} = Q\left(-M_{cI}\left(M_{mI}-\frac{\Delta t}{2}C_{mI}\right)+\left(M_{mI}+\frac{\Delta t}{2}C_{mI}\right)M_{cI}\right)\dot{u}_{Ii}^{k-1/2}+$$
$$-QM_{cI}\Delta t\left(f_{mIi}^{ext,tractions}+f_{mIi}^{body\ forces}-f_{mIi}^{int}\right)+$$
$$-QM_{cI}\left(\Delta t\left(f_{fIi}^{ext,pressure}+f_{fIi}^{body\ forces}+f_{fIi}^{int}\right)\right)+ \tag{3.69}$$
$$Q\Bigg[-M_{cI}{}^{2}+\left(M_{mI}+\frac{\Delta t}{2}C_{mI}\right)\left(M_{fI}-\frac{\Delta t}{2}C_{fI}\right)+$$
$$\left(M_{mI}+\frac{\Delta t}{2}C_{mI}\right)\left(M_{fI}+\frac{\Delta t}{2}C_{fI}\right)-M_{cI}{}^{2}\Bigg]\dot{w}_{Ii}^{k-1/2}$$

Canceling terms of opposite signs the following two equations are obtained:

$$\Delta\dot{u}_{Ii}^{k} = Q\left(M_{fI}+\frac{\Delta t}{2}C_{fI}\right)\left(-\Delta tC_{mI}\right)\dot{u}_{Ii}^{k-1/2}+$$
$$Q\Delta t\left(M_{fI}+\frac{\Delta t}{2}C_{fI}\right)\left(f_{mIi}^{ext,tractions}+f_{mIi}^{body\ forces}-f_{mIi}^{int}\right)+ \tag{3.70}$$
$$-QM_{cI}\Delta t\left(f_{fIi}^{ext,pressure}+f_{fIi}^{body\ forces}+f_{fIi}^{int}\right)+$$
$$Q\Delta tM_{cI}C_{fI}\dot{w}_{Ii}^{k-1/2}$$

$$\Delta\dot{w}_{Ii}^{k} = QM_{cI}\Delta tC_{mI}\dot{u}_{Ii}^{k-1/2}+$$
$$-QM_{cI}\Delta t\left(f_{mIi}^{ext,tractions}+f_{mIi}^{body\ forces}-f_{mIi}^{int}\right)+$$
$$-Q\left(M_{mI}+\frac{\Delta t}{2}C_{mI}\right)\left(\Delta t\left(f_{fIi}^{ext,pressure}+f_{fIi}^{body\ forces}+f_{fIi}^{int}\right)\right)+ \tag{3.71}$$
$$Q\left(M_{mI}+\frac{\Delta t}{2}C_{mI}\right)\left(\Delta tC_{fI}\right)\dot{w}_{Ii}^{k-1/2}$$

Collecting terms we finally get

$$\Delta\dot{u}_{Ii}^{k} = Q\Delta t\Bigg[-\left(M_{fI}+\frac{\Delta t}{2}C_{fI}\right)C_{mI}\dot{u}_{Ii}^{k-1/2}+M_{cI}C_{fI}\dot{w}_{Ii}^{k-1/2}+$$
$$\left(M_{fI}+\frac{\Delta t}{2}C_{fI}\right)\left(f_{mIi}^{ext,tractions}+f_{mIi}^{body\ forces}-f_{mIi}^{int}\right)+ \tag{3.72}$$
$$-M_{cI}\left(f_{fIi}^{ext,pressure}+f_{fIi}^{body\ forces}+f_{fIi}^{int}\right)\Bigg]$$

$$\Delta \dot{w}_{Ii}^{k} = Q\Delta t\Bigg[M_{cI} C_{mI} \dot{u}_{Ii}^{k-1/2} - \left(M_{mI} + \frac{\Delta t}{2} C_{mI} \right) C_{fI} \dot{w}_{Ii}^{k-1/2} + - M_{cI} \left(f_{mIi}^{ext,tractions} + f_{mIi}^{body\ forces} - f_{mIi}^{int} \right) + \left(M_{mI} + \frac{\Delta t}{2} C_{mI} \right) \left(f_{fIi}^{ext,pressure} + f_{fIi}^{body\ forces} + f_{fIi}^{int} \right) \Bigg] \tag{3.73}$$

References of SECTION 3.4

Bardenhagen, S. G. (2002). Energy conservation error in hte material point method for solid mechanics. *Journal of Computational Physics*, 180:383–403.

Bathe, K. (1996). *Finite element procedures*. Prentice-Hall.

Burgess, D., Sulsky, D., and Brackbill, J. (1992). Mass matrix formulation of the flip particle in cell method. *J. Comp. Phys.*, 103:1–15.

Chan, A., Famiyesin, O., and Wood, M. D. (1991). A fully explicit u-w scheme for dynamic soil and pore fluid interaction. In Cheung, Lee, and Leung, editors, *Asian Pacific Conference on Computational Mechanics*, pages 881–887. Balkema, Rotterdam.

Flanagan, D. P. and Belytschko, T. (1981). A uniform strain hexahedron and quadrilateral with orthogonal hourglass control. *International Journal of Numerical Methods in Engineering*, 17:679–706.

Harlow, F. H. (1964). The particle-in-cell computing method for fluid dynamics in fundamental methods in hydrodynamics.

In *Experimental Arithmetic, High-Speed Computations and Mathematics*, pages 319–345. Academic Press.

Herle, I. and Gudehus, G. (1999). Determination of parameters of a hypoplastic constitutive model from properties of grain assemblies. *Mech. Cohes.-Frict. Mater.*, 4:461–486.

Hughes, T. J. R. (1983). Numerical implementation of consitutive models: Rate-independant deviatoric plasticity. In *Theoretical foundation for large-scale computations of nonlinear material behavior*, pages 29–64. Martinus Nijhoff Publishers.

Konagai, K. and Johansson, J. (2001a). "Lagrangian Particles for Modeling Large Soil Deformations." *Proc., Seismic Fault-induced Failures*, Konagai et al. eds., IIS, University of Tokyo, 99-106.

Konagai, K. and Johansson, J. (2001b). "Two dimensional Lagrangian Particle Finite Difference Method for modeling large soil deformations." *Structural Eng./ Earthquake Eng.* **18(2)**, 91s-95s.

Kuessner, M. and Reddy, B. D. (2001). The equivalent parallelogram and parallelipiped, and their application to stabilised finite elements in two and three dimensions. *Computer Methods in Applied Mechanics and Engineering*, 190:1967–1983.

Lewis, R. and Schrefler, B. (1998). *The finite element method in the static and dynamic deformation and consolidation porous media*. John Wiley and Sons, West Sussex, England, 2 edition.

Mukoyama, S. (2000). Fault induced surface configuration features (in japanese). In *Mountain Geomorphology*, pages 82–100. Kokonshoin Press.

Nagtegaal, J., Rice, D. M., and Park, J. R. (1974). On numerically accurate finite element solutions in the fully plastic range. *Comput. Methods Appl. Mech. Engrg.*, 4:153–177.

Sulsky, D., Chen, Z., and Schreyer, H. L. (1994). A particle method for history-dependent materials. *Comput. Methods Appl. Mech. Engrg.*, 118:179–196.

Sulsky, D., Zhou, S. J., and Schreyer, H. L. (1995). Application of particle-in-cell method to solid mechanics. *Comp. Phys. Comm.*, 87:236–252.

Wieckowski, Z., Youn, S.-K., and Yeon, J.-H. (1999). A particle-in-cell solution to the silo discharging problem. *International Journal of Numerical Methods in Engineering*, 45:1203–1225.

Zienkiewicz, O., Chan, A., Pastor, M., Paul, D., and Shiomi, T. (1990). Static and dynamic behaviour

of geomaterials - a rational approach to quantitative solutions, part i: Fully saturated problems. *Proc. Roy. Soc. London*, A429:285–309.

Zienkiewicz, O., Chan, A., Pastor, M., Schrefler, B., and Shiomi, T. (1999). *Computational geomechanics with special reference to earthquake engineering*. John Wiley and Sons, West Sussex, England.

3.5 APPLICATION OF 3D-MPM
–BEHAVIOR OF PILE GROUPS IN THE VICINITY OF SURFACE FAULT RUPTURES –

(by Sadr A. and Konagai, K.)

3.5.1. Introduction

The trace of the surface rupture that appeared in the 1999 ChiChi earthquake closely followed the frontal slope of the local mountain range where the range trends north south (Chen et al., 2003). Some major rivers cut this range, and bridges crossing these rivers were seriously damaged by large deformations of soils caused by the fault rupture.

Many foundations supporting the damaged bridges were embedded in deposits of sands, gravel and other suspended matters that rivers have carried over centuries. Therefore due attention should be directed to deformation buildup in soil deposits that cover hidden faults. When a base rock comes steadily up into a soft soil deposit, strains will be distributed over some wide zones, which extent depends largely on the material properties, dip angle, etc. Consequently an embedded foundation will be shifted from its original location, and deformed even though it is located off the major rupture zone. For analyzing this problem, two phenomena should be discussed simultaneously; deposit rupturing and pile-soil interaction. Some researches have been conducted both for soil deformations caused by dip-slip and strike-slip fault dislocations. Most of them were experimental works with numerical verifications (see e.g. Bray 1990, Stone 1988); but there are few studies on structures affected by fault ruptures. A material point method (MPM) is used herein for numerical modeling of fault rupture effects on structures. The MPM is categorized as one of the mesh-free methods formulated in an arbitrary Lagrangian-Eulerian description of motion. In MPM, a body to be analyzed is described as a cluster of material points. The material points, which carry all Lagrangian parameters, can move freely across cell boundaries of a stationary Eulerian mesh. This mesh, called a computational mesh, should cover the virtual position of the analyzed body. The computational mesh can remain constant for the entire computation, thus the main disadvantage of the conventional finite element method related to the problem of mesh distortions is eliminated. Its main drawback, however, is that any localization, heterogeneity and boundaries that can exist within one cell are not sharply outlined (see **Figure 3.34**). In other word, a cell size determines the resolution of MPM.

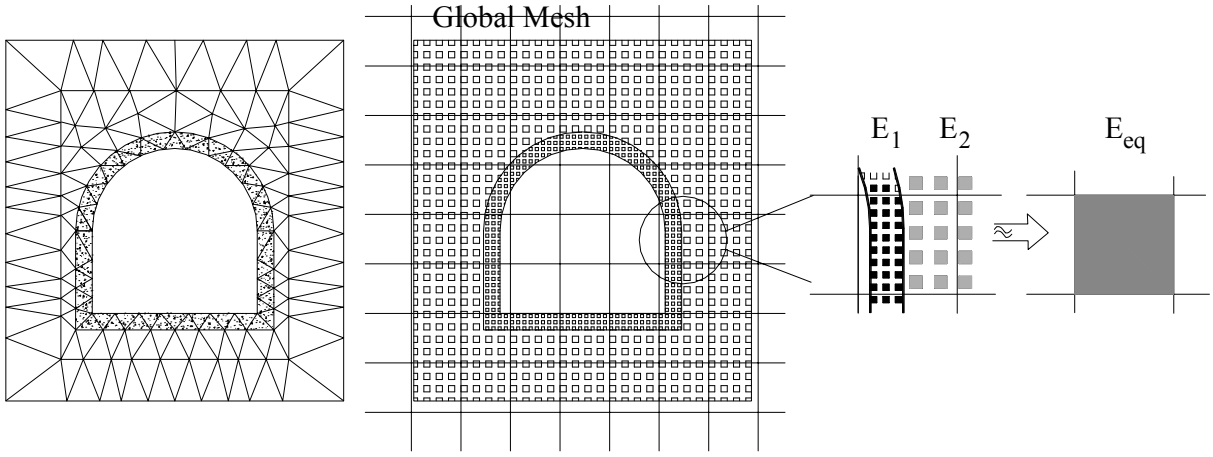

Discretization by Element FEM

Digitized domains by Material points MPM

Figure 3.34. FEM and MPM: Resolution of MPM greatly depends on cell size.

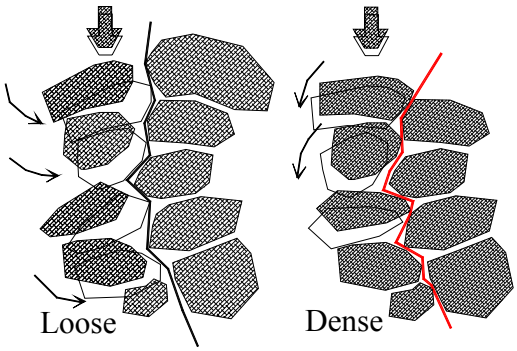

Figure 3.35. Dilating and contracting behavior of granular assemblage

3.5.2. Soil-Structure Model

Soil:

Soils in nature are often rich-graded granular assemblages. When a soil is sheared, it keeps dilating without showing any clear sign of contraction (**Figure 3.35**), and reaches its maximum volume when the shearing displacement reaches two to three times of its shear band thickness. The soil discussed herein is thus assumed to be a homogenous and isotropic material with constant elasticity properties. Mohr Coulomb criterion with Associated flow rule describes its plastic behavior. Taking into account that natural soil deposit includes large boulders among other finer matters, its shear band is assumed to dilate over the entire shearing process.

Pile group:

Piles, grouped beneath a superstructure, interact with the surrounding soil, and the pile-soil-pile interaction often affects the motion of its superstructure to a considerable extent. Straightforward evaluation of the pile-soil-pile interaction, however, is cumbersome especially in dealing with tens or hundreds of piles grouped together. Hence a simplified approach for the evaluation of such pile-soil-pile interaction is highly desirable for the purpose of treating the behavior of an entire soil-foundation-structure system. Recently, the second author developed a further simplified approach in which a group of piles is viewed as an equivalent single upright beam (Konagai et al., 2000, 2002 and 2003), the idea based on the fact that a group of piles often trap soil among them as observed when pulled out (Railway Technology Research Institute, 1995).

The following assumptions were taken to derive the stiffness matrix of the equivalent single beam:

(1) Pile elements within a horizontal soil slice are all deformed at once keeping their intervals constant, and the soil caught among the piles moves in a body with the piles.
(2) Frictional effects due to bending of piles (external moments on each individual pile from soil) are ignored.
(3) The top ends of piles are fixed to a rigid cap.
(4) All upper or lower ends of the sliced pile elements arranged on the cut-end of a soil slice remain on one plane (Note this assumption does not necessarily mean that each pile's cross-section remains in parallel with this plane. See **Figure 3.36(b)**).

The stiffness matrix includes two stiffness parameters, EI_{sway} and EI_{rock} (see Konagai et al. 2000, 2003). The first parameter EI_{sway} that governs the sway motion of the beam is the product of the bending stiffness of an individual pile EI_{single} and the number of piles n_p. The second stiffness parameter EI_{rock} is most strongly associated with the rocking motion of the beam.

In the following discussion, it is necessary to introduce the idea of active pile length. Under lateral loading at the pile cap, the horizontal deflection of a pile decreases with increasing depth. In practice, most laterally loaded piles are indeed 'flexible' in the sense that they are not deformed over their entire

length L. Instead, pile deflections become negligible below an active length (or effective length) L_a. The active length, an important parameter in the design of a pile foundation (Wang MC, Liao WP, 1987), depends largely on the ratio of the pile stiffness EI_{sway} for flexural deformation and the soil stiffness μ, and is given by:

$$L_a = \alpha_0 L_0 \tag{1}$$

where, the parameter α_0 reflecting, in theory, only different soil profiles rationally excluding the pile group effect, and

$$L_0 = \sqrt[4]{EI_{sway} / \mu}. \tag{2}$$

For the present study, the ratio of pile length L to L_0 is set at 2.16, 2.71 and 3.84. These values correspond to pile-soil stiffness ratios E / E_{soil} = 1, 4 and 10, respectively.

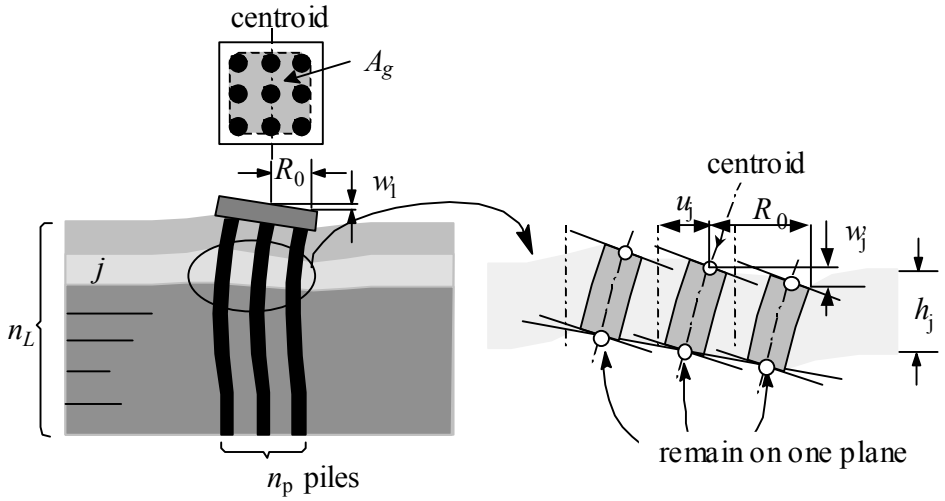

(a) soil- pile-group system **(b)** sliced elements

Figure 3.36. Assumptions for evaluation of equivalent single beam

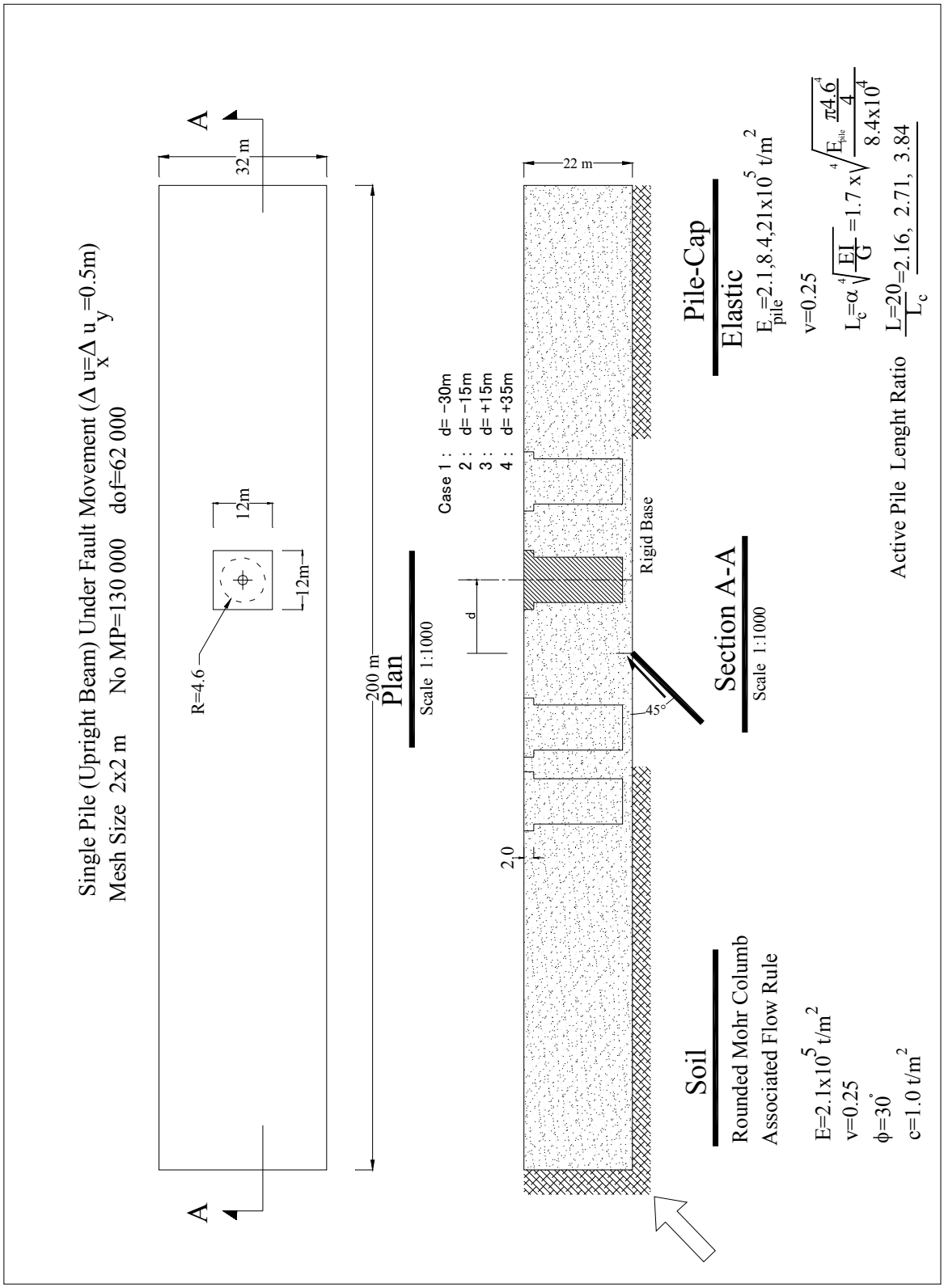

Figure 3.37. Fault geometry

Fault geometry

A reverse fault movement is given at the mid bottom of a 200m-long, 22 m-deep and 32m-thick surface soil deposit (**Figure 3.37**). Dip angle is set at 45 degrees. Two rigid walls retaining both sides of the surface soil deposit move with the bedrock. The walls were made slippery so that their presence has little affect on the numerical results. A pile group (equivalent upright beam) is located –30m, -15m (on the hanging wall side), +15m and 35m (on the footwall side) off the point of the bedrock rupture for CASE 1, 2, 3 and 4, respectively. For keeping pile group stresses below allowable range, a thin layer of soil is put between pile head and bedrock.

3.5.3. Soil-Pile Interaction

Deformation of the surface soil deposit is first analyzed by excluding the pile group. The deformation is then compared to that with a pile group. This procedure allows a rational evaluation to be made for the effect of the pile-group inclusion in the vicinity of the fault rupture zone. In addition, the result allows the verification of a 2D MPM, which can be used for this particular case in place of the 3D MPM decreasing drastically the number of material points.

Figure 3.38 shows the distribution of the maximum shear strains. Since the range of the strain was too wide to describe detail features of strain distribution pattern, they were mapped with gray halftones in logarithmic scale. Two conjugate shear bands propagate up through the soil deposit, and one in the direction of the fault dip is clearer than the other. **Figure 3.39** shows spatial distributions of both horizontal and vertical displacements.

Figure 3.38. Maximum shear strain distribution

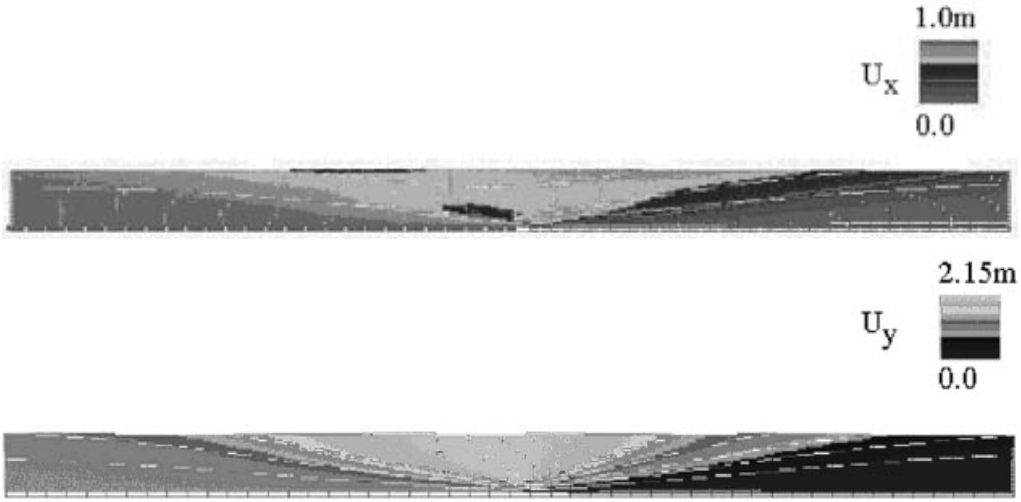

Figure 3.39. Horizontal and Vertical Displacement Plot After Fault 1 m 45^{o} offset

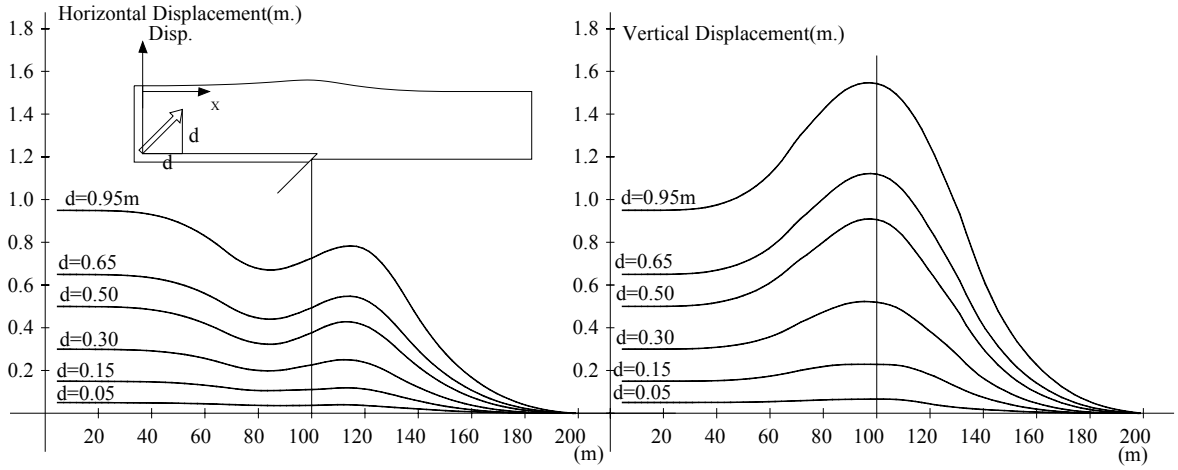

Figure 3.40. Horizontal and vertical displacements after a 45^o fault offset of 1 m.

For a thorough discussion, variations of ground surface displacements are shown in **Figure 3.40** at different bedrock dislocations with respect to the distance along the bedrock. Parameter d in this figure denotes either lateral or vertical component of the bedrock dislocation. It is noted here that vertical displacement reaches its peak exactly above the point of bedrock dislocation, and is larger than the vertical component of dislocation d. Dilative feature of soil may have caused part of this upheaval, but it seems mainly that the thrusting movement of the fault pushed up the soil block in between the two conjugate shear bands. All curves showing horizontal soil displacements (left chart of **Figure 3.40**) go down gently oscillating towards right. These oscillations have their first bottom values appearing at around 80m lateral distance. This means that there is a lateral compressive movement between the leftmost soil mass and that at the 80m distance.

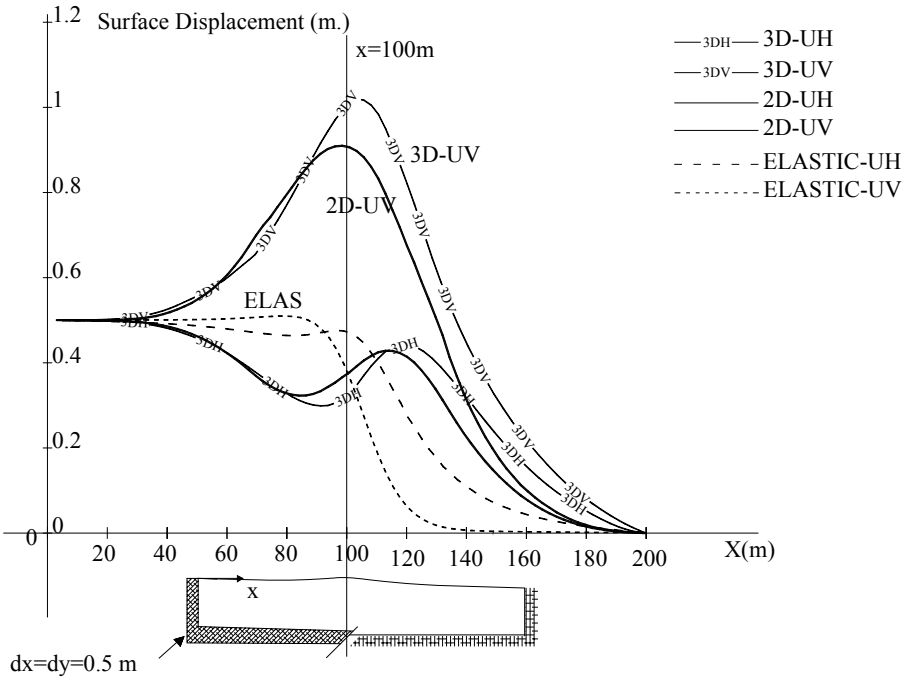

Figure 3.41. Results from 2D and 3D MPM analyses

Figure 3.41 compares the surface soil displacements from 2D and 3D MPM analyses when d reaches 0.5m. Slight difference seems to have caused by the plane-strain assumption for the 2D model, while out-of-plane motions of material points are not completely restricted in the 3D MPM analysis. **Figure 3.41** also shows the variation of displacements for an elastic soil deposit. There is no clear soil upheaval appearing in this figure because the soil does not exhibit any plasticity.

The surface soil deformation was than calculated putting a pile group in the surface soil deposit (see **Figure 3.42**). **Figure 3.43** shows surface soil displacements calculated for different locations of a pile group, +15m and +35m (on the footwall side) and –15m, -30m (on the hanging wall side) off the point of bedrock fault rupture. The presence of the pile group certainly caused the displacement distribution to change in the vicinity of it. However, no serious difference can be seen among cases for different pile-soil stiffness ratios examined (E / E_{soil} = 1, 4 and 10). As for horizontal displacements, the flexural pile group followed rather closely the motion of the surrounding soil, while clear changes in vertical displacements indicate that the pile group, though flexible in its lateral direction, is stiff enough to pull down the heaving soil.

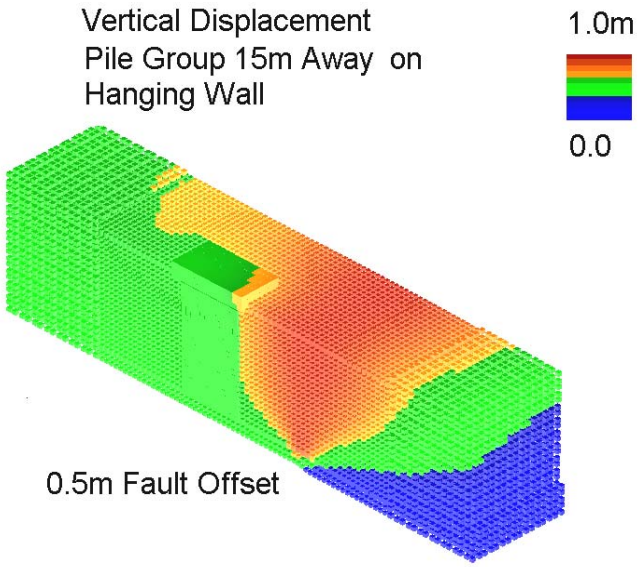

Figure 3.42. Spatial distribution of vertical soil displacement

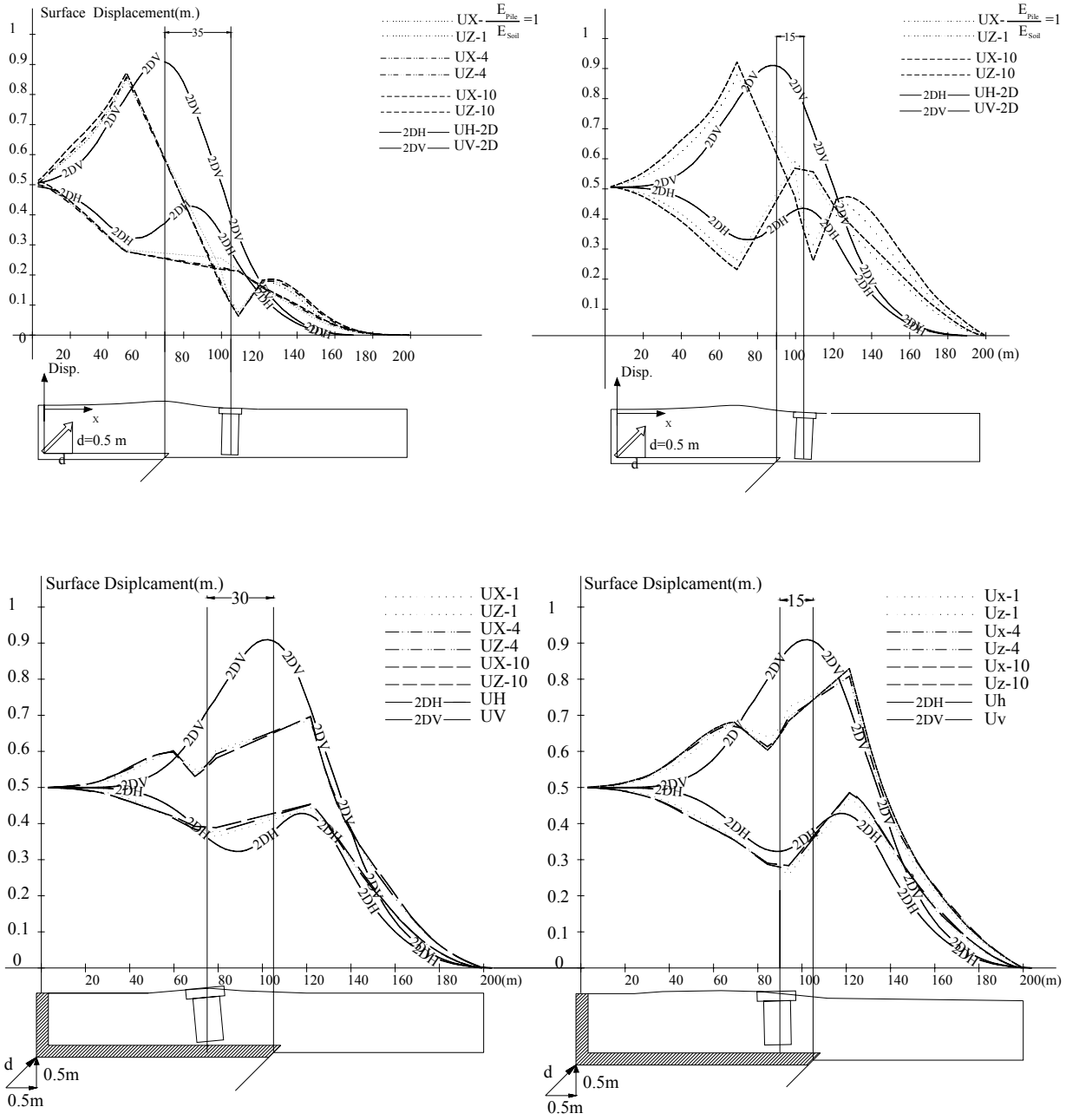

Figure 3.43. Surface soil displacements calculated for different locations of pile group, +35m and +15m (on the footwall side) and –30m, -15m (on the hanging wall side) off the point of bedrock fault rupture.

Figure 3.44 shows the increasing rotation angle of the pile cap with the increasing bedrock dislocation. No remarkable difference can be seen among cases for different pile-soil stiffness ratios examined. Kinks appeared at around 0.42 m vertical offset probably because the bedrock offset exceeded one cell size

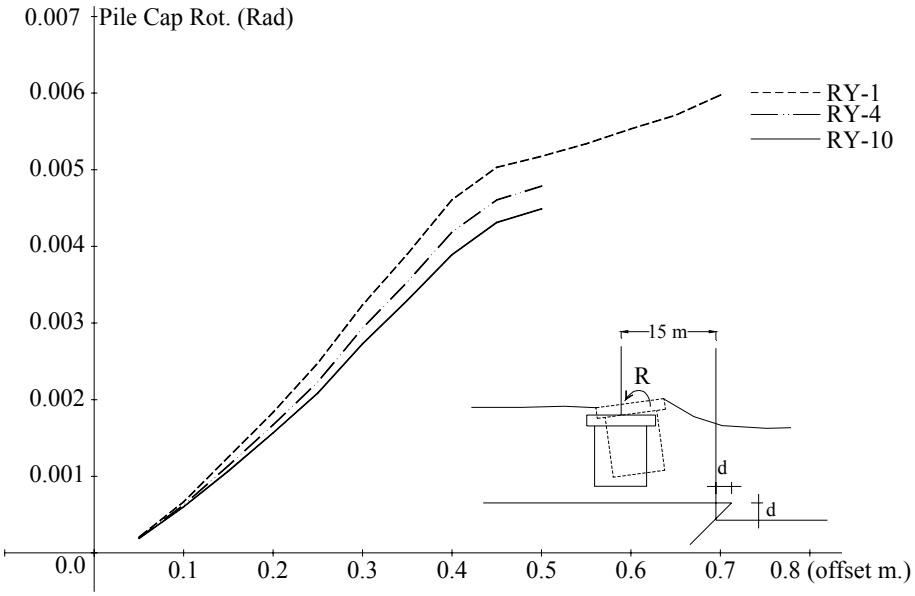

Figure 3.44. Pile Cap rotation history with increasing fault offset

3.5.4. Summary

Behavior of a pile group subjected to soil deformation caused by faulting at its bedrock is numerically studied using Material Point Method (MPM). Conclusions obtained through the numerical examinations are summarized as follows:

1. Deformation of the surface soil deposit is first analyzed by excluding the pile group. Two conjugate shear bands propagate up through the soil deposit, and one in the direction of the fault dip is clearer than the other. The vertical component of displacement reaches its peak exactly above the point of bedrock dislocation. Dilative feature of soil may have caused part of this upheaval, but mainly the thrusting movement of the fault seems to have pushed up the soil block in between the two conjugate shear bands.
2. The presence of the pile group certainly caused the displacement distribution to change in the vicinity of it. As for horizontal displacements, the flexural pile group followed rather closely the motion of the surrounding soil, while clear changes in vertical displacements indicate that the pile group, though flexible in its lateral direction, is stiff enough to pull down the heaving soil.

Refernces of SECTION 3.5

Bray, J., (1990). "The Effects of Tectonic Movements on Stresses and Deformation in Earth Embankments" *PhD. Dissertation*, University of California, Berkeley

Chen, C., Chou, H. ,Yang,C, Shieh, B. (2003). "Chelungpu fault inflicted damages of pile foundations on FWY rout 3 and Fault zoning regulations in Taiwan " *Workshop on Seismic Fault-induced Failures*, Jan 2003.

Konagai, K., Yin, Y. and Murono, Y. (2003). "Single beam analogy for describing soil-pile group interaction." *Soil Dynamics and Earthquake Engineering*, 23(1), 1-9.

Stone. , (1988) "Modeling of rupture development in soils" *PhD dissertation*, Cambridge University

Chapter 4

INTRICACIES OF SOIL MODELING

3.1 INTRODUCTION

Numerical tools in Chapter 3 brought out some important features of surface fault rupturing in full relief. NL-SSFEM successfully described some important geometry of the Riedel shear, the small right-lateral faults, which are gently inclined to the strike of the main fault. An AEM simulation showed that the peak response exactly above a surface rupture is not always the largest among those off the fault rupture plane. MPM simulations and a fault-surface rupture experiments for both dry and water-saturated sands showed that the negative pore water pressure built up around the wedge cutting deep in the surface soil increased the failure strength and strain of this soil noticeably.

These numerical tools, however, inevitably require all parameters for an entire domain of soil to be provided. It is quite often, however, only a limited number of parameters are available. Moreover, a soil deposit spreading over a seismic fault often includes gravels and boulders that rivers from mountains rising behind have carried over centuries, and mechanical characteristics of these well-graded soils are not thoroughly studied yet. In this chapter, some findings through a parametric study using Discrete Element Method (DEM) by Matsushima, M. will be first given.

In the case of dam, constructing concrete dams over or near active faults are not advisable because of their rigid and brittle nature. On the other hand, such examples as Coyote, Ceder Springs and Palmdale Dams, which withstood safely deformations imposed by fault movement, suggested that a fill dam can be constructed over or across an active fault unless the bedrock dislocation does some serious damage to its impervious zone (Sherard *et al*., 1974). One of the most practical measures will be to construct a thick, transition zone of cohesionless filter material. A discussion on this material is given by Yamaguchi, Y. in the latter half of this chapter.

4.2. NUMERICAL STUDY ON THE SHEAR BEHAVIOR OF BINARY GRANULAR ASSEMBLY

(by Matsushima, T.)

4.2.1. Introduction

Researches of well-graded or gravelly soils have been conducted mainly in relation to constructions of rock-fill dams (Leps 1970, Marsal 1972, JSSMFE 1986). Recently, some researchers have tried to investigate natural gravelly-soil deposits concerning their undrained cyclic behaviors (Tanaka et al. 1992, Evans and Zhou 1995) and/or the development of undisturbed sampling technique for gravelly soils (Kokusho and Tanaka 1994, Goto et al. 1994).

In spite of such extensive efforts, mechanical characteristics of well-graded soils are not clear yet because of the many microscopic properties necessary to consider: grain size distribution, grain shape, grain crushability, cementation at particle contacts, granular packing structure including void ratio, etc. In order to draw a clearer picture of the mechanical behavior of a well-graded soil, it is necessary to do research under a systematic parameter control. Numerical discussion by using the Discrete Element Method (DEM) is suitable for such a purpose, since the above-mentioned microscopic parameters can

be controlled as one desires. Recent development of computer capability enables us to deal with a sufficient number of particles to study well-graded assemblies.

This section concerns the relationship between grain size distribution and simple shear behavior,and void ratio characteristics. In order to make the problem simple, the behavior of a binary pack is investigated in this study. After introducing a void ratio theory for a binary pack, the mixture void ratio's relations to peak strength, dilation property, and localization width are investigated through a series of DEM simulations with various mixture ratios.

4.2.2. Void Ratio Characteristics of Binary Packing

The void ratio characteristics of a binary granular pack was studied in details by Lade et al.(1998). **Figure 1** is a classical theory between the mixture ratio of the two granular materials and the resulting void ratio. This theory presupposes that the difference in diameter of particles of the two materials is sufficiently large. Then the theory describes two idealized conditions, corresponding to lines A and B in **Figure 1**. When the content of the bigger particles is sufficiently large, the smaller particles are presumed to be located within the void of the packing structure of the bigger particles. On this condition, the volume of the void is partly occupied by the volume of the smaller particles, which makes the overall void ratio smaller. This tendency can be expressed by:

$$e = \frac{e_B V_{sB} - V_{sS}}{V_{sB} + V_{sS}} = (1-x)e_B - x \tag{1}$$

where e_B is the void ratio only with the bigger particles, V_{sB} and V_{sS} are the volumes of the bigger and the smaller particles, respectively, and x is the volume content of the smaller particles:

$$V_{sS} : V_{sB} = x : (1-x) \tag{2}$$

On the other hand, when there are much more smaller particles than bigger particles, the void ratio of the mixture can be estimated by replacing a particular amount of the smaller particles with the bigger ones, which yields:

$$e = \frac{e_S V_{sS}}{V_{sS} + V_{sB}} = x\, e_S \tag{3}$$

where e_S is the void ratio only with the smaller particles.

The minimum void ratio of the mixture is attained when the void of the bigger-grains packing are filled up with the smaller grains, which corresponds the point C in **Figure 1**. As was mentioned above, this theoretical relation is derived from the presumed packing conditions, and the relation of real binary packing shows a smooth transition between the two lines.

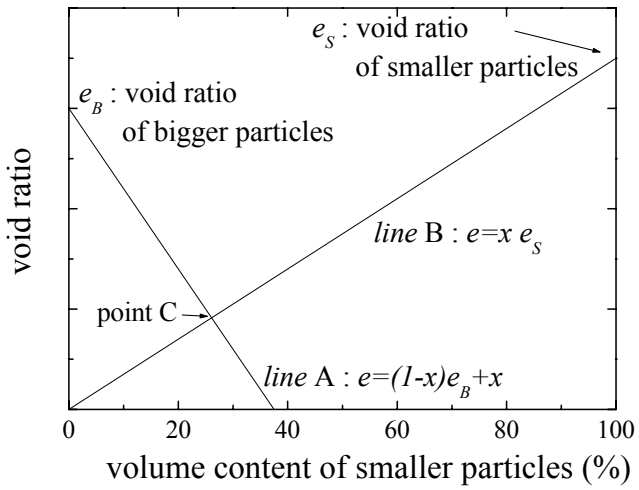

Figure 4.1. Theory of void ratio with mixture ratio in binary packing

Figures 4.2(a) and **(b)** show the experimental results of the standard maximum and minimum void ratio tests (Aizaki 2002). A mixture of two glass beads whose average diameters are 0.215mm and 1.7mm, respectively, was used in **Figure 2(a)**, while a mixture of two different clean sands (Toyoura sand: D=0.162mm and another silica sand: D=1.50mm) was used in **Figure 2(b)**. In both cases the theoretical relations indicated by dashed lines in the figures express the global tendency of the results. Therefore, the microscopic conditions presumed in the theory are regarded as reasonable.

4.2.3 DEM Simulations of Binary Packing

The main objective of this section is to connect the mechanical properties during shear deformation with the void ratio characteristics. The DEM is a powerful tool to study the essence of the phenomenon by eliminating other ambiguous factors. In the present simulation, our focus is put on the effect of mixture ratio of binary packing on shear behavior. Two types of granular material are used in the series of simulation. One is a set of circular particles whose diameter varies from 1.0mm to 2.0mm, and the other is the set of the particles each of which is composed of two equal-sized circles rigidly connected, as shown in **Figure 4.3**, and their equivalent diameters varies from 10mm to 20mm. The former material is denoted as SS (Small, Single circles), while the latter as BT (Big, Twin circles) in this study. The grain size distributions for the two materials are shown in **Figure 4.3**.

The DEM parameters used in the present simulation are listed in **Table 4.1**. Five specimens were prepared by changing the mixture ratio of the two materials. The parameters of these five specimens are listed in **Table 4.1**. In order to make the computational load equal, the total number of particles for a specimen was at around 1000.

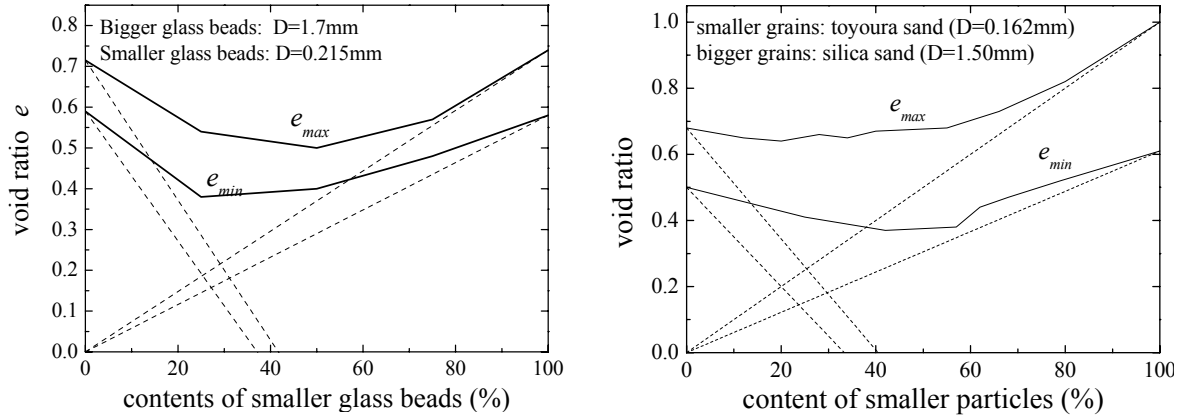

(a) the mixture of two types of glass bead (b) the mixture of two types of sand

Figure 4.2. Experimental results: void ratio vs. contents of smaller particles (Aizaki 2002)

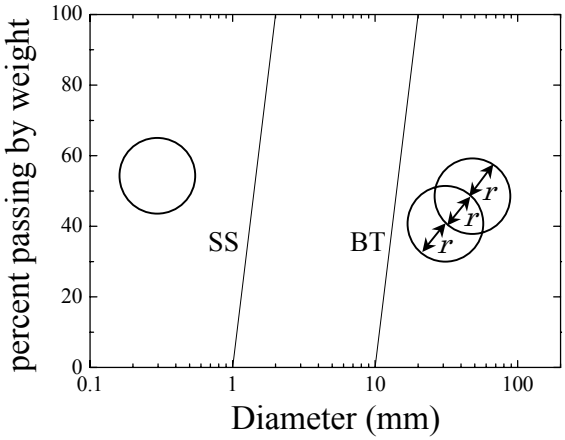

Figure 4.3. Grain size distributions used in the simulation

Table 4.1. DEM parameters

Density of grain	2.5 (g/cm^2)
spring constant (normal)	1.0e8 (g/s^2)
spring constant (shear)	2.5e7 (g/s^2)
damping coefficient (normal)	1.0e1 (g/s)
damping coefficient (shear)	0.5e1 (g/s)
Friction coefficient	27 (deg.)
time increment	5.0e-5 (s)

Table 4.2 Information of the specimens

Specimen Name	Content of smaller particles	Number of particles (SS, BT)	width and height of the specimen (mm)	initial void ratio	internal friction angle (deg.)	shear band width (mm)
BT100SS0	0 %	1000, 0	446 by 423	0.110	36.3	50
BT90SS10	10 %	100, 1112	150 by 134	0.0604	37.1	40
BT80SS20	20 %	40, 1001	101 by 90.0	0.0654	33.3	20
BT50SS50	50 %	10, 1002	64.0 by 58.5	0.101	28.8	20
BT0SS100	100 %	0, 1000	45.0 by 44.0	0.164	27.2	15

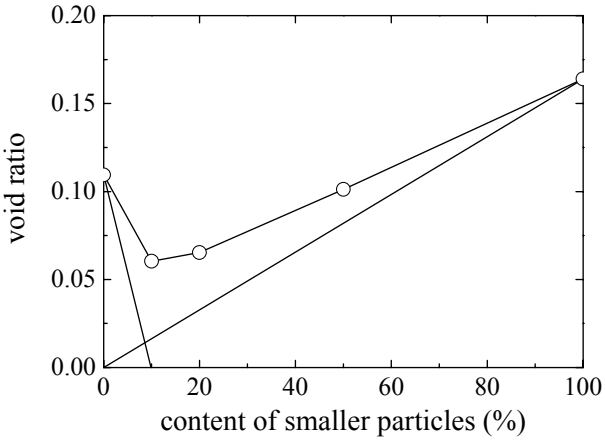

Figure 4.4. Void ratio vs. mixture ratio.

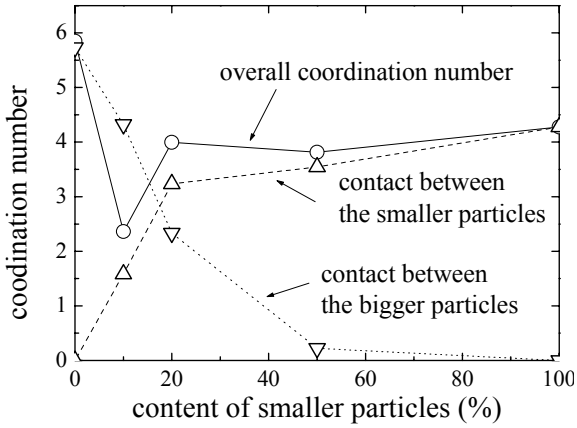

Figure 4.5. Coordination number vs. mixture ratio

This implies that the size of the specimen differs in different specimen.

For each specimen, the particles were randomly located in a square domain at first. Periodic boundary is set to the left and right sides of the domain. Then the assembly was compacted in the vertical direction under a constant confining pressure (9.9e5 (g mm/s2 /mm)) keeping the inter-particle friction angle zero. After sufficient time steps, the assembly becomes the most dense, and the final void ratio can be regarded as the minimum one.

Figure 4.4 shows the void ratio variation with different mixture ratios. The obtained curve fits well with the theoretical asymptotes, as did the experiments shown above. It is worth noting that the void ratio only with BT particles (connection of two circles) is much smaller than that only with SS particles (single circles). This difference is due to the difference in particle shape. Considering the similarity in shape between the BT particle and ellipse, this result is consistent with that obtained by Rothenburg and Bathurst (1992) and Matsushima and Konagai (2001) for elliptic particles.

It is widely believed that the number of contact points increases in decreasing void ratio, which causes the increase of shear strength. However, checking the five specimens, it was found that the coordination number (number of contacts per particle) has the minimum value when the void ratio is minimum (with 10% of the smaller particles), as shown in **Figure 4.5**. This can be explained as follows: Beginning with the assembly only with the bigger particles, smaller particles, which are added little by little, gradually fill the voids of the bigger-particle assembly without experiencing a large confining pressure. Therefore, the coordination number decreases even though the void ratio decreases. As the state of the minimum mixture ratio is reached, the smaller particles have more contact points, and the overall coordination number increases again. Then around the 20% of the smaller-particles content, the effect of the bigger particles becomes negligible. The overall coordination number is almost same as that only with the smaller particles.

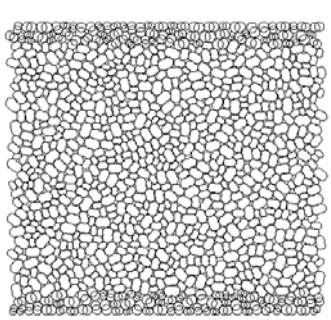

(a) BT100SS0 (before shear)

(b) BT100SS0 (at 50% shear strain)

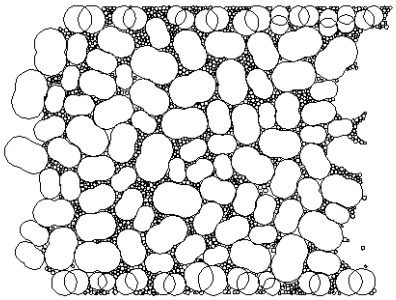

(c) BT90SS10 (before shear)

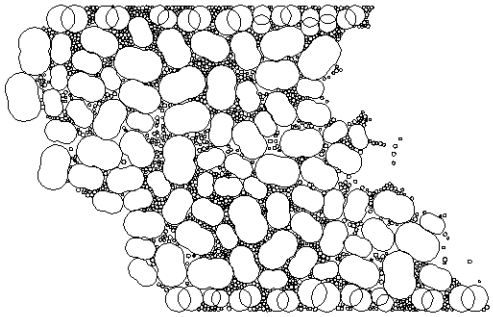

(d) BT90SS10 (at 50% shear strain)

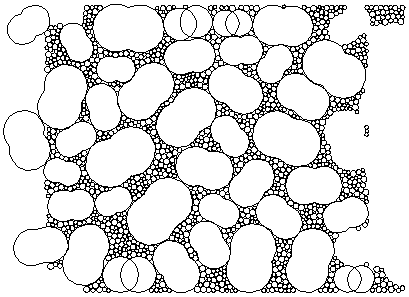

(e) BT80SS20 (before shear)

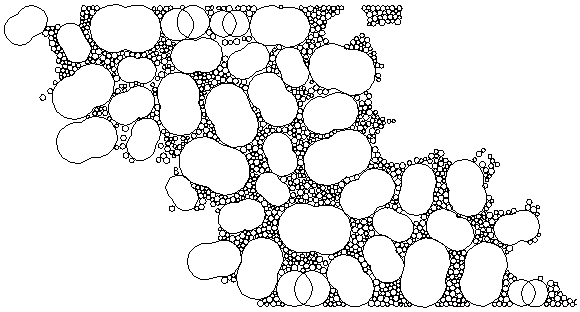

(f) BT80SS20 (at 50% shear strain)

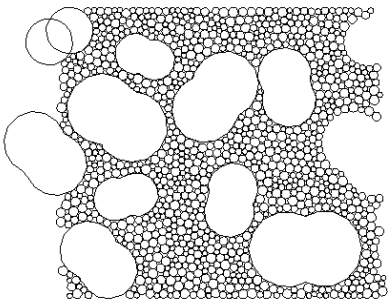

(g) BT50SS50 (before shear)

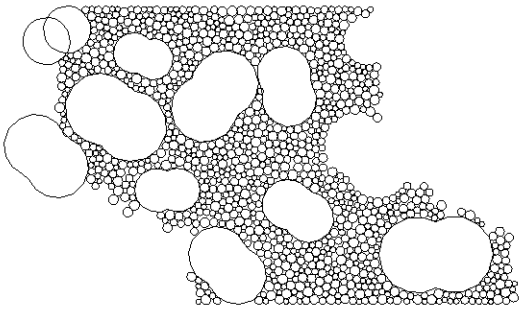

(h) BT50SS50 (at 50% shear strain)

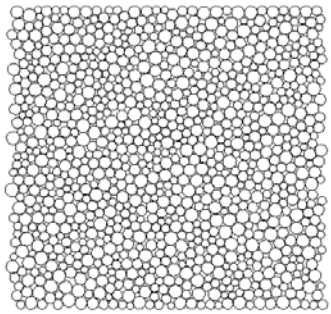

(i) BT0SS100 (before shear)

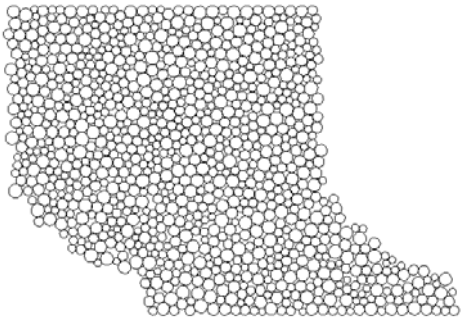

(j) BT0SS100 (at 15% shear strain)

Figure 4.6. initial configurations and shear deformation patterns of specimens

Figure 4.5 also shows the coordination numbers for the contacts between the bigger particles and for those between the smaller particles.

Figures 4.6 (a)(c)(e)(g)(i) show the prepared five specimens. The particles around the top and the bottom boundaries were rigidly connected and were controlled to apply simple shear deformation to the assembly under the constant confining pressure. **Figures 4.6** (b)(d)(f)(h)(j) show the resultant deformation patterns for each specimen, which seem to be quite complicated due to strong heterogeneity. Based on the least square approximation, the width of shear band (localization width) is roughly estimated as shown in **Table 4.2**. In general the localization width is about ten to twenty times as big as particle diameter for a poorly-graded assembly. In case of binary packing, the width seems to change from that only with the bigger particles to that only with the smaller particles.

Figure 4.7(a) shows the evolution of mobilized friction angle $\phi_{mob} = \tan^{-1}(\tau / \sigma_n)$ with respect to the shear strain. Every specimen has its peak strength around 3 to 5% of shear strain. After the peak state, the localization of strain occurs within the specimen, and the global stress-strain curve and the dilation curve, shown in **Figure 4.7(b),** are affected by the size of localization.

In **Figure 4.7(a)**, there is a clear difference in peak strength among the specimens. **Figure 4.8** shows the peak strength with respect to the content of the smaller particles. The specimen only with the bigger particles exhibits higher strength than that only with the smaller particles, which is due to the difference in particle shape (Matsushima and Konagai 2001). More importantly, the peak strength suddenly changes around 10 to 20% of the smaller-particles content, which corresponds to the condition at the minimum void ratio, and to the condition that the contacts between the bigger grains are drastically lost.

Dilation characteristics also changes suddenly around 20% of the smaller-particles content as shown in **Figure 4.7(b)**. In the specimen of 50% of the smaller-particles content, the overall behavior is almost the same as that only with the smaller particles (this is coinciding with Prof. Wood's findings on clay gravel mixtures). According to the **Figures 4.6(g)** and **4.6(h)**, the bigger particles seem to be floating within the material of the smaller particles. Therefore it seems to be natural that the mechanical behavior of such mixture is governed by the smaller particles. However, one can think that the inclusion of the bigger particles may avoid the formation of localization zone during the large shear deformation, which makes the global response different. The simulation result suggests that such kinematic constraint to shear-banding is not predominant. This should be verified by further simulations with different particle shapes or the experiments with real sands.(Have the sample only been tested in one direction? What happens if one use the same mixture ratio but just changes the configuration of the particles?)

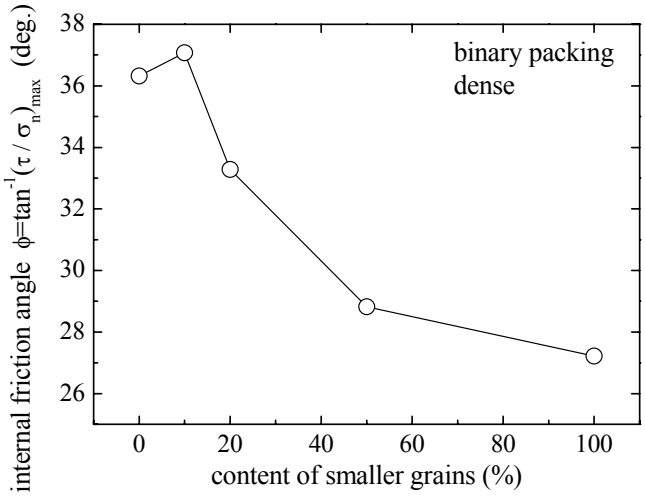

Figure 4.8. Internal friction angle vs. mixture ratio

4.2.4. Summary

A series of DEM simulations for binary packing were conducted and the effect of mixture ratio on the shear behavior was investigated. The void ratio of binary packing with respect to the mixture ratio has two asymptotes showing larger and smaller grains assemblies. The transition of peak strength, dilation behavior and localization width of the mixture with the increasing mixture ratio can be explained in the same manner When the content of the smaller particles is over 60%, the mechanical properties of the mixture are almost the same as those of the smaller particles.

References of SECTION 4.2

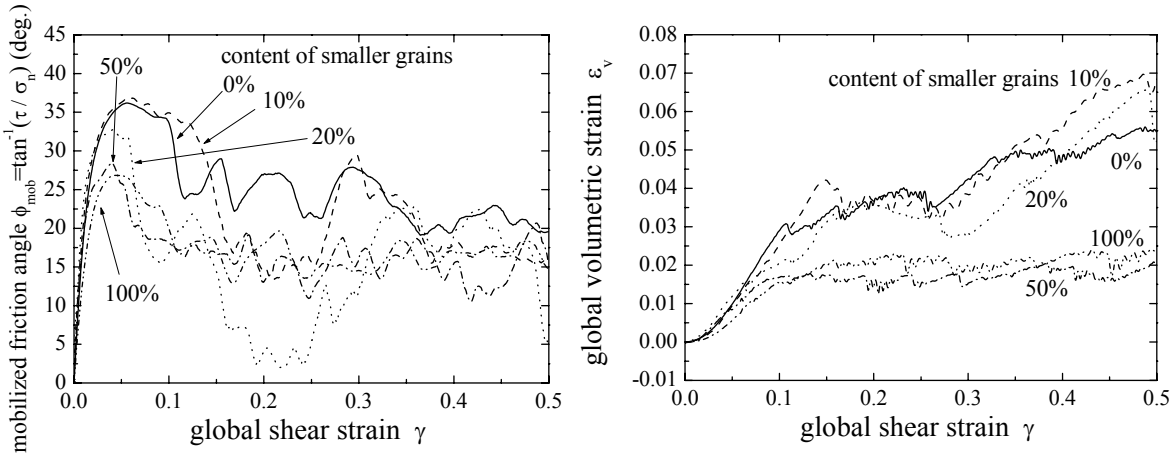

(a) Evolution of mobilized friction angle **(b)** Global dilation curve

Figure 4.7. Overall response of the specimens

Aizaki, N. (2002) “Effect of grain size distribution on the mechanical properties of granular materials”,

Master thesis, University of Tsukuba (In Japanese).
Evans, M.D. and Zhou, S. (1995) “Liquefaction behavior of sand-gravel composits, Journal of Geotechnical Engineering, ASCE, Vol.121, No.3, pp.287-298.
Goto, S., Nishio, S.and Yoshimi, Y. (1994) “Dynamic properties of gravels sampled by ground freezing, Geotechnical Special Publication, No.44, ASCE, pp.141-157.
JSSMFE(Japanese Society of soil Mechanics and Foundation engineering) (1986). “Deformation and strength characteristics of coarse-grained materials”, edited by Tatsuoka et al. (in Japanese).
Kokusho, T. and Tanaka, Y. (1994) “Dynamic properties of gravel layers investgated by in-situ freezing sampling, Geotechnical Special Publication, No.44, ASCE, pp.121-140.
Lade, P.V., Liggio, C.D., Yamamuro, J.A (1998) “Effects of non-plastic fines on minimum and maximum void ratios of sand, Geotechnical Testing Journal, Vol.21, No.4, pp.336-347.
Leps, T.M. (1970) “Review of shearing strength of rackfill”, Journal of Soil Mechanics and Foundation Division, ASCE, Vol.36, No.SM4, pp.1159-1170.
Marcal, R. J. (1972) “Mechanical properties of rockfill”, Embankment dam engineering : Casagrande volume / Editors: Ronald C. Hirschfeld and Steve J. Poulos, John Wiley & Sons, pp.109-200.
Matsushima, T. and Konagai, K (2001). “Grain-shape effect on Peak Strength of Granular Materials”, *Computer Methods and Advances in Geomechanics, Proc. 10ACMAG, Desai et al. eds.*, Vol. 1, pp.361-366.
Tanaka, Y., Kudo, K., Yoshida, Y. and Kokusho, T. (1992) “Undrained cyclic strength of gravelly soil and its evaluation by penetration resistance and shear strength”, Soils and Foundations, Vol.32, No.4, pp.128-142.
Rothenberg, L. and Bathurst, R.J. (1992), “Micromechanical features of granular assemblies with planner elliptical particles”, Geotechnique, 42(1), 79-95.

4.3. EXPERIMENTAL STUDY ON IDENTIFICATION OF FILTER COHESION

(by Yamaguchi, Y.)

4.3.1. Introduction

Of most of dams built in regions of high earthquake potential, there are few in locations where faults are not recognized or suspected to exist. Any dam site located near an active fault can be subjected to strong earthquake shakes, and therefore measures for designing dams to withstand both strong ground motions and fault dislocations in their foundations are to be discussed simultaneously (Sherard *et al*., 1974). Because design details to ensure safety against such possible fault displacements are difficult to realize, a dam is desirable to be constructed avoiding an active fault trace. In Japan, thorough investigations are systematically made not to miss any suspicious marks of an active fault (Wakizaka, 1999).

In Sept. 2, 1999 Chi-Chi Earthquake, Taiwan, one branch of the activated fault crossed the northern end of the Shih-Kang Dam causing three of its spillways to be completely destroyed by vertical offsets of up to 10 m. In Aug. 17, 1999 Kocaeli Earthquake, Turkey, fault-induced ground ruptures destroyed a lot of buildings and modern engineered structures. Theses examples showed that it is very important to comprehend how soils and rocks immediately next to active fault traces will be deformed. With this knowledge provided, damage to a variety of structures can be minimized.

Construction of a concrete dam on an active fault, or near some major active fault traces, are not advisable because of their rigid and brittle features. On the other hand, previous examples of the Coyote, Ceder Springs and Palmdale Dams, which withstood safely the deformations imposed by fault movements (Sherard *et al*., 1974), suggest that an embankment dam can be constructed safely if its interior zone is kept impervious. One of the most effective measures to minimize the damage to the impervious zone is to construct thick, protective zones of cohesion-less filter (transition) materials. Any open crack, which is formed momentarily in a cohesion-less material, will be immediately stopped up with itself, and these protective zones will act as ‘crack stoppers’. Sands, gravels, and sand-gravel mixtures are cohesion-less as long as their voids are not clogged up with admixtures of finer-grained soils such as clays and silts.

The design of filters in Japan is based on the criteria used throughout the world (JANCOLD, 1971, MOC, 1985) including the following rule; Filters should not contain more than about 5% of fines passing a #200 (0.074mm) sieve, and the fines should be cohesion-less. However, preparation of filter materials meeting this regulation is getting more costly in Japan, while no systematic research on identification of filter cohesion has been made.

With this background, Sand Castle test (SC test) (Vaughan, 1978, Vaughan and Soares, 1982) is examined if it will be used as a method for identifying cohesions of filter materials. In addition, possibility of relaxing the fine content regulation is discussed based on the quantitative relation between fine content and the cohesion, and other physical properties, such as permeability and plasticity.

4.3.2. Sand Castle Test (SC Test)

Type of tests:

The idea of the SC test proposed by Vaughan is illustrated in **Figure 4.9**. A filter material compacted in a mold is submerged in water, and the mold is quietly pulled up. When the collapsed filter material shows an angle larger than its angle of repose (AOR), it is identified to be cohesive. However, no detail for evaluating test results has been established based on thorough scientific discussions. For this, the following three AOR tests are carried out.

Test A = AOR test in air,
Test B = AOR test in water,
Test C = AOR test under submerged condition.

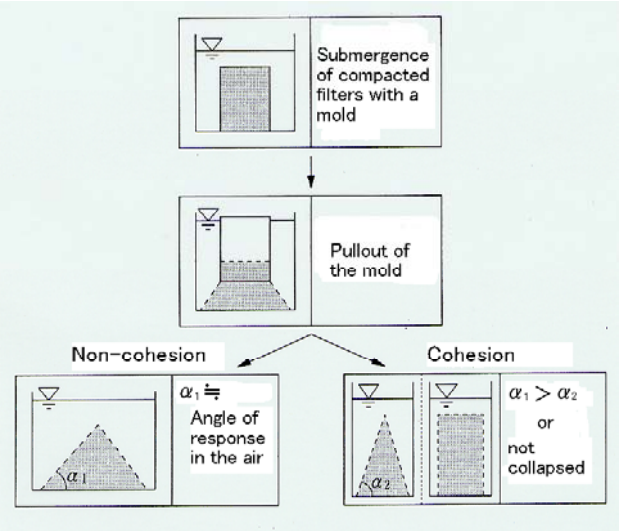

Figure 4.9. Procedure of SC test proposed by Vaughan

Test A:

From a funnel or a hand scoop at a particular height, an air-dried material was fallen to form a stable cone. Cone's height H and the diameter D of its basal plane are measured. Diameters were measured in four different directions, and their average was taken as D. AOR θ is then calculated from D and H as:

$$\theta = \arctan(2H / D) \tag{4.1}$$

The mean value of the three tests for the same material is reported as an AOR in air, after confirming that there is no serious difference among three results.

Test B:

An air-dried material was slowly fallen into a water tank from a funnel or a hand scoop put slightly above the water surface. Excluding this, the procedure is the same as in Test A. Though this procedure is totally different from that proposed by Vaughan, it is carried out for discussing Vaughan's method in detail.

Test C:

A specimen was prepared by compacting a test material in a mold of 150mm inner diameter and 175mm high. This material packed in the mold was then submerged in a water tank quietly, and the mold was slowly pulled up for observation of the course of collapsing events. After the heap was brought in its stable shape, height of the heap H and diameter of the basal plane D were measured, and the AOR is calculated by Equation (4.1) for this case. The method for compacting a test material for Test C follows.

(1) ***Compaction method A for materials without fines***

The compaction of a material without fines was performed in conformity to the JIS Standards of maximum density test (JIS-A-1224). The material was put layer by layer at a regular 15 mm interval in a mold of 150mm inner diameter and 175mm height. After each layer was finished, it was compacted with 100 blows of a mallet (stroke plane diameter = 35mm, mass = 162.6g) dropped alongside the inner wall of the mold. The total number of blows thus became 1000.

(2) ***Compaction method B for materials with fines***

The compaction for a material with fines was performed in conformity to the JIS Standards of soil compaction test using rammer (JIS-A-1210). The material with the optimum water content was

compacted in a mold of 150mm inner diameter and 175mm high with the energy of 1Ec in order to realize the maximum dry density. This specimen hardly collapses. In short, a test of this material yields the safest (the most cohesive) estimation.

4.3.3. Materials and Conditions of Test

Grain size gradations of the examined materials are shown in **Figure 4.10**. **Figure 4.10(a)** shows uniform filter materials (uniformity coefficient Uc = 1.2-2.4) without fines (clays or silts) which were used in case 1. **Figure 4.10(b)** shows well-graded filter materials (Uc = 3.4-30) used in case 2. Gradations ⑦-1, ⑦-2, ⑦-3 and ⑦-4 have fines of 0, 5, 10 and 20% by weight respectively. Maximum grain size of the filter materials is set at 38.1mm or less to minimize the size effect of the mold's inner diameter (= 150 mm). Both rounded and angular gravels are prepared to examine the effect of the particle shape on test results. In addition, filter materials used for an existing embankment dam (mixtures of phyllites and limestones) are also prepared. Here, rounded gravel, angular gravel and filter material for an existing dam are respectively called material A, material B and material C. Toyoura sands and glass beads are also used as uniform filters. Furthermore, fines with a size of 0.074mm or less, were added to materials B and C in Case 2.

Physical properties of the added fines are summarized in **Table 4.3**. **Table 4.4** shows physical test results for filter materials. The results of the compaction tests for filters without fines are summarized in **Table 4.5**. In addition, the results of compaction and permeability tests for filters with fines are shown in **Table 4.6** and **Figure 4.11**. Although material B and material C with gradation ⑦-1, do not contain fines, two kinds of compaction methods mentioned above are made for them. However, for material B, the optimum water content and the maximum dry density could not be identified clearly from the result of compaction test B. Then, in Test C, material B with gradation ⑦-1 was compacted by compaction method A. But two compaction methods were used to prepare the specimen of the material C with gradation ⑦-1 for Test C.

Cases and results of the SC tests are summarized in **Table 4.7**.

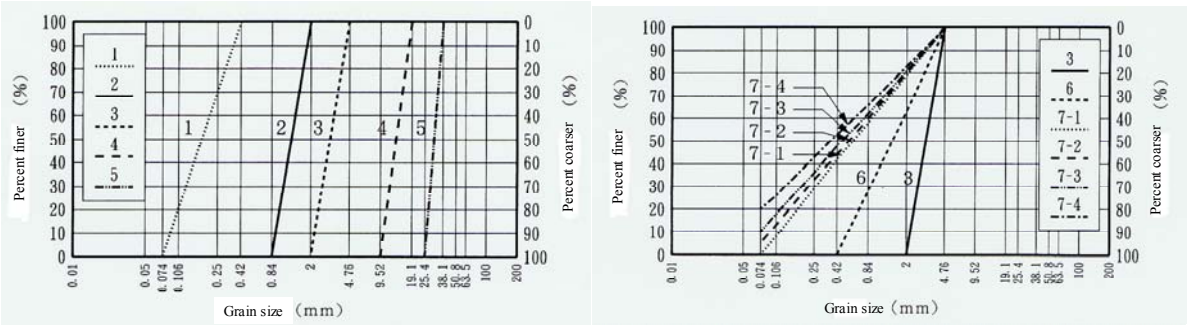

(a) Uniform filters for Case 1 **(b)** Broadly graded filters for Case 1

Figure 4.10. Gradations of filters used in program

Table 4.3. Physical properties of added fines

Fines added to	Material B	Material C
Specific gravity Gs	2.725	2.754
Liquid limit w_L (%)	42.4	52.4
Plastic limit w_P (%)	20.1	30.5
Plasticity index I_P	22.3	21.9

Table 4.4. Physical properties of filter materials

Filters	Gradation #	Gs	Gb	Q(%)	w_L(%)	w_P(%)	I_P
Toyoura sands	①	2.645	—	—	—	—	—
Glass beads	②	2.510	—	—	—	—	—
	④	—	2.507	—	—	—	—
Material A	②	2.647	—	—	—	—	—
	③	2.659	—	—	—	—	—
	④	—	2.596	0.895	—	—	—
	⑤	—	2.599	0.908	—	—	—
Material B	②	2.709	—	—	—	—	—
	③	2.717	—	—	—	—	—
	④	—	2.649	1.030	—	—	—
	⑤	—	2.689	0.584	—	—	—
	⑥	2.700	—	—	—	—	—
	⑦−1	2.709	—	—	NP	NP	NP
	⑦−2	2.709	—	—	NP	NP	NP
	⑦−3	2.711	—	—	16.0	13.2	2.8
	⑦−4	2.712	—	—	20.9	12.8	8.1
Material C	①	2.750	—	—	—	—	—
	②	2.699	—	—	—	—	—
	③	2.714	—	—	—	—	—
	④	—	2.634	1.370	—	—	—
	⑤	—	2.651	0.890	—	—	—
	⑥	2.716	—	—	—	—	—
	⑦−1	2.730	—	—	NP	NP	NP
	⑦−2	2.730	—	—	NP	NP	NP
	⑦−3	2.729	—	—	18.9	15.7	3.2
	⑦−4	2.728	—	—	26.6	18.8	7.8

Gs = Specific gravity of soil particle, Gb = Specific gravity of gravel, Q = Water absorption, w_L = Liquid limit, w_P = Plastic limit, I_P = Plasticity index, NP = Non plastic.

Table 4.5. Results of compaction test for filters without fines

Filters	Gradation #	ρ_d(g/cm^3)	Gs/Gb	e
Toyoura sands	①	1.625	2.645	0.628
Glass beads	②	1.633	2.510	0.537
	④	1.483	2.507	0.690
Material A	②	1.654	2.647	0.600
	③	1.761	2.659	0.510
	④	1.688	2.596	0.538
	⑤	1.664	2.599	0.562
Material B	②	1.541	2.708	0.757
	③	1.562	2.717	0.739
	④	1.559	2.649	0.699
	⑤	1.504	2.689	0.788
	⑥	1.758	2.700	0.536
	⑦−1	1.894	2.709	0.430
Material C	①	1.442	2.750	0.907
	②	1.521	2.699	0.774
	③	1.531	2.714	0.773
	④	1.536	2.634	0.715
	⑤	1.509	2.651	0.757
	⑥	1.680	2.716	0.617
	⑦−1	1.883	2.730	0.450

ρ_d = Dry density, e = Void ratio.

Table 4.6. Results of compaction and permeability tests for filters with fines

Filters	Gradation #	Fine content(%) Before compaction	Fine content(%) After compaction	w_{opt}(%)	ρ_{dmax}(g/cm^3)	k_{opt}(cm/s)	k_{min}(cm/s)	w_{kmin}(%)
Material B	⑦−1	0.0	3.5(+3.5)	−	−	5.1×10^{-3}*	5.1×10^{-3}*	−
	⑦−2	5.0	8.5(+3.5)	9.6	1.946	9.2×10^{-5}	2.6×10^{-5}	11.5
	⑦−3	10.0	13.4(+3.4)	8.5	2.024	1.7×10^{-5}	1.4×10^{-6}	10.8
	⑦−4	20.0	21.5(+1.5)	9.6	2.092	1.0×10^{-6}	1.6×10^{-7}	11.6
Material C	⑦−1	0.0	9.3(+9.3)	8.5	1.917	5.7×10^{-3}	5.6×10^{-3}	8.0
	⑦−2	5.0	14.2(+9.2)	9.4	1.934	6.0×10^{-4}	2.4×10^{-4}	11.6
	⑦−3	10.0	18.2(+8.2)	9.4	1.960	5.4×10^{-5}	2.9×10^{-5}	10.7
	⑦−4	20.0	27.9(+7.9)	10.5	2.006	2.7×10^{-6}	9.0×10^{-7}	12.1

w_{opt} = Optimum water content, ρ_{dmax} = Maximum dry density,
k_{opt} = Coefficient of permeability at w_{opt},
k_{min} = Minimum coefficient of permeability,
w_{kmin} = Water content at kmin, *) = Mean value.

Table 4.7. Cases and results of SC tests

Filters	Gradation #	Test A water content	Test A AOR(°)	Test B water content	Test B AOR(°)	Test C water content	Test C AOR(°)	A−C(°)
Toyoura sands	①	Air-dried	32.3	Air-dried	30.5	Air-dried	27.6	4.7
Glass beads	②	Air-dried	20.5	Air-dried	21.8	Air-dried	18.3	2.2
	④	Air-dried	18.6	−	−	Air-dried	17.2	1.4
Material A	②	Air-dried	34.3	Air-dried	33.9	Air-dried	29.2	5.1
	③	Air-dried	32.4	−	−	Air-dried	30.6	1.8
	④	Air-dried	34.9	−	−	Air-dried	32.9	2.0
	⑤	Air-dried	34.9	−	−	Air-dried	32.5	2.4
Material B	②	Air-dried	35.7	Air-dried	35.3	Air-dried	31.5	4.2
	③	Air-dried	37.2	−	−	Air-dried	33.8	3.4
	④	Air-dried	39.4	Air-dried	41.8	Air-dried	38.7	0.7
	⑤	Air-dried	39.5	−	−	Air-dried	41.3	−1.8
	⑥	Air-dried	34.6	−	−	Air-dried	31.8	2.8
	⑦−1	Air-dried	35.2	−	−	Air-dried	31.3	3.9
	⑦−2	Air-dried	36.5	Air-dried	31.5	W_{opt}	33.4	3.1
	⑦−3	Air-dried	38.1	−	−	W_{opt}	41.7	−3.6
	⑦−4	Air-dried	39.8	−	−	W_{opt}	43.9	−4.1
Material C	①	Air-dried	33.6	Air-dried	23.6	Air-dried	27.2	6.4
	②	Air-dried	35.0	Air-dried	35.8	Air-dried	32.4	2.6
	③	Air-dried	34.2	−	−	Air-dried	31.1	3.1
	④	Air-dried	36.7	Air-dried	38.8	Air-dried	34.5	2.2
	⑤	Air-dried	38.5	−	−	Air-dried	33.2	5.3
	⑥	Air-dried	34.2	−	−	Air-dried	31.1	3.1
	⑦−1	Air-dried	35.8	−	−	Air-dried	34.6	1.2
						W_{opt}	32.7	3.1
	⑦−2	Air-dried	37.1	Air-dried	30.9	W_{opt}	38.5	−1.4
	⑦−3	Air-dried	36.2	−	−	W_{opt}	42.2	−6.0
	⑦−4	Air-dried	35.8	−	−	W_{opt}	45.6	−9.8

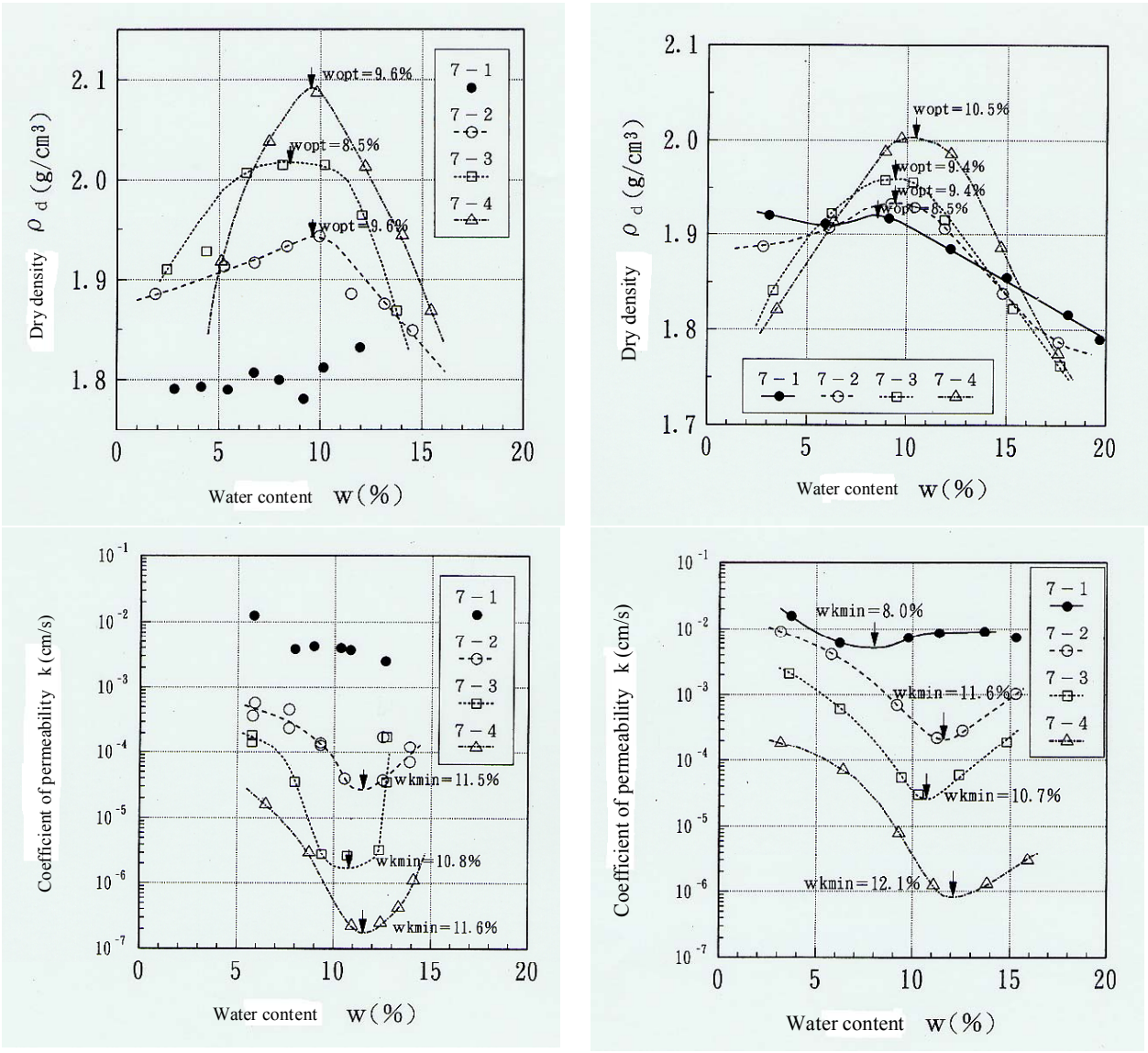

(a) Material B (b) Material C

Figure 4.11. Results of compaction and permeability tests

4.3.4. Test Results

Results of Test A:

Figure 4.12 shows the AOR in air obtained from case 1 for uniform filters without fines. With exception of glass beads with only two data points, the AOR in air increases with the maximum grain size D_{max}. This tendency is stronger for angular gravels (materials B and C) than for rounded gravels (material A). The AOR in air test helps in understanding the effect of the surface roughness of grains on the angle of repose.

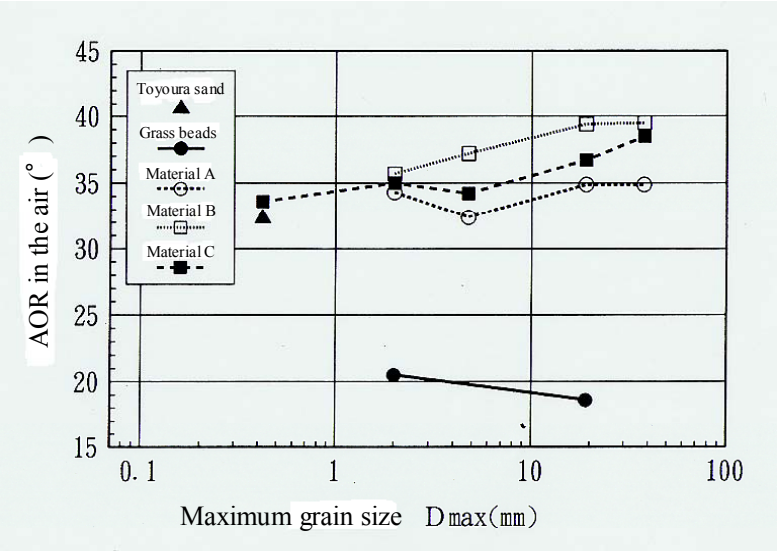

Figure 4.12. Angle of response in air of Case 1

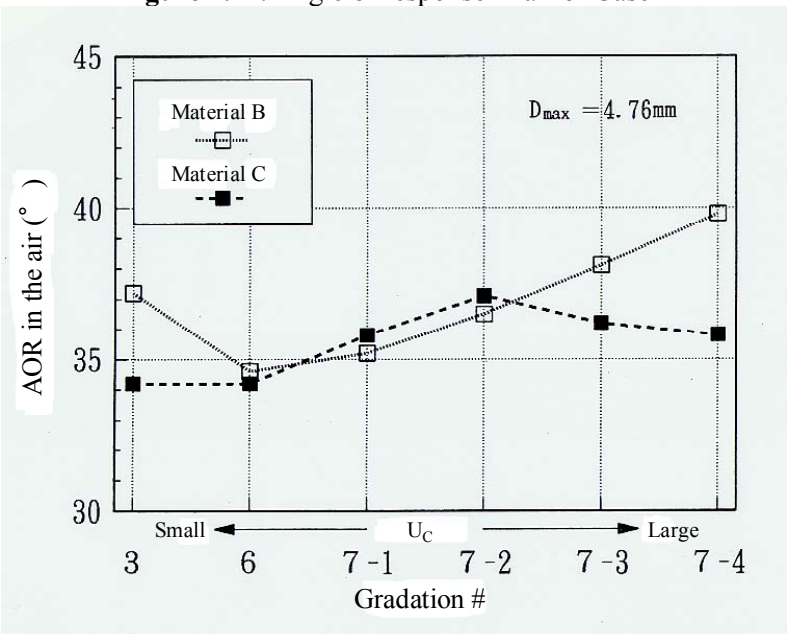

Figure 4.13. Angle of response in air in case 2

Next, the AOR in air obtained from case 2 is illustrated in **Figure 4.13**. The AOR in air of material B without fines (gradations ③, ⑥, ⑦-1) decreases whit increasing uniformity coefficient, and increases with the increasing fines content. On the other hand, in the case of material C, the effect of fines content is not recognized in the comparison of gradations ⑦-1 to ⑦-4, but the AOR in air tends to increase with increasing uniformity coefficient the fines content is zero (gradations ③, ⑥, ⑦-1).

Results of Test B

Figure 4.14 compares the AOR in air (a) with the AOR in water (b). In the case of uniform filters, except for the material C with gradation ①, the AOR does not differ much and is distributed within b=a±2°. On the other hand, for the broadly graded materials B and C (⑦-2), the AORs in water become slightly smaller than in air because segregation of materials takes place when they fall in water.

According to the hydraulic filling effect, the dry density of a conical heap formed in Test B seems to be larger than that in Test A. Actually this magnitude correlation could be confirmed by calculating the dry density with the weight of materials and the volume of conical mountain.

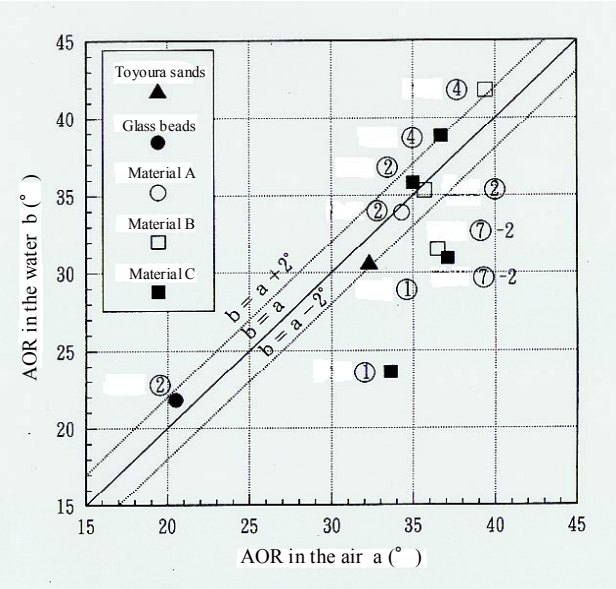

Figure 4.14. Comparison of AOR in air and AOR in water

When the density of a gravelly material becomes larger, its AOR increases reflecting the increase of its strength. However, the strength of a water-saturated gravelly material is generally smaller than the air-dried material. Consequently one cancels the other, and the difference between the AORs in air and in water becomes less significant.

AS for the case of uniform filters without fines, which are clearly cohesion-less, there is seemingly insignificant difference among AORs in water, in Test C (see the next section) and in air. In conclusion, cohesion-less materials can be identified by either the AORs in air or AORs for submerged materials in Vaughan ‘s SC tests.

Results of Test C and identification of non-cohesion:

Figure 4.15 shows the difference between AORs of uniform filters (Case 1) in air and under submerged condition for different maximum grain sizes. Differing from the other materials A and C, AOR difference for material B decreases as the maximum grain size increases, and becomes negative when the maximum rain size of 40 mm is reached. This implies that material B can exhibit smaller AOR in Vaughan’s method than in air, though Vaughan’s method itself categorizes material B as a cohesive one. This may be caused by an error in the measurement of the shape of a conical heap made up of large angular grains. Following the Vaughan’s definition, a cohesion-less material should have the same AOR values in air and under submerged condition. However, density, strength and stress state are not completely identical with each other between two different testing conditions. As the consequence, two AORs do not exactly agree even in the test for cohesion-less materials, and the overall AOR differences (referred to as differential value hereafter) lie approximately between 0 and 6° for the cohesion-less materials examined in Case 1.

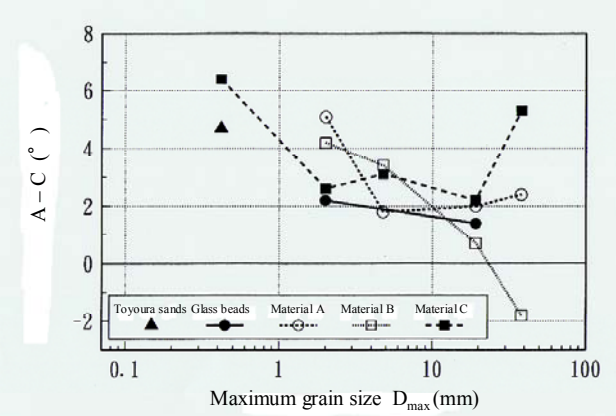

A=AOR in the air, C=AOR under submerged condition.

Figure 4.15. Difference between AOR in air and submerged AOR in case 1.

Figure 4.16 describes AOR differences for Case 2 in terms of uniformity. **Table 4.5** shows that two different compaction methods cause little difference in AORs for material C with gradation ⑦-1. However material C with gradation ⑦-1 was prepared by using compaction method B considering that an optimum water content could be clearly defined. In Test C, materials with gradation ⑦-2 or coarser started collapsing immediately after submerging, while materials with gradations ⑦-3 and ⑦-4 did not start to collapse quickly or did not collapse completely. Judging from this observation, there seems to be a boundary of gradation between materials exhibiting cohesive and cohesion-less features. As for material B, those with positive differential values of AOR (+3 - +4° for gradations ⑦-1 and ⑦-2) may be identified to be cohesion-less, while those with negative values (-3 - -4° for gradations ⑦-3 and ⑦-4) are considered to be cohesive. In the material C, the boundary is not so clear as that in material B, but it seems to be between gradation ⑦-1 and gradation ⑦-2, since the difference has shifted from positive to negative at this point. This suggests that the differential values of AOR can be used as an important measure for describing cohesive and/or cohesion-less features of filter material.

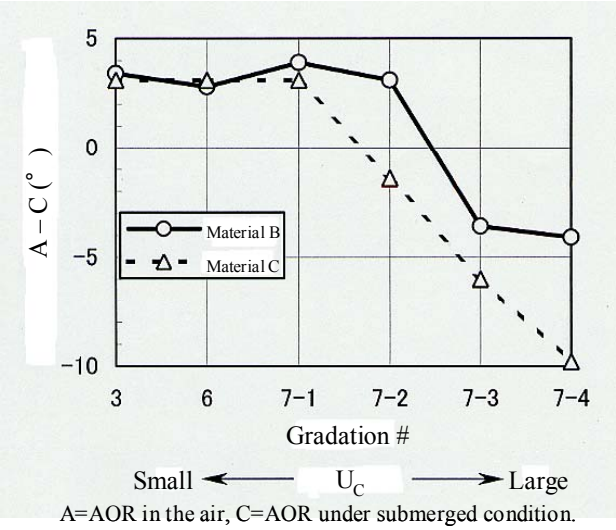

A=AOR in the air, C=AOR under submerged condition.

Figure 4.16. Difference between AOR in air and Submerged AOR of Case 2

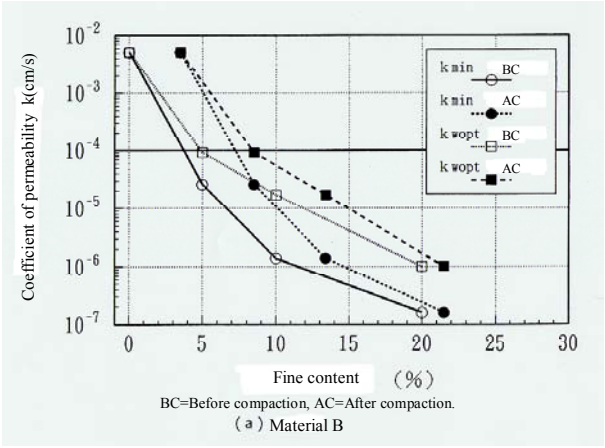

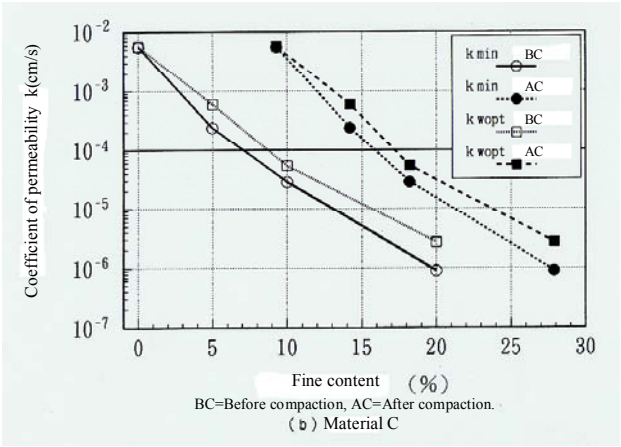

Figure 4.17. Fine content vs. coefficient of permeability

4.3.5. Discussion

A careful examination of the Sand Castle (SC) test method was carried out, and rational ways to evaluate its result have been discussed. Based on this discussion, the allowable maximum fine contents for filter materials are tentatively presented herein in terms of cohesion and permeability.

(1) *Relationship between plasticity index and cohesion*

The criterion of U. S. Department of Agriculture, Soil Conservation Service (SCS) (1986) regulates NP as the identifying condition of non-cohesion of filter materials. Based on the results of liquid and plastic limits tests shown in **Table 4.4**, materials B and C with gradations ⑦-1 and ⑦-2 are NP, while those with gradations ⑦-3 and ⑦-4 are not NP. Liquid and plastic limits tests were carried out for filters before compaction.

(2) *Relationship between fine content and permeability*

Fine contents of gradations ⑦-1, ⑦-2, ⑦-3 and ⑦-4 are respectively set at 0, 5, 10 and 20% before compaction. As shown in **Table 4.4**, after the compaction, fine contents of material B increased to 3.5, 8.5, 13.4 and 21.5%, and those of material C to 9.3, 14.2, 18.2 and 27.9%. It is found that material C, when compacted, is more liable to be crushed than material B.

Figure 4.17 shows the relationship between fine content and the minimum permeability coefficient k_{min}, and the permeability coefficient at the optimum water content k_{wopt}. In addition, when arranging these figures, fine contents both before and after the compaction, are used. It is proven that the permeability decreases, when fine content increases in all cases.

The permeability of filters is generally required to be over 1.0×10^{-4}cm/s in order for their drainage functions to be maintained. At present, a content of fines after the compaction should be used to evaluate the filter function, because the features of compacted materials control the function of the filter zone. From this viewpoint, the allowable maximum fine contents for materials B and C are estimated to be 7.2% and 15.8% respectively.

(3) *Total evaluation*
From the results of SC tests and physical property tests, the allowable maximum fines content to meet non-cohesion and permeability conditions for filters is investigated. The results of the investigation are summarized in **Table 4.8**.

Table 4.8. Allowable maximum fine content based on filter function

Identification item		Identification criterion	Allowable maximum fine content Before compaction After compaction	
			Material B	Material C
Non-cohesion	Plasticity Index	NP	5～10%≧ <u>8.5～13.5%≧</u>	5～10%≧ 14.2～18.2%≧
	SC test	(AOR in Test A)−(AOR in Test C)	5～10%≧ <u>8.5～13.5%≧</u>	0～5%≧ 9.3～14.2%≧
Permeability		$k \geqq 1 \times 10^{-4}$cm/s	3.7%≧ <u>7.2%≧</u>	7.0%≧ 15.8%≧

*) The smallest value in allowable maximum fine contents of each item is underlined.

In the case of material B, the allowable maximum fines content is not determined from the non-cohesion condition but from the permeability condition. The allowable maximum fine content after the compaction is found to be 7.2%. Meanwhile, the material C's allowable maximum fines content is determined from the results of the SC test, which is one of the non-cohesion conditions. The allowable maximum fine content after the compaction can be read to be 9.3-14.2%.

When the present Japanese filter criterion, in which filters should not contain more than about 5% of fines, is met, it is found that both the non-cohesion and permeability conditions for filters are satisfied. In addition, some filters are proven to meet the non-cohesion and permeability conditions, even if they contain 7-8% of fines. Therefore, when the present filter criterion on fine content is not met, it is recommended that several tests, such as liquid and plastic limit test, the SC test and permeability test, should be made to verify the non-cohesion and permeability conditions from the viewpoint of cost reduction in dam construction.

4.3.6. Summary

In this study, for the purpose of confirmation of the Sand Castle (SC) test procedure proposed by Vaughan, and an examination of the evaluating method of non-cohesion of filter materials, three kinds of angle of repose (AOR) tests were carried out using uniform filters without fines and broadly graded filters with fines. The following summarizes the findings.

(1) When maximum grain size of filters becomes larger, the AOR in air increases. The tendency is stronger in angular gravels than rounded gravels.
(2) In the case of the materials with the same maximum grain size, the AOR in air becomes larger, when the fine content increases to some extent.
(3) There is no large difference between the AOR in air and the AOR in water of the uniform filters without fines, which seem to be cohesion-less.
(4) The difference of the in air AOR and the submerged AOR obtained from the SC test seems to lie approximately between 0 and6° for cohesion-less materials. From the results of the SC tests for broadly graded filters as well as uniform filters, an identification criterion of the cohesion of filters based on the positive or negative difference in AOR is proposed. In addition, the attention to collapsing condition of compacted materials as well as the differential value is very important in

identifying the cohesion of filters.

An investigation on the method of the SC test and the evaluation of the test results has been carried out, and the allowable maximum fine content of filters is discussed from the viewpoint of non-cohesion and permeability. The following findings are obtained.

(5) Considering the results of the SC test, non-plastic filters can be identified to be cohesion-less. There is the possibility that plasticity index is able to become an index to identify the cohesion of filters.

(6) The function of filters should be examined based on the permeability condition as well as non-cohesion condition.

4.3.7. Acknowledments

This study was partially supported by Japan Society for the Promotion of Science as "Research Project 2000 Grant-in-Aid for Scientific Research (A) (No.12355020). I express thanks to Mr. Hiroyuki SATOH of Fill Dam Division, Public Works Research Institute, Ministry of Land, Infrastructure and Transportation for his great support during the preparation of this report.

References of SECTION 4.3

Japanese National Committee on Large Dams (JANCOLD) [1971] *Design Criteria for Dams*, 87-88.

Ministry of Construction (MOC), Japanese Government [1985] *Manual for River Works in Japan –Design of Dams-*, 128-129.

Shearad, J. L., Cluff, L. S. and Allen, C. R. [1974] "Potentially Active Faults in Dam Foundations," *Geotechnique*, 24(3), 367-428.

U. S. Department of Agriculture Soil Conservation Service (SCS) Engineering Division [1986] "Guide for Determining the Gradation of Sand and Gravel Filters," *Soil Mechanics Note*, No.1201-V1.

Vaughan, P. R. [1978] "Design of Filters for the Protection of Cracked Dam Cores Against Internal Erosion," *Preprint 3420 Presented to ASCE Convention*, Chicago.

Vaughan, P. R. and Soares, H. F. [1982] "Design of Filters for Clay Cores of Dams," *Journal of Geotechnical Engineering*, ASCE, 108(GT1).

Wakizaka, Y. [1999] "Investigations of Active Faults for Dam Construction –Present State at the Ministry of Construction-," *Proc. 31st Joint Meeting of U.S.-Japan Panel on Wind and Seismic Effects, UJNR*, 231-244.

Chapter 5

DISCUSSION FOR BETTER DESIGNS OF CIVIL-INFRASTRUCTURES

5.1. INTRODUCTION

One of the important aims of this JSPS project was to discuss the possible measures for minimizing losses of life and damage to a variety of structures, and it was timely that the Japan Society of Civil Engineers (JSCE) organized a technical committee for establishing remedial measures for damage to civil-infrastructures. It was thus a natural course of events that the JSPS research activity of this project incorporated individual works of many others, especially with respect to risk identification and analysis. During the course of this study, the following guide was discussed among the JSPS project members as a springboard for integrating individual works.

5.2. POSSIBLE REMEDIAL MEASURES

5.2.1. Project defined

"Project" used hereafter means any of the followings:

(1) Structures for human occupancy
(2) Lifelines for human transportation
(3) Important civil-infrastructures such as dams etc.

They determine ***stakeholders***. The stakeholders are colleague researchers, and senior management and practitioners in key enterprises. They also include cities and counties responsible for requiring seismic-retrofitting, permitting constructing buildings for human occupancy etc.

5.2.2 ZONING

Since few structures can hold in a fault rupturing, discussions of zoning are inevitable. In some less populated regions, limiting development within known and active fault zones will be very effective, and in California, USA, a law to this effect has been enacted since the early 1970s. This law, "Alquist-Priolo Fault Zoning act" (California Geological Survey, 2002), requires the State Geologists to establish regulatory zones (Earthquake Fault Zones) around the surface traces of active faults. Before a project is permitted, a geological investigation is required, and the construction of a building is permitted only if the building is located more than 50 feet off a fault trace. The law requires Prefecture Geologists to establish regulatory zones called "Earthquake Fault Zones" around the surface traces of active faults and to issue appropriate maps. The zones vary in width, but average about 300 m wide with a strike-slip fault trace put in its middle. A similar zoning act has been enacted in Auckland, New Zealand (Wellington Regional Council, 2002) too.

It is, however, noted that the laws in California and New Zealand deal with strike-slip faults, while about two thirds of active faults in Japan are thrust faults. As contrasted with strike-slip faults, a bundle of thrust faults make up a "wider brush" with many fault traces hidden in areas off the most suspicious line recognized from surface configurations. In addition, these areas are often densely populated in overpopulated countries such as Taiwan and Japan. **Figures 5.1** and **5.2** show

respectively the location of a newly found Morimoto fault trace and a photo of a trench excavated across it. The fault was found about 100 m off the recognized old fault trace along the mountainside. A base mud rock is cutting sharply into an overlying soft soil deposit, while the soil deposit is gently bent by the base rock. There was no evidence on the ground surface indicating the presence of this hidden fault. It is noted here that the right-hand side of the base rock (hanging wall) that had penetrated about 1m up into the surface soil deposit was not on the mountain side but on the flat land side. Assuming that a soil wedge was pushed up and we were looking at just one side of the wedge, this fact suggests the presence of another new fault hidden further away from the mountains, and actually, this new fault was found in 2001 about 500m off the mountains (Nakata and Imaizumi, 2002). This indicates that the width of 300m for the Fault Hazard Zone may not be wide enough. The hidden fault, however, will not reach the ground surface through a thick soil deposit. Taking this advantage, some restrictions may be eased.

From these mentioned above, a thrust fault zone, along a boundary between mountains and a flat land, may be determined in such a way that **"the zone shall cover about several hundreds meters wide the flat land with the fault trace put aside along the zone's edge"**.

This does not necessarily mean the exterior area on the mountains side is safer than that on the flatland side. As for intense shakes are concerned, it is quite often that the shake is very intense on the hanging wall side. It is also to be noted that soft soil deposits are often responsible for amplifying base input motions. "Earthquake Fault Zones" are just for accounting for considerable deformations of soils.

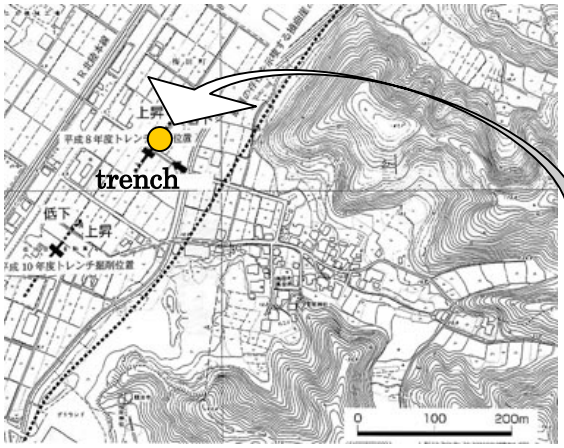

Figure 5.1. Location of a fault trace found 100 m off the older fault along mountains

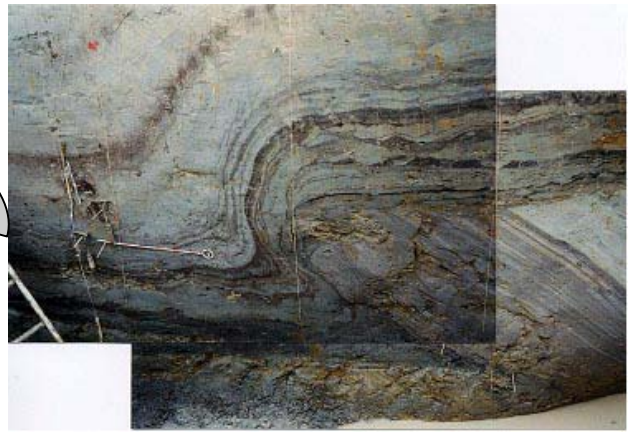

Figure 5.2 Trench wall of Morimoto fault (Photo by Sangawa)

5.2.3. Soil Strain Parameter Determining Restriction Level

As a distinct base rock rupture propagates up through overlying soil material, strains will spread and decrease. The overall strain induced within the surface soil deposit will be represented by D/H where D= dislocation of the base rock and H = thickness of the soil deposit. If the material is brittle, the distance that the base rock rupture propagates will be large, while in a soft overlying material strains will be absorbed. Thus, comparing D/H with the soil's failure strain γ_y will provide necessary information for possible remedial measures for fault-inflicted damage to civil infrastructures. Bray (1994) found through both his numerical and experimental studies that at a specified amount of bed rock fault displacement, the height that the shear rupture will propagate up into the overlying soil can be related to the failure strain of the soil as shown in **Figure 5.3**. The curve in **Fig. 5.3** seemingly exhibits some hyperbolic feature, and the product of the normalized height H/D by the soil's failure strain γ_y is about 100%. This means that the shear rupture reaches the overlying ground

surface when $\zeta(=D/\gamma_y H)$=1.0.

The parameter $\zeta = D/\gamma_y H$ thus can determine the restriction levels for projects in a fault zone.

As for important civil infrastructures, numerical simulations are necessary to ensure that the restrictions and/or measures taken will be effective.

A possible D value may be determined from either:

(1) the maximum credible dislocation observed at nearby trenches, outcrops etc., or
(2) the possible maximum dislocation of an asperity that has ever been estimated for an event in the concerned fault system.

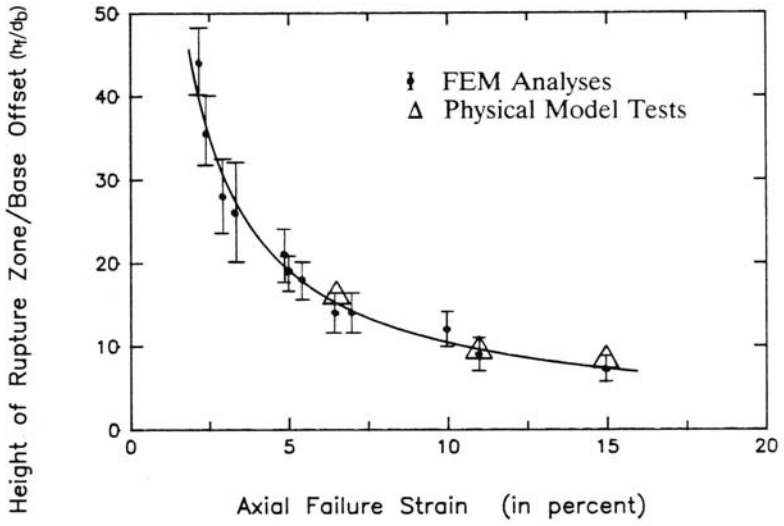

Figure 5.3 Normalized height of shear rupture zone in soil overlying base rock fault as a function of soil's failure strain (after Bray et al. [8])

5.2.4. **Active length of a flexural underground structure**

An embedded foundation is often very flexible, and follows closely the motion of the surrounding soil, which is deformed due to a distinct base rock rupture. In practice, most piles are indeed 'flexible' in the sense that they are not deformed over their entire lengths when loaded at their caps. Instead, pile deflections become negligible below an active length (or effective length) L (**Figure 5.4**). The active length, an important parameter in the design of a pile foundation, depends largely on the ratio of the pile stiffness EI (= number of piles grouped together × EI for a single pile) for flexural deformation and the soil stiffness G, and is proportional to:

$$L_0 = \sqrt[4]{EI/G}$$

Assuming that the pile cap displacement is proportional to $H\zeta$ ($\zeta = D/\gamma_y H$), the overall strain within the pile will be represented by $H\zeta/L_0$ (=ξ hereafter). Details of countermeasures will be determined depending upon ξ, and it will be useful to summarize a nomograph describing pile cap displacements and rotations in terms of $H\zeta$ and ξ.

For tunnels, $H\zeta$ in ξ may be replaced with the fault rupture displacement D_z at the point where the tunnel meets the fault plane (**Figure 5.5**).

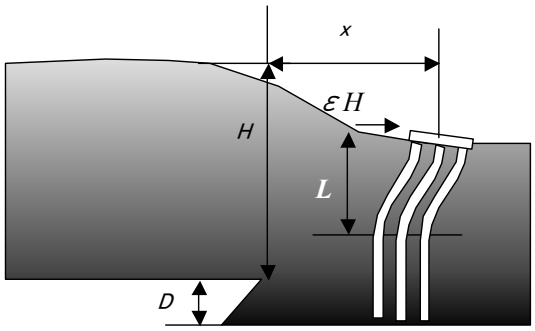

Figure 5.4 Piles deformed in the overlying soil deposit

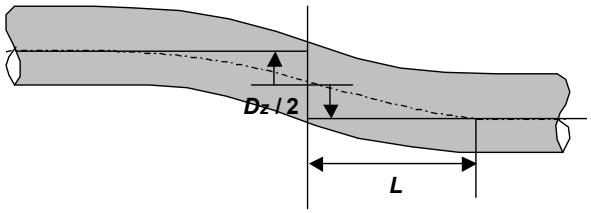

Figure 5.5 Tunnel experiencing fault dislocation

Table 5.1. Possible Restrictions

Restriction Level	ζ	Project in **(1)** (Dwellings etc.)	Project in **(2)** (Railways, Roads etc.)
1	$1>\zeta$	A structure **can** be placed over a suspicious trace of fault **only if** it has a stiff mat foundation with no or little embedment depth.	**Tunnels:** A tunnel can be constructed across a fault only if expected ξ value is staying below the critical value for the structure. Parameter ξ describes the representative strain induced within a tunnel (See **Section 4.2**).
2	$x>\zeta>1$	If an active fault is found, a structure for human occupancy cannot be placed over the trace of the fault and must be set back by $\alpha \times \zeta \times H$ from the fault. Parameter α differs in different types of faults (Normal, Reverse, Strike-slip).	In principle, it is desirable not to construct a tunnel across a fault. But if unavoidable, necessary measures for keeping its cross-section open as it was must be taken. In this case also ξ determines the details of the measures.
3	$\zeta>x$	Ditto.	Avoid construction

With the above-mentioned parameters ζ and ξ, a possible scenario of remedial measures for Project (1) and (2) may be summarized as seen in **Table 5.1**. The table was intended to be a springboard for a thorough discussion, threshold values for the parameters ζ and ξ need to be discussed examining a number of cases using the tools provided in **Chapter 3**. However, the table offers a proper perspective on the possible countermeasures, which follow below.

Possible Countermeasures for Project (1):

In principle, avoid construction of structures over a fault trace. If an active fault is found, a structure for human occupancy must be set back by $\alpha \times \zeta \times H$ from the fault. But if unavoidable, it is allowed to do it only when parameter ζ is less than 1.0 and the structure has a stiff mat foundation with no or little embedment depth so that a fault rupture can be diverted around or go beneath the foundation.

***Possible Countermeasures for Project (2) (Tunnels, piles etc.)*:**
Parameter ξ is directly related to strain induced within an underground structure or a foundation. Therefore, it is desirable not to construct any tunnel across a fault when ξ is larger than a particular value for the tunnel. But if unavoidable, necessary measures must be taken to keep its cross-section adequately open. In this case also ξ determines the details of the measures. If ξ value stays below the critical value for the structure, the construction of this structure can be allowed. But if the structure is a foundation supporting a superstructure like a bridge pier, special attention should be paid to displacements at the top of the foundation. The displacements will be amplified at the top end of the bridge pier, which amplification may cause the bridge to fall.

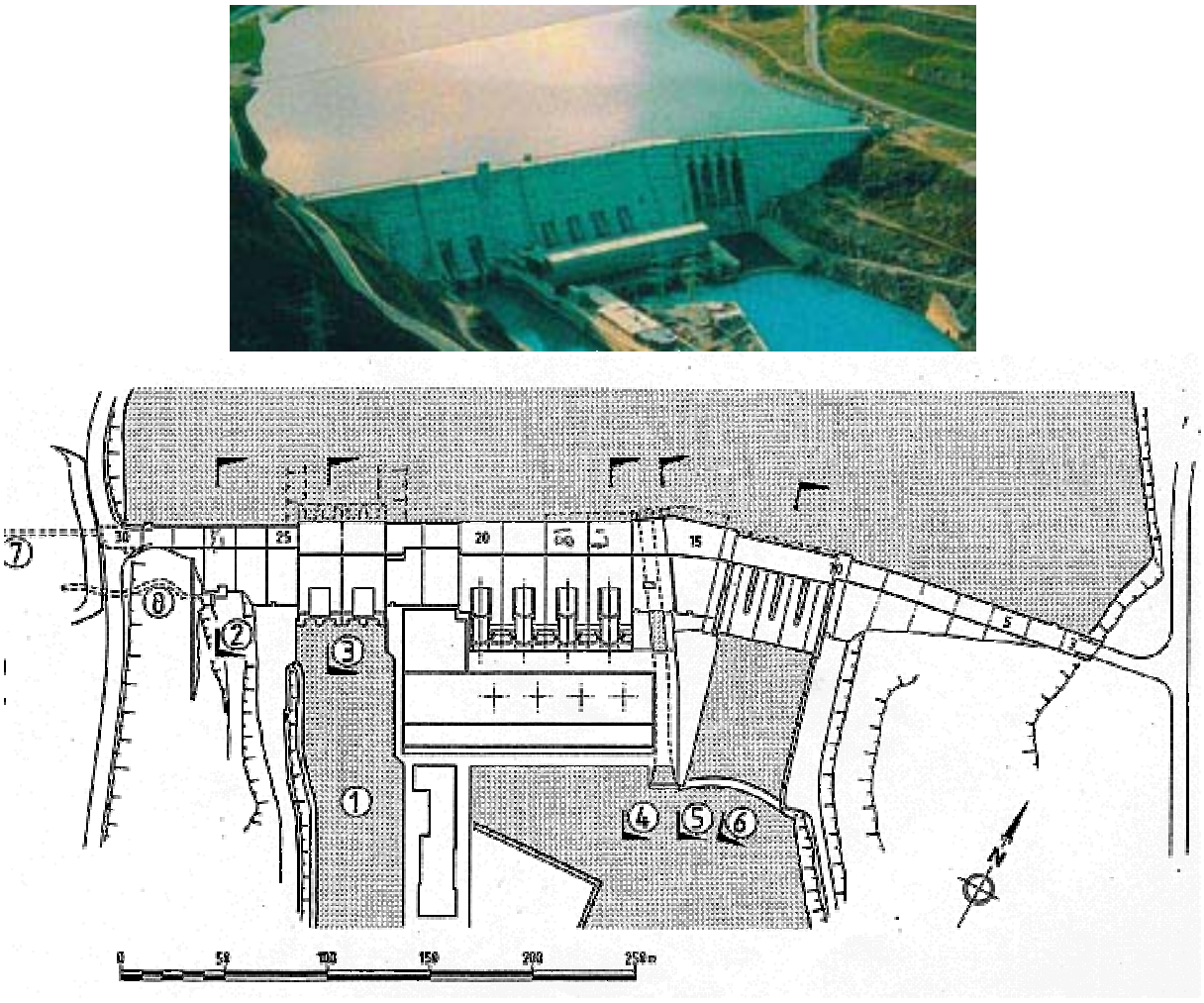

Figure 5.6. Clyde dam with a slip Joint against Fault Movement in New Zealand

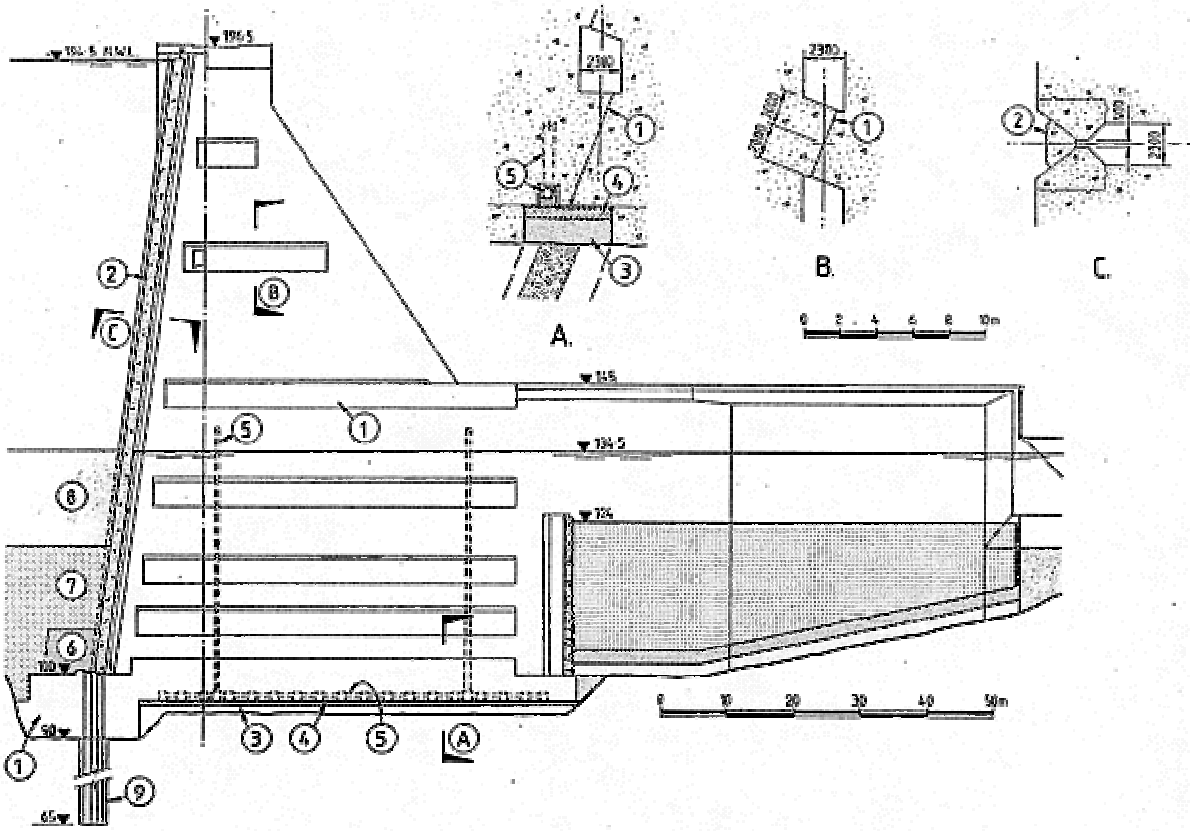

1. Contact surfaces
2. Wedge plug
3. Filter zone
4. Drainage zone
5. Drainage pipe
6. Riprap
7. Gravel blanket
8. Low permeability blanket
9. Cutoff shaft

Figure 5.7. River Channel Fault joint

5.2.5. **Possible Remedial Measures for Project (3), Example of Clyde Dam, New Zealand**

As for such important civil-infrastructures as dams, individual remedial measures should be taken to meet individual situations. Construction of a concrete dam over or near an active fault is in general not advisable because of its brittle features (see Section 2.3). However, an example from New Zealand, Clyde dam (**Figure 5.6**) constructed across the River Channel Fault, will give a hint for possible remedial measures. The following description was taken from (Hatton, J.W. et al, 1987, 1994).

The presence of the River Channel Fault was known before the construction of the dam, and the original geological opinion was that it and the other faults did not appear active because of its strike being near 90 degrees with respect to the nearby Cairnmuir and Dustan Faults, and the lack of displacement terrace. However, the geological investigation program, which has continued into the construction period, indicated that a major rupture of the Dustan Fault (Ms 7.0-7.5) could induce up to 200mm of sympathetic movement of the River Channel Fault.

The major change required to the dam layout was to relocate its sluice intake as far as possible to the right to accommodate the joint along the fault strike. The slip joint, as shown in **Figure 5.7**, can accommodate a 2 m displacement of the fault in a strike slip sense, and 1 m in a dip slip sense, either normal or reverse movement. To accommodate a strike-slip displacement, the joint cuts the dam body into two blocks along the fault strike (see **Figure 5.6**). To provide mutual support for the dam blocks, contact surfaces have been provided at eight different levels within the open vertical joint, and the contact surfaces are parallel to the fault plane to accommodate a dip-slip displacement. The open joint has been kept water tight under usual loading conditions by a wedge plug that extents up the full

height of the dam. In the event of rupturing of the River Channel Fault, the wedge plug will move to limit flow through the joint.

5.3. SUMMARY

Surface fault rupture has been more strongly recognized as a principal earthquake hazard since the dramatic Kocaeli (Turkey), Chi-Chi (Taiwan) and Dutze (Turkey) earthquakes of 1999. Damage to bridges, dams and tunnels in these earthquakes motivated the enactment of a fault-zoning act in Taiwan. In some less populated regions, limiting development within known and active fault zones will be very effective. This limitation, however, may be very difficult in overpopulated areas. In Japan, at least 2000 faults inland are known to be active, and some cities of large populations exceeding a million are found just on thick fault traces. They include Kyoto of 1.5 millions population above Hanaori fault, a historical city with a large number of temples and shrines, Osaka with 2.6 millions population above Uemachi fault, Nagoya, 2.2 million, with Tenpaku fault and Kobe spreading over a bundle of faults. Zoning thus necessarily requires extensive discussions with clear scientific evidences provided so that a social consensus is reached. In this discussion, it is noted that soil strain is not always localized on a particular fault rupture plane, but can be distributed within a certain band along the fault. It is noted that the most faults dealt with fault hazard mapping acts in both California and New Zealand are strike-slip faults, while about two thirds of active faults in Japan are thrust faults. As contrasted with strike-slip faults, a bundle of thrust faults make up a "wider brush" with many fault traces hidden in areas off the most suspicious line recognized from the surface configuration.

The JSPS project members have been investigating the previous examples of faulting and fault-related damages, and is archiving them as a digital data set. This chapter was summarized to introduce discussions among the project members for better design of civil-infrastructures. The overall strain induced within a surface soil deposit overlying a stiff base rock can be represented by D/H where D= dislocation of the base rock and H = thickness of the soil deposit. If the material is brittle, the distance that the base rock rupture propagates will be large, while in a soft overlying material strains will be absorbed. Thus, the parameter $\zeta = D/\gamma_y H$ will determine the restriction level in an established Fault Zone. Active length, $L_0 = \sqrt[4]{EI/G}$, is also an important parameter. For a flexible structure embedded or buried in soil, L_0 is short. When L_0 is compared with a possible fault dislocation D, it provides an idea of possible strain induced within this structure.

However, the assumed scheme for now is just for integrating works of many individual researchers. Many problems are to be solved for more practical details. Along faults, for example, alluvial soil deposits including large boulders are often found (see SECTION 4.2). To see how these large inclusions in a soil matrix affect the soil's overall behavior, an extensive study will be necessary, and is to be addressed in a later publication.

REFERENCES

Anders, M. and Hori, M. (2001). "Three-dimensional stochastic finite element method for elasto-plastic body," *Int. J. Numer. Meth. Engng*., **51**, 449-478.

Bray, J.D., Seed, R.B. and Seed, H.B. (1994). "Analysis of earthquake fault rupture propagation through cohesive soil," *Journal of Geotechnical Engineering*, ASCE, **120(3)**, 562-580.

California Geological Survey (2002). "Alquist Priolo Earthquake Fault Zones," California Department of Conservation, http://www.consrv.ca.gov/cgs/rghm/ap/index.htm.

Hatton, J.W., Black J.C. and Foster, P.F. (1987). "New Zealand's Clyde Power Station," *Water Power and Dam Construction*, 15-20.

Hatton, J.W., Foster, P.F. and Thomson, R. (1991). "The influence of foundation conditions on the design of Clyde Dam, *Commission Internationale*," Q.66, R.10, 157-179.

Headquarters for earthquake research promotion (2002): http://www.jishin.go.jp/main/index-e.html.
Konagai, K., Mikami, A., Katagiri, T., Ahsan, R. and Maruyama, D. (1999). "Report of damage caused by the Mid-North Iwate Earthquake of September 3, 1998," *Bull., Earthquake Resistant Structure Research Center*, IIS, University of Tokyo, **32**, 3-13.
Konagai, K. and Johansson, J. (2001). "Two dimensional Lagrangian Particle Finite Difference Method for modeling large soil deformations," *Structural Eng./ Earthquake Eng.* **18(2)**, 91s-95s.
Ramancharla, P.K. and Meguro, K (2001): "Applied element simulation of non-linear behavior of dip-slip faults for studying ground surface deformation," *Proceedings of A Workshop on Seismic Fault-induced Failures*, JSPS, 109-114.
Wellington Regional Council (2002). "Hazard management," http://www.wrc.govt.nz/em/hazrep.htm.

APPENDIX I: *"NL-SSFEM"*

Non-Linear Spectral Stochastic Finite Element Method (NL-SSFEM) has been developed by Hori for simulating unconsolidated surface layers, which are soft such that fault rupture can be dissipated within them. In Japan, more than 2000 faults are known to be active, and are classified into the following two categories:

(1) 1st category active faults that have been activated in the past 10,000 years, and have caused some damage to existing structures and/or responsible for earthquake occurrences,

(2) 2nd category active faults that have been known activated in the past 10,000 years, and have deformed diluvial terraces.

Among the 1st category active faults, those having high average slipping rates λ larger than 1m/1000 years are referred to as "Class A" faults, and those with 1m/1000 years $> \lambda >$ 0.1m/1000 years and 0.1m/1000 years $> \lambda$ are "Class B" and "Class C" faults, respectively. The target faults for NL-SSFEM will include "Class A" faults with

.

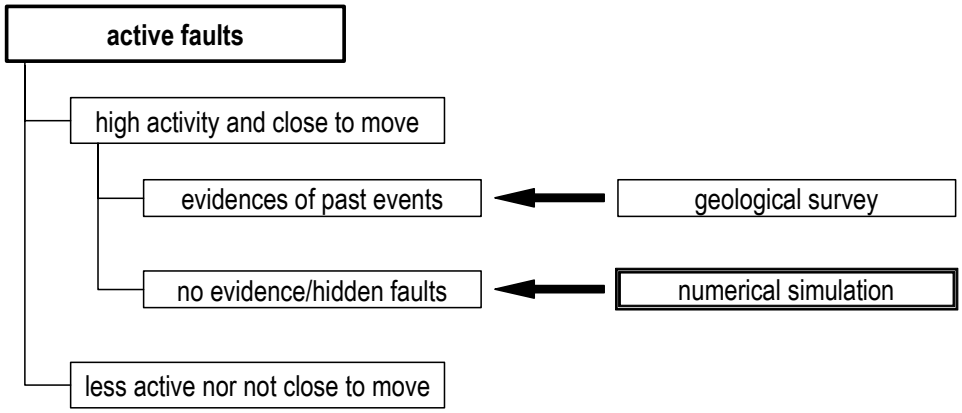

図 1　非線形スペクトル確率有限要素法が対象とする断層

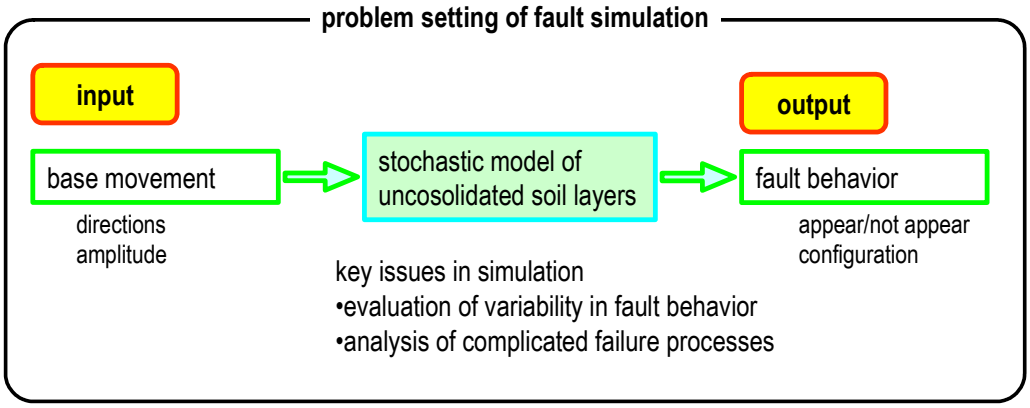

図 2　非線形有限要素法の概要

マニュアル
1．該当地点の未固結層の確率モデルを構築する.
2．断層変位を確率モデルに入力する.
3．断層挙動が出力される.

確率モデル:
構造等が不確かな未固結層に対するものである. ヤング率が非一様であり, その分布が不確かであることを想定している. モデルの構築に必要な材料特性のパラメータは, ヤング率の平均・分散・相関距離, 及び, ポアソン比, 粘着力, 内部摩擦角である(このパラメータは該当地区の地盤調査データから決定されるが, データがない場合には地盤種類から推定される).

入力:
モデルの底部に断層変位を入力する. 断層面の走向･傾斜を指定し, 断層変位量を 0 から所定の値まで増加させる. 走向･傾斜及び断層変位量の最大値は, 震源断層のシナリオを参考に決定することができる.

出力:
所定の断層変位が入力した時のばらつきを含む断層挙動を出力する. 断層挙動とは出現／非出現, 出現する場合には断層の入力地点からの相対位置・形状・ずれ変位量である. ばらつきは分散や確率密度関数のように確率的に評価される. 入力の断層変位量を確率的に与えてもかまわない.

APPENDIX II: *"AEM"*

The Applied Element Method (AEM) is a general purpose structural analysis method. It is considered a pioneering method to analyze and solve progressing nonlinear behavior until collapse that the Finite Element Method restrains from solving accurately.

AEM was first introduced with the need for a method that can solve discontinuous or cracked elements.

Formulation using Finite Element Method (FEM) depends on the assumption of having continuum material. As displacement functions correlate, the nodal displacements to displacement at any point inside an element with discontinuity or cracks results in breaking the base upon which the method depends.

To overcome these problems, researchers adopting the FEM use one of these assumptions:

1-**Smeared Crack Approach** Cracks are assumed to be considered in an implicit way. The effects of cracking is considered in the element stiffness matrix only

2-**Discrete Crack Approach** A special interface element is assumed to be set between elements expected to separate during simulation

The main disadvantage of the smeared Crack Approach is that it cannot deal with cracks of wide widths or real separation between elements, which is the case in a collapse situation. While using the Discrete Crack Approach, the location of cracks should be defined before the analysis, which is not practical especially in cases of structural collapse. The following table shows a comparison between AEM and FEM:

	AEM	FEM
CPU time	Short	Short
Degrees of freedom	2 elements (6)	8-node element (16)
Cracking model	Only physical cracks	Smeared cracks and interface cracks (physical cracks)
	No need for joint elements	Joint elements (interface elements) at large crack locations
	No need for joint elements	Joint elements location (large cracks) should be decided before analysis
	Crack propagation can be followed	Crack propagation cannot be followed accurately in smeared crack zones
Modeling time	Short	Long
Reinforcement details	Can be taken into account all reinforcement details without complication.	Difficult to input
Accuracy	At least the same as FEM before collapse, but can be extended easily to follow collapse behavior	High (before collapse)

See further details at:
http://www.collapseanalysis.org/ (English)

APPENDIX III: *"LPFDM"*

Material Point Method (MPM, Sulsky, 1994), by virtue of its scheme formulated in an arbitrary Lagrangian-Eulerian description of motion, allows the problem of mesh distortions to be eliminated, and thus large deformation of soils is easily described. Lagrangian Particle Finite Difference Method (LPFDM, Konagai et al, 2000) was the first trial and prototype program in this project simply combining MPM with Fast Lagrangian Analysis for Continum (Cundall 1977). LPFDM was then followed by more sophisticated programs (Johansson, 2004, Sadr, 2004), in which more realistic soil features are described by using hypoplasticity model etc.

This trial version (LPFDM Version .2.1), with simplified 2D Mohr-Coulumb criterion and Darcy's law implemented, is too primitive to describe complicated features of real soils as two-phases (solid and liquid) materials. However we put it up here just for providing a clear perspective of its high potential for describing large soil deformations and its intrinsic problems. This version is not fully tested and may contain bugs. If you find any bug(s), please contact us

---

Terms of use (**TOU**)

1. The program is free to copy, to change its source file(s) as long as it is used for educations and/or studies.

2. When you distribute it in its original shape or with some modification(s), refer to the original LPFDM Ver. 2.1 (copyrights reserved by K. konagai, 2001).

3. This version of LPFDM is not fully tested and may include some bugs. You must use it on your own risk.

4. Reflecting notice(s) from users, some changes may be put at any time without notice.

INSTRUCTIONS FOR DOWNLOADING

(1) Visit the **LPFDM** download page:
http://shake.iis.u-tokyo.ac.jp/home/ → **"softwares"**

(2) A password is needed to get in the site. The default password is '**opensesame**'.

Guide to "LPFDM"

(***L**agrangian **P**oint **F**inite **D**ifference **M**ethod*: **Ver. 2.1**)

by

Kazuo KONAGAI

First prepared: May 4, 2001

Last updated: March 10, 2004

Konagai Laboratory
Institute of Industrial Science
University of Tokyo

TWO DIMENSIONAL LAGRANGIAN PARTICLE FINITE DIFFERENCE METHOD FOR MODELING LARGE DEFORMATIONS OF SOILS

Kazuo KONAGAI

1. INTRODUCTION

A number of devastating earthquakes took tragically place in rapid succession in 1999, the closing year of the International Decade for Natural Disaster Reduction (IDNDR). Among them, the earthquakes in Kocaeli, Turkey Aug. 17 and Chi-Chi, Taiwan Sept. 21 were extraordinary. One of the most spectacular aspects of these earthquakes was the fault-inflicted damage to structures. Faultings are not the sole cause of large deformations of soils. Kobayashi found that more than half of all deaths in large (M > 6.9) earthquakes in Japan between 1964 and 1980 were caused by landslides. To discuss plausible remedial measures, it is necessary to study the possible extent of the very large plastic deformations taking place in soils. For such studies, suitable numerical tools are needed.

For studying large deformations of soils numerical methods as FEM or FDM have been widely used. For example, the finite difference based FLAC (Fast Lagrangian Analysis of Continua; Cundall[2)]) successfully calculates large strains by using low-order strain elements. The explicit finite difference formulation of FLAC makes it ideally suited for modeling geomechanical problems that often consist of several stages of construction. However, for highly distorted elements, the strains are not accurately computed. This is not a problem specific to FLAC, large element distortions have to be accounted for when dealing with large strains also in e.g. Lagrangian FEM codes

In the field of computational fluid dynamics, where history-dependent materials are less common, purely Eulerian methods are often used. However, to model highly distorted flows, Harlow et. al [3)] introduced the partially Lagrangian Particle-In-Cell method (PIC). Unfortunately it had high numerical dissipation, and to avoid this problem, Brackbill et. al.[4), 5)] developed the fully Lagrangian method, FLIP (Fluid implicit particle). It uses not only particles to model convection as in PIC, but also it was extended to model the fluid during the whole calculation cycle. Later, Burgess et. al.[6)] included a global consistent mass matrix into the FLIP method to reduce the so called “ringing” instability and Sulsky et al.[1)] extended it further to solid mechanics. The method is now referred to as the Lagrangian Particle Method (LPM) or the Material Point Method (MPM). In LPM particles move through the cells of a computational mesh carrying all the necessary Lagrangian parameters such as mass, stress, strain, position, strength etc. Any mesh type could be chosen to suit the typical problem, but a fixed Eulerian mesh is the simplest. The method thus takes advantage of both Eulerian and Lagrangian features, by avoiding mesh distortion and convection problems.

LPFDM (Lagrangian Particle Finite Difference Method) presented herein is intended to be a projection of FLAC formulations on the LPM scheme so that the present method allows for extremely large deformations of soils retaining the merits of FLAC.

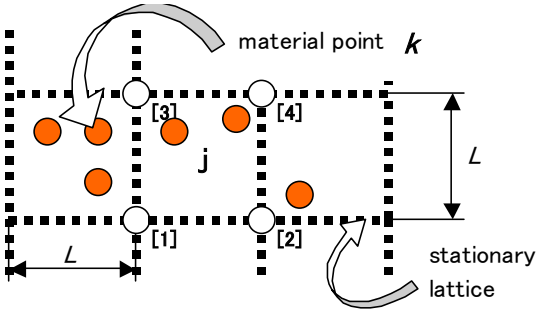

Figure 1. Stationary lattice and material points

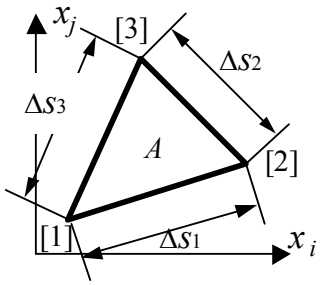

Figure 2 Triangular cell

2. CALCULATION SCHEME

2.1 *Solid Phase*

LPFDM embodies an explicit time-marching scheme, while implicit, matrix-oriented solution schemes are more common in finite element methods. As mentioned, all Lagrangian variables are carried by unconnected Lagrangian material points (see **Figure 1**); the points, as an entire cluster, describe the mass of the material. A Eulerian mesh is used to solve the equations of motion in each time step. Data mapped from the material points in one cell of the mesh contribute to cell's nodes, and accelerate them. The material points' variables are updated with mesh solution.

For the mesh solution, conventional FLAC[2)] uses an overlay scheme, in which a quadrilateral element is modeled as two overlaid pairs of constant-strain triangles (Mixed discretization procdure; Marti and Cundall[7)]). The forces exerted on each node are taken to be the mean of those exerted by the two quadrilaterals, and strains are eventually smeared over the quadrilateral. The overlay scheme thereby ensures isotropy, and successfully restrains hourglass deformations. The procedure, however, is not appropriate especially when the quadrilateral is badly distorted and paired triangles' areas are considerably out of balance (See **APPENDIX 1**). As contrasted with FLAC, hourglass deformations do not occur in LPFDM simulations because a fixed Eularian grid is used; hence the overlay scheme is not used in LPFDM allowing strains to be more rationally computed by simply invoking the Gauss' divergence theorem. For an area A enclosed by a surface S, the Gauss' theorem has the following form in the Cartesian coordinate system as:

$$\int_S n_j u ds = \int_A \frac{\partial u}{\partial x_j} dA \tag{1}$$

where,

$\int_S ds$ is an integral along the boundary S of a closed area A,

n_j $= \mathbf{n} \cdot \mathbf{j}$; Here $\mathbf{n}$ and $\mathbf{j}$ are unit vectors normal to the surface S and along the direction of x_j axis, respectively,

x_j can be either x or y in the Cartesian coordinate system (x, y),

u can be a scalar, vector or tensor, and

$\int_A dA$ is an integral over the area A.

Defining the average value of the gradient over the area as:

$$\left\langle \frac{\partial u}{\partial x_j} \right\rangle = \frac{1}{A}\int_A \frac{\partial u}{\partial x_j} dA \tag{2}$$

one obtains from Equation (1):

$$\left\langle \frac{\partial u}{\partial x_j} \right\rangle = \frac{1}{A}\int_S n_j u ds \tag{3}$$

When the closed area is a triangle as shown in **Figure 2**, and u is assumed to vary linearly along each side, the following finite difference formula is obtained:

$$\left\langle \frac{\partial u}{\partial x_j} \right\rangle = \frac{1}{A}\sum_{k=1}^{3} \langle u \rangle_k n_j \Delta s_k \tag{4}$$

where, the summation is taken over the three sides, and $\langle u \rangle_k$ is the average value of u over the side k.

Keeping in mind that $n_j \Delta s_k$ is the projection of Δs_k on x_i axis, Equation (4) for the triangle in **Figure 2** is rewritten as:

$$\left\langle \frac{\partial u}{\partial x_j} \right\rangle = \frac{1}{A}\{\frac{u^{[1]}+u^{[2]}}{2}\cdot(x_i^{[1]}-x_i^{\{2]}) + \frac{u^{[2]}+u^{[3]}}{2}\cdot(x_i^{[2]}-x_i^{[3]}) + \frac{u^{[3]}+u^{[1]}}{2}\cdot(x_i^{[3]}-x_i^{[1]})\} \tag{4a}$$

or

$$\left\langle \frac{\partial u}{\partial x_j} \right\rangle = \frac{1}{2A}\left\{u^{[1]}\left(x_i^{[1]}-x_i^{[2]}\right) + u^{[2]}\left(x_i^{[2]}-x_i^{[3]}\right) + u^{[3]}\left(x_i^{[3]}-x_i^{[1]}\right)\right\} \tag{4b}$$

with

$$A = \frac{1}{2}\begin{vmatrix} 1 & x_i^{[1]} & x_j^{[1]} \\ 1 & x_i^{[2]} & x_j^{[2]} \\ 1 & x_i^{([3]} & x_j^{[3]} \end{vmatrix} \tag{4c}$$

where, superscripts [1], [2], [3] denote local nodal point numbers in **Figure 2**.

Equation (4) can be used for any arbitrarily-shaped polygon to describe the strain increments in terms of the nodal displacement increments by simply replacing u with $\Delta u^{[k]}$. In LPFDM, a regular square mesh with sides parallel to x and y axes of the Cartesian coordinate system is used (**Figure 1**). Replacing in Equation (4b) x_i and x_j with x and y, and increasing the node number to 4, the average strain increment of J-th element is obtained as:

$$\left(\Delta\varepsilon_{xx}\right)_J = \frac{\left(\Delta u_x^{[2]} + \Delta u_x^{[4]} - \Delta u_x^{[1]} - \Delta u_x^{[3]}\right)_j}{2L} \tag{5a}$$

$$\left(\Delta\varepsilon_{yy}\right)_J = \frac{\left(\Delta u_y^{[3]} + \Delta u_y^{[4]} - \Delta u_y^{[1]} - \Delta u_y^{[2]}\right)_j}{2L} \tag{5b}$$

$$\left(\Delta\varepsilon_{xy}\right)_J = \frac{\left(\Delta u_x^{[3]} + \Delta u_x^{[4]} - \Delta u_x^{[1]} - \Delta u_x^{[2]}\right)_j}{2L} \tag{5c}$$

$$\left(\Delta\varepsilon_{yx}\right)_J = \frac{\left(\Delta u_y^{[2]} + \Delta u_y^{[4]} - \Delta u_y^{[1]} - \Delta u_y^{[3]}\right)_j}{2L} \tag{5d}$$

where L is the cell side length.

The representative shear strain increment $\Delta\gamma_{xy}$ satisfies:

$$\left(\Delta\gamma_{xy}\right)_J = \left(\Delta\varepsilon_{xy}\right)_J + \left(\Delta\varepsilon_{yx}\right)_J \tag{5e}$$

and the corresponding rotational increment $\Delta\theta$ is given by:

$$\left(\Delta\theta\right)_J = \frac{1}{2}\left(\Delta\varepsilon_{yx} - \Delta\varepsilon_{xy}\right)_J \tag{5f}$$

All material points included in Cell *J* are assumed to experience the same strain increments given by equations (5a)-(5f), and the stresses for a material point *k* included in cell *J* are computed by means of a specified constitutive model:

$$\left(\sigma_{ij}\right)_{k,\,updated} = M\left(\left(\Delta\varepsilon_{ij}\right)_J, \left(\sigma_{ij}\right)_k, \left(s_1\right)_k, \left(s_2\right)_k, \cdots\right) \tag{6}$$

where, *M*( ) is the constitutive model, and $\left(s_i\right)_k$ are state variables for this material point. For the explicit scheme used in LPFDM, the constitutive law is only consulted once per material point during one time step.

The location of material point *k* $\{x(k), y(k)\}$ in the cell *J* deformed at the previous time step is updated as:

$$\begin{aligned} x(k) \Leftarrow x(k) &+ \Delta u_x{}^{[1]} \cdot \left(1 - \frac{\Delta x(k)}{L}\right)\left(1 - \frac{\Delta y(k)}{L}\right) + \Delta u_x{}^{[2]} \cdot \frac{\Delta x(k)}{L}\left(1 - \frac{\Delta y(k)}{L}\right) + \\ &\Delta u_x{}^{[3]} \cdot \left(1 - \frac{\Delta x(k)}{L}\right)\frac{\Delta y(k)}{L} + \Delta u_x{}^{[4]} \cdot \frac{\Delta x(k)}{L}\frac{\Delta y(k)}{L} \end{aligned} \tag{7a}$$

$$\begin{aligned} y(k) \Leftarrow y(k) &+ \Delta u_y{}^{[1]} \cdot \left(1 - \frac{\Delta x(k)}{L}\right)\left(1 - \frac{\Delta y(k)}{L}\right) + \Delta u_y{}^{[2]} \cdot \frac{\Delta x(k)}{L}\left(1 - \frac{\Delta y(k)}{L}\right) + \\ &\Delta u_{yx}{}^{[3]} \cdot \left(1 - \frac{\Delta x(k)}{L}\right)\frac{\Delta y(k)}{L} + \Delta u_y{}^{[4]} \cdot \frac{\Delta x(k)}{L}\frac{\Delta y(k)}{L} \end{aligned} \tag{7b}$$

where,

$\Delta x(k)$= $x(k)$ - (x-coordinate of node (1) of Cell *J*)
$\Delta y(k)$= $y(k)$ - (y-coordinate of node (1) of Cell *J*).

When all the Lagrangian variables are updated at all material points, the equations of motion are solved at each nodes of the Eulerian mesh, which is shifted back to its original position for the following calculation cycle. The mass of each cell is obtained by adding up all the masses of material points included in the cell *J*:

$$\left\langle M\right\rangle_J = \sum_{k\in J} m_k \tag{8}$$

Here, it in noted that a set of material points included in the cell *J* has been also updated.

Stress is smeared over the cell:

$$\left\langle \sigma_{ij}\right\rangle_J = \left\{\sum_{k\in J}\left(\frac{m_k}{\rho_k}(\sigma_{ij})_k + p_k\delta_{ij}\right)\right\} / L^2 \tag{9}$$

where, the quotient of material point mass and density m_k / ρ_k is the volume of the material point *k*, p_k is pore water pressure, which will be discussed in the following section, and δ_{ij} is Kronecker's delta. In order to obtain the nodal forces at node [k] of Cell *J* (see **Figure 1**), a virtual unit displacement is applied to node [k]. The stress components $\left\langle\sigma\right\rangle_J$ smeared over Cell *J* must perform the same amount of work done by the nodal forces $F_i^{[k]}$ ($i = x$ or y): this calls for;

$$F_i^{[k]} = \frac{\left\langle\sigma_{ii}\right\rangle_J (x_j{}^{[k-1]} - x_j{}^{[k+1]})}{2} + \frac{\left\langle\sigma_{ij}\right\rangle_J (x_i{}^{[k-1]} - x_i{}^{[k+1]})}{2} \tag{10}$$

where, $(x_i \quad x_j)$ is either $(x \quad y)$ or $(y \quad x)$.

At each node, the forces from all surrounding lattice zones (elements) are summed up to give

the net nodal force, $\sum_{[k]\in(k)} F_i^{[k]}$ ($i = x$ or y). This vector includes contributions from applied loads and body forces due to gravity. Gravity forces are computed from:

$$F_{g,i}{}^{(k)} = g_i m^{(k)} \tag{11}$$

where $m^{(k)}$ is the lumped mass at the node (k), defined as 1/4 of the masses of the cells connected to the node. If a connected cell does not contain any material point, its contribution to the nodal force is omitted. The nodal force accelerates the lumped mass, and the acceleration is integrated to obtain the nodal displace increment:

$$\Delta u_i^{(k)}(t+\Delta t/2) = \Delta u_i^{(k)}(t-\Delta t/2) + \frac{\Delta t^2}{m^{(k)}} \sum F_i^{(k)} \tag{12}$$

It is noted in Equation (11) that the nodal displacement increment $\Delta u_i{}^{(k)}(t-\Delta t/2)$ is not exactly identical to that evaluated at the previous time step of the calculation cycle, because the increment must be evaluated at the node on the Eulerian lattice shifted back to its original position while the point where the previous increment was evaluated has passed by this node. Compensation for this is made by the following procedure:

$$\Delta u_x{}^{(k)}(t-\Delta t/2) \Leftarrow \Delta u_x{}^{(k)}(t-\Delta t/2)\cdot\left(1-\left(\Delta\varepsilon_{xx}\right)_{j^{(k)}}\right) - \Delta u_y{}^{(k)}(t-\Delta t/2)\cdot\left(\Delta\varepsilon_{xy}\right)_{j^{(k)}} \tag{13a}$$

$$\Delta u_y{}^{(k)}(t-\Delta t/2) \Leftarrow \Delta u_y{}^{(k)}(t-\Delta t/2)\cdot\left(1-\left(\Delta\varepsilon_{yy}\right)_{j^{(k)}}\right) - \Delta u_x{}^{(k)}(t-\Delta t/2)\cdot\left(\Delta\varepsilon_{yx}\right)_{j^{(k)}} \tag{13b}$$

where, $J^{(k)}$ is the cell in which the previous mark of nodal point (k) on the material is found.

When quasi-static behaviors are concerned, the motions of nodes must be damped with minimal computational effort. A form of artificial damping, called local non-viscous damping (Cundall[2]), is used in *LPFDM* in which the damping force on a node is proportional to the magnitude of the unbalanced force. The direction of the damping force is taken in such a way that energy is always dissipated. Equation (12) is thus replaced with the following equation:

$$\Delta u_i{}^{(k)}(t+\Delta t/2) = \Delta u_i{}^{(k)}(t-\Delta t/2) + \frac{\Delta t^2}{m_k}\left(\sum F_i^{(k)} - D_i{}^{(k)}\right) \tag{14}$$

where,

$$D_i{}^{(k)} = \alpha\left|\sum F_i^{(k)}\right| \mathrm{sgn}(\Delta u_i{}^{(k)}(t-\Delta t/2)) \tag{15}$$

$D_i{}^{(k)}$ is the damping force, α is a constant.

2.2 *Pore Water Pressure*

Usually soils are water-saturated in reality, and thus pore-water behavior should be taken appropriately into account. In this version of LPFDM, soils are assumed to be completely saturated with water that flows through their granular fabrics obeying Darcy's law. The longitudinal wave velocity v_L in water is about 1500 m/s. The compressibility of water (Bulk modulus K = 2.22 GPa) is thus much smaller that that of quartz. For this reason, not a granular fabric but its void is assumed to change its volume. In the time-marching calculation scheme, an element size should satisfy the following condition:

$$v_L \Delta t << L \tag{16}$$

where Δt = time increment, L = cell size

It is customary in geotechnical engineering to describe compressive pressure as positive. But notation here follows the conventional way for FEM formulations, and thus sucking pore pressure p is described as positive. Excessive pore pressure Δp at z below the water level is given by:

$$\Delta p = p + \rho g z \tag{17}$$

In Lagrangian point k included in Cell j, the initial volumes of solid phase and pore-water are

given respectively by:

$$V_{k,solid} = \frac{1}{1+e}\left(V_k\right)_{t=0} \tag{18a}$$

$$\left(\overline{V}_{k,0}\right)_{t=0} = \frac{e}{1+e}\left(V_k\right)_{t=0} \tag{18b}$$

where, V_k is the volume of the material point *k*.

A change in void causes an excessive pore pressure $\Delta\overline{p}_k$ as:

$$\Delta p_k = K\left(\left(\overline{V}_k\right)_t - \left(\overline{V}_{k,0}\right)_t\right)/\left(\overline{V}_{k,0}\right)_t \tag{19a}$$

where

$$\left(\overline{V}_k\right)_t = \left(V_k\right)_t - V_{k,solid} \quad \text{with}$$

$$\left(V_k\right)_t = \left(\overline{V}_k\right)_{t-\Delta t}\left(1+\left\langle\Delta\varepsilon_{xx}\right\rangle_{k\in J}\right)\cdot\left(1+\left\langle\Delta\varepsilon_{yy}\right\rangle_{k\in J}\right) \tag{19b}$$

This change of pore pressure causes pore water to flow through granular fabric. Velocities of percolation in *x* and *y* directions are respectively given by:

$$v_x = k_d\frac{\partial\Delta p_k}{\partial x} \quad \text{and} \quad v_y = k_d\frac{\partial\Delta p_k}{\partial y} \tag{20a), (20b}$$

where, $k_d = k_s/\rho g$ and k_s = coefficient of permeability.

The volume of water flowing into the material point *k* within the time increment Δt is given by

$$\Delta\overline{V}_{k,0} = -\left(\frac{\partial v_x}{\partial x}+\frac{\partial v_y}{\partial y}\right)V_k\Delta t \tag{21}$$

Substituting Equations (20a) and (20b) into Equation (21) leads to:

$$\Delta\overline{V}_{k,0} = -k_d V_k\Delta t\cdot\nabla^2\Delta p_k \tag{22}$$

This $\Delta\overline{V}_{k,0}$ is then added to $\left(\overline{V}_{k,0}\right)_{t-\Delta t}$, and this procedure updates $\overline{V}_{k,0}$ in Equation (3a).

$$\left(\overline{V}_{k,0}\right)_t = \left(\overline{V}_{k,0}\right)_{t-\Delta t} + \Delta\overline{V}_{k,0} \tag{23}$$

In Equation (6), $\nabla^2\Delta p_k$ is obtained on the Eularian mesh assuming that Δp_k is uniformly distributed over Cell *J*. The average excessive pore pressure for Cell *J* is thus given as:

$$\left\langle\Delta p\right\rangle_J = \frac{\sum_{k\in J}V_k\Delta p_k}{\left\langle V\right\rangle_J} \quad \text{with} \quad \left\langle V\right\rangle_J = \sum_{k\in J}V_k \tag{24}$$

Laplacian operation for $\left\langle\Delta\overline{p}\right\rangle_J$ is described on the square Eularian mesh (**Figure 3**) as:

$$\nabla^2\left\langle\Delta p\right\rangle_J = \frac{\left\langle\Delta p\right\rangle_{J+\Delta x}+\left\langle\Delta p\right\rangle_{J-\Delta x}+\left\langle\Delta p\right\rangle_{J+\Delta y}+\left\langle\Delta p\right\rangle_{J-\Delta y}-4\left\langle\Delta p\right\rangle_J}{L^2} \tag{25}$$

where, *L* is the cell size of the Eularian mesh.

This $\nabla^2\left\langle\Delta p\right\rangle_J$ approximates $\nabla^2\Delta p_k$ in Equation (22).

Given the excessive pore pressure Δp_k from Equation (19a), and using Equation (17), pore water pressure p_k is obtained for Equation (9). In this LPFDM, however, Δp_k is used in stead in Equation (9), and in compensation for that, weights of all immersed Lagrangian points are reduced by their buoyancies. This manipulation reduces the error caused by coarse-meshed Eularian lattice especially when a node of the mesh is slightly off the material boundary.

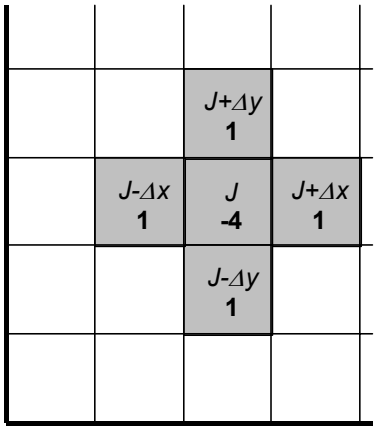

$\langle \Delta p \rangle_{J+\Delta x} + \langle \Delta p \rangle_{J-\Delta x} + \langle \Delta p \rangle_{J+\Delta y} + \langle \Delta p \rangle_{J-\Delta y} - 4\langle \Delta p \rangle_J$

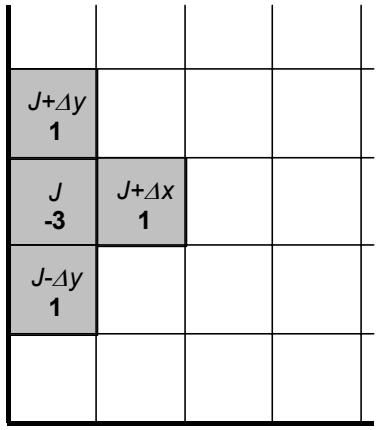

$\langle \Delta p \rangle_{J+\Delta x} + \langle \Delta p \rangle_{J+\Delta y} + \langle \Delta p \rangle_{J-\Delta y} - 3\langle \Delta p \rangle_J$

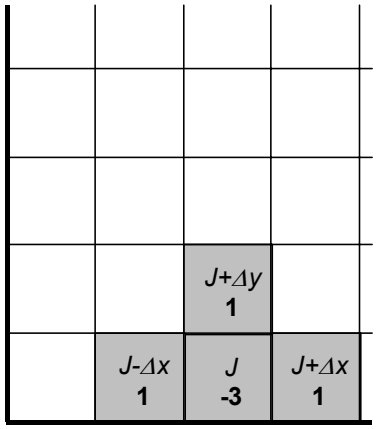

$\langle \Delta p \rangle_{J+\Delta x} + \langle \Delta p \rangle_{J-\Delta x} + \langle \Delta p \rangle_{J-\Delta y} - 3\langle \Delta p \rangle_J$

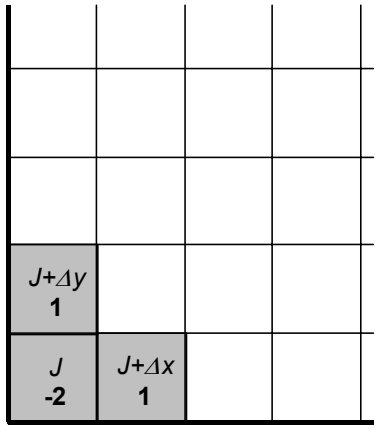

$\langle \Delta p \rangle_{J+\Delta x} + \langle \Delta p \rangle_{J+\Delta y} - 2\langle \Delta p \rangle_J$

Figure 3 Laplacian operation $\nabla^2 \langle \Delta p \rangle_J L^2$ on Eularian square mesh

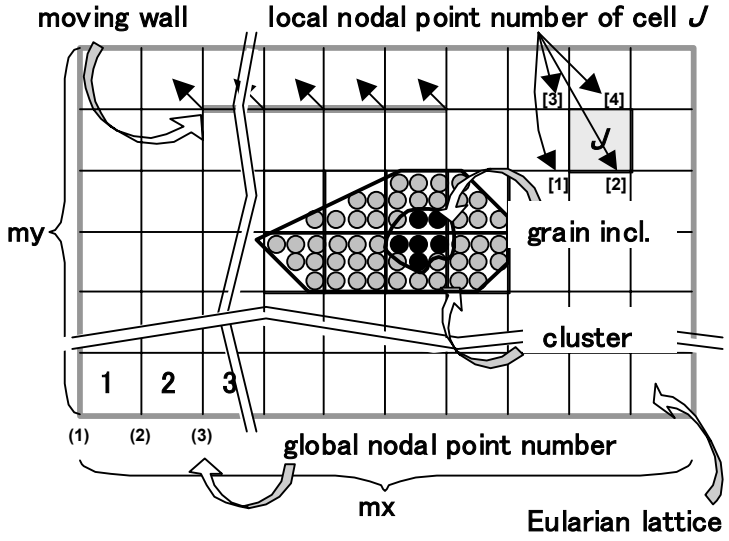

Figure 4. Necessary items in LFPDM.

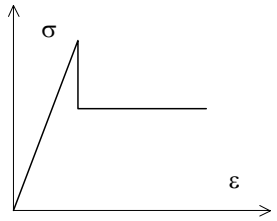

Figure 5 Assumed Stress-strain curve for a material point

3. NECESSARY ITEMS

A fixed mesh, in an arrangement of $mx \times my$ square cells with "***nodal points***", is used to describe the locations of "***Lagrangian points***" (**Figure 3**). Polygonal areas filled with Lagrangian points are referred to as "***clusters***". Initially, Lagrangian points are arranged in square in a cluster**.** An arbitrarily shaped "***grain inclusion***" is also a smaller cluster of Lagrangian points within a perimeter described in terms of radial distance r from its center of gravity. The radial distance r varies with azimuth θ, and is Fourier-expanded.

In addition to the abovementioned items, "***moving walls***" are introduced into LPFDM. A *moving wall* is realized by giving all designated nodes lined up on the lattice the same displacement increments at once.

When the accumulation of the increments given to each node reaches one cell size, the displacement increments are given to the next line of nodes.

Lagrangian points discussed herein is assumed to be elasto-plastic, obeying the simple Mohr-Coulomb's yield criterion. Once the peak strength is reached in one intact Lagrangian point, chemical bonds or granular fabrics are assumed to be broken causing the material strength to be reduced from it initial value to some prescribed extent (**Figure 5**). Both the internal friction angles and the cohesions for Lagrangian points were modified to fluctuate randomly around their mean values so that the deviations eventually exhibit the Gaussian distributions. This manupulation is based on the idea that a material exhibiting a complicated hysterisis is comprised of a number of elements exhibiting simple and ideal features (Iwan[8], Ogawa[9]).

Young's modulus of soil is dependent on the confining pressure, and thus buildup of pore-water pressure will cause the change of it. In the present version of LPFDM, however, this interactive effect is excluded because this program was intended to be a simple platform for any further possible developments in which more sophisticated constitutive laws will be implemented.

4. DATA FILES

4.1 *Input Data Files*

LPFDM requires eight input data files. SI units are used.

(1) **frame.dat**

This data file provides a (mx, my) size Eularian lattice. Lagrangian points are arranged in $ns \times ns$ squares in a $L \times L$-sized cell.

<1>	<2>	<3>	<4>
10	20	4	1.0

where,

<1> (I5)	mx	Eularian lattice in an arrangement of $mx \times my$ square cells.
<2> (I5)	my	
<3> (I5)	ns	Lagrangian points are initially arranged in $ns \times ns$ squares in a cell.
<4> (F10.5)	L	Cell size $L \times L$ **[m]**

(2) **accel.dat**

This data file provides, at each time step, <1> time increment, <2> x and <3> y components of acceleration given o the base of the model, and the <4> damping constant α for local non-viscous damping (Cundall). In the following example, no acceleration is given to the model's base. If all numbers in column <3> are replaced with 1G (9.8 m/s^2), the model is put in the gravitational field. A lateral seismic motion can be given in column <2>. When "0" is met in column <1>, the time-marching calculation stops.

<1>	<2>	<3>	<4>
.5000E-04	.0000E+00	.0000E+00	.8000E+00
.5000E-04	.0000E+00	.0000E+00	.8000E+00
.5000E-04	.0000E+00	.0000E+00	.8000E+00
.5000E-04	.0000E+00	.0000E+00	.8000E+00
⋮	⋮	⋮	⋮
.0000E+00			

where.

<1> (F10.5)	Δt	Time increment **[s]**
<2> (F10.5)	g_x	Acceleration given in x direction **[m/s^2]**
<3> (F10.5)	g_y	Acceleration given in y direction. **[m/s^2]**
<4> (F10.5)	α	A form of artificial damping, called local non-viscous damping (Cundall[2)]), is used in *LPFDM*. α is the constant for this damping.

(3) **cluster.dat**
This data file provides vertices of polygonal clusters put in the Eularian lattice. In the following example, a rectangular cap (Cluster No. 2) is put on a rectangular soil mass (Cluster No.1).

<1>
2
<2>
4

<3>	<4>
2.0	0.0
8.0	0.0
8.0	15.0
2.0	15.0

<2>
4

<3>	<4>
2.0	15.0
8.0	15.0
8.0	17.0
2.0	17.0

where,

<1> (I5)	nc	Number of clusters
<2> (I5)	nvrt	Number of vertices making up the a polygonal cluster
<3> (F10.5)	x_j	Coordinates (*x, y*) of vertices making up the polygonal cluster *j*. They must be arranged counter-clockwise. **[m]**
<4> (F10.5)	y_j	

(4) **grains.dat**
This data file provides grains included in clusters. A grain shape (perimeter) is described in terms of radial distance *r* from its reference point. The reference point is not necessarily the center of gravity, but should be within the interior of the grain. The radial distance *r* varies with azimuth θ, and is expressed as:

$$r = \sum_{j=1}^{ntrm} \left(r_j \cos j\theta + \phi_j \right) \tag{26}$$

<1>
2

<2>	<3>	<4>
3	4.0	10.0

<5>	<6>
1.0	0.0
0.0	0.0
0.3	-1.0

<2>	<3>	<4>
1	6.5	7.0

<5>	<6>
1.0	0.0

where,

<1> (I5)	ngrain	Number of grain inclusions (ngrain = 0, when you have no grain inclusion.)
<2> (I5)	ntrm	Number of Fourier terms describing the first grain perimater
<3> (F10.5)	x_i	Center of gravity of grain *i*. "Radius" is defined as the distance between (x_i , y_i) to a point on the perimeter. **[m]**
<4> (F10.5)	y_i	
<5> (F10.5)	r_j	Perimeter of a grain is described in terms of radius *r* varying with azimuth θ. $r = \sum_{j=1}^{ntrm}\left(r_j \cos j\theta + \phi_j\right)$ **[m]** and **[rad],** respectively.
<6> (F10.5)	ϕ_j	

(5) **mtrnum.dat**
This data file provides lists of correspondence between clusters and materials and between grains and materials.

<1>	
3	
<2>	
2	
<3>	<4>
1	1
2	3
<5>	
2	
<6>	<7>
1	2
2	2

where,

<1> (I5)	mtrn	Number of materials
<2> (I5)	nc	Number of clusters
<3> (I5)	ic	Cluster number
<4> (I5)	mclst	Material number corresponding to cluster, ic.
<5> (I5)	ngrain	Number of grains (ngrain = 0, when you have no grain inclusion.)
<6> (I5)	ig	Grain number
<7> (I5)	mgrain	Material number corresponding to grain, ig.

(6) **mtprm.dat**
This data file provides Lagrangian parameters for different materials. When the program starts running, a question is displayed on your console, asking if you will be implementing pore pressure effects in LPFDM. If yes, Poisson's ration of the soil **po** (Column <2>) should describe its completely dried condition. As for the unit weight of the soil (Column <3>), it is to be obtained assuming that the soil contains both air and water in its granular fabric.

<1>	<2>	<3>	<4>	<5>	<6>	<7>	<8>	<9>
5.000E+07	0.47	1.7E+04	0.5	1.0E+04	1.0	0.1E-06	0.33	0.5
5.000E+08	0.47	2.5E+04	0.5	1.0E+08	1.0	0.1E-06	0.00	1.0
5.000E+09	0.47	5.1E+04	0.5	1.0E+08	1.0	0.1E-06	0.00	1.0

where,

<1> (F10.5)	E	Young's moduli **[N/m^2]**	for all materials
<2> (F10.5)	po	Poisson's ratios	
<3> (F10.5)	$\rho_s g$	Unit weights **[N/m^3]**	
<4> (F10.5)	phi	Internal friction angles	
<5> (F10.5)	c	Cohesions **[N/m^2]**	
<6> (F10.5)	e	Void ratios	
<7> (F10.5)	k_d	Permeability coefficients /unit weight of water **[m^4/N/s]**	
<8> (F10.5)	σ	Both internal friction angles and cohesions for the materials were modified to fluctuate randomly around their mean values so that the deviations eventually exhibit the Gaussian distributions. (standard deviations = $\sigma \times$ their mean values)	
<9> (F10.5)	reduce	Once granular fabrics are broken, cohesions are reduced by these ratios.	

(7) **walls.dat**
This data file provides the initial location and the speed of a steadily moving rigid wall.

<1>
1

<2>	<3>	<4>	<5>	<6>	<7>	<8>	<9>	<10>
3	16	1	8	16	2	0	0.0	-0.0001

where,

<1> (I5)	nwall	Number of walls (nwall = 0, when you have no wall.)
<2> (I5)	mwx1	Location of cell including left (or bottom) end of wall
<3> (I5)	mwy1	
<4> (I5)	nd1	Corresponding local node number in cell (mwx1, mwy1)
<5> (I5)	mwx2	Location of cell including right (or top) end of wall
<6> (I5)	mwy2	
<7> (I5)	nd2	Corresponding local node number in cell (mwx2, mwy2)
<8> (F10.5)	dxinc	Displacement increments given to the wall. **[m]**
<9> (F10.5)	dyinc	

(8) **transducer.dat**
This data file provides the locations of force transducers that detect both normal and shear forces applied to them.

<1>
1

<2>	<3>	<4>
3	1	8

where,

<1> (I5)	ntrns	Number of force transducers
<2> (I5)	jt1	Both ends of the transducer are located at local node **lcn1** in Cell **jt1** and in Cell **jt2**.
<3> (I5)	lcn1	
<4> (I5)	jt2	

4.2 *Output files*

(1) **clusterJ.dat** (J is the cluster number)
This output data file provides the following Lagrangian parameters carried by all Lagrangian points included in Cluster J.

<1>	<2>	<3>	<4>
0.2123E+01	0.1250E+00	0.0000E+00	-0.1333E+04
0.2373E+01	0.1249E+00	0.0000E+00	-0.1333E+04
0.2623E+01	0.1249E+00	0.0000E+00	-0.1333E+04
0.2873E+01	0.1248E+00	0.0000E+00	-0.1333E+04
¦	¦	¦	¦

where,

<1> (E15.7)	x	Locations of all Lagrangian points included in Cluster J. **[m]**
<2> (F15.7)	y	
<3> (E15.7)	Δp_k	Excessive pore-water pressures at all Lagrangian points **[N/m^2]**
<4> (E15.7)	σ_{xy}	Shear stresses at all Lagrangian points **[N/m^2]**

(2) **inclusion.dat**
This output data file provides the following Lagrangian parameters carried by all Lagrangian points included in all grain inclusions.

<1>	<2>	<3>	<4>
0.6761E+04	0.6103E+01	0.0000E+00	0.6761E+04
0.6392E+01	0.6104E+01	0.0000E+00	0.6761E+04
0.6642E+01	0.6105E+00	0.0000E+00	0.6761E+04
0.6892E+01	0.6106E+00	0.0000E+00	0.6761E+04
¦	¦	¦	¦

where,

<1> (E15.7)	x	Locations of all Lagrangian points included in all grains. **[m]**
<2> (F15.7)	y	
<3> (E15.7)	Δp_k	Excessive pore pressures at all Lagrangian points in all grains **[N/m^2]**
<4> (E15.7)	σ_{xy}	Shear stresses at all Lagrangian points in all grains **[N/m^2]**

(3) **react.dat** (Only for PSC test simulations)
This is tentatively included in the present version of LPFDM only for PSC test simulations.

<1>	<2>	<3>
0.1000E-03	0.0000E+01	0.0000E+00
0.2000E-03	0.0000E+01	0.0000E+00
0.3000E-03	0.0000E+00	0.0000E+00
0.4000E-03	0.0000E+00	0.0000E+00
¦	¦	¦

where,

<1> (E15.7)		Cap displacement **[m]**
<2> (E15.7)	$-\sigma_{xx}$	Normal stress detected by the force transducer **[N/m^2]**
<4> (E15.7)	$-\sigma_{xy}$	Shear stress detected by the force transducer **[N/m^2]**

5. NUMERICAL EXAMPLES

5.1 *Simulations without pore-pressure effect implemented*

Table 1 shows the parameters for the material used in the following examples. Both the internal friction angles and the cohesions for Lagrangian points were given a Gaussian distributions with mean values in **Table 1** and a standard deviation of 25% for the following simulations **(3)** and 33% for the others.

Table 1. Mechanical properties

Young's modulus:	5×10^7 N/m^2
Poisson's ratio:	0.47
Density:	1700 kg/m^3
Internal friction angle:	0.5 rad
Cohesion:	9800 N/m^2
Strength reduction:	Cohesion is reduced by 50%

(1) *Failure of steep slope*

Figure 5 shows a soil mass that collapses under its own weight. The α variable was set at 0.8 in Equation (15) for the local non-viscous damping. Despite the coarse discretization ($L = 1$m), detailed features of this cliff failure were vividly described. Initially the deformation is slow, but as plastic strains begin to accumulate, certain regions become softened and rapid shear-band formation occurs from the toe up through the cliff. The corner wedge of the soil mass then starts sliding down the softened slope, being accompanied by a secondary shear-band formation just behind the scar.

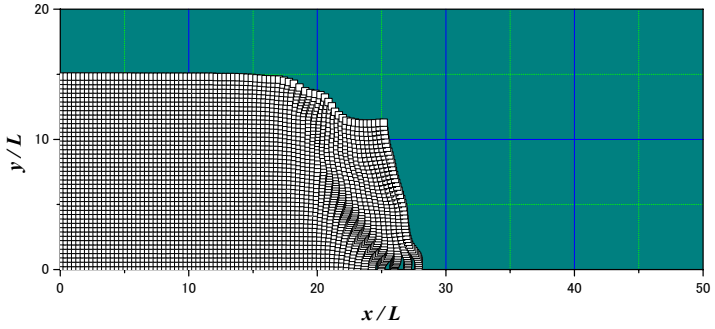

(a) 2.5s

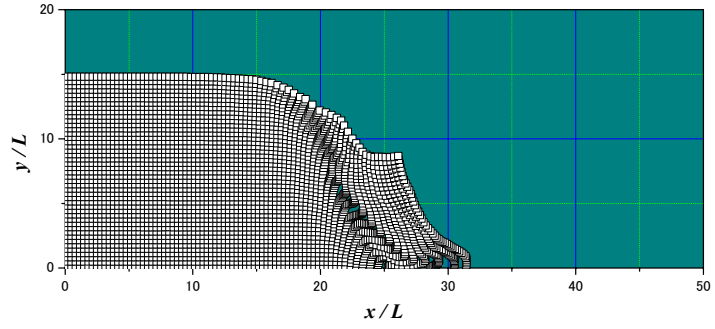

(b) 5.0s

Figure 6 Simulation of cliff failure ($\Delta t = 0.0005s$)

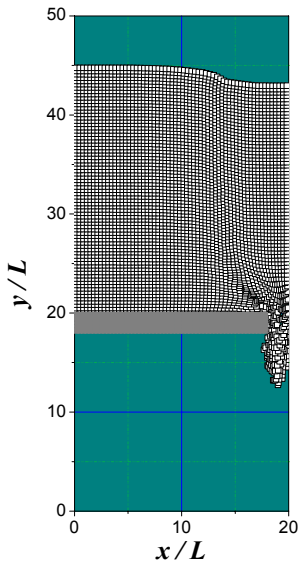

(a) 2.5s

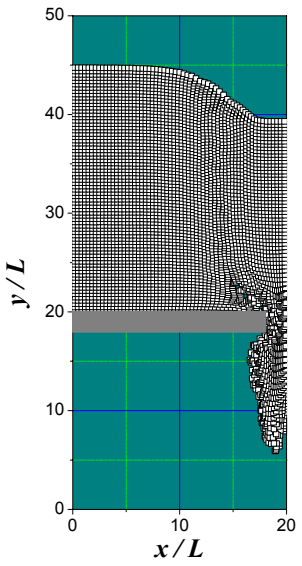

(b) 5.0s

Figure 7 Mass flow through a trapdoor ($\Delta t = 0.0005s$)

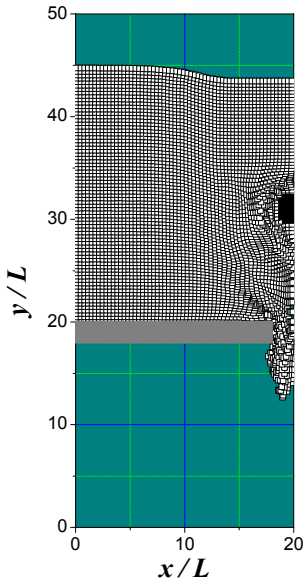

(a) 2.5s

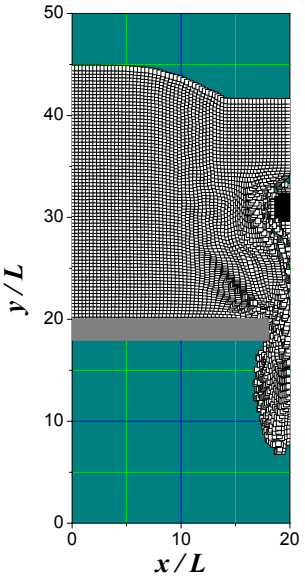

(a) 5.0s

Figure 8 Mass flow through a trapdoor with an obstacle right above ($\Delta t = 0.0005s$)

(2) *Mass Flow through a Trap door*

A mass flow through a trap door was simulated (**Figure 7**). The internal friction angle was set at 0.0 for this simulation; except that, mechanical properties are the same as those listed in **Table 1**. The gravitational acceleration was given at once to the mass, and the mass started flowing under its own weight. The opening of the door is just twice the cell size L, and yet, the mass exhibiting a noticeably flexible nature can flow through the narrow opening. In the second simulation (**Figure 8**), an obstacle was placed right above the trap door. One can see that the soil flows past the obstacle and through the trap door. Some flow stagnation occurs around the obstacle.

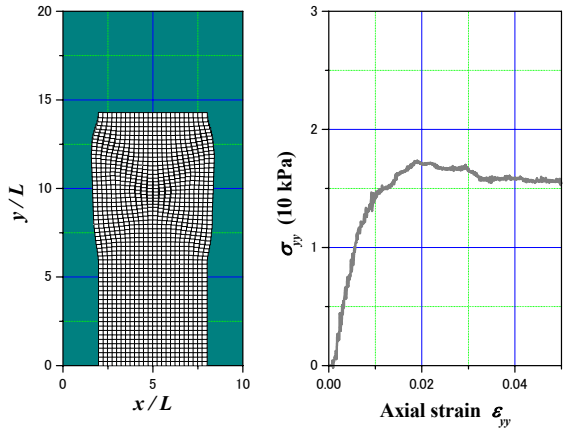

(a) No grain inclusion

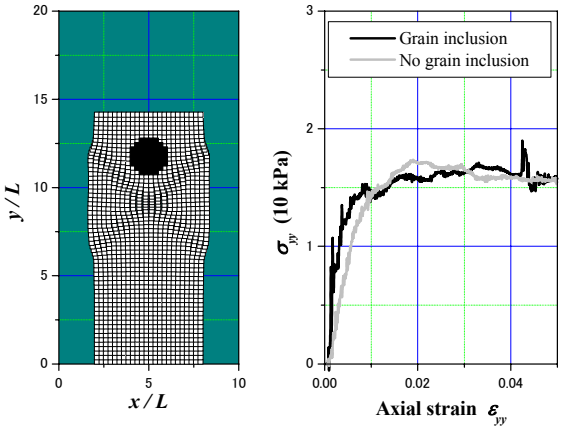

(b) Grain location: 2.5*L* below the top

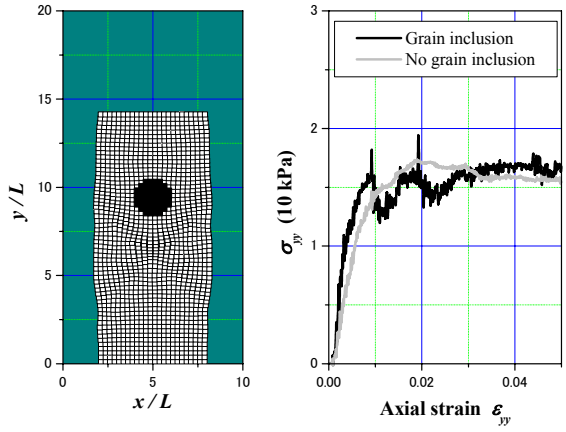

(c) Grain location: 5.0*L* below the top

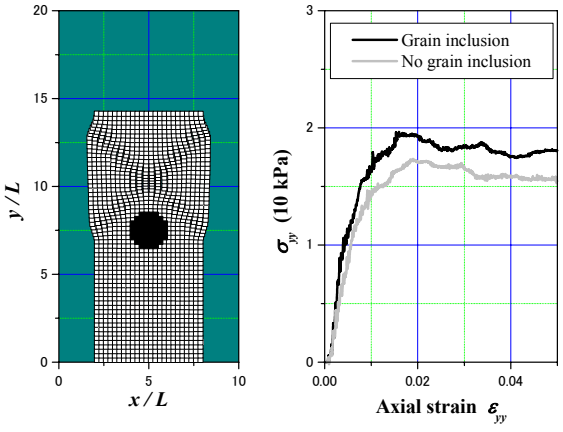

(d) Grain Location: 7.5*L* below the top

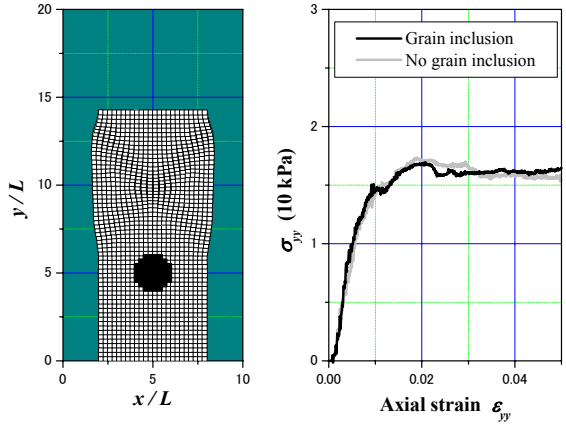

(e) Grain Location: 10.0*L* below the top

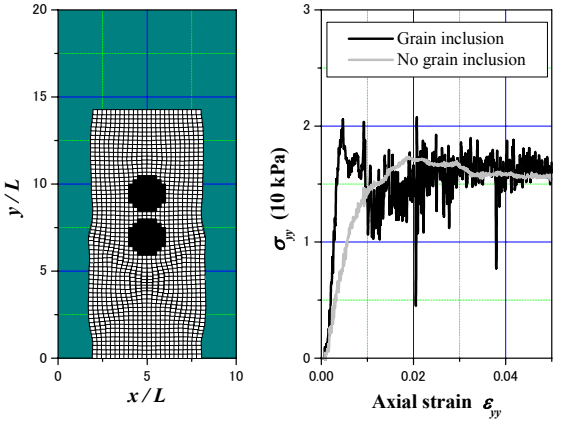

(f) Two grain inclusions: 5.0L & 7.5L below the top

Figure 9 PSC test simulations

(3) *Plane-Strain Compression Tests*

Alluvial deposits including large boulders are often found. To see how these large inclusions in a soil matrix affect the soil's overall behavior, and to demonstrate the potential of the Lagrangian particle technique, some examples of PSC test with inclusions of large grains/boulders follow below.

Figure 9 shows the simulation of a plane-strain compression test on a soil with the properties given in **Table 1**. In order to compress the specimen, a stiff cap was put immediately above the top end of the specimen, and was slowly driven down at a constant velocity. The confining pressure was zero. In the figures, both the height and width of the specimen are normalized by the cell width L. and material points were initially arranged in 4×4 square in each cell. The stress was measured at the bottom of the specimen.

Though each material point has simple mechanical features as described in **Table 1**, the overall deviatoric stress-strain relationship (**Figure 9a**) exhibits rather realistic curvature. This is because the values given in **Table 1** were given random deviation and the strain is the ratio of cap displacement and the height of the specimen. Two diagonal shear bands can be seen across the specimen. The shear-band width is strongly affected by the cell size L because strain increments are assumed to be equally distributed over each cell. **Figures 9b-9f** show the PSC tests results of specimens with grain inclusions. A perfect bonding is assumed between the grain and the soil matrix. As can be seen, the shear bands avoid the inclusion and form below the grain in **(b)** and **(c)**, but with the grains placed further down, the shear bands can form at the top of the specimen. When the shear bands form below the grain, the stress-strain curves fluctuate, whereas it is smoother when the shear band forms above the grain.

5.1 *Simulations with pore-pressure effect implemented*

A water-saturated triangular soil mass starts collapsing under its own weight. With a relatively low value of permeability coefficient (k_s = 0.01 m/s), dissipation of pore-pressure through the soil mass is fast, and several failure surfaces appear within the soil mass.

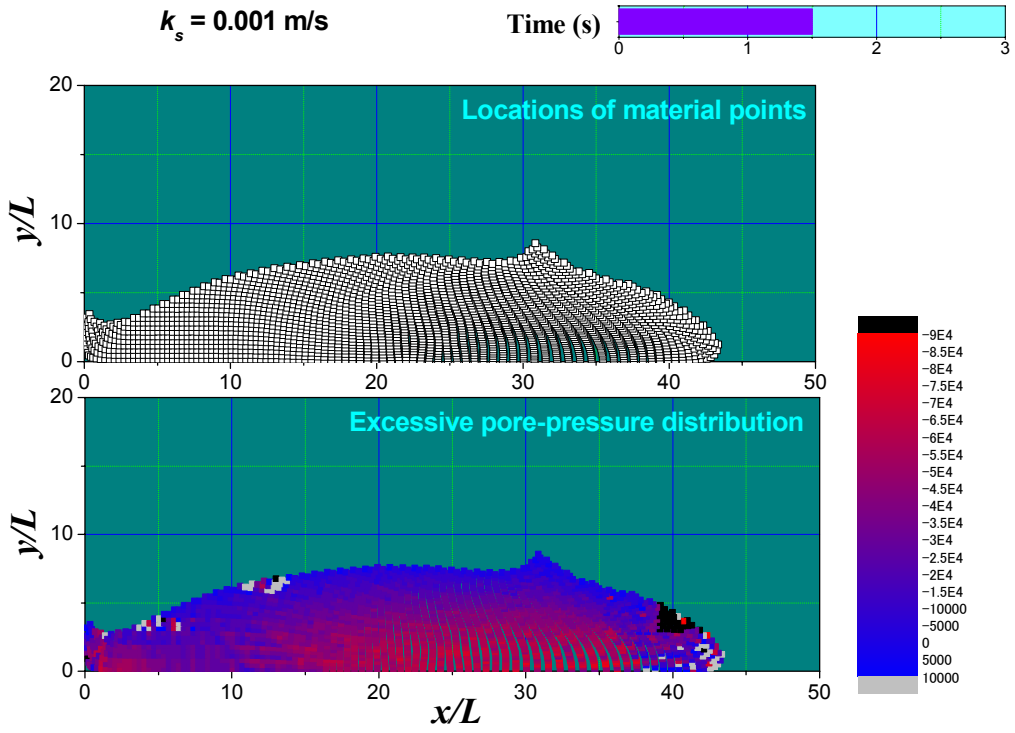

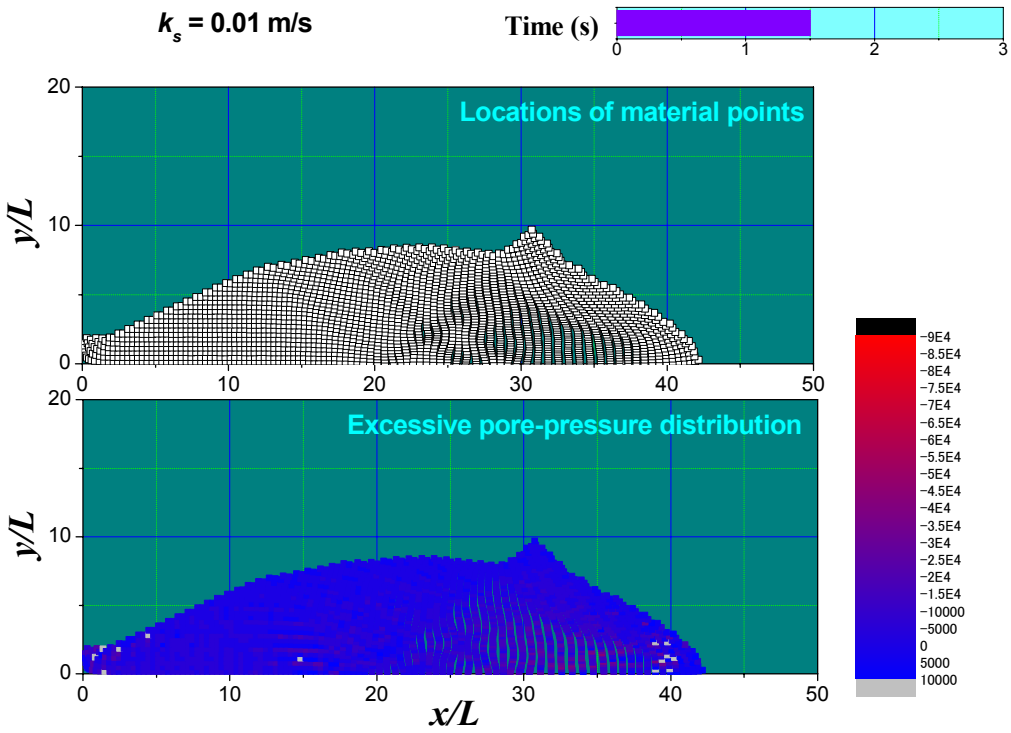
k_s = 0.01 m/s
Time (s)
0
1
2
3
Locations of material points
Excessive pore-pressure distribution
y/L
x/L
0
10
20
30
40
50
−9E4
−8.5E4
−8E4
−7.5E4
−7E4
−6.5E4
−6E4
−5.5E4
−5E4
−4.5E4
−4E4
−3.5E4
−3E4
−2.5E4
−2E4
−1.5E4
−10000
−5000
0
5000
10000